

University of Windsor

Scholarship at UWindor

Electronic Theses and Dissertations

Theses, Dissertations, and Major Papers

1-1-1999

Electrochemical performance of ball-milled magnesium(2)-nickel electrodes.

Hao (Shirley) Niu
University of Windsor

Follow this and additional works at: <https://scholar.uwindsor.ca/etd>

Recommended Citation

Niu, Hao (Shirley), "Electrochemical performance of ball-milled magnesium(2)-nickel electrodes." (1999). *Electronic Theses and Dissertations*. 6928.
<https://scholar.uwindsor.ca/etd/6928>

This online database contains the full-text of PhD dissertations and Masters' theses of University of Windsor students from 1954 forward. These documents are made available for personal study and research purposes only, in accordance with the Canadian Copyright Act and the Creative Commons license—CC BY-NC-ND (Attribution, Non-Commercial, No Derivative Works). Under this license, works must always be attributed to the copyright holder (original author), cannot be used for any commercial purposes, and may not be altered. Any other use would require the permission of the copyright holder. Students may inquire about withdrawing their dissertation and/or thesis from this database. For additional inquiries, please contact the repository administrator via email (scholarship@uwindsor.ca) or by telephone at 519-253-3000ext. 3208.

INFORMATION TO USERS

This manuscript has been reproduced from the microfilm master. UMI films the text directly from the original or copy submitted. Thus, some thesis and dissertation copies are in typewriter face, while others may be from any type of computer printer.

The quality of this reproduction is dependent upon the quality of the copy submitted. Broken or indistinct print, colored or poor quality illustrations and photographs, print bleedthrough, substandard margins, and improper alignment can adversely affect reproduction.

In the unlikely event that the author did not send UMI a complete manuscript and there are missing pages, these will be noted. Also, if unauthorized copyright material had to be removed, a note will indicate the deletion.

Oversize materials (e.g., maps, drawings, charts) are reproduced by sectioning the original, beginning at the upper left-hand corner and continuing from left to right in equal sections with small overlaps.

Photographs included in the original manuscript have been reproduced xerographically in this copy. Higher quality 6" x 9" black and white photographic prints are available for any photographs or illustrations appearing in this copy for an additional charge. Contact UMI directly to order.

ProQuest Information and Learning
300 North Zeeb Road, Ann Arbor, MI 48106-1346 USA
800-521-0600

UMI[®]

NOTE TO USERS

Page(s) not included in the original manuscript and are unavailable from the author or university. The manuscript was microfilmed as received.

15

This reproduction is the best copy available.

UMI

ELECTROCHEMICAL PERFORMANCE OF BALL-MILLED Mg₂Ni ELECTRODES

By

Hao (Shirley) Niu

A Thesis

**Submitted to the College of Graduate Studies and Research
through the Engineering Materials Program
of the Faculty of Engineering
in partial fulfillment of the requirements for the
Degree of Master of Applied Science at the
University of Windsor**

Windsor, Ontario, Canada

1999

© Hao (Shirley) Niu 1999



National Library
of Canada

Acquisitions and
Bibliographic Services

395 Wellington Street
Ottawa ON K1A 0N4
Canada

Bibliothèque nationale
du Canada

Acquisitions et
services bibliographiques

395, rue Wellington
Ottawa ON K1A 0N4
Canada

Your file *Votre référence*

Our file *Notre référence*

The author has granted a non-exclusive licence allowing the National Library of Canada to reproduce, loan, distribute or sell copies of this thesis in microform, paper or electronic formats.

The author retains ownership of the copyright in this thesis. Neither the thesis nor substantial extracts from it may be printed or otherwise reproduced without the author's permission.

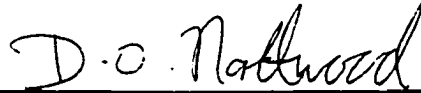
L'auteur a accordé une licence non exclusive permettant à la Bibliothèque nationale du Canada de reproduire, prêter, distribuer ou vendre des copies de cette thèse sous la forme de microfiche/film, de reproduction sur papier ou sur format électronique.

L'auteur conserve la propriété du droit d'auteur qui protège cette thèse. Ni la thèse ni des extraits substantiels de celle-ci ne doivent être imprimés ou autrement reproduits sans son autorisation.

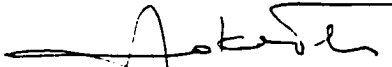
0-612-62259-2

Canada

APPROVED BY:



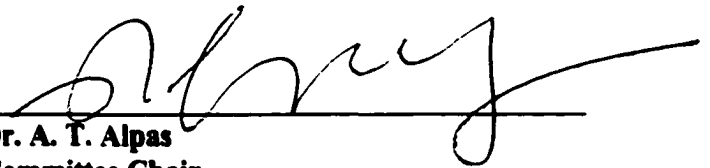
Dr. D. O. Northwood
Advisor
Engineering Materials Program



Dr. J. Sokolowski
Engineering Materials Program



Dr. R. Aroca
Department of Chemistry Science



Dr. A. T. Alpas
Committee Chair
Engineering Materials Program

ABSTRACT

A Mg_2Ni alloy was chosen to investigate the effects of a ball milling treatment on the alloy's electrochemical characteristics when the alloy was used as an electrode in a Ni-MH (metal hydride) battery. The mechanical grinding (MG) treatment was carried out in a Spex 8000 high-energy mill with ball milling times ranging from 0.5hrs to 80hrs, and ball-to-powder weight ratios ranging from 1:1 to 10:1. The structural changes taking place on ball milling were determined using X-ray diffraction and SEM (Scanning Electron Microscopy) techniques. Electrodes were fabricated from the ball-milled Mg_2Ni powders, and electrochemical measurements were made in a 6M KOH solution using a Solartron 1285 Potentiostat/Galvanostat. These measurements were used to determine electrochemical properties, including exchange current density, i_0 , polarization resistance, R_p , and charge/discharge characteristics.

Ball milling significantly accelerated the hydriding/dehydriding processes for the Mg_2Ni electrode. It reduced the particle size and correspondingly increased the specific surface area (SSA). Ball milling also produced an amorphous structure. As a result, the kinetic and thermodynamic parameters (the exchange current density, i_0 , hydrogen diffusion coefficient, D_0 ,

and internal strain, ϵ) increased. Defects, such as dislocations, and the large SSA introduced by ball milling were responsible for the acceleration of hydrogen absorption/desorption. The addition of elemental powders of either Ni or Cu to the Mg_2Ni electrode was beneficial in increasing the discharge capacity.

The equivalency of P-C-T and E-C-T curves at room temperature was demonstrated for a $LaNi_{4.7}Al_{0.3}$ alloy. The thermodynamic parameters, ΔH and ΔS for $LaNi_{4.7}Al_{0.3}$ alloy, calculated from the electrochemical measurements at room temperature are equivalent to the parameters determined in a gaseous environment. Based on the equivalency of the P-C-T and E-C-T curves, the P-C-T curve for the Mg_2Ni alloy was constructed from the electrochemical measurements at room temperature and 1atm pressure, rather than from the measurements at high temperatures and high pressures in a gaseous environment.

TO MY PARENTS

ACKNOWLEDGEMENTS

I would like to express my sincere thanks to Dr. D. O. Northwood for his supervision, interest, encouragement and friendship. The technical expertise of Mr. J.W. Robinson is much appreciated. I would also like to thank the people in the Hydrogen Storage Group at the University of Windsor for their valuable suggestions and helpful discussions.

Financial support from NSERC is also gratefully acknowledged.

Finally, I would like to extend my appreciation to the professors, staff and students of Engineering Materials Group, and the staff in the Technical Support Center.

TABLE OF CONTENTS

Abstract

Dedication

Acknowledgements

List of Tables

List of Figures

Nomenclature

Chapter 1

Introduction

Chapter 2

Literature Review

- 2.1 Hydrogen Storage Materials
 - 2.1.1 Metal Hydrogen Systems
 - 2.1.2 Thermodynamics and Kinetics of Metal Hydride Formation
 - 2.1.2 Hysteresis
- 2.2 Electrochemical Properties of Metal-Hydride Electrodes
 - 2.1.3 Development History
 - 2.2.2 Desirable Properties and Criteria for MH Electrode Materials
 - 2.2.3 Charge-Discharge Processes and Electrode Reactions
 - 2.2.4 The Electrochemical Characteristics of Metal-Hydride Electrodes
 - 2.2.5 Approaches Used to Improve Properties of MH Electrode Materials
- 2.3 Ball Milling
 - 2.3.1 Development History
 - 2.3.2 Equipment
 - 2.3.3 Mechanisms of Ball Milling
 - 2.3.4 Factors Affecting the Ball Milling Process
 - 2.3.5 Effect of Ball Milling on Hydrogen Storage Materials

Chapter 3

Experimental Details

- 3.1 Materials
- 3.2 Ball Milling Treatment
- 3.3 Materials Characterization Techniques
 - 3.3.1 Scanning Electron Microscopy
 - 3.3.2 X-ray Diffraction
 - 3.3.3 Calculation of Strain Introduced by Ball Milling
- 3.4 Electrochemical Measurements
 - 3.4.1 Metal Hydride Electrodes
 - 3.4.2 Measurement Parameters

Chapter 4 Electrochemical Properties of Ball-Milled Mg₂Ni Alloys

- 4.1 Specific Discharge Capacity
 - 4.1.1 Charge/Discharge Curves
 - 4.1.2 Specific Discharge Capacity
- 4.2 Electrochemical Kinetics: Polarization Behavior
 - 4.2.1 Open Circuit Potentials of Charged/Discharged Mg₂Ni Electrodes
 - 4.2.2 Polarization Properties
- 4.3 Oxidation of MG-Mg₂Ni Electrodes
- 4.4 Electrochemical Kinetics: Exchange Current Density
- 4.5 Hydrogen Diffusion Rate (D₀)
- 4.6 High Rate Dischargeability of Ball-Milled Mg₂Ni Electrodes
- 4.7 Effect of Additives on Charge/Discharge Properties of Ball-Milled Mg₂Ni Electrode
 - 4.7.1 Effect of Additives on Discharge Capacity
 - 4.7.2 Effect of Additives on Electrochemical Activity of Hydrogen Evolution Reaction
 - 4.7.3 Polarization Characteristics of MG-Mg₂Ni Alloy + Cu or Ni

Chapter 5 Transformation from Electrochemical Measurements to a P-C-T Curve

- 5.1 The transition from electrochemical measurements to P-C-T curve for LaNi_{4.7}Al_{0.3} electrode
- 5.2 Determination of ΔH and ΔS from electrochemical reactions for LaNi_{4.7}Al_{0.3} electrode
- 5.3 The construction of P-C-T curve from electrochemical measurements of the Mg₂Ni alloy

Chapter 6 Acceleration Mechanisms for Hydriding of MG-Mg₂Ni Electrodes

- 6.1 Amorphization of Mg₂Ni by Ball Milling
- 6.2 Surface Area and Particle Size
- 6.3 Internal Strain

Chapter 7 Conclusions and Recommendations for Future Work

7.1 Conclusions

7.2 Recommendations for Future Work

References

Vita Auctoris

LIST OF TABLES

Table 2.1	Summary of hydriding alloys and their properties
Table 2.2	The various properties for the $Mg_2Ni_{1-x}M_x$ and $Mg_{2-x}M_xNi$ alloys
Table 2.3	Thermodynamic data for the $LaNi_{5-x}Al_x+nH_2=LaNi_{5-x}Al_xH_{2n}$ reaction
Table 2.4	Relative partial molar quantities per gram-atom of hydrogen for FeTi alloys
Table 2.5	Thermodynamic data for Mg-Ni and Mg-Cu alloys
Table 2.6	Variation of the electrochemical capacity as a function of number of cycles in a sealed cell
Table 2.7	Effect of Cerium coating and ball milling on the electrochemical performance of metal hydride electrodes
Table 3.1	Ball milling parameters for Mg_2Ni alloy
Table 3.2	Mg_2Ni electrodes fabricated for this study
Table 4.1	Discharge capacities of ball milled Mg_2Ni at a ball-to-powder weight ratio of 5:1
Table 4.2	Relationship of discharge capacity to number of discharge cycles (Different ball milling times at ball-to-powder weight ratio of 5:1)
Table 4.3	Specific discharge capacity of 25 Hour ball milled Mg_2Ni electrodes at different ball-to-powder weight ratios
Table 4.4	Relationship of discharge capacity to number of discharge cycles (Different ball-to-powder weight ratios and T=25 hours)
Table 4.5	Electrochemical parameters for ball-milled Mg_2Ni electrodes (different ball milling times at a ball-to-powder weight ratio of 5:1)
Table 4.6	Electrochemical parameters for ball-milled Mg_2Ni electrodes (ball milling 25 hours at a ball-to-powder weight ratio of 10:1)
Table 4.7	The oxidation potentials for Mg_2Ni electrodes (ball milling 25 hours at a ball-to-powder weight ratio of 5:1)
Table 4.8	Exchange current density, i_0 , and polarization resistance, R_p , at 10 th cycle (Different ball milling times at a ball-to-weight ratio of 5:1)
Table 4.9	Exchange current density, i_0 , and polarization resistance, R_p , at 10 th cycle (Ball milling time of 25 hours at different ball-to-weight ratios)

Table 4.10	Hydrogen diffusion coefficients, D_0 , for MG-Mg ₂ Ni electrodes (Different ball milling times at a ball-to-powder weight ratio of 5:1)
Table 4.11	Hydrogen diffusion coefficients D_0 for MG-Mg ₂ Ni electrodes (Different ball-to-powder weight ratios at 25 hours ball milling)
Table 4.12	Discharge capacities at each discharge cycle of Mg ₂ Ni + Cu or Ni electrodes
Table 4.13	Overpotentials of Mg ₂ Ni Electrodes with Cu or Ni at the 5 th Cycle
Table 5.1	Measured potential, E_{eq} , and calculated P_{eq} for MG-Mg ₂ Ni electrodes
Table 6.1	Particle size and specific surface area of Mg ₂ Ni at different ball milling times

LIST OF FIGURES

- Fig.2.1 The AB_5 structure, using both the hexagonal or trigonal (right) and the orthorhombic (left) lattices. Also shown are tetrahedral (\bullet) and octahedral (\square) hydrogen sites and their possible degeneracy (-)[8].
- Fig.2.2 P-C-T plots for the $LaNi_5$ -H system at temperatures of 20,40 and 80°C[6].
- Fig.2.3 P-C-T plot for the $FeTi$ -H system. The initial alloy composition was 53.6%Fe and 46.7%Ti[13].
- Fig.2.4 The hexagonal (C14) Laves. The solid circles represent B atoms and the open circles are A atoms. The interstitial sites are shown: (a) B_4 sites, (b) AB_3 sites, (c) A_2B_2 sites[23].
- Fig.2.5 The cubic (C15) Laves phase. The A atoms are shown as open circles and the B atoms as solid ones. The three types of interstitial sites are given :a) B_4 sites, b) AB_3 sites, c) A_2B_2 sites[24].
- Fig.2.6 P-C-T plots for the Mg_2Ni - H_2 system at 298, 322 and 349°C. The initial alloy composition is 45.9wt%Mg and 54.6wt%Ni[30].
- Fig.2.7 P-C-T plots for the Mg_2Cu - H_2 system at 295, 325 and 347°C[31].
- Fig.2.8 Schematic of charge-discharge process[30].
- Fig.2.9 P-C-T plot showing the relationship between the equilibrium hydrogen pressure and the hydrogen concentration[31].
- Fig.2.10 Plot of $\ln P$ (P =dissociation pressure) vs. $1/T$ for $LaNi_{5-x}Al_x$ hydrides[10].
- Fig.2.11 Equilibrium dissociation pressure vs. $1/T$ for $FeTiH_x$: (a) $FeTiH_{0.1}$ - $FeTiH_1$, (b) $FeTiH_{1.2}$, (c) $FeTiH_{1.4}$, (d) $FeTiH_{1.6}$ [13].
- Fig.2.12 P-C-T plots for the Mg_2Ni -Mg- H_2 system at 303 and 323°C. The initial alloy composition is 72.9wt%Mg and 25.2wt%Ni. The arrow indicates predicated appearance of upper plateau[30].
- Fig.2.13 P-C-T diagram showing hysteresis in a metal-hydrogen system[31].
- Fig.2.14 Charge-discharge reaction mechanism of Ni/MH battery[66].
- Fig.2.15 Discharge capacity of $Mg_{1.9}Al_{0.1}Ni_{1-x}Y_x$ alloy electrodes vs. Y content (discharged at 5mA/g)[86].
- Fig.2.16 Influence of casting conditions on capacity decay curves at 20°C for $MmNi_{3.5}Co_{0.7}Al_{0.8}$ [91].
- Fig.2.17 Ideal microstructure of an encapsulated hydrogen-storage alloy[88].

- Fig.2.18 Discharge capacity behavior for prototype test cells with the anode of MH ($\text{MmNi}_{3.5}\text{Al}_{0.8}\text{Co}_{0.7}$) sample; ○: modified by mechanical treatment for 1h with 20w/o added cobalt; ●: chemical-coated with 11w/o Ni; □: only metal hydride without any modification[91].
- Fig.2.19 Hydrogen absorption curves for the first cycle for $\text{TiFe}_{1-x}\text{Cr}_x$ alloys at room temperature and a hydrogen gas pressure of 3.92MPa. AM: as melted; H: homogenized[93].
- Fig.2.20 Schematic diagrams of ball-powder-ball collision[112].
- Fig.2.21 Schematic illustration of various milling methods: (a) attrition, (b) planetary, (c) vibratory, (d) horizontal ball milling[113].
- Fig.2.22 The hydrogen absorption curves of LaNi_5 powder at 293K and 2MPa H_2 after ball milling for 0, 0.015, 0.06, 0.3 and 0.6 ks[116].
- Fig.2.23 (a) The hydrogen absorption curves of FeTi powder at 283K and 2MPa H_2 after ball milling for 0, 1.8, 11 and 86 ks in an argon atmosphere and without exposure to the air[79].
(b) SEM micrographs of original FeTi powder and powders the ball-milled for 1.8, 1.1 and 86ks in an argon atmosphere[117].
- Fig.2.24 The hydrogen absorption curves of Mg_2Ni powder at 283K and 2MPa H_2 after ball milling for 0, 0.06, 0.3 and 1.8 ks in an argon atmosphere[118].
- Fig.2.25 XRD patterns of (a) Mg_2Ni and (b) MG- Mg_2Ni [119].
- Fig.3.1 SEM morphology of as-cast Mg_2Ni and Ni powder.
- Fig.3.2 X-ray diffraction pattern of as-received Mg_2Ni and Ni powders.
- Fig.3.3 Photograph of the Spex 8000 mill/mixer.
- Fig.3.4 Photograph of Spex 8000 mill/mixer and its single clamp.
- Fig.3.5 Schematic drawing of the ball trajectories for the Spex 8000 mill/mixer.
- Fig.3.6 Photograph of tungsten carbide container and milling balls.
- Fig.3.7 (a) Microstructure of as-cast Mg_2Ni alloy, (b) Magnified eutectic structure and interface area.
- Fig.3.8 Qualitative compositional analysis of dendrites and interface area.
- Fig.3.9 Effect of lattice strain on Debye-line width and position.
- Fig.3.10 X-ray diffraction pattern for annealed Mg_2Ni powder.
- Fig.3.11 Schematic drawing of standard tri-electrode measurement system.
- Fig.3.12 Photograph of electrochemical measurement system.

- Fig.3.13 Photograph of the tri-electrode measurement system.
- Fig.3.14 Schematic diagram of experimental electrode.
- Fig.3.15 Schematic diagram of the experimental Sievert's apparatus.
- Fig.4.1 Charge potential vs. charge time for as-cast Mg_2Ni electrode
- Fig.4.2 Charge potential vs. charge time for MG- Mg_2Ni electrode (MG 10 hours at a ball-to-powder weight ratio of 5:1)
- Fig.4.3 Charge potential vs. charge time for MG- Mg_2Ni electrode (MG 25 hours at a ball-to-powder weight ratio of 5:1)
- Fig.4.4 Charge potential vs. charge time for MG- Mg_2Ni electrode (MG 50 hours at a ball-to-powder weight ratio of 5:1)
- Fig.4.5 Charge potential vs. charge time for MG- Mg_2Ni electrode (MG 25 hours at a ball-to-powder weight ratio of 1:1)
- Fig.4.6 Charge potential vs. charge time for MG- Mg_2Ni electrode (MG 25 hours at a ball-to-powder weight ratio of 10:1)
- Fig.4.7 Discharge potential vs. discharge time for as-cast Mg_2Ni electrode
- Fig.4.8 Discharge potential vs. discharge time for MG- Mg_2Ni electrode (MG 10 hours at a ball-to-powder weight ratio of 5:1)
- Fig.4.9 Discharge potential vs. discharge time for MG- Mg_2Ni electrode (MG 25 hours at a ball-to-powder weight ratio of 5:1)
- Fig.4.10 Discharge potential vs. discharge time for MG- Mg_2Ni electrode (MG 50 hours at a ball-to-powder weight ratio of 5:1)
- Fig.4.11 Discharge potential vs. discharge time for MG- Mg_2Ni electrode (MG 25 hours at a ball-to-powder weight ratio of 10:1)
- Fig.4.12 Discharge potential vs. discharge time for MG- Mg_2Ni electrode (MG 25 hours at a ball-to-powder weight ratio of 1:1)
- Fig.4.13 Discharge capacity of MG- Mg_2Ni electrodes vs. number of discharge cycles for different milling times
- Fig.4.14 Discharge capacity of MG- Mg_2Ni electrodes vs. number of discharge cycles at different ball-to-powder weight ratios
- Fig.4.15 Open circuit potential vs. time for MG- Mg_2Ni electrode (MG 10 hours at a ball-to-powder weight ratio of 5:1)
- Fig.4.16 Open circuit potential vs. time for MG- Mg_2Ni electrode (MG 25 hours at a ball-to-powder weight ratio of 5:1)

- Fig.4.17 Open circuit potential vs. time for MG-Mg₂Ni electrode
(MG 50 hours at a ball-to-powder weight ratio of 5:1)
- Fig.4.18 Polarization characteristics for MG-Mg₂Ni electrode
(MG 10 hours at ball-to-powder weight ratio of 5:1 and discharged at 200mA/g)
- Fig.4.19 Polarization characteristics for MG-Mg₂Ni electrode
(MG 25 hours at a ball-to-powder weight ratio of 5:1 and discharged at 200mA/g)
- Fig.4.20 Polarization characteristics for MG-Mg₂Ni electrode
(MG 50 hours at a ball-to-powder weight ratio of 5:1 and discharged at 200mA/g)
- Fig.4.21 Experimental and calculated polarization curves for 25 hours ball milled Mg₂Ni electrode at a ball-to-powder weight ratio of 5:1
- Fig.4.22 Polarization characteristics for MG-Mg₂Ni electrode
(MG 25 hours at a ball-to-powder weight ratio of 10:1)
- Fig.4.23 Anodic peak current change vs. number of charge/discharge cycles for MG-Mg₂Ni electrodes (MG 25 hours at a ball-to-powder weight ratio of 5:1)
- Fig.4.24 Cyclic voltammograms of MG-Mg₂Ni electrode after discharge
- Fig.4.25 Linear polarization curves for MG-Mg₂Ni electrodes at different number of charge/discharge cycles
(MG 25 hours at a ball-to-powder weight ratio of 5:1 and discharged at 50mA/g)
- Fig.4.26 Polarization resistance, R_p , for MG-Mg₂Ni electrodes
(Ball-to-powder weight ratio of 5:1 at different ball milling times)
- Fig.4.27 Exchange current density, i_0 , for MG-Mg₂Ni electrodes
(Ball-to-powder weight ratio of 5:1 at different ball milling times)
- Fig.4.28 Exchange current density, i_0 , for MG-Mg₂Ni electrodes
(MG 25 hours at different ball-to-powder weight ratios)
- Fig.4.29 Hydrogen concentration, H/M, and exchange current density, i_0 , vs. milling time
- Fig.4.30 Hydrogen concentration, H/M, and exchange current density, i_0 , vs. ball-to-powder weight ratio at 10th cycle
- Fig.4.31 Correlation between discharge capacity and discharge current density
(Ball-to-powder weight ratio of 5:1 at different milling times)
- Fig.4.32 Correlation between discharge capacity and discharge current density
(MG 25 hours at different ball-to-powder weight ratios)
- Fig.4.33 Discharge capacity vs. number of cycles for different discharge current density and high rate dischargeability
- Fig.4.34 High rate dischargeability vs. exchange current density i_0

- Fig.4.35a Charge potential vs. charge time for MG-Mg₂Ni+Ni electrode (MG 25 hours at a ball-to-powder weight ratio of 5:1)
- Fig.4.35b Charge potential vs. charge time for MG-Mg₂Ni+Cu electrode (MG 25 hours at a ball-to-powder weight ratio of 5:1)
- Fig.4.36a Discharge potential vs. charge time for MG-Mg₂Ni+Ni electrode (MG 25 hours at a ball-to-powder weight ratio of 5:1)
- Fig.4.36b Discharge potential vs. charge time for MG-Mg₂Ni+Cu electrode (MG 25 hours at a ball-to-powder weight ratio of 5:1)
- Fig.4.37 Effect of adding Cu or Ni on the discharge capacity of MG-Mg₂Ni electrodes (MG 25 hours at a ball-to-powder weight ratio of 5:1)
- Fig.4.38 Open circuit potential vs. time for MG-Mg₂Ni+Ni electrode (MG 25 hours at a ball-to-powder weight ratio of 5:1)
- Fig.4.39 Polarization resistance, R_p , for MG-Mg₂Ni electrodes with different additives (MG 25 hours at a ball-to-powder weight ratio of 5:1)
- Fig.4.40 Exchange current density, i_0 , of MG-Mg₂Ni electrodes with different additives (MG 25 hours at a ball-to-powder weight ratio of 5:1)
- Fig.4.41 Diffusion coefficient, D_0 , of hydrogen through Mg-Mg₂Ni electrodes
- Fig.4.42 Polarization characteristics for MG-Mg₂Ni+Cu electrode (MG 25 hours at a ball-to-powder weight ratio of 5:1)
- Fig.4.43 Polarization characteristics for MG-Mg₂Ni+Ni electrode (MG 25 hours at a ball-to-powder weight ratio of 5:1)
- Fig.5.1 Transition from electrochemical measurements to P-C-T curve for LaNi_{4.7}Al_{0.3} at room temperature
- Fig.5.2 P-C-T diagram for MG-Mg₂Ni electrode at room temperature (MG 25 hours and ball-to-weight ratio of 5:1)
- Fig.6.1 X-ray diffraction patterns of Mg₂Ni alloy for different ball milling times at a ball-to-powder weight ratio of 5:1
- Fig.6.2 Crystal size vs. ball milling time for Mg₂Ni alloy
- Fig.6.3 Particle morphologies of Mg₂Ni alloy at different ball milling times for Mg₂Ni alloy
- Fig.6.4 Internal strain vs. ball milling time for Mg₂Ni alloy
- Fig.6.5 Internal strain vs. crystal size for ball-milled Mg₂Ni alloy
- Fig.6.6 Internal strain and exchange current density vs. ball milling time for Mg₂Ni alloy

Fig.6.7 Internal strain and hydrogen diffusion coefficient, D_0 , vs. ball milling time for Mg_2Ni alloy

Fig.6.8 Internal strain and hydrogen concentration, H/M , vs. ball milling time for Mg_2Ni alloy

NOMENCLATURE

C	the hydrogen concentration at time t
C_0	the hydrogen concentration at time t=0
d_0	the interplanar spacing
D	the crystal size
D_0	hydrogen diffusion coefficient
f	fugacity
F	the Farady constant
F'	the reacted fraction
ΔG_f	the standard free energy of formation of the metal hydride
ΔH	enthalpy change
ΔH_f	the standard enthalpy of formation of a metal hydride
i_d	limit current density
i_0	exchange current density
K	the Scherrer constant
K_p	the equilibrium constant
Q	the electrochemical capacity per unit weight of alloy (in mAh/g)
r	the atomic radius of element
r'	the radius of the sphere
R	gas constant
R_p	polarization resistance
ΔS_f	the standard entropy of formation
T	absolute temperature (K)
W	the average molecular weight of the alloy
ΔX_H	the partial molar enthalpy
ε	internal strain
μ_{op}	the chemical potential of the hydrogen in gaseous phase
μ_{eq}	the chemical potential of the hydrogen in hydride phase
θ	Bragg angle
β	the width of a diffraction line measured at the full width at its half intensity
λ	the wavelength of the radiation used
η	overpotential
δ	constant representing the decay exponent

CHAPTER 1 INTRODUCTION

Hydrogen storage alloys, which were discovered about 20 years ago, have been widely studied for their application as energy storage media and battery electrodes. The hydriding alloys (metal hydrides: MH) are used as the negative electrode of a rechargeable battery, essentially replacing the Cadmium electrode in the widely used Ni-Cd battery. The main driving force for replacing the Cadmium is environmental, Cd being a relatively toxic material. There are, of course, other advantages of the Ni-MH battery over the Ni-Cd battery, including potentially higher energy density, higher charge/discharge rates, low temperature capability and an absence of a memory effect ^[1, 2].

Magnesium and Mg-based alloy as hydrogen storage materials meet two very important storage criteria: large amount of hydrogen storage (7.6wt% and 3.8wt% respectively), which is more than twice as much as either the rare-earth hydrogen-storage alloys (e.g., LaNi₅ absorbs 1.4wt% hydrogen) or the titanium hydrogen-storage alloys (e.g., FeTi absorbs 1.9wt% hydrogen), and it is inexpensive. Magnesium-based alloys are considered to be the most promising materials for hydrogen storage because of their high hydrogen storage capacity, light weight, abundance as a constituent in the earth's crust ^[3]. Of all the magnesium-based alloys, Mg₂Ni is the most remarkable due to its relative high capacity. However, the reaction of magnesium alloys with hydrogen requires appreciably high temperatures (200°C to 300°C) and pressures (up to 10atm) due to hydriding/dehydriding difficulties. The kinetics of hydriding and dehydriding are slow. It is almost impossible to absorb and desorb hydrogen for Mg₂Ni at either 1atm or room temperature in a gaseous environment.

Chapter 1 Introduction

To improve the hydrogen absorbing/desorbing properties of Mg_2Ni and make the Mg_2Ni alloy applicable as a commercial rechargeable-battery negative electrode, work is required in three areas namely: 1) understanding the mechanisms of hydriding/dehydriding in the Mg_2Ni alloy; 2) improving the thermodynamics and kinetics of hydriding/dehydriding for the Mg_2Ni alloy; and 3) developing electrochemical methods to study the hydriding/dehydriding characteristics of the Mg_2Ni rather than the gaseous (manometric) method which requires high pressures and temperatures and is time consuming.

Mechanical grinding, alloying and surface modification can be utilized to modify the structure and surface properties and thus improve the characteristics of the negative electrode. In this investigation, mechanical grinding (MG) and alloying methods were applied. This resulted in a marked improvement in the activation and hydrogen storage properties such that hydrogen can be absorbed easily and to sufficiently high levels by the Mg_2Ni alloys. Room temperature electrochemical measurements, such as, exchange current density, overpotential, polarization resistance and the discharge capacity, were conducted to investigate the characteristics of the ball-milled Mg_2Ni alloy.

In this investigation, the mechanical grinding was utilized to prepare the Mg_2Ni alloy powders. The electrochemical property measurements were carried out on MG- Mg_2Ni electrode and finally the equivalency of P-C-T and E-C-T properties were demonstrated.

CHAPTER 2 LITERATURE REVIEW

2.1 The Hydrogen Storage Materials

Intermetallic compounds (IMCs) are highly ordered (usually brittle) alloys of two or more metallic elements, usually having narrow, integer stoichiometries (A_xB_y) and crystal structures that are different from either of the parent elements (A and B). There are several classes of IMCs, based on composition and crystal structure. The key to all IMCs hydride technology is the combination of strong hydride forming elements, A, with weak hydride forming elements, B, in a natural interger ratio to form intermetallic compounds A_xB_y that can react reversibly with H_2 to form an intermediate strength hydride $A_xB_yH_z$ ^[4].

2.1.1 Metal Hydride Systems

Storage Criteria

For hydrides to be useful as energy storage media, a number of requirements must be met.

The hydride should:

- (1) Be capable of storing large quantities of hydrogen;
- (2) Be readily formed and decomposed;
- (3) Be as safe as other energy carriers;
- (4) Have reaction kinetics satisfying the charge/discharge requirements of the system;
- (5) Have the capability of being cycled without alteration in pressure or temperature during the life of the system;
- (6) Have low hysteresis;

Chapter 2 Literature Review

(7) Have resistance to poisoning from contaminants such as O_2 , H_2O , CO , etc.;

(8) Have low cost.

Types and Characteristics of Metal Hydride Systems

The metal hydride systems currently under investigation can be mainly divided into four classes, namely, AB_5 , AB , AB_2 and Mg-based compounds. Table 2.1 summarizes the properties of each alloy class as they relate to the storage criteria^[5].

AB₅ Compounds

In the AB_5 system, the majority of work has been done on $LaNi_5$. This material has a hexagonal or orthorhombic structure with a $CaCu_5$ type lattice (Fig. 2.1). Hydrides are formed with plateau pressures of a few atmospheres at temperatures up to $100^\circ C$ (Fig. 2.2^[6]). The enthalpy change, ΔH , is of the order -30.1 kJ/mol H_2 . Attractive properties include high hydrogen capacity, low hysteresis and good tolerance to gaseous impurities, and ease of activation in the initial cycle.

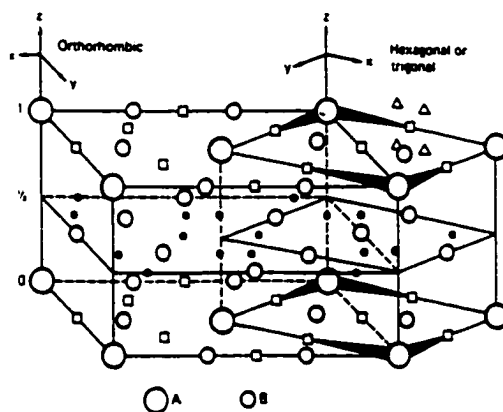


Fig.2.1 The AB_5 structure, using both the hexagonal or trigonal (right) and the orthorhombic (left) lattices. Also shown are tetrahedral (\bullet) and octahedral (\square) hydrogen sites and their possible degeneracy (-)[6].

Table 2.1^[2]

Summary of Hydriding Alloys and Their Properties

ALLOY TYPES	QUANTITY OF HYDROGEN ABSORBED		KINETICS	STABILITY OF HYDRIDE	CYCLING DEGRADATION	HYSTERESIS	RESISTANCE TO POISONING	COST
	H/M	Wt%						
AB₅ Examples LaNi ₅ LaCo ₅ CeCo ₅ LaMn ₃ Co ₂	1.0 up to 1.5	1.4% to max 1.9%	Rapid kinetics, of the order of a few seconds due to surface segregation. Heat transfer controlled. No activation required.	Relatively stable. $\Delta H \sim -29.26$ kcal/mole, 12.54 kJ/mole. Stability changes, up or down, with alloy substitutions. $P_{eq} \sim 2.2$ MPa at R.T. for LaNi ₅ .	May be degradation after 300-400 cycles due to formation of stable hydrides (LaNi ₃)	Moderate hysteresis at low temperatures.	Good resistance to H ₂ O and O ₂ poisoning. Susceptible to CO poisoning, partial reactivation possible.	Quite expensive because of cost of La and Ni.
AB Examples FeTi ZrNi TiAl Fe _{1-x} Mn _x Ti	1.0	1.8% max	Moderate kinetics partially controlled by heat transfer. Needs activation for surface segregation.	Stability varies from $\Delta H \sim -12.54$ kJ/mole for FeTi based alloys to $\Delta H = -45.98$ to -79.42 kcal/mole for other AB compounds. $P_{eq} \sim 4-5$ MPa at R.T.	No evidence as yet, but no high cycle experiments have been done.	Pronounced hysteresis in FeTi, however can be reduced by addition of Mn.	General poor resistance to poisoning for FeTi. Especially susceptible to CO. Partial reactivation possible. Addition of Mn gives better CO resistance.	Relatively inexpensive. Fe fairly cheap.

Table 2.1 (continued)

Summary of Hydriding Alloys and Their Properties

<p>AB₂ Examples ZrV₂ ZrCr₂ ZrMn₂ LaNi₂ Zr (Fe, V_{1-x})₂ Zr (Co, Cr_{1-x})₂</p>	<p>From 1.0 up to 2.0</p>	<p>From 1.5 to 2.0%</p>	<p>Rapid kinetics. no activation necessary in most cases. not much data on kinetics.</p>	<p>Generally quite stable. $\Delta H \sim -75.24$ kJ/mole for binaries. pseudobinaries decrease stability to acceptable levels.</p>	<p>No evidence as yet, but no high cycle experiments have been done.</p>	<p>Low hysteresis in binary compounds. moderate hysteresis in pseudobinaries</p>	<p>No report poisoning problems, but little work has been done in this area.</p>	<p>Quite expensive because of cost of Zr metal.</p>
<p>Mg-Based Compounds Examples Mg Mg₂Ni Mg₂Cu</p>	<p>1.3 up to 2.0</p>	<p>From 3.5% up to 6.7%</p>	<p>Sluggish kinetics. Activation is necessary and difficult. Rate limited by diffusion of H atoms (when activated). If segregation stops rate limited by dislocative chemisorption and associative desorption. Ni, Cu, etc. are added as catalysts.</p>	<p>Very stable. $\Delta H \sim -75.24$ kJ/mole. $P_{eq} \sim 1$MPa at 300°C</p>	<p>Cycling may cause reduction in desorption rate of Mg-Mg₂Ni.</p>	<p>None reported.</p>	<p>Very susceptible to poisoning by O₂, H₂O, CO, etc.</p>	<p>Relatively inexpensive because of high Mg content.</p>

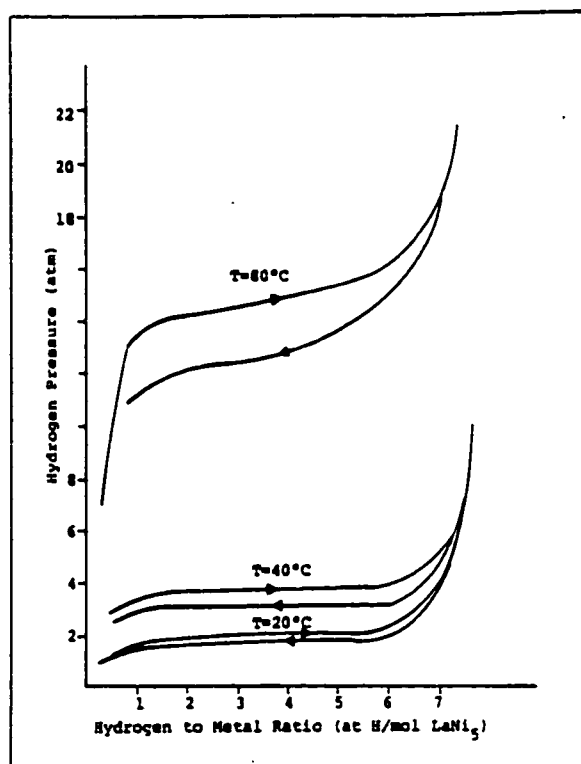


Fig.2.2 P-C-T plots for the LaNi₅-H system at temperatures of 20,40 and 80°C[6].

LaNi₅ also shows good kinetics, the reaction rate being controlled by heat transfer, with nickel serving as a catalyst for the hydriding reactions. The major problem associated with these materials lies in the area of alloy cost and cyclic degradation. Alloy cost can be lowered somewhat by substituting Ce, Nd, Gd, Y, Er, Th and Zr for La^[7-9] and Al, Co, Fe, Cr and Cu for Ni^[7, 10-12]. The LaNi₅-H₂ system has been extensively investigated. In many applications, materials are required whose plateau pressure is different from those of LaNi₅H_{6.7}. The desorption pressure of LaNi₅H_{6.7} in decomposition pressure without impairing the kinetics or the hydrogen carrying capacities. The important new result is that Al substitutions allow a wide range of decomposition pressure to be spanned in a continuous fashion. In the range 0-20%Al, the plateau pressures of the LaNi₅-LaNi₄Al hydride system are reduced by a factor of ~300.

Chapter 2 Literature Review

AB Compounds

The AB alloys store hydrogen at a low cost and exhibit plateau pressures of a few atmospheres at temperatures up to 100°C. Most of the work done on AB compounds has been restricted to FeTi, which has a CsCl type crystal structure. Pressure-composition isotherms for the FeTi-H system are shown in Fig. 2.3. Reilly *et al.*^[13] reported that iron and titanium form two known stable intermetallic compounds, FeTi and Fe₂Ti. It is also generally accepted that a third compound, FeTi₂, exists above 1000°C, decomposing to FeTi and Ti below that temperature. Two hydrides are formed, i.e., a monohydride with a tetragonal structure and a dihydride which forms a cubic structure. The ΔH value for the monohydride is -28.0 kJ/mol H₂.

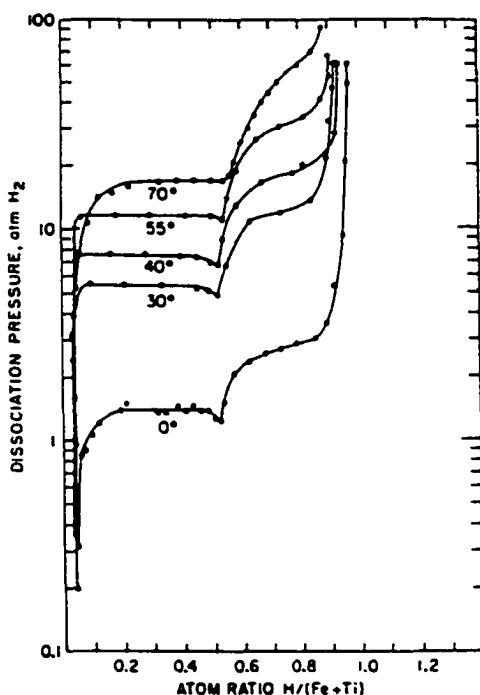


Fig.2.3 P-C-T plot for the FeTi-H system.
The initial alloy composition was 53.6%Fe and 46.7%Ti[13].

Chapter 2 Literature Review

It is necessary to initially activate FeTi before it will react at a practical rate with hydrogen. Reaction kinetics is considerably slower than in the AB₃ case and can be affected severely by contaminants such as O₂, H₂O and CO^[14,16]. Other disadvantages of the FeTi-H system are pronounced hysteresis and the weight of the alloys. These problems can be alleviated to a degree by the substitution of various alloying elements, such as Mn and Al for Fe. Manganese assists by reducing hysteresis and providing some resistance to poisoning^[14,16], while aluminum lowers the overall weight of the alloy^[17].

AB₂ Compounds

The research on AB₂ type Laves phase hydrogen storage alloys started early in the 1960's. Wang^[18] worked on ZrB₂ (B=V, Cr, Mn, Fe, Co, Mo, Al) and found that for B=V, Cr, Mn, the alloys could absorb and desorb large quantities of hydrogen (H/M=5). In AB₂ Laves phase alloys, as the atomic radius of element A is much bigger than that of B (optimum ratio $r_A/r_B=1.225$), the atoms are arranged in very compact layered lattice structures with 17 tetrahedral interstitial cavities, which are potential sites for storing hydrogen atoms. Due to electrostatic repulsion forces, any two tetrahedral cavities with an adjacent surface can not store hydrogen atoms simultaneously. The maximum absorbable number of hydrogen atoms is around 6 for both AB₂ and AB₃ alloys. AB₂ compounds have much higher hydrogen wt.% capacity than AB₃ compounds.

The AB₂ compounds have a high storage capacity, show good resistance to impurities and exhibit low hysteresis^[19-22]. These alloys form one of two Laves phase structures, either the hexagonal C14 structure (Fig. 2.4^[23]) or the cubic C15 structure (Fig. 2.5^[24]). The best sorption characteristics have been observed for ZrV₂, ZrCr₂ and ZrMn₂ with hydrogen pickups approaching ~6 H atoms per formula unit. Hydrided AB₂ compounds tend to be quite stable, with ΔH values

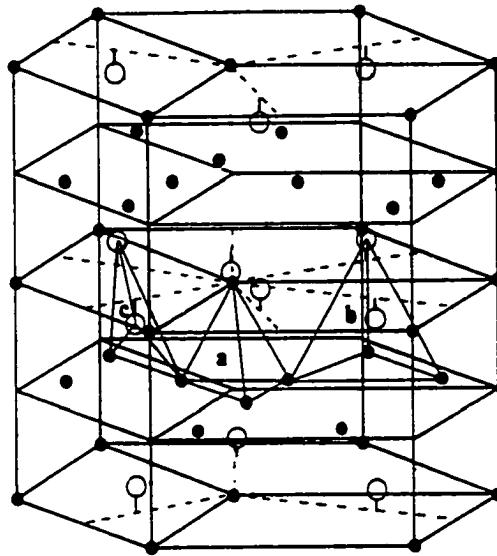


Fig.2.4 The hexagonal (C14) Laves. The solid circles represent B atoms and the open circles are A atoms. The interstitial sites are shown:
 (a) B₄ sites, (b) AB₃ sites, (c) A₂B₂ sites[23].

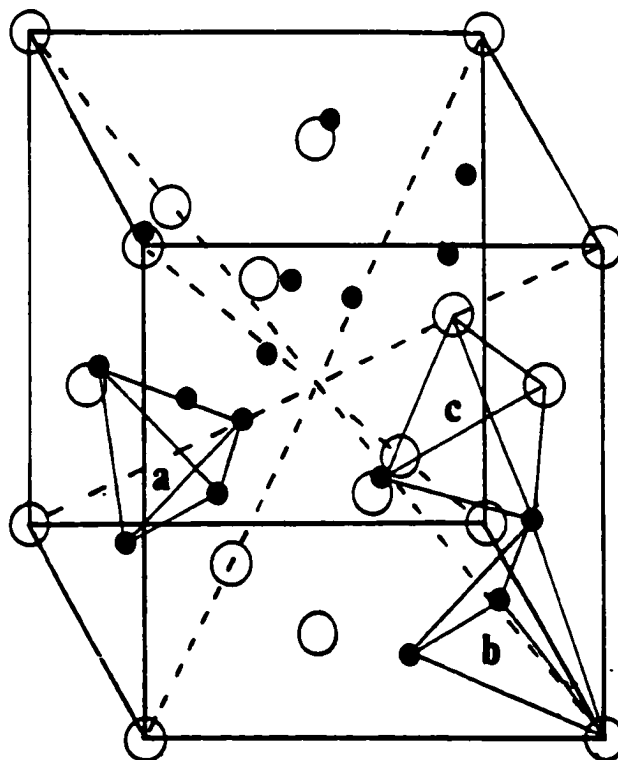


Fig.2.5 The cubic (C15) Laves phase. The A atoms are shown as open circles and the B atoms as solid ones. The three types of interstitial sites are given:
 a) B₄ sites, b) AB₃ sites, c) A₂B₂ sites[24]

Chapter 2 Literature Review

greater than 50.2 kJ/mol in magnitude. The methods available to lower the stability, while at the same time maintaining adequate absorption capacity include: (1) substitute some of the Mn, Cr, Mo or V with Fe or Co^[19,25-27]; (2) On the A side, substitute Ti or Ho for Zr, e.g. $Zr_{0.7}Ti_{0.1}Mn_{0.2}$, $Zr_{0.2}Ho_{0.8}Co_2$; (3) On the B side, substitute transitional elements Ni, Fe, Co, Mo, Mn, V or Cr, e.g. $Zr_{0.5}Co_{0.5}Mn_{1.2}Fe_{0.8}$; (4) Substitute A and B elements simultaneously, e.g. $Zr_{0.9}Ti_{0.1}Cr_{0.6}Fe_{1.4}$, $Zr_{0.7}Ti_{0.3}CrFe$; (5) Use excess B to form a non-stoichiometric alloy, e.g. $ZrCr_2Fe_{0.8}$, $ZrCrFeNi_{0.8}$. In these ways, the stabilities can be reduced to acceptable levels. Partial substitution of Ti for Zr can also be employed in order to reduce the cost of the hydriding alloy^[28,29].

Magnesium and Magnesium-Based Compounds

Magnesium and Mg-based alloys as hydrogen storage materials meet two very important storage criteria: they can store large amounts of hydrogen (7.6wt% and 3.8wt% respectively), more than twice as much as either rare-earth hydrogen-storage alloys (e.g., $LaNi_5$ absorbs 1.4wt% hydrogen) or titanium hydrogen-storage alloys (e.g., FeTi absorbs 1.9wt% hydrogen), and they are inexpensive. Magnesium-based alloys are considered to be most promising materials for hydrogen-storage because of their high hydrogen-storage capacity, light weight, abundance of the constituents in the earth's crust, and low-cost compared with alternative systems^[3]. On the debit side, however, the reactions of Mg-and Mg alloys with hydrogen require appreciably higher temperatures (200-300°C) and pressures (up to 10atm) due to sluggish hydriding/dehydriding kinetics at room temperature. Additions of rare earth and transition metals have been somewhat successful in increasing desorption rates of hydrogen in magnesium. Reilly and Wiswall^[30,31] reported successful hydriding and dehydriding experiments with Mg_2Ni and Mg_2Cu in the 1960's. Owing to the relative stability of MgH_2 , modifications of $MgMH_x$ (M=transition metal) were made to decrease the dissociation temperature of the hydride^[32]. Cu and Ni have been added to Mg either as alloying

Chapter 2 Literature Review

additions or catalysts. Although the absorption capacity is diminished, these elements can improve the reaction kinetics by providing an oxide-free path for hydrogen sorption. The pressure-composition isotherms for Mg_2Ni-H system and Mg_2Cu-H system are shown in Figs 2.6^[30] and 2.7^[31].

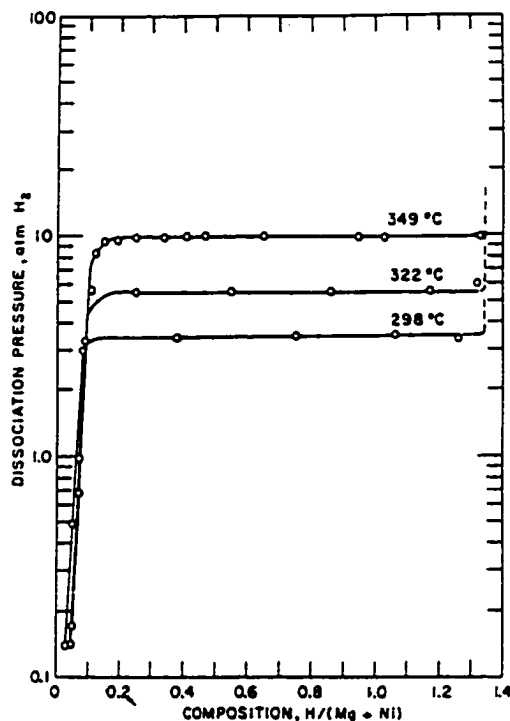


Fig.2.6 P-C-T plots for the Mg_2Ni-H_2 system at 298, 322 and 349°C. The initial alloy composition is 45.9wt%Mg and 54.6wt%Ni[30].

Oesterricher et al.^[33] have suggested that the partial substitution of Mg in Mg_2Ni by an element of a more exothermic heat of hydride formation, such as Ca, Sc or Y may result in a rise of equilibrium pressure for the substituted Mg_2Ni . This would bring Mg_2Ni into the range of reversible room temperature hydrogen sorption. The absorption and desorption rates for these alloys are close to those obtained with Mg_2Ni . Other properties of these compounds are listed in Table 2.2^[34-39]. The ΔH value for the Mg_2Ni alloy is -64.4 kJ/mol H_2 .

Table 2.2^[32-37]The Various Properties for the $Mg_2Ni_{1-x}M_x$ and $Mg_{2-x}M_xNi$ alloys (M=transition and non-transition metals; $0 \leq x \leq 1$)

ALLOY COMPOSITION (ATOMIC RATION)	CELL PARAMETERS (HEXAGONAL STRUCTURE)		HYDROGEN CONTENT			HYDRIDE DISSOCIATION TEMPERATURE AT $P_{H_2}=1$ MPa (°C)	THERMODYNAMIC DATA FOR THE HYDRIDE	
	A (Å)	C (Å)	H-Atoms per molecule	Expl. Wt%	Theo. Wt%		ΔH (kJ/mol /H ₂)	ΔS (kJ/molK/H ₂)
Mg	3.21	5.21	2.00	7.60	7.65	287	-74.5	-135.0
Mg ₂ Ni	5.19	13.25	4.20	3.60	3.62	250	-64.5	-122.0
Mg ₂ Ni _{0.75} V _{0.25}	5.22	13.29	3.17	2.90	3.66	250	-62.2	-119.1
Mg ₂ Ni _{0.75} Cr _{0.25}	5.21	13.26	3.29	3.00	3.65	248	-60.0	-114.9
Mg ₂ Ni _{0.75} Fe _{0.25}	5.22	13.28	3.09	2.80	3.62	253	-63.2	-121.0
Mg ₂ Ni _{0.75} Co _{0.25}	5.21	13.18	3.45	3.10	3.59	279	-64.5	-123.5
Mg ₂ Ni _{0.75} Cu _{0.25}	5.20	13.43	3.30	227	-53.2	-101.9
Mg ₂ Ni _{0.75} Zn _{0.25}	5.24	13.46	3.66	246	-61.5	-117.8
Mg ₂ Ni _{0.75} Bc _{0.25}	5.28	13.41	250	-79.9	-153.0
Mg _{1.92} Al _{0.08} Ni	5.19	13.25	-70.5	-135.0

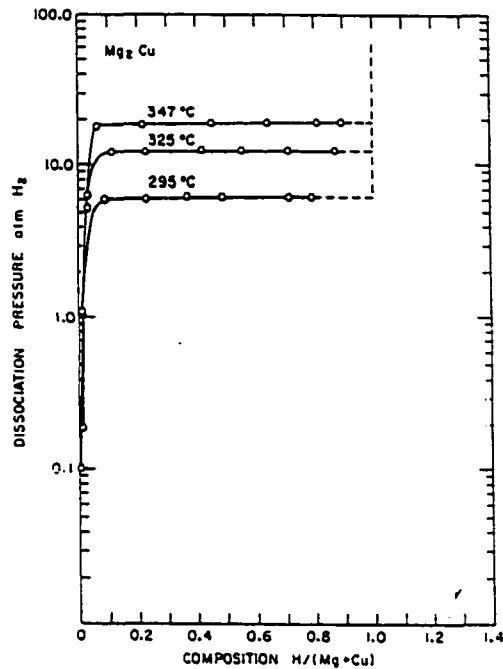


Fig.2.7 P-C-T plots for the Mg₂Cu-H₂ system at 295, 325 and 347°C[31].

2.1.2 Thermodynamics and Kinetics of Metal Hydride Formation

General Considerations

The reaction of hydrogen with a metal M to form a stable hydride can be described by the following reaction:



(i.e. a direct reaction of metal with hydrogen gas). The transition to MH_y is the absorption process, and in general is an exothermic reaction, with the heat of formation approaching the heat of combustion of hydrogen compounds. The reverse reaction is the desorption process. Fig. 2.8^[40] is a schematic showing the charge (hydriding) and discharge (dehydriding) processes.

NOTE TO USERS

Page(s) not included in the original manuscript and are unavailable from the author or university. The manuscript was microfilmed as received.

This reproduction is the best copy available.

UMI

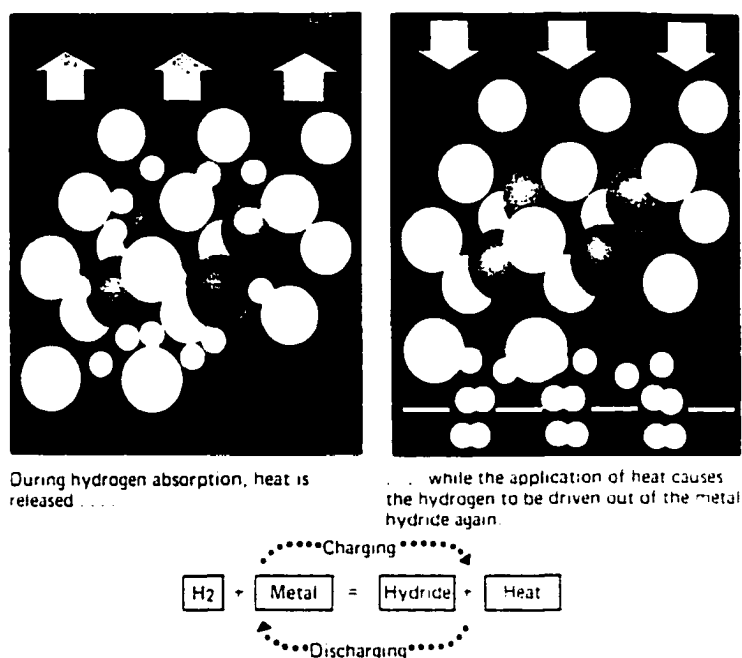


Fig.2.8 Schematic of charge-discharge process[40].

The behavior of metal-hydride systems can be best represented by a pressure, composition and temperature (P-C-T) diagram. This diagram is a plot of pressure or composition at various temperatures as shown in Fig. 2.9^[41]. At low hydrogen concentrations there is a strong composition dependence of hydrogen pressure. This region (i.e., the α -phase) corresponds to hydrogen going into solid solution without the occurrence of a second phase. When the curve starts to change slope on the P-C-T diagram this indicates the start of the next 'stage' which involves a region where the pressure is independent of the hydrogen concentration. In this region the saturated solid solution of hydrogen in the α -phase is in equilibrium with a hydrogen-rich hydride phase, the β -phase. As the second phase (β -phase) forms, the pressure remains constant and a 'plateau' result as more hydrogen is added. Further increases in hydrogen concentration after the α -phase has been completely converted into the β -phase, give rise to an increase in pressure. An additional hydride phase, the γ -

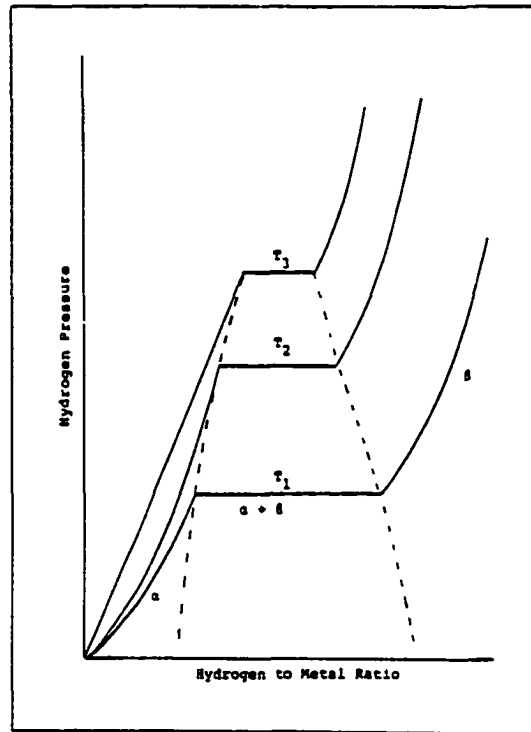


Fig.2.9 P-C-T plot showing the relationship between the equilibrium hydrogen pressure and the hydrogen concentration[41].

phase, may also be formed, in which case a second, and higher plateau will appear.

The standard enthalpy of formation, ΔH_f , of a metal hydride MH_x can be calculated from the van't Hoff equation:

$$\frac{d \ln K_p}{dT} = \frac{\Delta H_f}{RT^2} \quad (2.2)$$

Where R = gas constant

T = temperature (K)

K_p = the equilibrium constant and is given by:

Chapter 2 Literature Review

$$K_p = \frac{a_{MH_y}}{a_M f_{H_2}^y} \quad (2.3)$$

Where f = fugacity

or

$$K_p = \frac{a_{MH_y}}{a_M a_{H_2}^y} \quad (2.4)$$

In this equation, the activities (a) can be considered to be ~ 1 , since the standard states of hydrogen and metal are taken as the pure solids in each case and $a_{H_2} = P_{H_2}$. Assuming H to be constant (over a relatively small temperature range), the van't Hoff equation can be written as:

$$d \ln P_{H_2}^y = \frac{\Delta H}{RT^2} dT \quad (2.5)$$

or

$$\ln P_{H_2}^y = \frac{2}{y} \frac{\Delta H}{RT} + C' \quad (2.6)$$

where C' is the constant of integration. If the hydride is stoichiometric and the solubility of hydrogen is small in the α -phase, the standard enthalpy of formation can be calculated from the slope of the straight line made by plotting $\ln P_{H_2}$ vs. $1/T$.

The standard free energy of formation ΔG_f of the metal hydride can be determined from the equation:

$$\Delta G_f = -RT \ln K_p = \frac{y}{2} RT \ln P_{H_2} \quad (2.7)$$

Chapter 2 Literature Review

The standard entropy of formation can then be determined as follows:

$$\Delta S_f = \frac{\Delta H_f - \Delta G_f}{T} \quad (2.8)$$

For most metal hydrogen systems where there is appreciable non-stoichiometry, the standard enthalpy of formation is the sum of three components, namely: (1) the integral heat of solution of hydrogen in the α -phase from zero hydrogen content to saturation, (2) the heat of reaction in going from the hydrogen saturated α -phase to the non-stoichiometric β -phase, and (3) the integral heat of solution of hydrogen in the hydrogen-poor β -phase up to the stoichiometric value. In the case where there are large deviations from stoichiometry, the thermodynamic quantities are usually expressed as relative molal quantities ($\Delta H_H - 1/2\Delta X_{H_2}$), where ΔX_H is the partial molal enthalpy^[42].

The reaction kinetics of hydrogen absorption and desorption in metal-hydrogen system is an important consideration in selecting materials for practical storage applications. Kinetics are hard to follow quantitatively because many hydriding reactions have rate constants of the order of a few seconds and conventional experimental methods can not follow such rapid changes. A temperature change of a few degrees Celsius is sufficient to alter the kinetics significantly^[5]. According to the equation for absorption of hydrogen by a metal, i.e. equation (2.1), if the concentration of hydrogen is represented by C , and if the volume of the sample remains essentially constant during the course of the reaction, a first-order rate law can then be written as follows:

$$\frac{dC}{dt} = -kC \quad (2.9)$$

If, for the desorption reaction, the hydrogen concentration at time $t=0$ is C_0 , and if at some later time t , the concentration has fallen to C , integration gives^[43]:

$$\ln \frac{C}{C_0} = -kt \quad (2.10)$$

For desorption, (C/C_0) is the fraction of hydrogen remaining in the sample. Thus, the reacted fraction F' can be defined as $F' = 1 - (C/C_0)$, and equation (2.10) can be rewritten as:

$$-\ln(1 - F') = kt \quad (2.11)$$

When the rate constant is being determined for the forward reaction, it is actually the net rate constant that is being measured, i.e.^[44]

$$k_{net} = k_{abs} - k_{des} \quad (2.12)$$

At constant temperature and pressure, the thermodynamic driving force for the reaction in equation (2.9) must be proportional to free energy change, i.e. difference in chemical potential ($\mu_{op} - \mu_{eq}$) between the hydrogen in the gaseous phase and in the hydride phase. This is given by:

$$\mu_{op} - \mu_{eq} = -RT \ln P^{-\frac{v}{2}} = \frac{v}{2} RT \ln \frac{P_{op}}{P_{eq}} \quad (2.13)$$

In the case of absorption, P_{op}/P_{eq} is identified as the N value, where P_{op} is the pressure of hydrogen in the gaseous phase and P_{eq} is the plateau pressure of the hydride phase. For desorption, the N value is defined as P_{eq}/P_{op} .

AB₂ Compounds

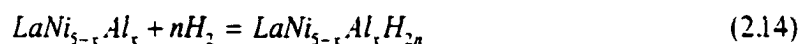
It is well known that almost all hydriding alloys must be activated in order to absorb H₂ the first time. This is a result of natural surface contamination from exposure to the air, usually in the

Chapter 2 Literature Review

form of oxides or hydroxides^[45-49]. Activation usually consists of two stages. First, there is the initial penetration of the original contamination layer by H₂, at which time the molecular H₂ can be dissociated to atomic H on the metallic substrate before entering the bulk lattice. Secondly, there is the fragmentation of the alloy particles (decrepitation) resulting from the bulk absorption of hydrogen and the associated embrittlement and volume changes. The first stage is highly dependent on the original surface contamination and the second stage creates new, clean surfaces.

The original (air-exposed) surface can be a formidable barrier to H₂ penetration. The rare earth-nickel AB₅ compounds fortunately do not have to be heated, but unfortunately require substantial overpressures for activation to occur within reasonable times at room temperature. Liu and Sandrock^[50] developed a powerful new approach for increasing the activation of LaNi_{4-x}Al_x alloys by chemically treating the original particle surface in an F-containing aqueous solution. They found that the longer AB₅ compounds are stored after crushing, the harder they are to be activated. Under the F-treatment, the material can be activated much faster than untreated material.

P-C-T diagrams have been used to determine thermodynamic properties of the rare-earth nickel hydride. Gruen *et al.*^[10] examined different compositions of the LaNi₅ alloys. Fig. 2.10 is a plot of ln*P* against 1/*T* for LaNi_{5-x}Al_x hydrides. From the slope and intercept of the van't Hoff plots, Δ*H* and Δ*S* values for the reaction (2.14) can be calculated and are given in Table 2.3.



Several workers have pointed to the importance of crystal structure and geometrical considerations with regards to the stability of metal alloy-hydrogen systems. Kisi and Buckley^[51] presented three possible mechanisms for activation of LaNi₅: (1) the decrepitation exposes large

Chapter 2 Literature Review

amounts of clean LaNi_5 surface which is then available for chemisorption and absorption at lower pressures; (2) decrepitation reduces the diffusion distances, causing faster absorption and facilitating stress relaxation in the particles, thus decreasing the pressure of hydrogen absorption; (3) that defect creation (manifested as microstrains) provides easy diffusion paths and facilitates motion of the α - β interface through the alloy.

Kinetic studies of the hydriding of LaNi_5 have shown it to be very difficult to obtain reliable and consistent kinetic data. Parameters such as temperature, pressure, particle size, surface conditions, etc., can change during the course of a reaction. When this occurs, kinetic data can vary substantially. In order to assess accurately the kinetic differences amongst the alloys, it is necessary to isolate and standardize all parameters which affect reaction rates. Methods have been developed to perform kinetics measurements under carefully controlled conditions^[52]. First, samples are kept at constant temperature. When comparing the kinetics of two or more samples, it is also necessary that each be measured at the same constant pressure driving force. In the case of desorption, it is accomplished by using the same ratio of the equilibrium plateau pressure to applied hydrogen pressure for all measurements. In the absorption case, the ratio of the applied hydrogen pressure to the plateau pressure is kept constant.

Table 2.3^[10] Thermodynamic Data For the $\text{LaNi}_{5-x}\text{Al}_x + n\text{H}_2 = \text{LaNi}_{5-x}\text{Al}_x\text{H}_{2n}$ Reaction

COMPOUND	ΔH° (KCAL/MOL H_2)	ΔS° (CAL/MOL·K H_2 °C)	TEMPERATURE (°C) FOR P=2.0 ATM
LaNi_5	7.2 ± 0.1	26.1 ± 0.4	~25
$\text{LaNi}_{4.8}\text{Al}_{0.2}$	8.3 ± 0.1	27.3 ± 0.4	~50
$\text{LaNi}_{4.6}\text{Al}_{0.4}$	9.1 ± 0.2	28.1 ± 0.7	~70
LaNi_4Al	12.7 ± 0.3	29.2 ± 0.7	~180
$\text{LaNi}_{3.5}\text{Al}_{1.5}$	14.5 ± 0.6	29.6 ± 1.4	~240

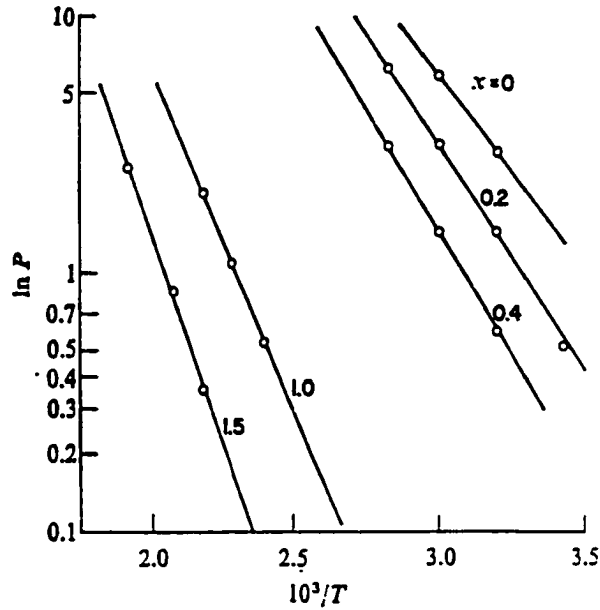
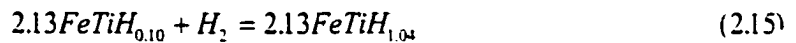


Fig.2.10 Plot of $\ln P$ (P =dissociation pressure) vs. $1/T$ for $\text{LaNi}_{5-x}\text{Al}_x$ hydrides[10].

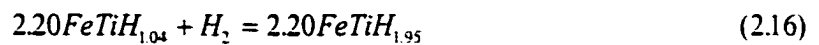
AB Compounds

The intermetallic compound FeTi reacts directly with hydrogen to form, in succession, hydrides of the approximate compositions FeTiH and FeTiH_2 . Both hydrides have dissociation pressures of over 1 atm at 0°C , unlike the very stable TiH_2 .

The reaction taking place in the lower plateau region ($H/M=0.10$ to $H/M=0.52$) may be written as^[13]:



which is followed by:



The variation of the log of the equilibrium dissociation pressure with the reciprocal temperature for several solid compositions is shown in Fig. 2.11^[13]. The relationship is linear and

Chapter 2 Literature Review

obeys the van't Hoff's equation in the form:

$$\ln P_{atm} = \frac{A}{T} + B \quad (2.17)$$

Where $A=-3383$, $B=12.76$ and T is the absolute temperature. Thermodynamic values for the FeTi-hydrogen system are given in Table 2.4.

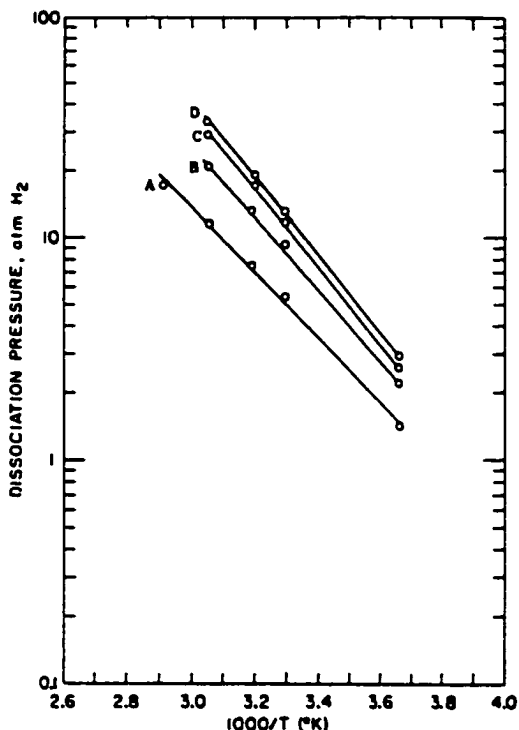


Fig.2.11 Equilibrium dissociation pressure vs. $1/T$ for FeTiH_x: (a) FeTiH_{0.1}-FeTiH₁, (b) FeTiH_{1.2}, (c) FeTiH_{1.4}, (d) FeTiH_{1.6}[13].

The activation process and the reaction kinetics of the hydrogenation of metal are of importance relative to their practical use as hydrogen storage materials. Activation of the FeTi system is particularly difficult and is one of the fundamental problems that must be overcome. The activation mechanism has been discussed by many researchers^[53]. Although their results are not in agreement, they all conclude that the activation process is necessary because of the presence of an

oxide film which obstructs hydrogen absorption.

**Table 2.4^[13] Relative Partial Molar Quantities
Per Gram-Atom of Hydrogen for FeTi Alloys**

COMPOSITION	$\bar{H}_H - 1/2H_{H_2}^\circ$ kcal	$\bar{S}_H - 1/2S_{H_2}^\circ$ eu	A	B
FeTiH _{0.1} -FeTiH _{1.04}	-3.36	-12.7	-3383	12.7612
FeTiH _{1.20}	-3.70	-14.4	-3728	14.4327
FeTiH _{1.40}	-3.98	-15.6	-4020	15.6610
FeTiH _{1.60}	-4.03	-15.8	-4057	15.9165

Magnesium-Based Compounds

In the Mg-Ni system, two intermetallic compounds are formed: Mg₂Ni and MgNi₂. MgNi₂ does not react with H₂ at pressures up to 2.76 MPa and temperatures up to 350°C; However, Mg₂Ni reacts readily with H₂ at 2.07 MPa and 325°C. On the basis of the stoichiometry of the system and X-ray diffraction studies, the reaction in the plateau region is believed to be:



Reilly and Wiswall^[30,31] calculated thermodynamic data by plotting the semilog of the dissociation pressure vs. the reciprocal of the absolute temperature, and found a straight line $\text{Log}P_{\text{atm}} = A/T + B$, where $A = -3360$ and $B = 6.389$.

If Mg is present in the alloy in excess of the composition corresponding to Mg₂Ni, the pressure-composition isotherm exhibits two plateaus as shown in Fig. 2.12. The lower plateau is due to the reaction:



Reilly and Wiswall also obtained a straight line relationship $\log P_{\text{atm}} = (-4045/T) + 7.224$,

$\Delta H_{f,298}^\circ = -77.33 \text{ kJ/mol}$ for reaction (2.19).

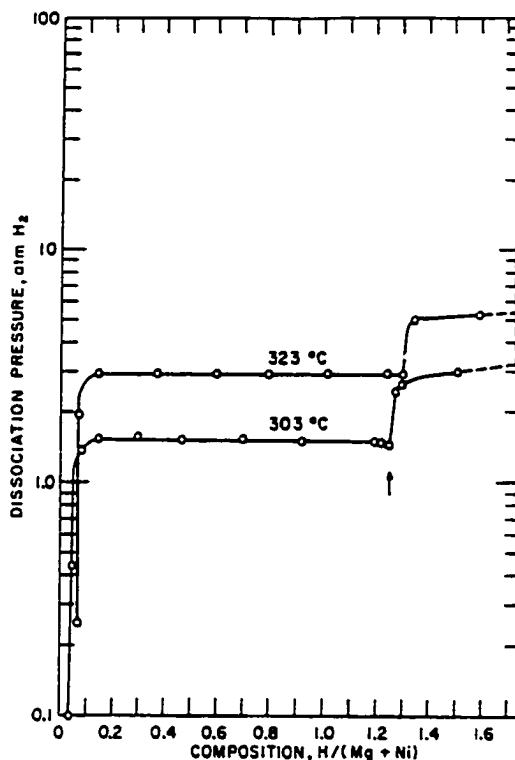


Fig.2.12 P-C-T plots for the Mg₂Ni-Mg-H₂ system at 303 and 323°C.
 The initial alloy composition is 72.9wt%Mg and 25.2wt%Ni.
 The arrow indicates predicated appearance of upper plateau[30].

Mg forms two intermetallic compounds with Cu, namely Mg₂Cu and MgCu₂. The latter, MgCu₂, does not react with H₂ at temperatures up to 350°C and H₂ pressures of 2.28 MPa; However, Mg₂Cu reacts fairly rapidly at 300°C and H₂ pressures of ~2.07 MPa. The reaction is:



A plot of dissociation pressure vs. the reciprocal of the absolute temperature gives a straight line for $\log P_{am} = (A/T) + B$, where $A = -3809$ and $B = 7.437$.

If Mg is present in the alloys in excess of the composition corresponding to Mg_2Cu , the pressure-composition isotherm exhibits two plateaus. In this case, the reaction is believed to be equation (2.20). They also got a straight line obeying the relationship $\log P_{am} = -4049/T + 7.299$. $\Delta H_{f,298}^\circ = -78.17$ kJ/mol for reaction (2.20). The thermodynamic data for Mg-Ni and Mg-Cu alloys are summarized in Table 2.5.

Table 2.5^[28,29] Thermodynamic Data for Mg-Ni and Mg-Cu Alloys

MG-BASED ALLOYS	$\Delta H_{f,298}^\circ$	$\Delta G_{f,298}^\circ$	$\Delta S_{f,298}^\circ$
	KCAL/MOL OF H ₂	KCAL/MOL OF H ₂	CAL/MOL OF H ₂
$Mg_2Ni + 2H_2 = Mg_2NiH_4$	-15.4 ± 1.0	-6.7 ± 1.0	-29.2 ± 1.5
$Mg + H_2 = MgH_2$	-18.5 ± 1.0	-8.7 ± 1.0	-33.0 ± 0.7
$2Mg_2Cu + 3H_2 = 3MgH_2 + MgCu_2$	-17.4 ± 1.0	-7.3 ± 1.0	-34.0 ± 0.7
$Mg + H_2 = MgH_2$	-18.7 ± 1.0	-8.7 ± 1.0	-33.4 ± 0.7

2.1.3 Hysteresis

Hysteresis is observed in nearly all metal-hydrogen systems during hydride formation and decomposition. This phenomenon occurs when the transition pressure in the P-C-T curve is higher for absorption than for desorption. Hysteresis is of considerable practical important since it reduces the efficiency of hydrogen (energy) storage systems. An example of hysteresis is shown in Fig.

Chapter 2 Literature Review

2.13^[41]. The cause of hysteresis is not fully understood although many explanations have been proposed. However, lattice expansion on hydriding is believed to be of importance. The hydride phase seems to cause an irreversible plastic deformation in the matrix. Desorption of a small amount of hydrogen primarily relaxes the residual stresses so that the phase is no longer under stress. Therefore, desorption should occur at a lower critical transition pressure. Because of strain sensitivity, the amount and size of impurities, as well as the processing history, have a considerable effect on the absorption pressure plateau.

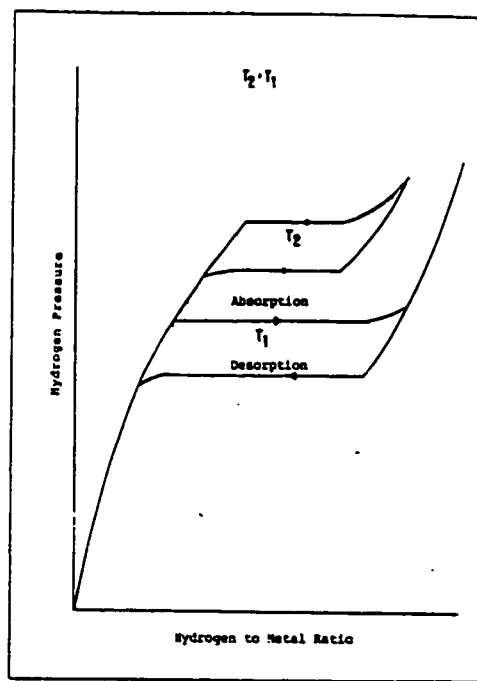


Fig.2.13 P-C-T diagram showing hysteresis in a metal-hydrogen system[41].

Qian and Northwood^[54] developed a model for the hysteresis that is observed in intermetallic compounds, such as $Zr(Fe_xCr_{1-x})_2$. This model suggested that elastic and plastic strain energies for both hydride formation and decomposition will contribute to pressure hysteresis for bulk samples.

Chapter 2 Literature Review

The pressure hysteresis for powder samples varies with aliquot size and is determined by a combined effect of the energy barrier for nucleation, which is built up by elastic strain energy in the purely elastic state, and the interfacial energy and the energy barrier for growth (which is created by elastic and plastic energy) in the elasto-plastic state.

Schotus and Hall^[55] related the hysteresis to plastic deformation during hydride formation. They assumed that strain was absent during hydride decomposition and, as such, the decomposition plateau pressure corresponds to true equilibrium. Flanagan and Clewely^[56] have proposed a model to explain hysteresis, which is based on the requirement for dislocation production during both hydride formation and hydride decomposition.

One of the better known theories is that originally proposed by Ubbelohde^[57] over 50 years ago for hysteresis in Pd-H systems. He proposed that the free energy of the hydride (β) phase for these systems is not determined solely by the temperature, pressure and composition, but is dependent on other variables such as mechanical strain for its full determination. In this way, it is possible to have more than one pressure for the same concentration of hydrogen. The metallic hydride phase is assumed to be both disordered and strained, thus giving rise to a greater plateau pressure for hydride formation than for hydride decomposition. He suggested that the phase rule has to be modified for such systems, and an additional variable such as strain has to be added.

The degree of hysteresis in a metal hydrogen system can be affected by the type of testing. Hysteresis is more pronounced in dynamic tests than in conventional static tests^[58]. This effect could be due to deformation disordering of the metal lattice by cycling through the high capacity range.

Although the causes of hysteresis are still not very clearly established, it is generally agreed that hysteresis reduces the efficiency of hydrogen storage systems.

2.2 Electrochemical Properties of Metal Hydride Electrodes

Hydrogen storage alloys, which were discovered about 20 years ago, have been widely studied for their application as energy storage media and battery electrodes. The hydriding alloys (metal hydrides: MH) are used as the negative electrode of a rechargeable battery, essentially replacing the cadmium electrode in the widely used Ni-Cd battery. The main driving force for replacing the cadmium is environmental consideration, Cd being a relatively toxic material. There are, of course, other advantages of the Ni-MH battery over the Ni-Cd battery, including potentially higher energy density, higher charge/discharge rates, low temperature capability and an absence of a memory effect^[1, 2].

2.2.1 Development History

Hydrogen storage alloys have been studied as potential negative electrodes for alkaline rechargeable batteries since 1970^[59]. However, due to various shortcomings including corrosion of the hydrogen storage alloy in the electrolyte, short cycle life and poor charge retention^[60, 61, 62], hydrogen storage alloys electrodes did not find acceptance by industry until a break-through was made in 1984 by Willems^[2] which significantly extended the cycle life of a LaNi₃ alloy electrode by partly substituting Ni with Co and a small amount of Si. Since then, the La-Ni-Co-Si (or Al), Mm-Ni-Co-Si (or Al) (Mm stands for Ce-rich mischmetal) and MI-Ni-Co-Si (or Al) (MI stands for La-rich mischmetal) and AB₅ type alloys have been systematically studied and have seen rapid development in both Japan and China. Also in 1985, AB₂ type V-Ti-Zr-Ni electrode alloys were developed and claimed to possess satisfactory properties by the Ovonic Battery Co.^[64] in the U.S.A. Since 1990, batteries with these alloys as negative electrodes have begun to appear on the market,

and the market is now growing at a fast rate.

2.2.2 Desirable Properties and Criteria for MH Electrode Materials

In comparison with Ni/Cd batteries, Ni/MH batteries have the following advantages^[18]:

- (i) MH electrodes have a 1.5 to 2 times higher energy density than Cd electrodes with capacities of 400 mAh/g or 2000mAh/l;
- (ii) they are free from the poisonous metal Cd;
- (iii) there is no concentration change in the electrolyte solution during charge/discharge cycling, as the cell reaction does not undergo a dissolution/precipitation process;
- (iv) there is no memory effect during charge/discharge and they can sustain a high rate of charge and discharge;
- (v) they have a higher tolerance to over-charging and over-discharging;
- (vi) the voltage characteristics of Ni/MH batteries are very close to Ni/Cd batteries, and hence lend themselves to ready substitution.

The following properties are regarded as desirable in MH electrodes:

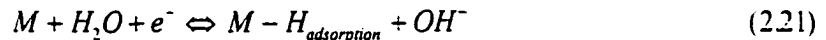
- (i) they should be stable in alkaline electrolyte solutions, with or without cycling (corrosion resistant and long cycle life);
- (ii) they should have a high electrochemical capacity (in mAh/g);
- (iii) they should exhibit a suitable equilibrium hydrogen pressure, generally 10^{-4} - 10^{-1} MPa within the working temperature range (-20°C~60°C);
- (iv) they should exhibit a good surface activity and kinetic properties (high rate capacity);
- (v) they should exhibit a high charge retention (high % charge retained after 14 or 21 days);
- (vi) low cost.

Chapter 2 Literature Review

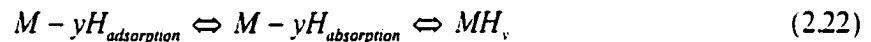
2.2.3 Charge-Discharge Processes and Electrode Reactions

A nickel-metal hydride battery is a battery adopting a hydrogen storage alloy as its negative electrode, which is able to absorb and desorb reversibly a large amount of hydrogen at the room temperature and pressure. The process of charge-discharge of the electrode can be described as follows:

(a) The movement of electrons:



(b) The diffusion of hydrogen into the bulk and the chemical reaction:

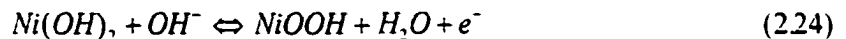


(c) The phase transformation of metal hydride:



(d) The charge and discharge reactions in an alkaline electrolyte at the negative and positive electrodes can be described as follows:

Positive electrode:



Negative electrode:



Thus the overall working of a Ni/MH battery can be expressed as:



where M stands for the hydrogen storage alloy and MH_{ab} stands for the absorbed hydrogen alloy (metal hydride). Fig. 2.14^[66] is schematic of the charge/discharge mechanisms in a Ni/MH battery. The nickel/metal hydride battery is characterized by moving hydrogen from the positive to the negative electrode during charging and from the negative to the positive electrode during discharging

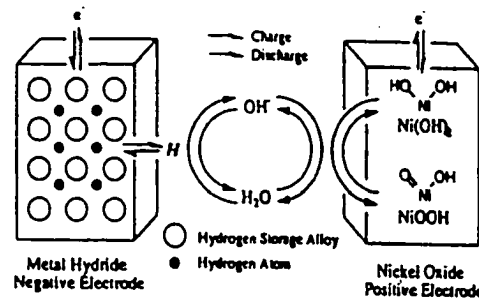


Fig.2.14 Charge-discharge reaction mechanism of Ni/MH battery[66].
with no loss, or gain, of the electrolyte.

2.2.4 The Electrochemical Characteristics of Metal-Hydride Electrodes

The performance of a Ni-MH battery is measured by the discharge capacity, the durability (cycle life), the dischargeability (kinetics) and self-discharge. This performance greatly depends on the metal hydride (MH) electrode, especially the hydrogen storage alloy in the electrode^[67].

Discharge Capacity

The equilibrium potential of the negative electrode at 20°C, 1.01MPa, in 6M KOH solution in reference to a mercury oxide electrode is related to the hydrogen dissociation pressure, P_{H_2} (in atm), by the Nernst equation:

$$E_{eq(H_2O/H)} - E_{eq(HgO/Hg)} = -0.9324 - 0.0291 \text{Log}P_{H_2} \quad (2.27)$$

Chapter 2 Literature Review

The electrochemical capacity per unit weight of alloy Q (in mAh/g) is determined by the hydrogen atoms absorbed per unit mole of alloy H/M ,

$$Q = \frac{2.68 \times 10^4}{W} (H / M) \quad (2.28)$$

where W is the average molecular weight of the alloys (in g).

The available hydrogen capacity of a metal hydride essentially depends on the plateau region, i.e. the α and β phase coexistence region. When the alloy is charged to hydride with a hydrogen content at the right end point of the plateau region in the P-C-T curve, i.e., the alloy is totally transformed from the α -phase to the β -phase, further charging results in a dramatic increase in the hydrogen equilibrium pressure because of solid solution behavior^[68].

The discharge capacities are determined by a galvanostatic method in an open standard tri-electrode cell which includes the counter electrode (nickel oxyhydroxide), the reference electrode (Hg/HgO/6mol/L KOH) and the working electrode (hydride alloy). The electrolyte is a 6 mol/L KOH solution. The electrode is fully charged at a given current density for several hours until the electrode potential is stable and hydrogen bubbles are generated at the surface of the electrode, or to an overcharge of about 20-40% to ensure a complete hydriding of the electrode. The electrode is then discharged galvanostatically to -0.5V and the discharge curves are recorded by a X-Y recorder or a computer^[69]. The discharge capacity is calculated as:

$$Q = It \quad (2.29)$$

where Q is the discharge capacity, I is discharge current density and t is the discharge time.

Cycle Life and Capacity Retention

The cycle life (CL) is usually defined as the number of cycles at which the discharge capacity

Chapter 2 Literature Review

decreases to half of the initial capacity^[70]. Other researchers, e.g. Chikano *et al.*^[71] define a capacity retention ratio as the ratio of the capacity after 1000 cycles against the initial capacity, i.e. $(Q_{1000}/Q_{initial})$.

Ye and Sakai^[72] studied the cycle life and suggested that the loss of cycle life is usually caused by a loss of the electrolyte, resulting in a drying out of the cells. This is either due to corrosion of the metal hydride that uses up the electrolyte, or by poor recombination reactions which leads to venting of the cells through the safety valve. In the final stage of the life-span of a hydride battery, both processes usually occur, and this is the reason for the fairly rapid decay of the hydride battery capacity when the battery reaches the end of its life expectancy. A characteristic hydride battery initially has a fairly stable capacity over several hundreds of cycles but eventually reaches a point where there is a sudden drop. A third cause for electrolyte dry out, which is common for both Ni-MH and Ni-Cd cells, is the incorporation of water molecules in the nickel hydroxide, leading to a swelling of the electrode. Ye and Sakai^[72] also suggested that some of the capacity drop was due to overcharging.

The electrochemical capacity of a number of different compounds has been measured in a sealed cell as a function of number of cycles^[73]. The values of capacity obtained after 3 and 10 cycles, which are summarized in Table 2.6, show the decay in capacity to be very large for LaNi_5 and a Mn substituted compound (about 25 to 20%), less for Co and Al substituted (10%) alloys and no decay was observed for LaNi_3S .

**Table 2.6^[73] Variation of the Electrochemical Capacity
as a Function of Number of Cycles in a Sealed Cell**

COMPOUND	CAPACITY AFTER 3 CYCLES		CAPACITY AFTER 10 CYCLES	LOSS OF CAPACITY
	mAh/g	H/mol	mAh/g	%
LaNi ₅	350	5.5	260	25
LaNi _{4.5} Mn _{0.5}	325	5.2	260	20
LaNi _{4.5} Al _{0.5}	330	5.1	300	10
LaNi _{4.5} Co _{0.5}	330	5.3	285	13
LaNi ₃ S	320	5.1	320	0

Percheron-Guegan and Latroche^[73] discussed this decay and considered it was essentially due to two factors: (1) self-discharge related to the value of the plateau pressure; and (2) a corrosion effect due to the chemical dissolution of the surface or passive film formation.

The Influence of Temperature

Nickel-metal hydride batteries are typically charged at high rates when installed in portable electronic devices, thus, they are used under comparatively higher temperature conditions than room temperature. Thus it is important to improve battery performance at these higher temperatures. The decline in battery capacity at higher temperatures is due more to the lowered charge acceptance of nickel electrodes with their smaller oxygen over-potential than the MH negative electrodes. Ye and Sakai^[72] measured the temperature dependence of the discharge capacity using a MH electrode with a composition of 85wt% AB₅ alloy, 10wt% Ni and 5wt% Co, and found that the discharge capacity is rather flat between -18°C and 40°C, except for a battery with a 10M KOH electrolyte, where the

Chapter 2 Literature Review

increased internal resistance at low temperatures significantly reduced the capacity at -18°C . On the other hand, Chen and Zhang^[74] studied the discharge capacities at 20°C , 0°C and -18°C of batteries which used a Ni-coated alloy and showed that the batteries exhibited good performance even when discharged at low temperatures.

2.2.5 Approaches Used to Improve Properties of MH Electrode Materials

In view of the promising features of the Ni-MH batteries, a large amount of research and development work has been carried out to improve the properties of these electrode materials. The following approaches have been used:

- (i) Alloying or multi-componenting which intrinsically determines the structures and properties of both the bulk and the surface of the materials;
- (ii) Processing control, which guarantees the presence of the desirable structures and surface properties;
- (iii) Surface modification, which changes the surface of the material to one with more desirable characteristics;
- (iv) Electrode preparations in which the desirable properties of the materials are not impaired or destroyed.

Main Methods for Decreasing the Capacity Decay on Cycling

Elemental Substitution

As has been demonstrated by Willems^[63,75], Lei *et al.*^[76], Meli and Schlapbach^[77] and many others, a striking decrease in capacity decay can be realized by substituting Co and a small amount of Si or Al for Ni. This approach has made AB_5 -type alloys a promising electrode material. It is

Chapter 2 Literature Review

believed that since Co greatly reduced the volume expansion on hydriding ($\Delta V/V=24\%$ for LaNi_5 and $\Delta V/V=13\%$ for LaNi_2Co_3), the pulverization of the powder on hydriding is also reduced. Al and Si concentrate on the grain boundaries, and in conjunction with segregated La, form a porous passivating oxide layer which protects the alloy from further corrosion in the KOH solution. However, too much Al or Si reduces the porosity and thus increases the surface resistance, thus degrading the high current rate performance.

Numerous attempts^[78-85] have been made to improve the kinetics of magnesium and magnesium-based alloys. The effects of yttrium additions on the electrode performance of $\text{Mg}_{1-x}\text{Al}_x\text{Ni}_{1-y}\text{Y}_y$ alloys have been investigated by Cui *et al.*^[86]. Fig. 2.15 shows that the addition of yttrium substantially increases the discharge capacity of the electrodes and effectively improves the electrode high-rate dischargeability. On the other hand, the addition of yttrium has a negative effect on the cycling stability for the Mg_2Ni -type alloy electrodes.

Control of Grain Size

Electrode alloys with a small grain size have longer cycle lives than large grain materials^[15]. Fig. 2.16 shows Sakai *et al.*^[87] results on the effects of solidification and heat treatment of $\text{MmNi}_{1.3}\text{Co}_{0.7}\text{Al}_{0.8}$ on the discharge capacity after cycling. The fine grained samples had much longer cycle lives. It is believed that the passivating elements are segregated to the grain boundaries on solidification and better protective layers are formed on the electrode particles processed from fine grained alloys.

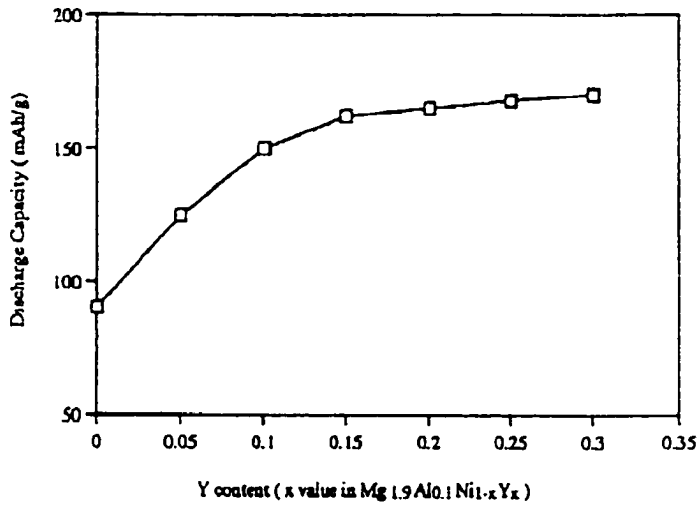


Fig.2.15 Discharge capacity of $Mg_{1.9}Al_{0.1}Ni_{1-x}Y_x$ alloy electrodes vs.Y content (discharged at 5mA/g)[86].

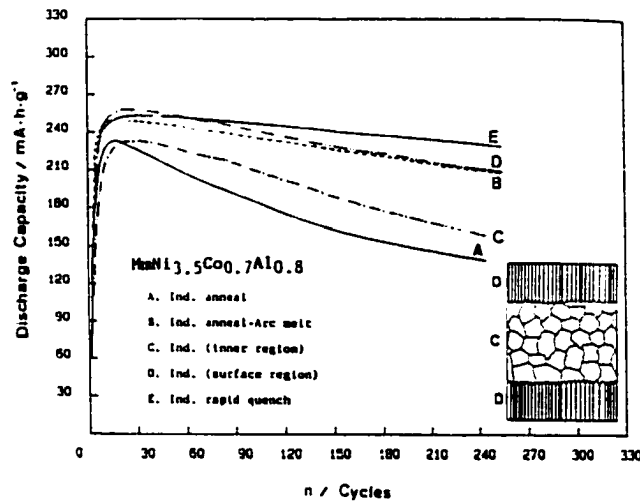


Fig.2.16 Influence of casting conditions on capacity decay curves at 20°C for $MmNi_{3.5}Co_{0.7}Al_{0.8}$ [91].

Zaluski *et al.*^[81] found that nanocrystalline FeTi with grain sizes of about 6-7 nm showed a relatively large solubility region (up to 0.3H/FeTi) and a plateau pressure of 0.7MPa, which is lower than the absorption pressure of the conventional alloy. Modification of this alloy by a small amount of Pd drastically changes the hydrogen sorption properties. Pd modified nanocrystalline FeTi readily absorbs hydrogen at room temperature with neither thermal activation nor previous exposure to high

Chapter 2 Literature Review

pressure of hydrogen being required. The hydrogen uptake was about 0.5 hydrogen atoms/FeTi at pressures lower than 0.1MPa. Further, they also found that nanocrystalline Mg₂Ni (with a grain size of 20-30 nm) exhibits significantly improved activity and hydrogen absorption kinetics, as compared to the polycrystalline materials. Modification of this material by Pd gives further improvement of the hydrogen storage characteristics.

Micro-Encapsulation

The deposition of a thin coating of porous Cu or Ni on the surface of hydrogen storage alloy particles by electroless plating is called micro-encapsulation. Fig. 2.17^[88] shows the ideal microstructure of a microencapsulated alloy. Sakai^[89] and Lei *et al.*^[90] found that batteries made from micro-encapsulated materials have better high rate capacity, better low temperature performance and lower capacity decay than non-microencapsulated ones. It is believed that the Ni or Cu coating on the particle forms an anti-oxidation barrier and at the same time acts as a microcurrent collector, facilitating electron transfer during charging and discharging.

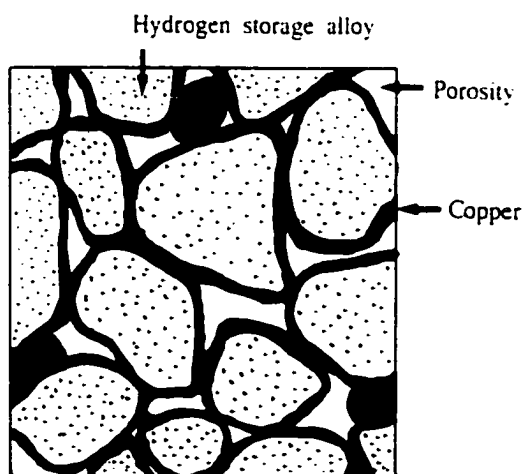


Fig.2.17 Ideal microstructure of an encapsulated hydrogen-storage alloy[88].

Ball-Milling

Recently, some researchers have begun to use ball milling to treat the hydrogen storage materials prior to use in battery applications. Ikeya *et al.*^[91] found that an alloy of $MmNi_{1.5}Al_{0.5}Co_0$ ground for 1h or less showed a higher discharge capacity and longer cycle life than for non-ground samples. However, longer grinding times eventually lead to a decrease in the discharge capacity due to amorphization

Sridhar Kumar *et al.*^[92] have reported the results of electrochemical studies on metal hydride electrodes containing alloy samples coated with cerium oxide by a ball-milling technique: see Table 2.7 for a summary of the results.

Table 2.7 Effect of Cerium Coating and of Ball-Milling on the Electrochemical Performance of Metal Hydride Electrodes^[92]

ALLOY	COATING MATERIALS	BALL-MILLING TIME	MAXIMUM CAPACITY (mAh/g)	DECAY (mAh/g.CYCLE)
La-Ni-Sn	---	9h	297	1.19
	5wt% CeO ₂	3h	317	0.73
	5wt% CeO ₂	9h	315	0.52
La-Ni-Mn-Al-Co	---	9h	292	0.51
	10wt% CeO ₂	3h	263	0.39
	10wt% CeO ₂	9h	256	0.39

Coating a La-Ni-Sn alloy sample with 5wt% cerium oxide resulted in a decrease in the capacity degradation rate on prolonged charge/discharge cycling. The exact mechanism by which cerium or its oxides protect the electrode surface is not very clear. However, studies^[65] on other metals and alloys suggested that Ce formed a protective insoluble oxide film preferentially on certain

Chapter 2 Literature Review

sites thereby preventing a corrosion reaction from occurring.

Methods for Increasing Electrochemical Capacity

Elemental Substitution for Ni on the B side

In order to increase the electrochemical capacity of an electrode alloy, the alloy should have large hydrogen storage capacity with long and flat P-C-isotherms and the plateau pressure of the P-C-isotherms should be 10^{-4} ~ 10^{-1} MPa in the -20°C to 60°C temperature range.

LaNi_5 is an alloy with a large capacity and favorable P-C-T characteristics for H_2 storage and dehydriding, yet as an electrode material, its plateau pressures are too high. Mn, Al, Cu and Co substitution for Ni, all lead to a lowering of the hydrogen equilibrium pressure^[15].

Surface Modifications with Metal Coatings and Organic/Inorganic Compounds

Researchers from the University of Wollongong^[83] surface-modified the Mg_2Ni type alloy by Ni-P microencapsulation and found that this improved the electrocatalytic activity of the negative electrode and thereby reduced the overpotential of charge/discharge. This resulted in a remarkable increase in electrode capacity and high-rate discharge capability, but had little influence on the cycle life.

Iwakura *et al.*^[82] improved the charge-discharge characteristics, especially discharge capacity and cycle lifetime, by ball milling the Mg_2Ni together with graphite. Such a remarkable effect for the Mg-graphite composite may be caused by an increase in the number of active sites for hydrogen absorption and desorption with the formation of bonds between Mg and graphite (Fig. 2.18).

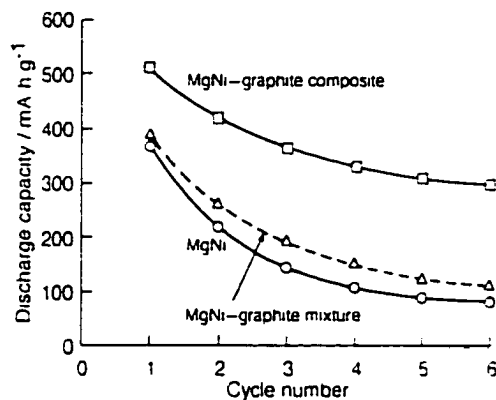


Fig.2.18 Discharge capacity behavior for prototype test cells with the anode of MH ($MmNi_{3.5}Al_{0.8}Co_{0.7}$) sample; ○: modified by mechanical treatment for 1h with 20w/o added cobalt; ●: chemical-coated with 11w/o Ni; □: only metal hydride without any modification[91].

Composite Formation of Magnesium and/or Magnesium-Based Alloys with Other Hydrogen-Storage Alloys

Cui *et al.*^[3] investigated the hydrogen storage characteristics of a $Mg_2Ni-10\%Ti_2Ni$ alloy which was synthesized by mixing the prefabricated Ti_2Ni with Mg_2Ni . The discharge capacity increased from 8 mAh/g for an uncoated Mg_2Ni electrode to 126 mAh/g for a Mg_2Ni-Ti_2Ni electrode. This may be attributed to the fact that the Ti_2Ni alloy has a much higher reaction rate with hydrogen than a Mg_2Ni alloy, and thus exerts an important catalytic effect on the hydriding/dehydriding rate of the composite alloy, thereby enhancing the discharge capacity.

Measures for Increasing Rate Capacity

Microencapsulation

The deposition of a thin coating of porous Cu or Ni on the surface of hydrogen storage alloy particles by electrodeless plating is called micro-encapsulation^[63]. It works as a micro-current collector in the electrode and hence it reduces the Ohmic loss and improves the rate capacity of the

Chapter 2 Literature Review

electrode^[88]. Sakai^[89] tested the electrode made of micro-encapsulated alloy powders and found that the batteries have better high rate capacity, better low temperature performance and low capacity decay.

Control of Additives

Small amounts of Al, Si, Ti or Zr are added to passify the surface. However, if too much is added, the oxide films of these elements impede hydrogen and current flow, and hence reduce the rate capacity^[15].

Measures for Promoting Activation

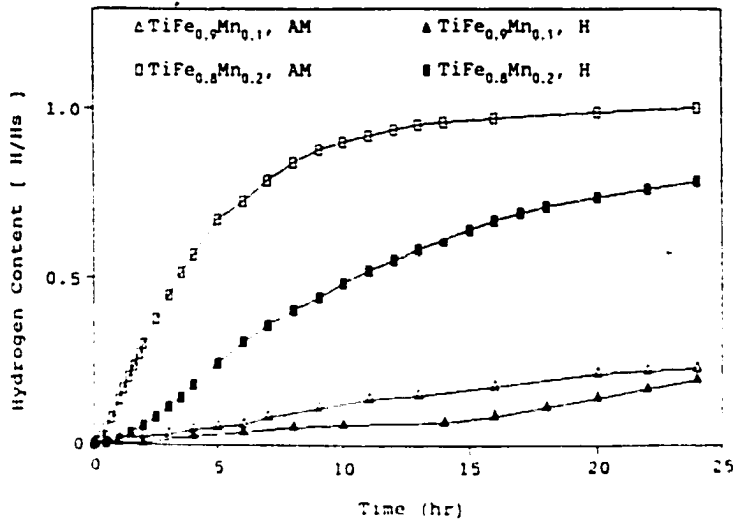
FeTi is one of the most effective materials for hydrogen storage. However, the virgin compound reacts very slowly with hydrogen at room temperature even at high hydrogen pressures. A high temperature heat treatment is required in order to activate the sample to absorb hydrogen at room temperature.

To overcome the disadvantages, it has been proposed that iron in TiFe be substituted by a third element such as Al, Mn, Ni Cr or S. Fig. 2.19 shows that when a small amount of Cr (a) or Mn (b) is substituted for Fe, activation is promoted and the resistance to impure gas poisoning is increased. Although the effects of this substitution have been widely reported, the reason behind the effect is still not well understood. Yang *et al.*^[93] proposed that, when $\text{TiFe}_{0.9}\text{Mn}_{0.1}$ was heated to 100°C in a vacuum, surface aggregation of Mn took place and a second phase was formed. Increasing the amount of Cr and Mn increased the amount of the second phase, and the effect became more pronounced.

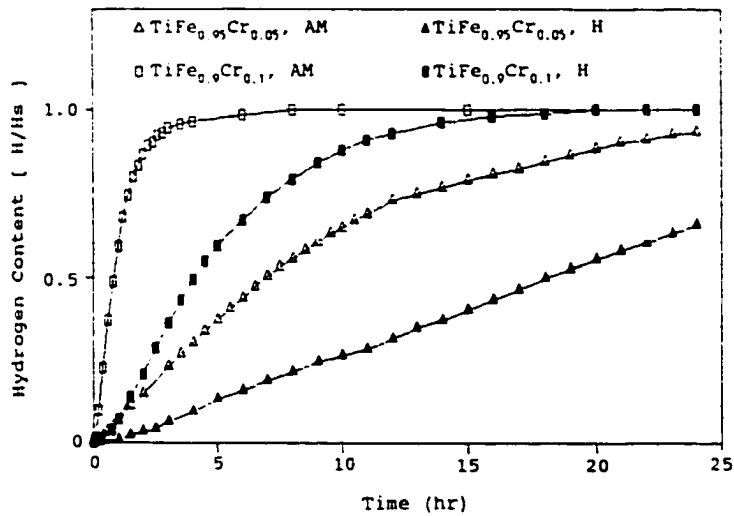
For an AB_2 alloy, it is generally agreed that the A:B ratio should not deviate too far from 1:2. Generally, A=Zr or Ti, B=Ni, Mn, Cr, V, Al, Fe or Co. Too large a deviation from 1:2 would reduce the number of tetrahedral interstitial cavities and hence the H-capacity, and thereby lower the

Chapter 2 Literature Review

pressure. Zr, Ti are hydride forming elements and a high Zr% is preferred, since Zr has a bigger atomic radius, and thus forms alloys with larger hydrogen capacities. Cr and Mn are used to weaken the M-H bond, or to raise the equilibrium hydrogen pressure. Additions of small amounts of Al, Mn, V or rare earth metals are helpful in promoting activation.



(a) Substitution of Fe with small amount of Mn



(b) Substitution of Fe with small amount of Cr

Fig.2.19 Hydrogen absorption curves for the first cycle for TiFe_{1-x}Cr_x alloys at room temperature and a hydrogen gas pressure of 3.92MPa. AM: as melted; H: homogenized[93].

Chapter 2 Literature Review

From the above discussion it can be seen that surface condition of electrode materials has a very important effect on charge/discharge properties. Both activation and decay are related to the surface condition. Increased surface area on grain disintegration, the segregation of catalytically active metal clusters to the surface, the formation of porous oxide layers, the corrosion and decay of active components, and the increase in contact resistances are all reactions on the surface. Many investigators are working on these different reactions and significant progress has been made.

2.3 Ball Milling

Ball milling has recently emerged as a novel technique for alloy formation^[94,95]. The resulting alloy can be either crystalline, amorphous or quasi-crystalline^[96]. One of the unique uses of mechanical alloying is to make alloys of entirely immiscible metals, e.g. the Cu-V system^[95]. In the early development of the ball milling technique, it has been frequently used to amorphize alloys. Recent developments include its use in making several kinds of alloys, particularly those in which the heat of mixing is negative and therefore a thermodynamic driving force is provided in a natural way. Another use of the technique is to make nanocrystalline materials^[97].

In the metal hydride systems, the surface area and particle size of the material are important parameters for the enhancement of the hydrogen uptake, reduction in the activation time, temperature and pressure, and improvement in the kinetics. Since mechanical alloying by ball milling leads to materials in fine particle form, and, as such, may result in a reduction of the activation time and temperature, it is well suited for the synthesis and formation of hydrogen storage materials^[98].

Chapter 2 Literature Review

2.3.1 Development History

Mechanical alloying (MA) is a high-energy ball milling technique used to prepare alloy powders with unique microstructures^[99]. MA had its origin at the International Nickel Company (INCO), where Benjamin and coworkers^[100,101] used MA to prepare nickel-based oxide-dispersion strengthened alloy powders. These powders were then hot pressed, which reacted the constituents into a homogeneous alloy with uniformly dispersed fine oxide particles. Commercial products prepared by this technique include the iron-based MA956, the aluminum-based MA952, and the nickel-based Inconel MA754 and MA6000 alloys^[102].

Mechanical alloying (MA) is a solid-state alloying process by dry ball milling of elemental or pre-alloyed powders. Ball milling of crystalline elemental powder mixture (Mechanical Alloying, MA) or of crystalline intermetallic compound (Mechanical Grinding, MG), is of particular interest not only for forming alloys which are dispersion strengthened by a uniform distribution of fine, stable particles, but for creating nanometer-sized crystalline materials in which the solubility of some elements may be several orders of magnitude larger than in the case of single crystals^[103].

2.3.2 Equipment

Laboratory scale equipment includes the Spex shaker mill, planetary ball mills, vibratory mills, and other specially designed mills. Larger quantities of powder are typically milled in attritors or large tumbler ball mills. The mill energy and alloy powder are important in determining the kinetics of a given process, and in some cases determine its feasibility for working. In general, the more highly energetic mills produce the desired end-product (nano-crystalline or amorphous) material more rapidly. The energy of the milling media depends upon the internal mechanics of the specific mill, the power supplied to drive the milling process, and the composition, size, and size

Chapter 2 Literature Review

distribution of the balls. Since the kinetic energy of the balls is a function of their mass and velocity, dense materials (steel or tungsten carbide) provide more energy than light materials (ceramic balls). The ball size and size distribution should be optimized for a given mill. Too dense a packing of the balls reduces the mean free path of the ball motion, while a 'dilute' distribution minimizes the collision frequency^[104].

2.3.3 Mechanisms in Ball Milling

Mechanical alloying (MA) is a complex process of fragmentation, deformation, cold welding and short range diffusion, occurring within a layer of powder particles trapped between the surfaces of two colliding balls^[105,106]. Lee and Shingu^[107] have pointed out that investigations of MA processes had always been done with elemental or intermetallic powders as starting materials. There had yet been no experimental data presented with MA characteristics using non-powder material.

Most of the systems studied have been binary, consisting of an early transition metal (Ti, Zr, Nb, Hf) with a late-transition metal (Fe, Co, Ni, Cu)^[108].

The central event in MA/MG is the ball-powder-ball collision. Powder particles are trapped between the colliding balls during milling and undergo deformation and/or fracture processes which define the ultimate structure of the powder. This is illustrated schematically in Fig. 2.20. The nature of these processes depends upon the mechanical behavior of the powder components, their phase equilibria, and the stress state during milling. In particular, component powders that are (i) both ductile, (ii) ductile/brittle, or (iii) both brittle, exhibit different morphologies during milling. Ductile/ductile components exhibit flattening and cold-welding into a lamellar structure which after sufficient repeated fracture and rewelding form homogeneous equiaxed particles. In ductile/brittle powder mixtures, the brittle particles fracture and are trapped at the weld interfaces between ductile

Chapter 2 Literature Review

particles. The continued fracture and cold-welding ultimately results in a uniform distribution of the brittle particles in the ductile matrix. It might be expected that milling brittle powders would only serve to fracture the particles into smaller segments. The morphology of the welded powder agglomerate does not assume the lamellar structure of ductile/ductile components, but an equiaxed 'popcorn ball' appearance. It has been demonstrated that significant plastic deformation occurs in even nominally brittle intermetallics like Nb_3Sn under the conditions of ball milling.

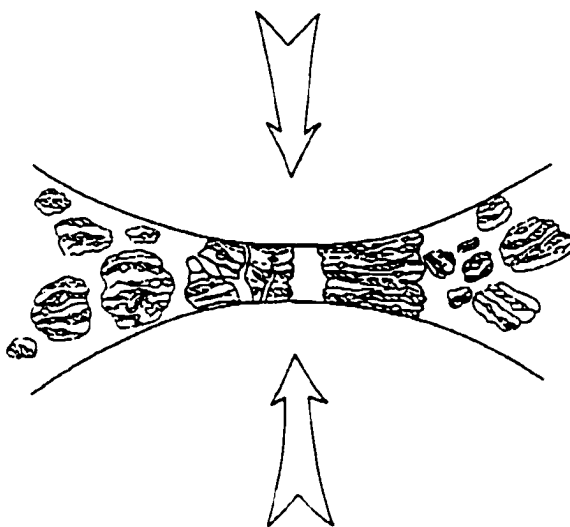


Fig.2.20 Schematic diagrams of ball-powder-ball collision[112].

Song^[109] pointed out that the principal effects of mechanical treatment or mechanical alloying by planetary milling are to increase both the specific surface area and the number of defects on the surface as well as in the bulk. Lee and Jang^[110] reported that MA formed many amorphous binary metal alloys and provided an intimate mixture of the elemental components and the severe plastic deformation introduces defects which may assist the diffusion process. In this case, the free energy of the amorphous alloy is lower than that of the mixture of the crystalline elements. However, Schwarz and Koch^[111] have prepared amorphous $\text{Ni}_{45}\text{Nb}_{55}$ and $\text{Ni}_{32}\text{Ti}_{68}$ powders by ball milling the

Chapter 2 Literature Review

respective crystalline intermetallics, Ni_6Nb_7 and NiTi_2 . To obtain amorphous material in this case, the free energy of the equilibrium intermetallic compounds must be raised to that of the amorphous alloy. It has been suggested by Koch and Kim^[112] that the defects introduced by milling raise the free energy of the intermetallic compound to that of the amorphous structure and that at a critical defect concentration the transition to the amorphous phase can occur. It has also been shown that the milling of two elemental components can first produce an intermetallic (or intermetallics) before subsequently transforming to the amorphous phase.

2.3.4 Factors Affecting the Ball Milling Process

There are various factors affecting the operation of the milling process such as:

(i) types of mills (e.g. horizontal rotating ball-mill, planetary ball-mill, stirred ball-mill or vibratory ball-mill);

Ahn and his co-workers^[113] used various ball milling methods (Fig.2.21) to obtain mechanically alloyed 50Ti-50Al. The microstructural evolution during the milling indicates that the mechanical alloying behavior is strongly affected by the milling method, and that horizontal ball milling is the most effective method for producing homogeneous metastable powders.

(ii) types of milling media (balls or rods);

(iii) types of milling tools (e.g. stainless steel or tungsten carbide);

Since the kinetic energy of the balls is a function of their mass and velocity, dense materials (steel or tungsten carbide) provide more energy than light materials (ceramic balls)^[101].

(iv) milling atmosphere (e.g. air, inert gas or nitrogen gas);

(v) milling mode (dry milling, wet milling);

(vi) ball-to-powder size ratio;

(vii) ball-to-powder weight ratio;

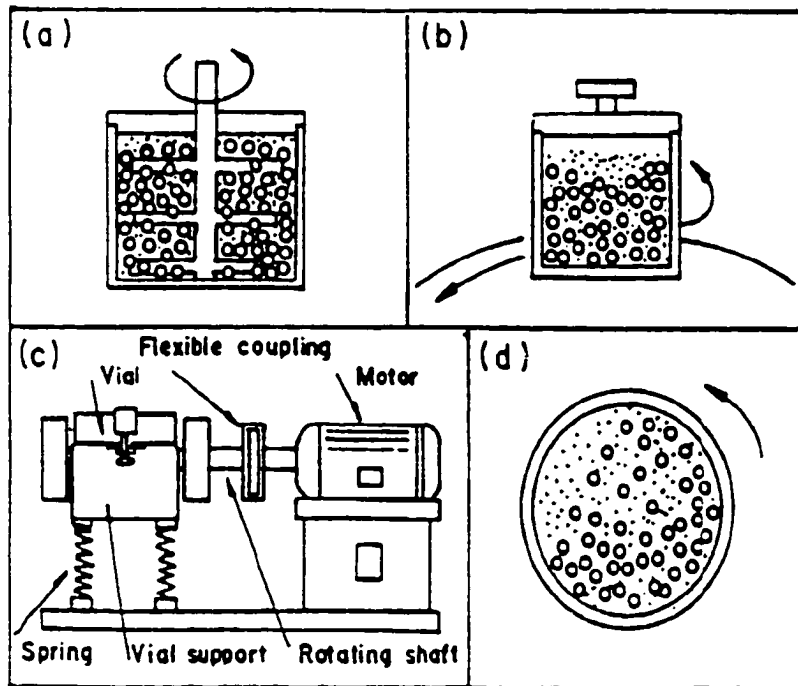


Fig.2.21 Schematic illustration of various milling methods: (a) attrition, (b) planetary, (c) vibratory, (d) horizontal ball milling[113].

El-Eskandarany and Aoki^[114] studied the effect of ball to powder weight ratio on the amorphization reaction of $Al_{50}Ta_{50}$ by ball milling. They concluded that the rate of amorphization depends strongly on the kinetics energy of the ball mill charge and this, in turn, depends on the number of opportunities for the powder particles to be reacted and interdiffused. Increasing the ball-to-powder weight ratio accelerates the rate of amorphization which is explained by the increase in the kinetic energy of the ball mill charge per unit mass of powder.

(viii) milling temperature;

(ix) speed of mill;

(x) dwell time of powders in the mill (milling time);

(xi) contamination.

2.3.5 Effect of Ball Milling on Hydrogen Storage Materials

Intermetallic compounds for hydrogen storage applications, e.g. Mg_2Ni , $LaNi_5$ and $FeTi$ have been investigated for about two decades^[115]. One of the most serious problems with these materials is that they do not absorb hydrogen under normal conditions and have to be activated prior to hydrogenation. The activation process is usually complicated, involving repeated annealing at high temperature and/or pressure.

Although $LaNi_5$ is regarded as an activation free alloy, it absorbs hydrogen slowly unless the activation treatment is performed. Fig.2.22 shows the hydrogen absorption curves of $LaNi_5$ at 293K and 2MPa H_2 after milling in an argon atmosphere. As the milling time increases, the hydrogen is

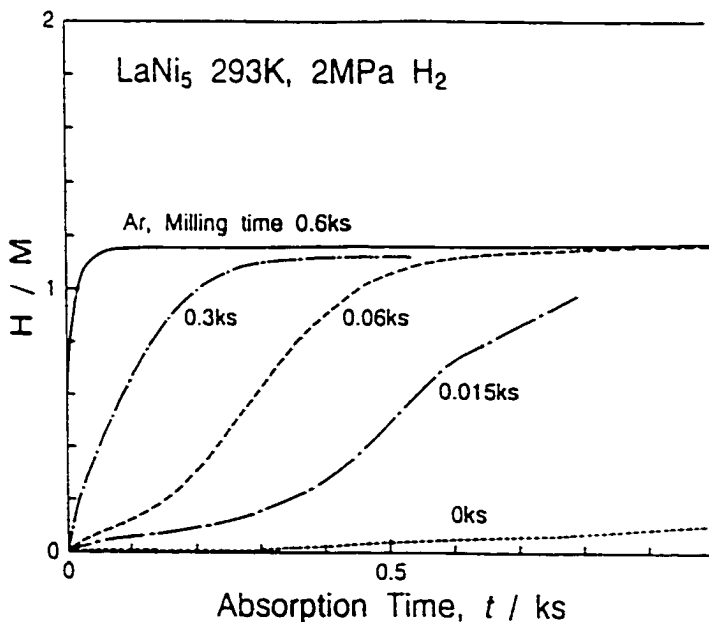
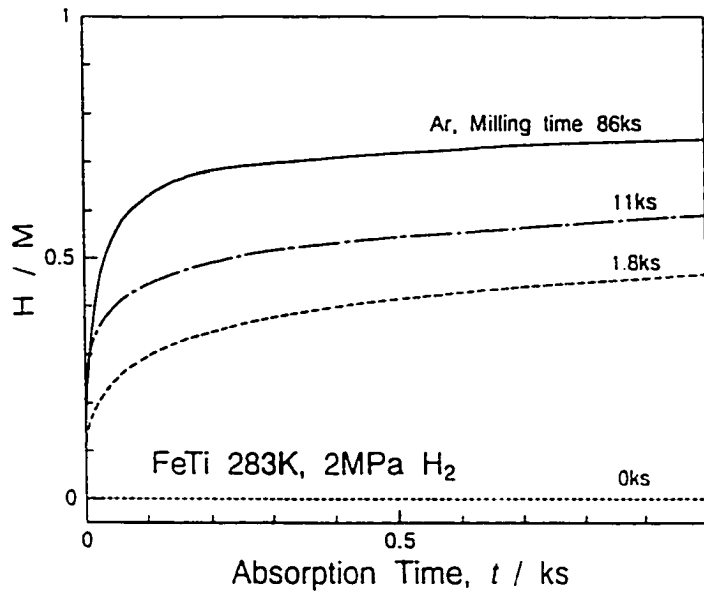


Fig.2.22 The hydrogen absorption curves of $LaNi_5$ powder at 293K and 2MPa H_2 after ball milling for 0, 0.015, 0.06, 0.3 and 0.6 ks[116].

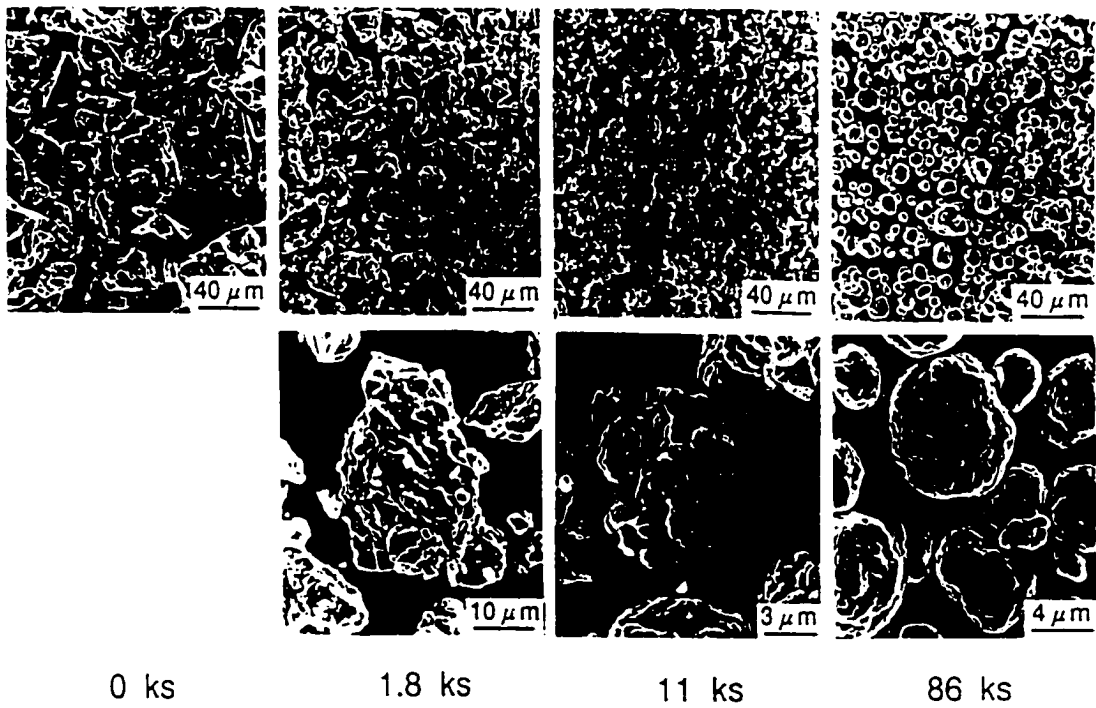
Chapter 2 Literature Review

absorbed more rapidly. Wasz and Schwarz^[116] examined the structure and reversible hydrogen storage capacity of alloys based on the LaNi_5 intermetallic alloys. Because the surface area is larger in the mechanically alloyed powders than in the as cast powders, it is anticipated that hydriding /dehydriding will be faster in the powders prepared by MA. For practical applications of LaNi_5 -based alloys (e.g., electrodes in Ni/metal hydride batteries), it is significant that alloys prepared by MA require neither surface activation nor hydrogen cycling to break down the powder to its 'terminal' particle size. The morphology of the activation or powder prepared by MA is virtually the same before and after hydrogen cycling, and hydrogen-induced cracking is minimal. The lack of hydride-induced cracking is partly due to the smaller initial particle size of the MA powder before hydriding, as well as the rounded agglomerate morphology that better accommodates the volume change caused by hydriding.

Aoyagi *et al.*^[79] suggest that the hydrogen absorption alloys FeTi and Mg_2Ni require an activation treatment before use, because their surfaces are covered by oxide layers, absorbed gases, moisture, etc., which impedes hydrogen absorption. The activation absorption treatment is usually performed by a number of heating-cooling cycles in a hydrogen atmosphere or in a vacuum. Although the mechanism of the activation is not as yet fully understood, the proposed mechanisms are divided roughly into two groups. The first group considers that the activation treatment of FeTi gives rise to Fe-rich clusters close to its surface and these clusters catalyze the dissociation of hydrogen gas. On the other hand, in powder metallurgy, it is well known that fresh surfaces are mechanically created by milling. Consequently, if the alloys are milled in an inert gas atmosphere and then hydrogenated without exposure to the air, hydrogen is expected to be readily absorbed. From Fig.2.23, we can see as the milling time increased, hydrogen is absorbed more rapidly, particularly at the initial stage. Tessier *et al.*^[117] found that ball milling the intermetallic compound



(a)



(b)

Fig.2.23 (a) The hydrogen absorption curves of FeTi powder at 283K and 2MPa H₂ after ball milling for 0, 1.8, 11 and 86 ks in an argon atmosphere and without exposure to the air[79].

(b) SEM micrographs of original FeTi powder and powders the ball-milled for 1.8, 1.1 and 86ks in an argon atmosphere[117].

Chapter 2 Literature Review

FeTi leads to progressive refinement of grain size and increasing chemical disorder of the alloy.

For a Mg_2Ni alloy, Chen and Dou^[118] found that the Mg and Ni powder particles are repeatedly cold welded by the colliding balls. Thus, composite powder particles with a characteristically layered microstructure (Mg_2Ni) are formed. Fig. 2.24 shows the effect of ball milling on the hydrogen absorption curve of Mg_2Ni milled in an argon atmosphere. It is worth noting that Mg_2Ni absorbs hydrogen even at room temperature after ball milling. Kohno *et al.*^[119,120] studied the hydrogen storage properties of a novel Mg_2Ni alloy powder prepared by a mechanical grinding method. The XRD pattern for Mg_2Ni alloy (Fig.2.25) showed that after 100h of mechanical grinding with Ni powder, the characteristic peaks of the Mg_2Ni phase had disappeared. The peaks of Mg_2Ni decreased in intensity and broadened [increased full width at half-maximum (FWHM)].

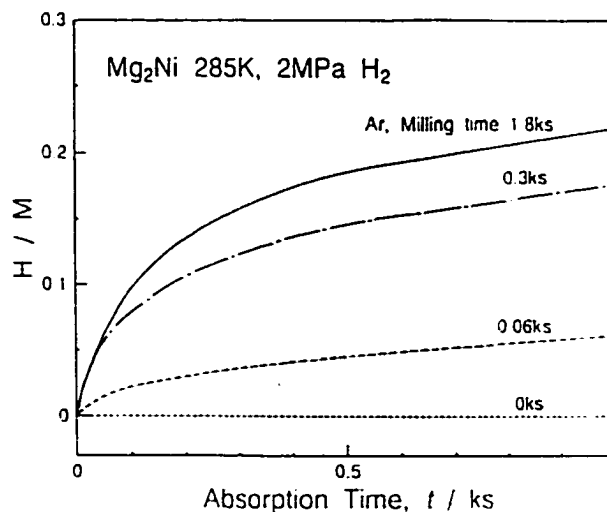


Fig.2.24 The hydrogen absorption curves of Mg_2Ni powder at 283K and 2MPa H_2 after ball milling for 0, 0.06, 0.3 and 1.8 ks in an argon atmosphere[118].

This profile indicated that the mechanically treated Mg_2Ni alloy (MG- Mg_2Ni) was transformed to an amorphous-like state. The discharge capacity of MG- Mg_2Ni electrodes at 25°C is 750mAh/g on

the first cycle in contrast to the low discharge capacity of untreated Mg_2Ni .

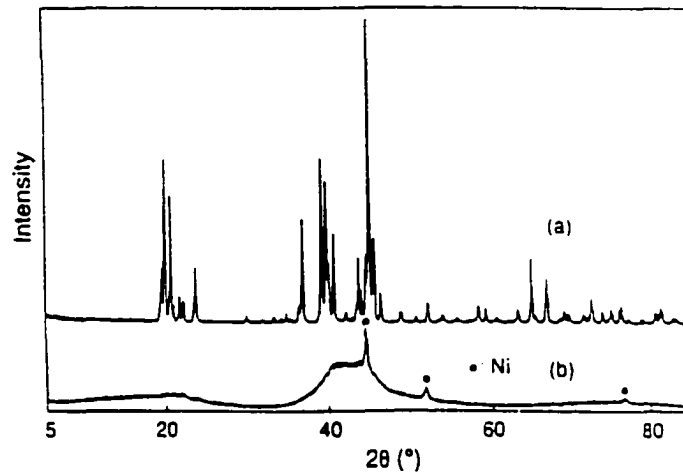


Fig.2.25 XRD patterns of (a) Mg_2Ni and (b) $MG-Mg_2Ni$ [119].

CHAPTER 3 EXPERIMENTAL DETAILS

This study had two main focii. The first purpose was to investigate the potential beneficial effects of ball milling a Mg_2Ni alloy which is then to be used as the negative electrode in a Ni-MH battery. The second purpose was to investigate the viability of constructing P-C-T curves, and calculating specific thermodynamic parameters, using electrochemical measurements, rather than the more conventional manometric (gas phase) experiments.

3.1 Materials

One of the more promising hydrogen storage alloys, Mg_2Ni , was chosen as the experimental material for the study of the battery negative electrode properties (such as the charge-discharge characteristics and electrochemical properties) and the effect of ball milling treatment of the alloy powder on these properties. A commercial $LaNi_{4.7}Al_{0.3}$ alloy was chosen for the study of the relationship between hydrogen-absorption/desorption parameters determined from electrochemical parameters and P-C-T curves as determined by manometric methods, which are the most commonly used technique for such measurements but are extremely time-consuming.

The Mg_2Ni and $LaNi_{4.7}Al_{0.3}$ alloys were manufactured by Ergenics Co. under the HY-STOR trade name. They were produced by induction melting of elemental powders, analyzed chemically and examined metallographically by the Ergenics Division of MPD Technology Corporation. The alloys had been pulverized into powders of -325 mesh size. The chemical formula of the Mg_2Ni is actually $Mg_{2.35}Ni$, which is a Mg-rich version of Mg_2Ni designed to avoid the formation of $MgNi_2$ during solidification. The density of Mg_2Ni is 3.2 g/cm^3

(unhydrided) and that of $\text{LaNi}_{4.7}\text{Al}_{0.3}$ is 8.0 g/cm^3 .

Pure elemental Ni powder (-325mesh, 99.99% purity) was mixed with Mg_2Ni alloy during ball milling. Elemental Ni or Cu powders were added to the ball-milled mixture in the electrode fabrication process. Figs.3.1 and 3.2 illustrate the morphology and X-ray diffraction patterns of the as-cast Mg_2Ni and Ni powders, respectively. The particles are irregular in shape. The large particles are Mg_2Ni alloy and remainder is Ni powder. The particle size is approximately $25\mu\text{m}$. The XRD patterns of the mixed powders clearly showed sharp peaks of Ni elemental powder and characteristic peaks for the crystalline Mg_2Ni alloy.

3.2 Ball Milling Treatment

Ball milling was performed in a laboratory high-energy ball mill Spex 8000 (Spex Industries, Inc., Edison, NJ), which was equipped with two fans for cooling: see Fig3.3. This single-clamp mill/mixer is an efficient, compact laboratory mill capable of pulverizing samples in the 10-gram range, and is typically used for pulverizing rocks, minerals, sand, cement, slag, ceramics, catalyst supports, and many other brittle, hard samples.

The Spex 8000 Mill/Mixer consists of a clamp and a vial, into which milling balls and samples are charged, as the main components to pulverize the samples. The vial (Fig.3.4) is clamped in place and shaken at a speed of 1200rpm in a complex motion, which combines both back-and-forth swings with short lateral movements, such that each end of the vial describes a figure-eight: see Fig.3.5. The milling vial is made of tungsten carbide and is 6.35cm in diameter and 7.62cm long. The milling balls, which are 1.27cm in diameter, are made from 440C martensitic stainless steel. Fig.3.6 is a photograph of the tungsten carbide container and the milling balls, from which the larger balls were used in this experiment.

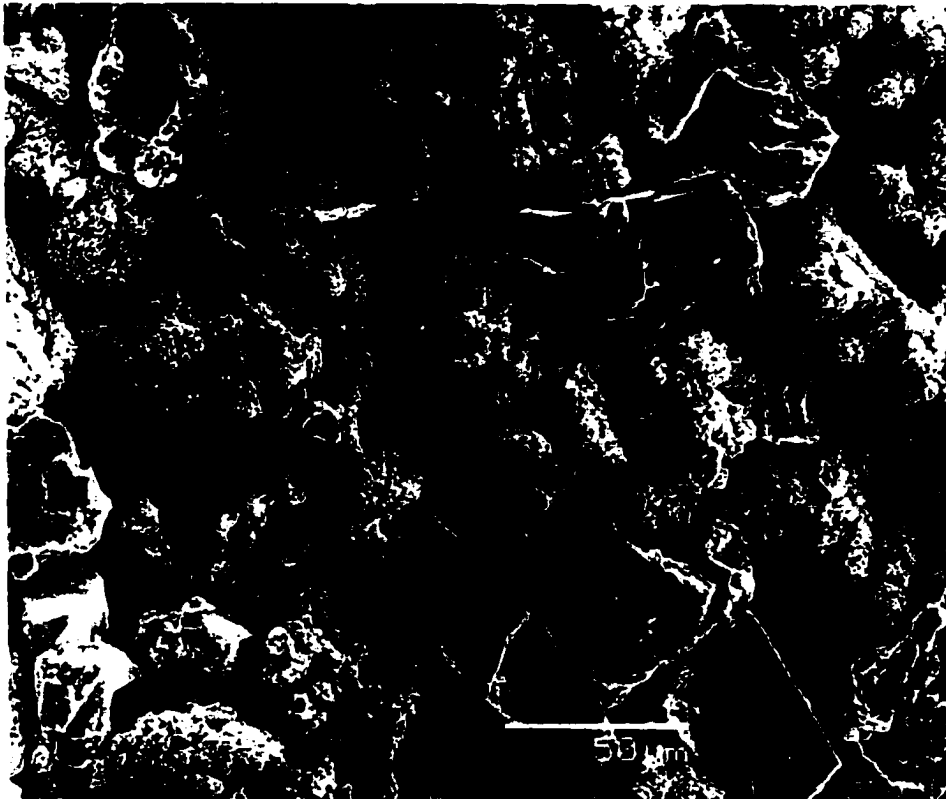


Fig. 3.1 SEM morphology of as-cast Mg₂Ni and Ni powders

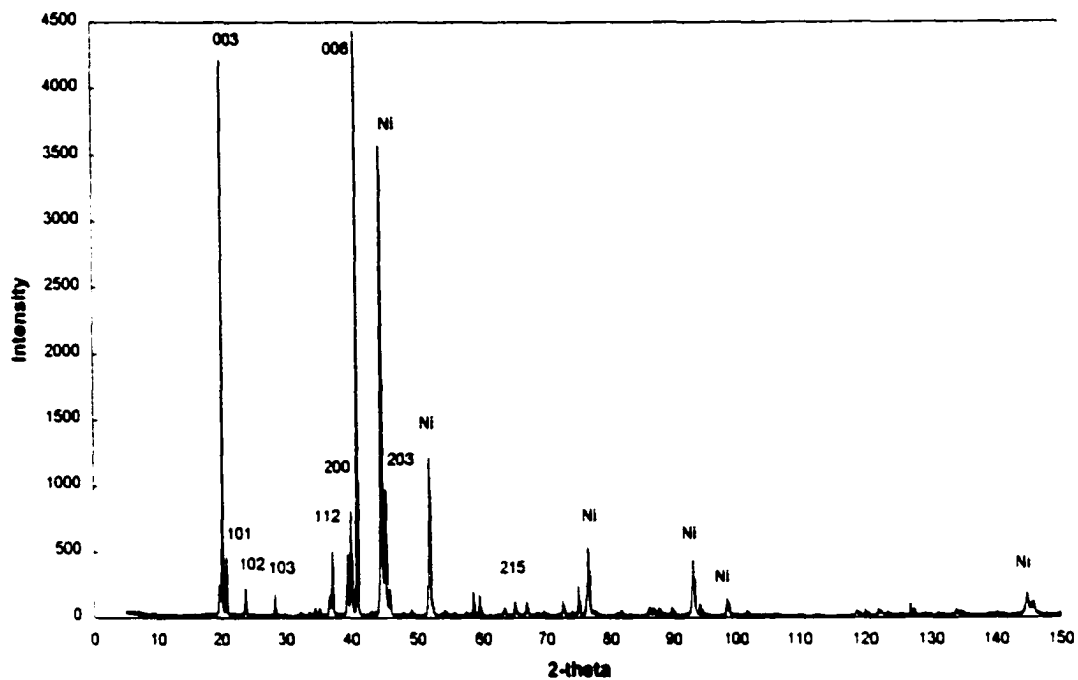


Fig. 3.2 X-ray diffraction pattern of as-received Mg_2Ni and Ni powders.

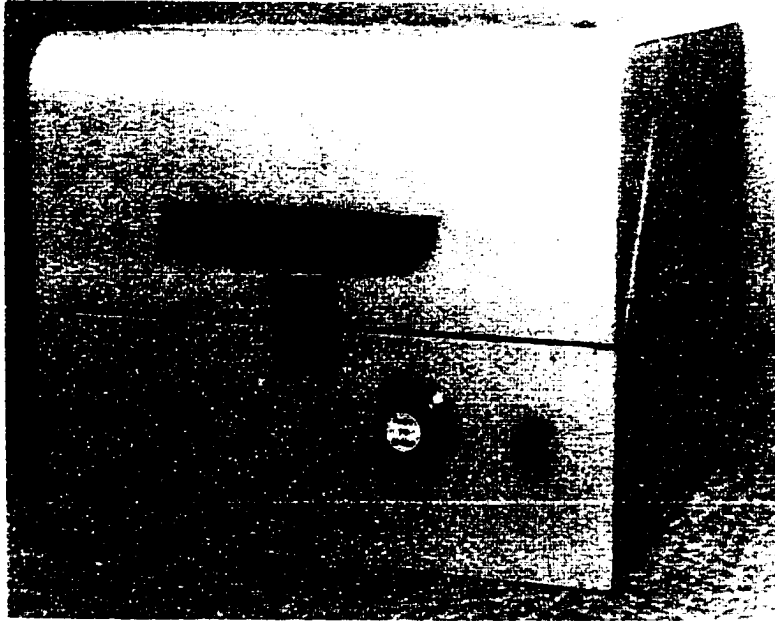


Fig. 3.3 Photograph of the Spex 8000 mill/mixer

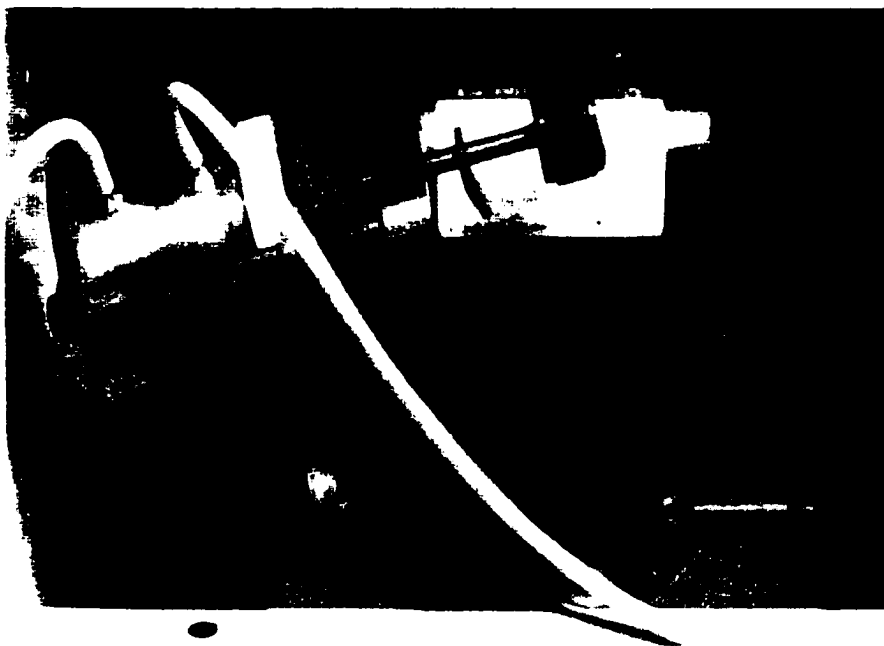


Fig. 3.4 Photograph of Spex 8000 mill/mixer and its single clamp.

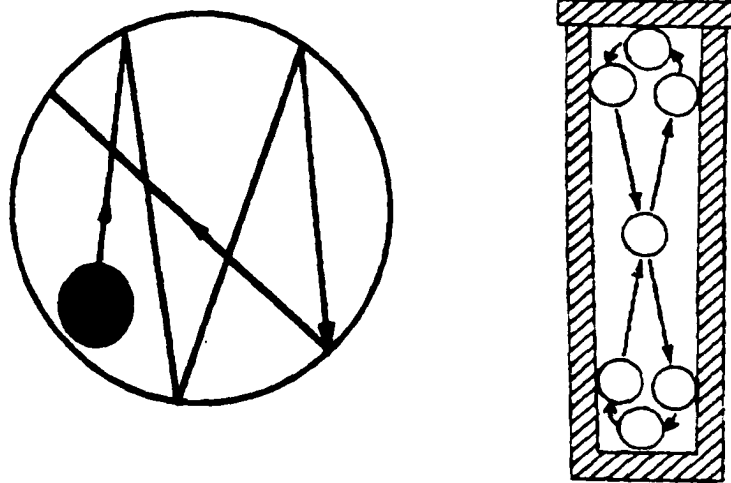


Fig. 3.5 Schematic drawings of the ball trajectories for the Spex 8000 mill/mixer.

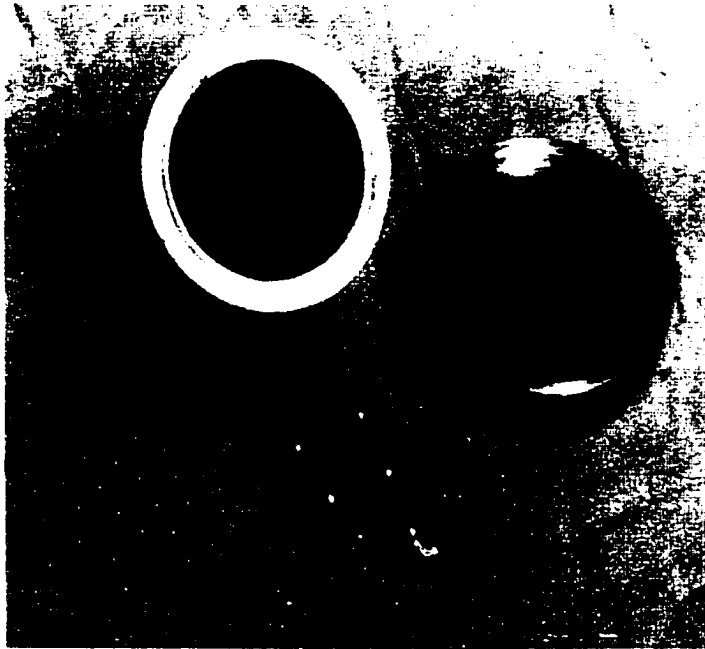


Fig. 3.6 Photograph of tungsten carbide container and milling balls

To minimize oxygen contamination, the vial was sealed with an elastomer O-ring under a pure nitrogen atmosphere. The mixture of milling balls and the materials, (2.147g Mg₂Ni and 1.174g Ni (mole ratio was 1:1) powder) was charged into the vial, and the vial was sealed. A continuous flow of pure nitrogen was maintained from the upper inlet and out of the vial from the lower outlet. The vial was saturated with pure nitrogen during the ball milling.

Theoretically, the rate of amorphization depends on the kinetic energy of the ball mill charge and this depends on the probability of the powder particles being reacted and inter-diffusing. Increasing the ball-to-powder weight ratio facilitates the pulverization (attrition) and accelerates the rate of amorphization by increasing the kinetic energy of the ball mill charge per unit mass of powder. However if there are too many balls, they will stick together due to space limitations in the vial and thus the kinetic energy is reduced. To avoid sticking of the powders to both the balls and the vial walls, the ball-to-powder weight ratios chosen for study were 1:1, 5:1 and 10:1. The various ball-milling conditions utilized in this study are listed in Table 3.1.

Table 3.1 Ball Milling Parameters for Mg₂Ni Alloy

BALL MILLING AT CONSTANT BALL-TO-POWDER WEIGHT RATIO (5:1)								BALL MILLING AT CONSTANT MILLING TIME (25 HOURS)		
Ball Milling Time (Hours)								Ball-to-Powder Weight Ratio of		
0	0.5	1	5	10	25	50	80	1:1	5:1	10:1

3.3 Materials Characterization Techniques

3.3.1 Scanning Electron Microscopy

Scanning electron microscopy (SEM) was used to: (i) characterize the microstructures of the as-cast Mg₂Ni alloy, (ii) determine the particle size, and (iii) observe the morphologies of the ball-milled Mg₂Ni powders after different ball-milling times.

The as-cast Mg₂Ni was sectioned and then mounted in epoxy thermosetting powder (blue) using a specimen mounting press. The specimen was wet polished on silicon carbide papers of 240, 320, 400 and 600 grit followed by polishing on 1.0 micron and 0.5 micron alumina wheels. The specimen was etched using 30%wt HNO₃ aqueous solution and then placed in the SEM for the microstructural observations. Fig.3.7 shows the microstructure of as-cast state Mg₂Ni alloy (Fig.3.7a) and a higher magnification micrograph of the interface area (Fig.3.7b). It clearly shows the eutectic phase which has formed on solidification of the alloy.

Because of their tendency to stick together, the ball-milled Mg₂Ni powders were first de-agglomerated using ultrasonic methods, and the dispersed particles placed on SEM specimen holders (stubs). These specimens were then placed in SEM to determine both the particle size and to characterize the morphologies of the ball-milled powders.

A JEOL5000-LV Scanning Electron Microscope was used at magnifications ranging from 50× to 2000×. The accelerating voltage was 15kV and the images were recorded on 10×12.5cm sheet film. Qualitative compositional analysis of the bulk dendrites and their interfaces was performed using a Kevex energy dispersive system that was attached to the SEM. Fig.3.8 is the qualitative compositional analysis of the eutectic (area A) and their interfaces (areas B and C). It demonstrates that Mg and Ni are the major elements in areas A, B and C, but a small amount of K and Si is present in areas B and C, which could be result of polishing using

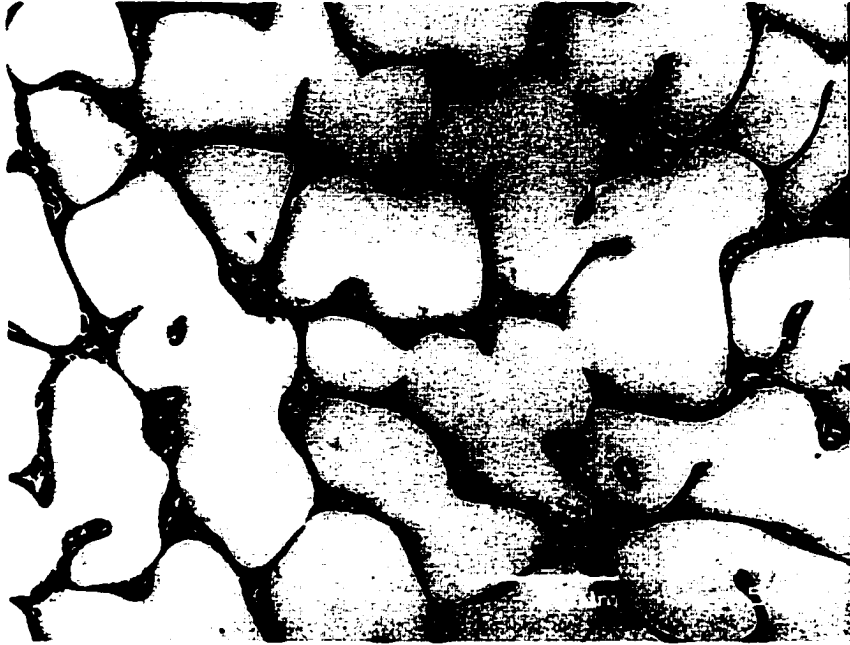
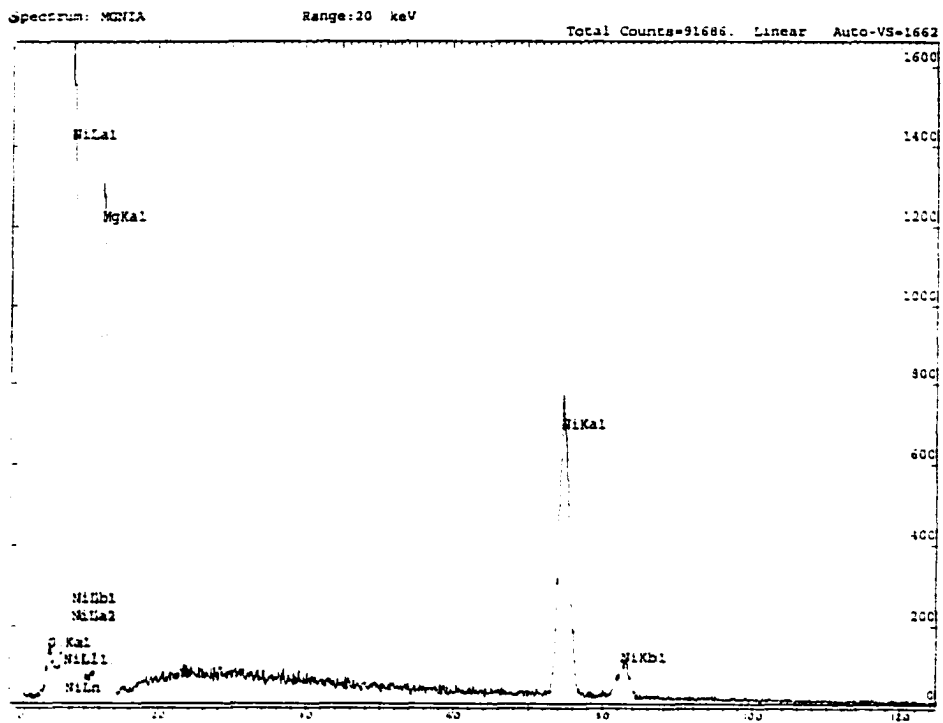


Fig. 3.7 (a) Microstructure of as-cast Mg₂Ni alloy

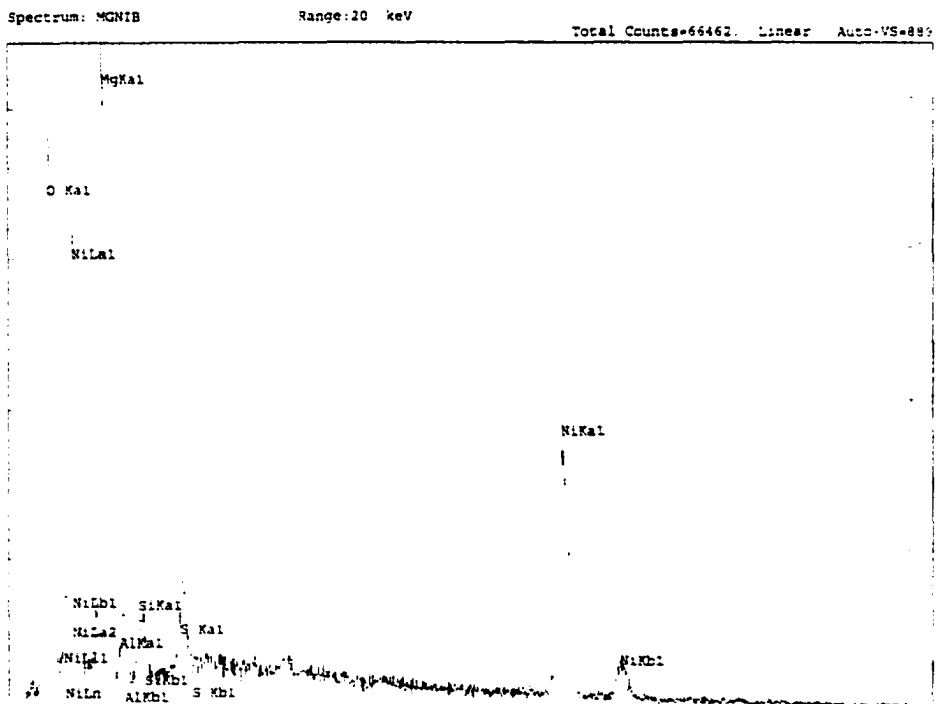


Fig. 3.7 (b) Magnified eutectic structure and interface area

Chapter 3 Experimental Details



(a)



(b)

Fig. 3.8 Qualitative compositional analysis of (a) dendrites and (b) interface area

sand paper and Al_2O_3 .

3.3.2 X-ray Diffraction

X-ray diffraction techniques were used for phase identification, lattice parameter determination, and the characterization of the internal strain and amorphization induced by the ball milling.

A Phillips X-ray diffractometer with a proportional counter detection head was used. Graphite monochromated $\text{CuK}\alpha$ radiation, at a voltage of 40 kV and a current of 20 mA, was utilized as the diffracting medium, along with a computer to count and display the diffraction pattern. The angular range (2θ) scanned was 5° to 150° with a 0.02° scanning step size.

Phase identification and lattice parameter calculations were accomplished through comparison of the results with data from the ASTM Diffraction Files. Appendix A contains the diffraction file cards that were used to identify the diffraction peaks. The degree of amorphization was determined by comparing the number, intensity and width of the diffraction peaks. The broadening and the reduction of intensity of the characteristic diffraction lines illustrate the beginning of the amorphous state.

The effects of strains, both uniform and non-uniform, on the direction of X-ray reflection are illustrated in Fig.3.9. If the grain is subjected to a uniform tensile strain at right angles to the reflection planes, the spacing becomes larger than d_0 , the equilibrium spacing for an unstrained grain in (a), and the corresponding diffraction line shifts to lower angles but does not otherwise change, as shown in (b). In (c) the grain is bent and the strain is non-uniform; the non-uniform strain due to residual micro-stress is the major cause of line broadening of the diffraction line.

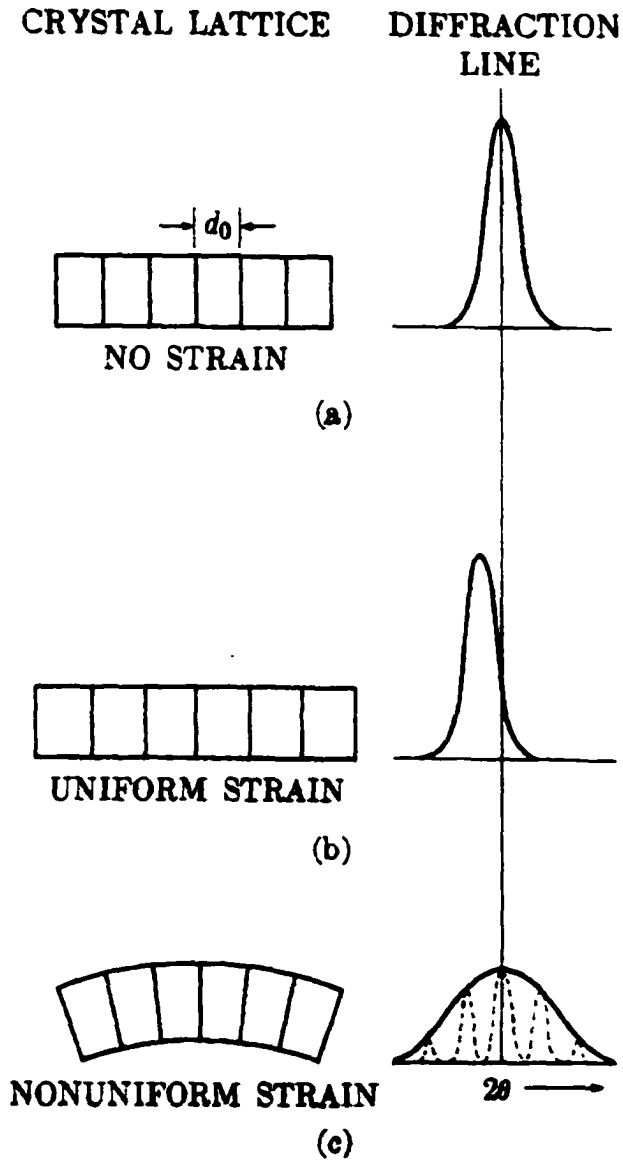


Fig. 3.9 Effect of lattice strain on Debye-line width and position.

After ball milling, the initial sharp diffraction lines of the Mg_2Ni powders broadened with milling time and the weaker lines disappeared into the background. To analyze these observations, the Williamson and Hall method^[121] was used to estimate the internal lattice strain and crystallite sizes from the diffraction line breadths.

For each peak, defined by its Bragg angle (θ), the width (β_{exp}) of a diffraction line was measured as the full width at half intensity. The instrumental broadening (β_{instr}) which is due to instrumental error, was removed as follows:

$$\beta_{sample}^2 = \beta_{exp}^2 - \beta_{instr}^2 \quad (3.1)$$

where β_{sample} is the broadening due to the sample itself. The instrumental broadening was determined using a pure Mg_2Ni powder sample which had been annealed for 2hrs at 300°C in vacuum: see Fig.3.10 for its diffraction pattern. The broadening due to the sample increased with Bragg angle, and was separated into a crystal size-dependent term and internal strain term: using the Hall-Williamson relationship:

$$\beta_{sample} \cdot \cos\theta = \frac{K\lambda}{D} + 2\varepsilon \sin\theta \quad (3.2)$$

where K is the Scherrer constant (value ≈ 1), λ is the wavelength of the radiation used, D is the crystal size (grain or dislocation cell size here), and ε is the internal strain (microstrain).

By examining the broadening of the sample powder peaks, $\beta_{sample} \cdot \cos\theta$, using a Hall-Williamson plot makes it possible to identify the internal strain from the slope of the $\beta_{sample} \cdot \cos\theta - \sin\theta$ plot. Half the slope of the $\beta_{sample} \cdot \cos\theta - \sin\theta$ plot is the internal strain ε . The intercept of the straight line, ($=K\lambda/D$), gives the crystal size, D .

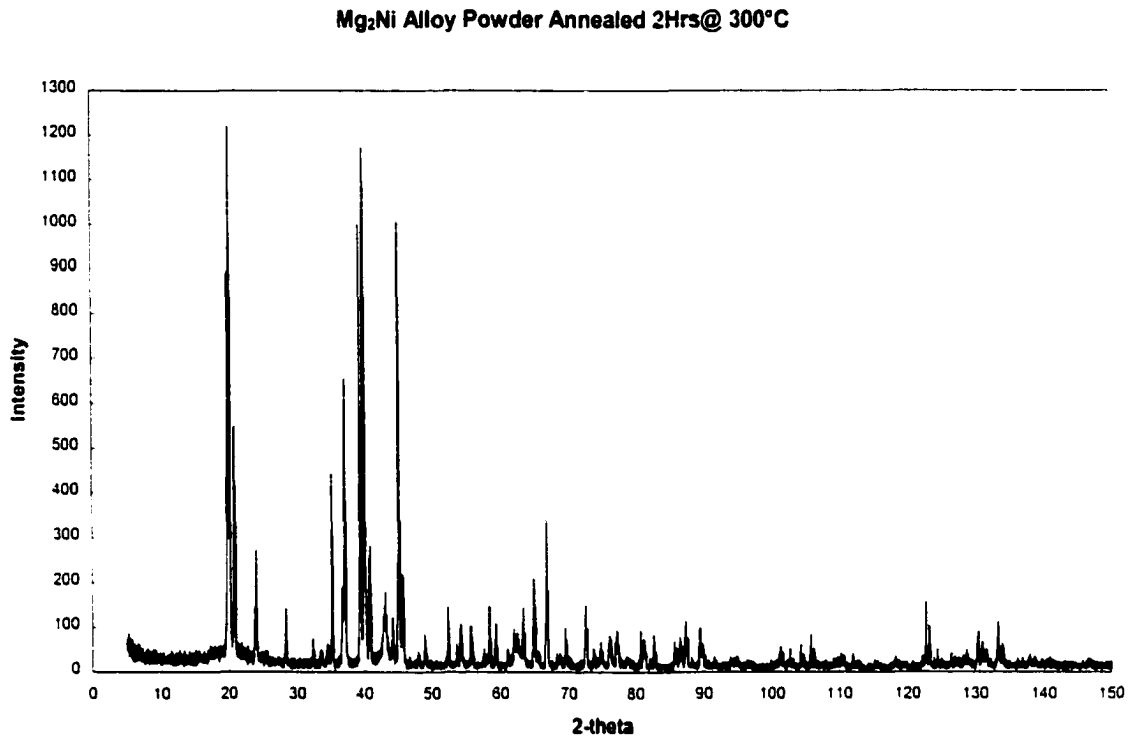


Fig. 3.10 X-ray diffraction pattern for annealed Mg₂Ni powder.

3.3.3 Specific Surface Area (SSA)

Specific surface area (SSA, m^2/g as the unit) is defined as the total surface area (m^2) of particles per 1 gram ball-milled Mg_2Ni alloy. The particle size can be obtained from the SEM observations, r_p was assumed to be the particle radius after different ball milling times and different ball-to-powder weight ratios. The surface area of one particle can be calculated by:

$S_{\text{OneParticle}} = 4\pi r_p^2$. The volume of one particle is: $V = \frac{4}{3}\pi r_p^3$. As the density ρ of Mg_2Ni alloy is $3.2\text{g}/\text{cm}^3$, the weight of one particle is: $W = \rho \cdot V$ and the specific surface area (SSA) is then obtained from equation (3.3):

$$SSA = \frac{3}{\rho \cdot r_p} \quad (\text{m}^2/\text{g}) \quad (3.3)$$

3.4 Electrochemical Measurements

Electrochemical measurements (DC) of the battery negative electrode made of ball-milled Mg_2Ni powder were carried out using an automatic charge-discharge unit, *Solartron 1285* Potentiostat/Galvanostat, interfaced with Pentium-PC and *Corrview 2.0* software.

The measurement of the electrochemical properties, such as charge/discharge characteristics, capacity, open circuit potential, polarization curves and cyclic voltammetry were carried out at room temperature using an open tri-electrode measurement system (Fig.3.11). A mercury oxide electrode, $\text{Hg}/\text{HgO}/6\text{M KOH}$, was used as the reference electrode (RE). The working electrode (WE, i. e. negative electrode of the battery) was made from the ball-milled Mg_2Ni powder. Two sintered NiOOH counter electrodes (CE) measuring $2\text{cm} \times 6\text{cm}$ were set up on either side of the working electrode. The negative electrode was immersed in 6M KOH aqueous solution together with counter electrodes and reference electrode, and separated by a

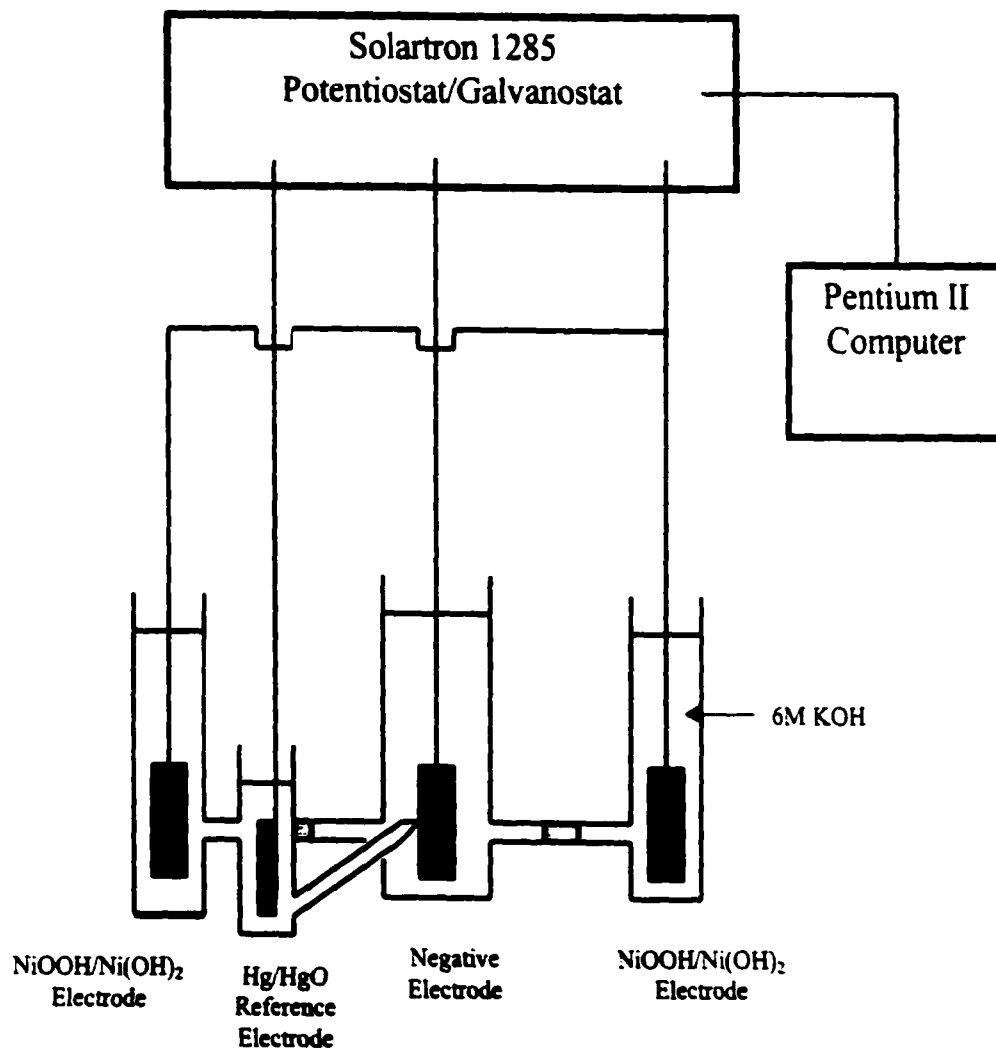


Fig. 3.11 Schematic drawing of standard tri-electrode measurement system.

Chapter 3 Experimental Details

porous filter. The tri-electrode system was connected to *Solartron 1285* Potentiostat/Galvanostat to conduct measurements. Figs 3.12 and 3.13 are photographs of the electrochemical measurement system and the tri-electrode measurement system, respectively.

3.4.1 Metal Hydride Electrodes

The negative electrodes were made from ball-milled Mg_2Ni alloy powders, nickel and copper powders and a 3 wt% polytetrafluoroethylene (PTFE) dispersion (60%). The working electrode should be fabricated as soon as possible after ball milling the powders so as to minimize any oxidation. First, about 50mg of Mg_2Ni powder was taken out of the vial and mixed thoroughly with pure nickel or copper powder (same weight as the Mg_2Ni powder). An appropriate amount (about 4 drops) of PTFE dispersion was then added to the mixture to form a paste. The paste was then placed onto both sides of a porous nickel plate (100mm × 15mm × 0.04~0.05mm) and mechanically pressed to make a sandwich electrode (Fig.3.14). The geometrical area of the working electrode was 2.25 cm². The electrodes were dried at room temperature for 24 hours before commencing the electrochemical measurements. Table 3.2 lists the various electrodes fabricated for this study.

3.4.2 Measured Parameters

Discharge Capacity

Discharge capacity is a very important characteristic for measuring the discharge ability per unit weight of electrode, and is calculated from the discharge current. The unit for discharge capacity is mAh/g.

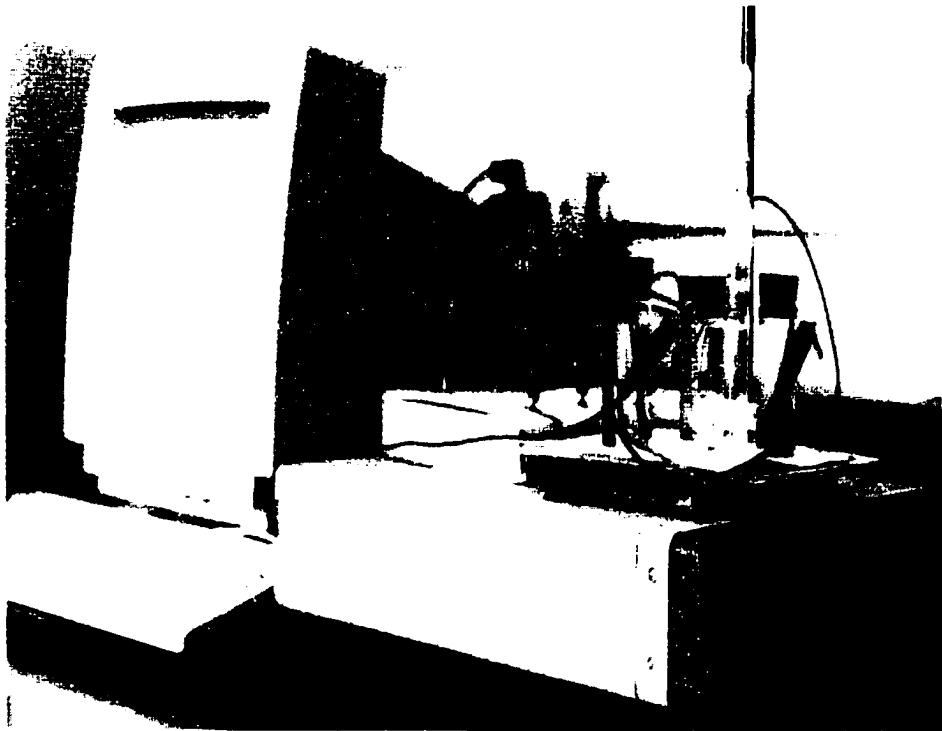


Fig. 3.12 Photograph of electrochemical measurement system.



Fig. 3.13 Photograph of the tri-electrode measurement system.

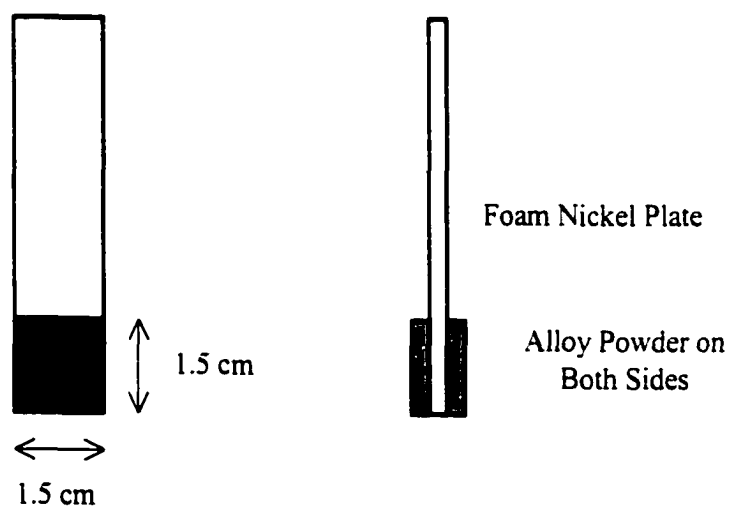


Fig. 3.14 Schematic diagrams of experimental electrode.

Table 3.2 Mg₂Ni Electrodes Fabricated for This Study

NO.	TIME OF BALL MILLING (HRS)	BALL-TO-POWDER WEIGHT RATIO	ELEMENTAL ADDITIVES
I	Different ball milling times at ball-to-powder weight ratio of 5:1		
1	0	5:1	N/A
2	10	5:1	N/A
3	25	5:1	N/A
4	50	5:1	N/A
5	80	5:1	N/A
II	25 hours ball milling at different ball-to-powder weight ratios		
6	25	1:1	N/A
7	25	5:1	N/A
8	25	10:1	N/A
III	Elemental addition of Cu and Ni		
9	25	5:1	Cu 1:1
10	25	5:1	Ni 1:1

The negative electrode was charged under a constant current density of 100mA/g for 10 hours and the hydrogen content reached its saturated value. After 10 minutes rest, the discharge process was conducted using a current density of 200mA/g until the potential of the negative electrode reached $-0.5V$ with respect to the Hg/HgO/6M KOH electrode. One electrode made from 25hrs ball-milled Mg₂Ni powder was discharged at 50mA/g to study the effect of high/low

Chapter 3 Experimental Details

discharge current on discharge capacity. The potential of the negative electrode was recorded as a function of time for both the charge and discharge processes. The discharge capacity for each cycle was calculated according to the equation (2.30): $Q_{Discharge} = It$, where Q is the discharge capacity (mAh/g), I is discharge current (mA/g), t is discharge time (hrs). A total of 25 cycles of charge-discharge cycles were conducted for each electrode.

Open Circuit Potential

Open circuit potential measurements were made so as to allow for the recovery of the electrode surface to an equilibrium state and thus eliminate the effects of polarization on the electrochemical parameter measurements in the subsequent cycles. The counter electrodes were disconnected from the tri-electrode system. The working electrode potential was then recorded with respect to the reference electrode as a function of time until it became stabilized, i.e. until the change of the potential was less than 1mV for a period of 1h.

Polarization Curves (Tafel Polarization Curve)

Polarization curves were used to obtain information on the charge-discharge behavior, surface film formation, and the thermodynamics and kinetics of the hydrogen absorption-desorption process.

After the open circuit potential was stabilized, polarization curve measurements were conducted at a scanning rate of 0.1667mV/sec^[122] from -0.15V to 0.15V vs. open potential. Polarization curves (E vs. $\log i$) were obtained after each charge-discharge cycle.

Exchange Current Density (Linear Polarization Curve)

The electrocatalytic activity for the metal hydride (MH) electrode can be estimated from the exchange current density, i_0 . The value of i_0 was determined from linear polarization curves in the vicinity of the equilibrium potential and can be calculated from the following equation:

$$i_0 = \frac{RTi}{F\eta} \quad (3.4)$$

where i and η are the discharge current density and corresponding over potential respectively; R is the gas constant; T is the absolute temperature and F is the Faraday constant.

The linear polarization measurements were conducted using the same technique ^[122] as for the Tafel polarization measurements except that the scanning potential was from -0.03 V to 0.03 V vs. the equilibrium potential.

Cyclic Voltammetry Measurements

Cyclic voltammetry measurements were used to determine the mechanisms of the electrochemical reactions and to identify the species present in the solution. Cyclic voltammetry measurements were carried out after the open circuit potential measurements at a scanning rate of 1mV/sec from -0.2V to 0.2V and back to -0.2V (vs. open potential) for every 5 charge-discharge cycles.

Pressure-Composition Isotherm Measurements

In order to understand the hydrogen absorption characteristics of hydrogen storage materials, P-C-T curves were generated both in the gas phase and in the 'electrochemical' environment. A schematic diagram of the Seivert's type apparatus used in this investigation for the gas phase (manometric) measurement is shown in Fig.3.15. The complete system is made of stainless steel. It is designed so that there are as few connections as possible. The reactor vessel was constructed from 304 stainless steel with two tapped parts for the inlet or outlet gas and thermocouple connections. An O-ring sealed endplate fastened with four stainless steel bolts, provides a good seal and facilitates loading and removal of the alloy specimens. The reactor volume is 31.6 ± 0.3 ml.

The absorption isotherm measurements are begun with a virgin sample, or a completely

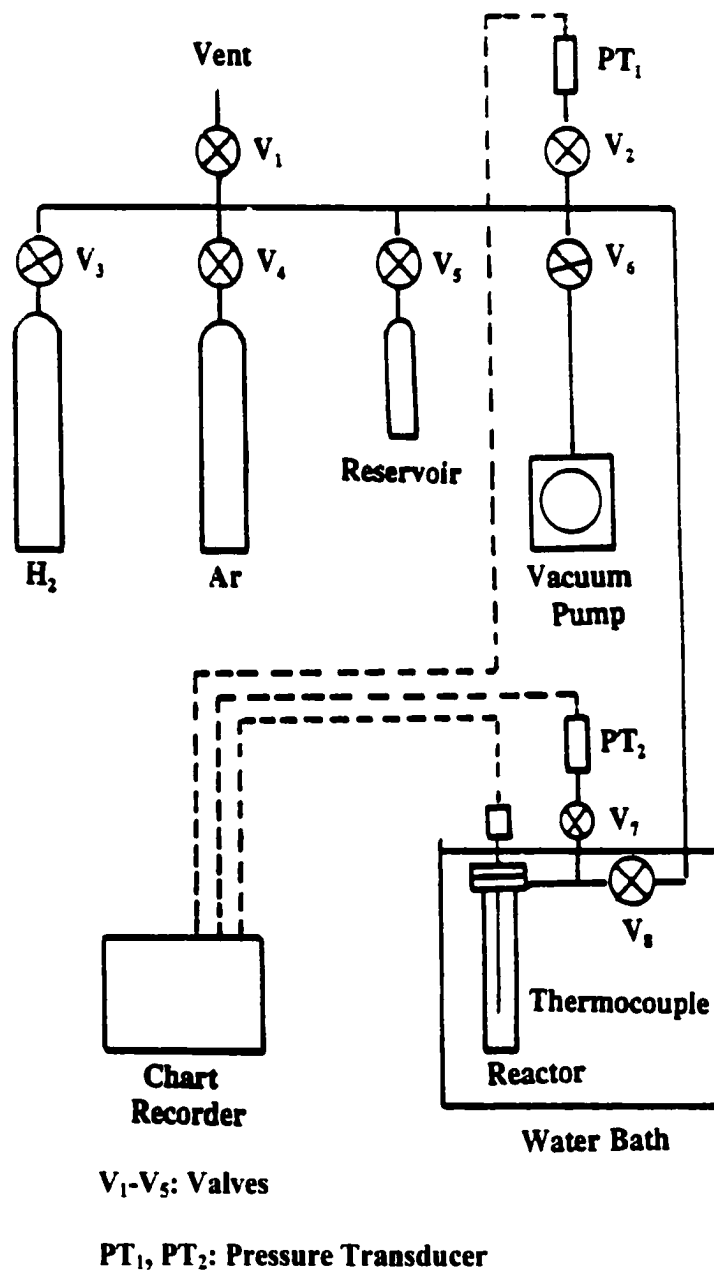


Fig. 3.15 Schematic diagram of the experimental Sievert's apparatus.

desorbed sample. An aliquot (dose) of hydrogen is introduced into the reactor. The pressure change is measured by a pressure transducer and recorded on a chart recorder until the equilibrium pressure is obtained. Additional aliquots are added, and same procedure is repeated. Desorption isotherms were obtained by essentially reversing the absorption isotherm procedure.

The amount of hydrogen absorbed or desorbed by a sample was calculated using pressure-temperature relationships. Since hydrogen behaves very nearly like an ideal gas at lower temperatures, the ideal gas law was assumed to apply, namely:

$$PV = nRT \quad (3.5)$$

where P is the pressure (Pa) in the reactor, V is the volume (m^3) of the reactor, R is the gas constant and has the value of $8.314441\text{J/mol}\cdot\text{K}$, T is the absolute temperature (K) of the reactor and n is the number of moles of hydrogen gas contained in the reactor. This equation is valid at room temperature where the temperature was uniform throughout the reactor.

For a material with a high hydrogen absorbing-desorbing ability at room temperature, the conventional P-C-T curve method is a very effective method for studying the hydrogen absorption-desorption characteristics. However this technique is not applicable to the Mg_2Ni alloy, since although its hydrogen absorbing ability is very high, the absorbing and desorbing processes are thermodynamically impossible at room temperature. The electrochemical measurement technique is a viable alternate method to study the absorbing and desorbing processes at room temperature. A $\text{LaNi}_{4.7}\text{Al}_{0.3}$ alloy has been used to evaluate the applicability of translating the electrochemical measurements to an equivalent P-C-T curve. In the electrochemical measurements, the negative electrode was charged at a current density of 50mA/g for 7 hours and then discharged at a current density of 20mA/g for 1 hour and rested 30 minutes. The discharge and rest processes were repeated continuously until the potential of

Chapter 3 Experimental Details

negative electrode reached -0.5V vs. the reference electrode. The potentials at every discharge and rest cycle were recorded with time.

The equilibrium pressure corresponding to conventional P-C-T measurement was calculated according to equation (2.27): $E = -0.9324 - 0.0296 \text{Log}P_{H_2}$, where E (in the unit of V) is the equilibrium potential after 1 hour discharge, i.e. the stable potential in the open circuit measurement after each discharge process, P_{H_2} (in the unit of atm) is the hydrogen equilibrium pressure. A series of P_{H_2} values were calculated using this equation from a series of potentials, E , and a P-C-T curve was constructed.

CHAPTER 4 ELECTROCHEMICAL PROPERTIES OF BALL-MILLED Mg₂Ni ALLOYS

Mechanical grinding has two main effects on the Mg₂Ni alloy. Firstly, it significantly increased the specific surface area because of the reduction in the Mg₂Ni particle size (see Chapter 6). Secondly, it creates many defects including fine cracks on the surface, which are highly permeable to hydrogen, and thus the powder is immediately activated. Thus the electrochemical kinetics of mechanical-grounded Mg₂Ni electrodes was highly accelerated.

The electrochemical kinetics properties and transport properties of Mg₂Ni electrodes, such as polarization resistance R_p , exchange current density i_0 and the hydrogen diffusion coefficient, D_0 , are important to characterize the performances of electrodes and the electrochemical capacity.

4.1 Charge/Discharge Capacity of MG-Mg₂Ni Alloy

Electrochemical galvanostatic charge/discharge is a more effective and less time-consuming technique to determine the absorbing hydrogen capacity than gaseous techniques. During the charge/discharge processes, a cathodic current was imposed to break down the water in 6M KOH aqueous solution, and atomic state hydrogen was absorbed into the interstitial sites of Mg₂Ni. A positive current was imposed on the hydrogen saturated Mg₂Ni to release the hydrogen.

4.1.1 Charge/Discharge Characteristics

Charge/discharge curves are the basis for the measurement of specific discharge capacity. Fig.4.1 gives the charge curves, i.e. potential vs. charge time, for as-cast Mg₂Ni after a different number of charge cycles. In each cycle, the equilibrium potential of the electrode depends on the hydrogen content in the alloy. At the initial stage of charging, the equilibrium potential shifted rapidly in the cathodic direction as the hydrogen content in the alloy increased. With further increase of the hydrogen content in the electrode, the equilibrium potential reached a plateau, which is an indication of hydrogen saturation in the alloy. With increasing number of charge cycles, the plateau potentials became more negative, indicating that the electrode becomes more active, i.e. higher hydrogen content. Similar behavior was observed for electrodes made from Mg₂Ni alloys which had been subjected to 10 hours (Fig.4.2), 25 hours (Fig.4.3) and 50 hours (Fig.4.4) ball milling. The electrochemical activity of MG-Mg₂Ni increases gradually with ball milling times and is much larger than that of the as-cast Mg₂Ni alloy.

Fig.4.5 shows the charge curves for electrodes made from alloy powder ball-milled 25 hours at a ball-to-powder weight ratio 1:1. Comparing these curves with those for electrodes made from material ball-milled with a ball-to-powder weight ratio of 5:1 (Fig.4.3) and 10:1 (Fig.4.6), it can be seen that the plateau potential difference between initial and final stages of charging increased from 20mV to 50mV with increasing ball-to-powder weight ratio. Large ball-to-powder weight ratios and longer ball milling times increased the activity of the Mg₂Ni alloys, and hydrogen absorption or oxidation reaction took place easier on the negative Mg₂Ni electrode.

The discharge process was terminated at -0.5V (Hg/HgO). The discharge potential of as-cast Mg₂Ni electrodes (Fig.4.7) increased gradually and discharge times decreased with increasing number of charge/discharge cycles. Similar behavior was observed for Mg₂Ni ball-

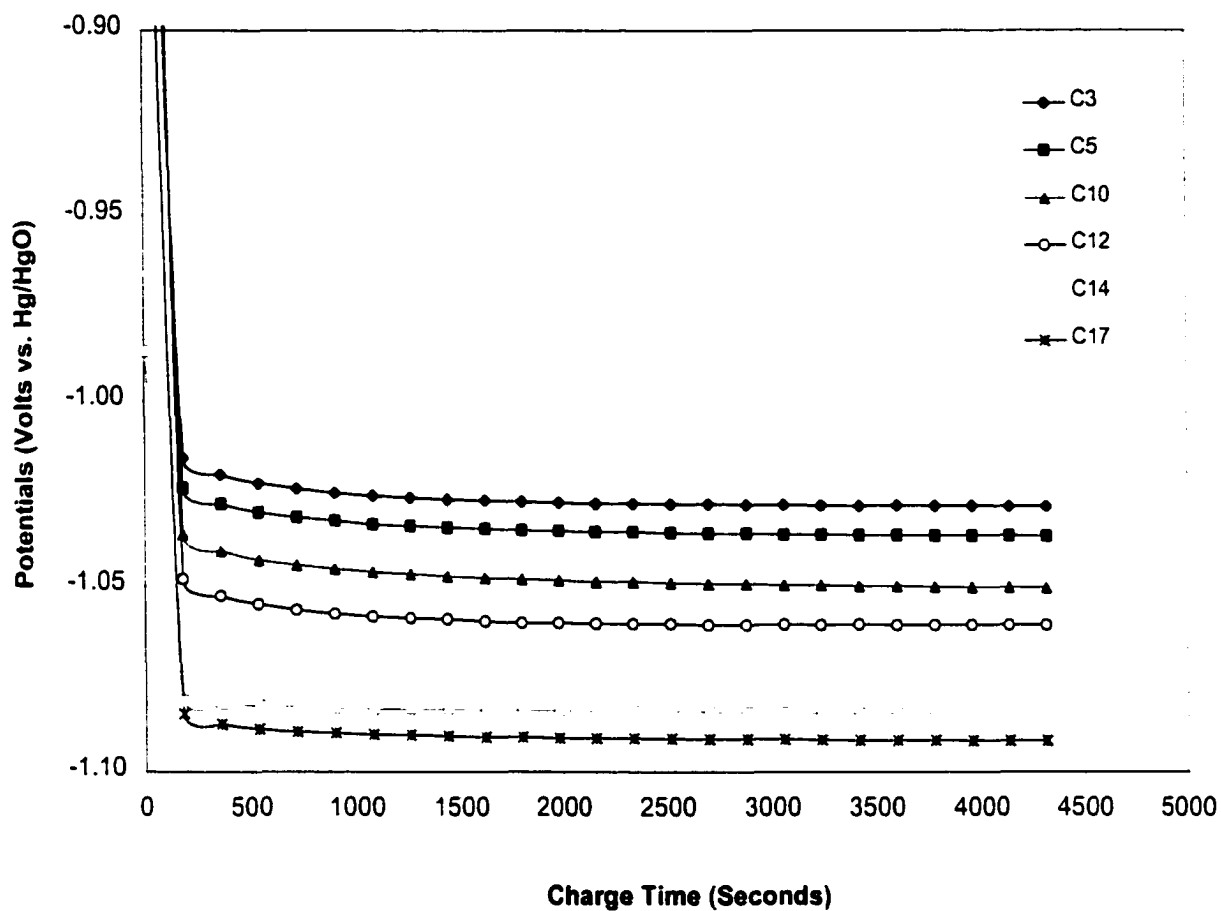


Fig.4.1 Charge potential vs. charge time for as-cast Mg₂Ni electrode

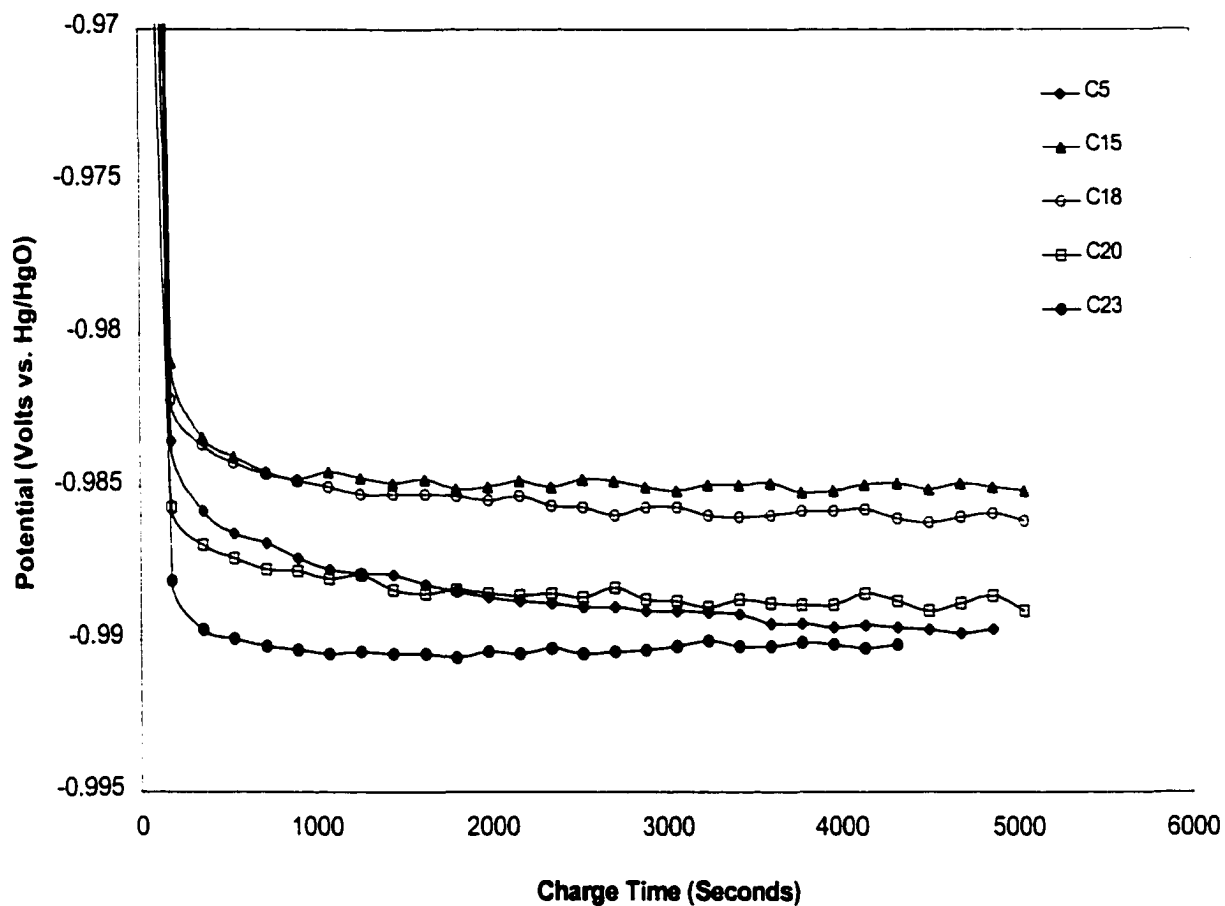


Fig.4.2 Charge potential vs. charge time for MG-Mg₂Ni electrode (MG 10 hours at a ball-to-powder weight ratio of 5:1)

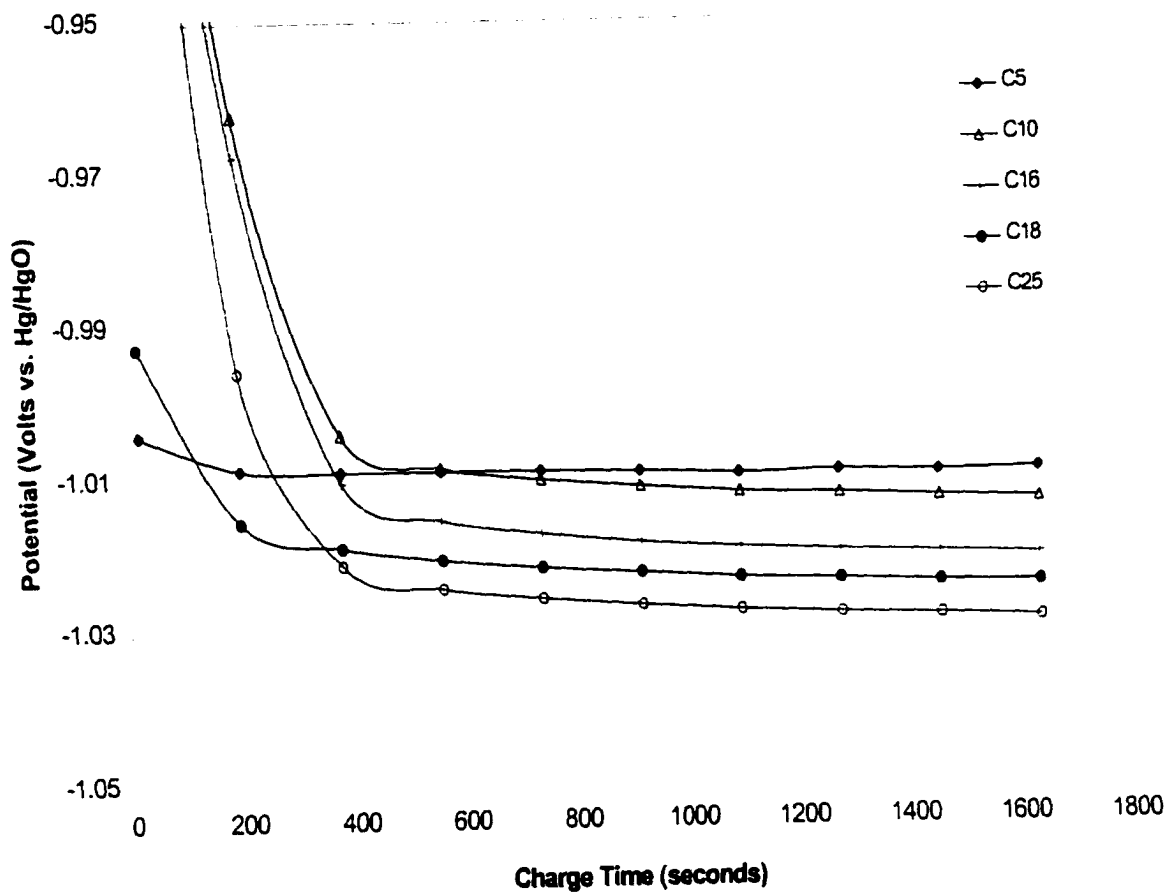


Fig.4.3 Charge potential vs. charge time for MG-Mg₂Ni electrode (MG 25 hours at a ball-to-powder weight ratio of 5:1)

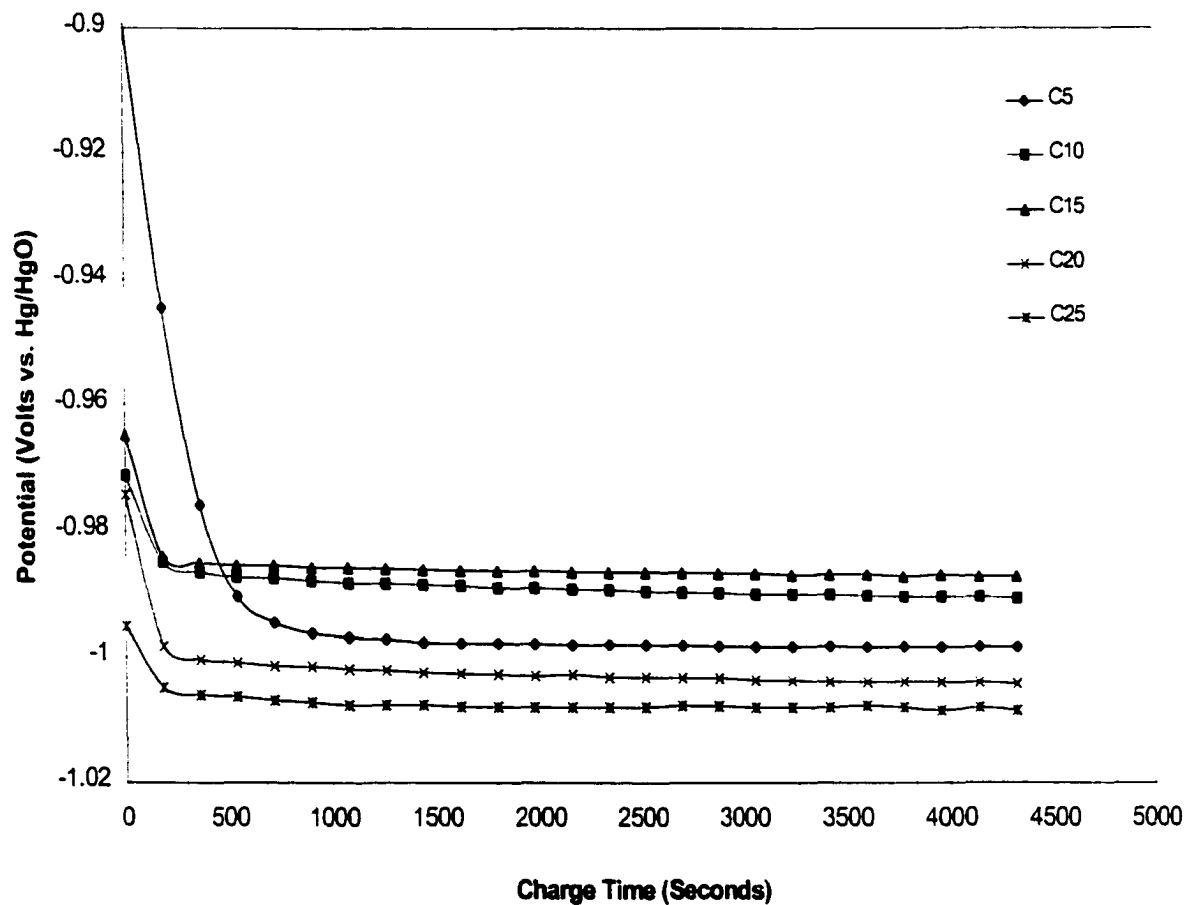


Fig.4.4 Charge potential vs. charge time for MG- Mg_2Ni electrode (MG 50 hours at a ball-to-powder weight ratio of 5:1)

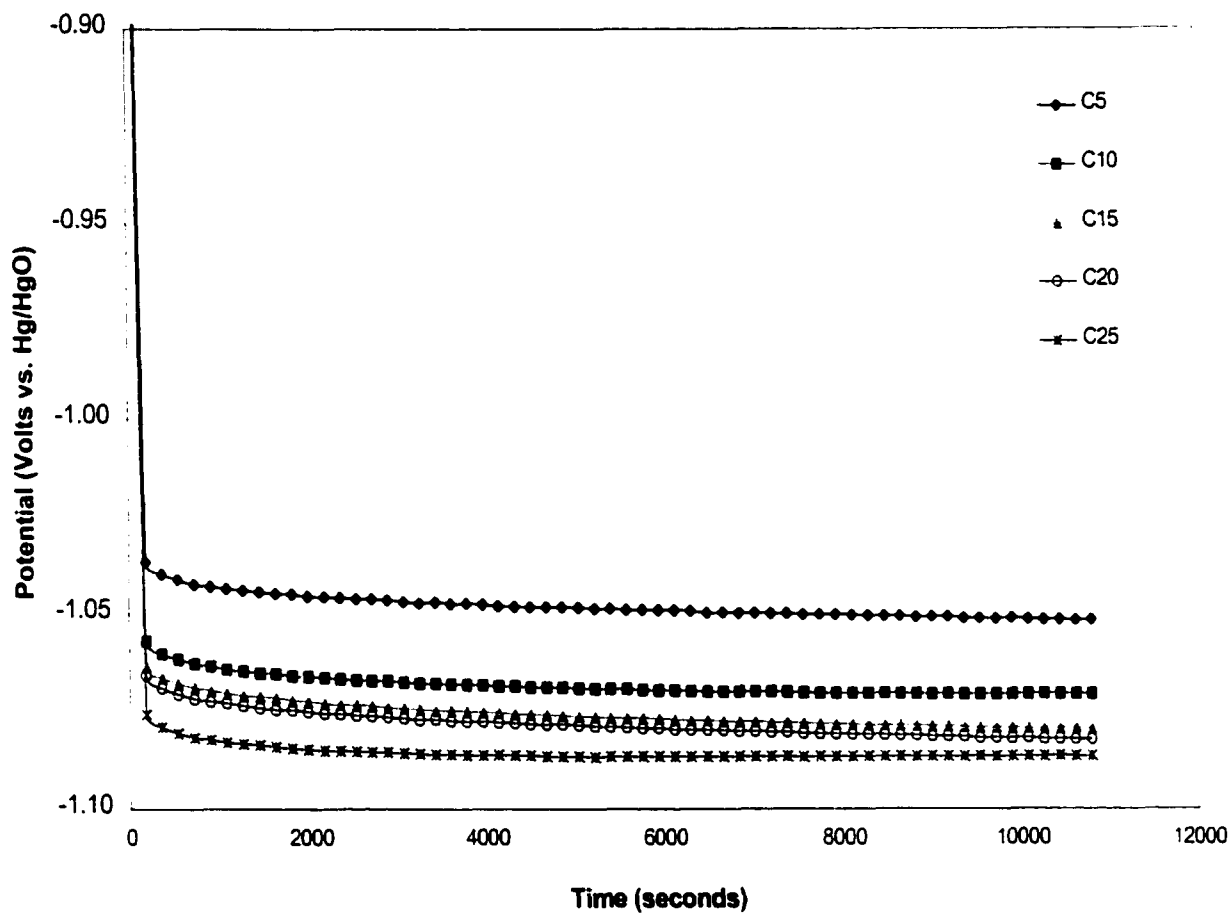


Fig.4.5 Charge potential vs. charge time for MG-Mg₂Ni electrode (MG 25 hours at a ball-to-powder weight ratio of 1:1)

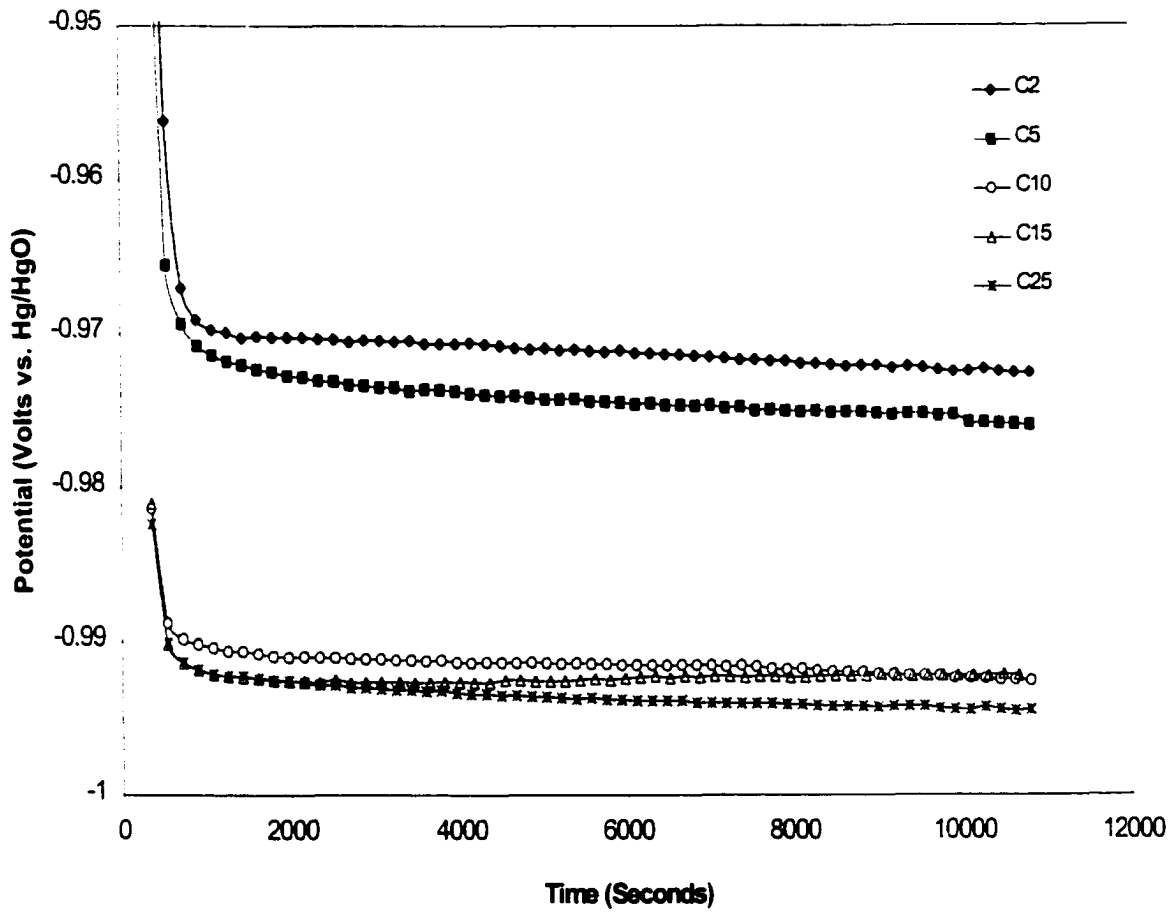


Fig.4.6 Charge potential vs. charge time for MG-Mg₂Ni electrode (MG 25 hours at a ball-to-powder weight ratio of 10:1)

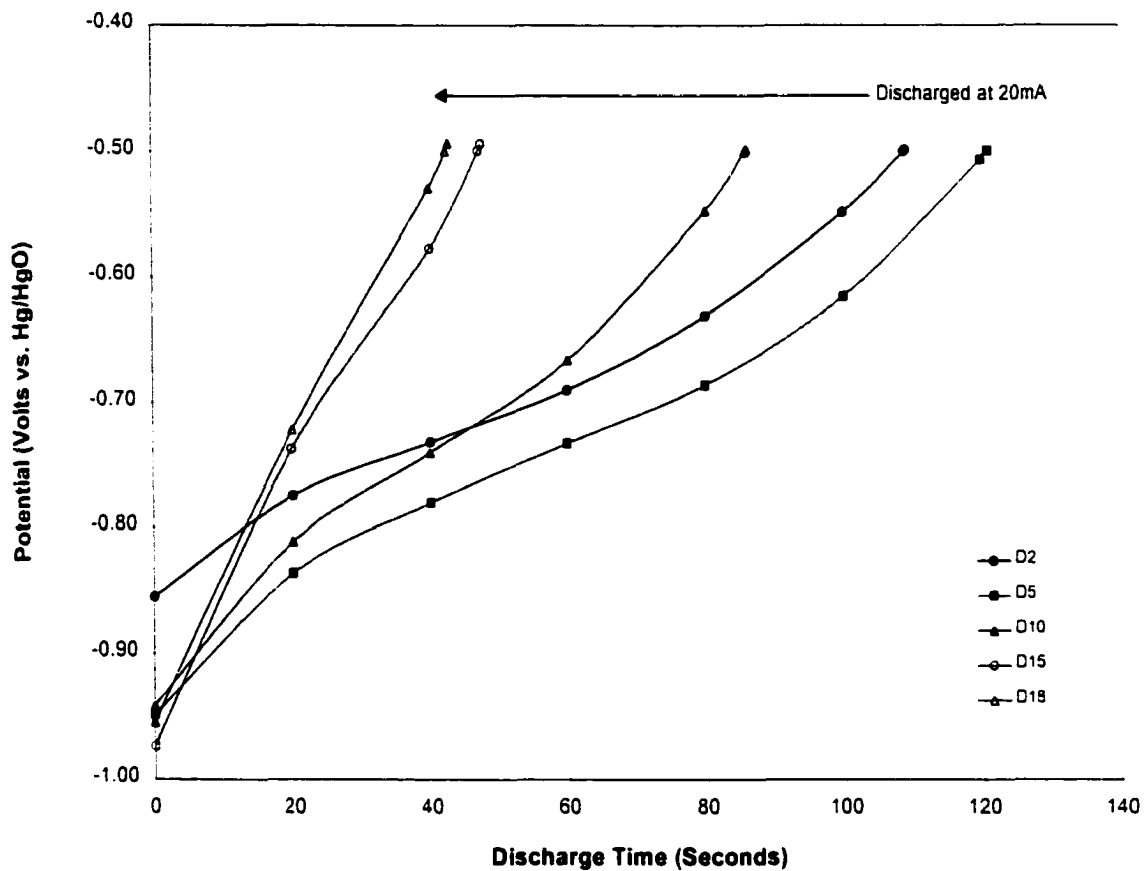


Fig.4.7 Discharge potential vs. discharge time for as-cast Mg₂Ni electrode

milled for 10 hours (Fig.4.8), 25 hours (Fig.4.9) and 50 hours (Fig.4.10). With increasing ball milling time, the discharge time increased, thus indicating a larger discharge capacity. As can be seen in Figs.4.8 to 4.10, after a certain period of time, there was a sharp increase in potential to compensate for the decreasing hydrogen surface concentration and thus maintain constant current. Thus, the knee in the discharge curve is assumed to be due to the depletion of hydrogen atoms on the surface of the electrode. For longer ball milling times, the potential increased gradually in the initial stages and then increased sharply after a critical potential of -0.80V (Hg/HgO). The time taken to reach a discharge potential of -0.80V (Hg/HgO) decreased with increasing number of charge/discharge cycles.

Ball milling at larger ball-to-powder weight ratios (Fig.4.11) resulted in a larger discharge time than for milling at a smaller ball-to-powder weight ratios (Fig.4.12). Comparison of the discharge curves of Mg₂Ni ball milled at different ball-to-powder ratios, Figs 4.11 and 4.12, further confirm that the ball milling treatment increased the hydrogen desorbing ability. This can also be seen in the specific discharge capacity measurements reported in Section 4.1.2.

4.1.2 Specific Discharge Capacity

The discharge capacity was calculated from the discharge current and the time required to reach a potential of -0.5V (Hg/HgO). Fig.4.13 shows the specific discharge capacity as a function of number of cycles for different ball milling times. For a specific time of ball milling, the specific discharge capacity decreases with increasing number of cycles. The largest change in discharge capacity occurs in the first few (~ 5) cycles and then it reaches a saturation value on further cycling. The discharge capacity increased with increasing ball-milling time up to 25 hours, but decreased on longer ball milling times. The negative Mg₂Ni electrode fabricated from

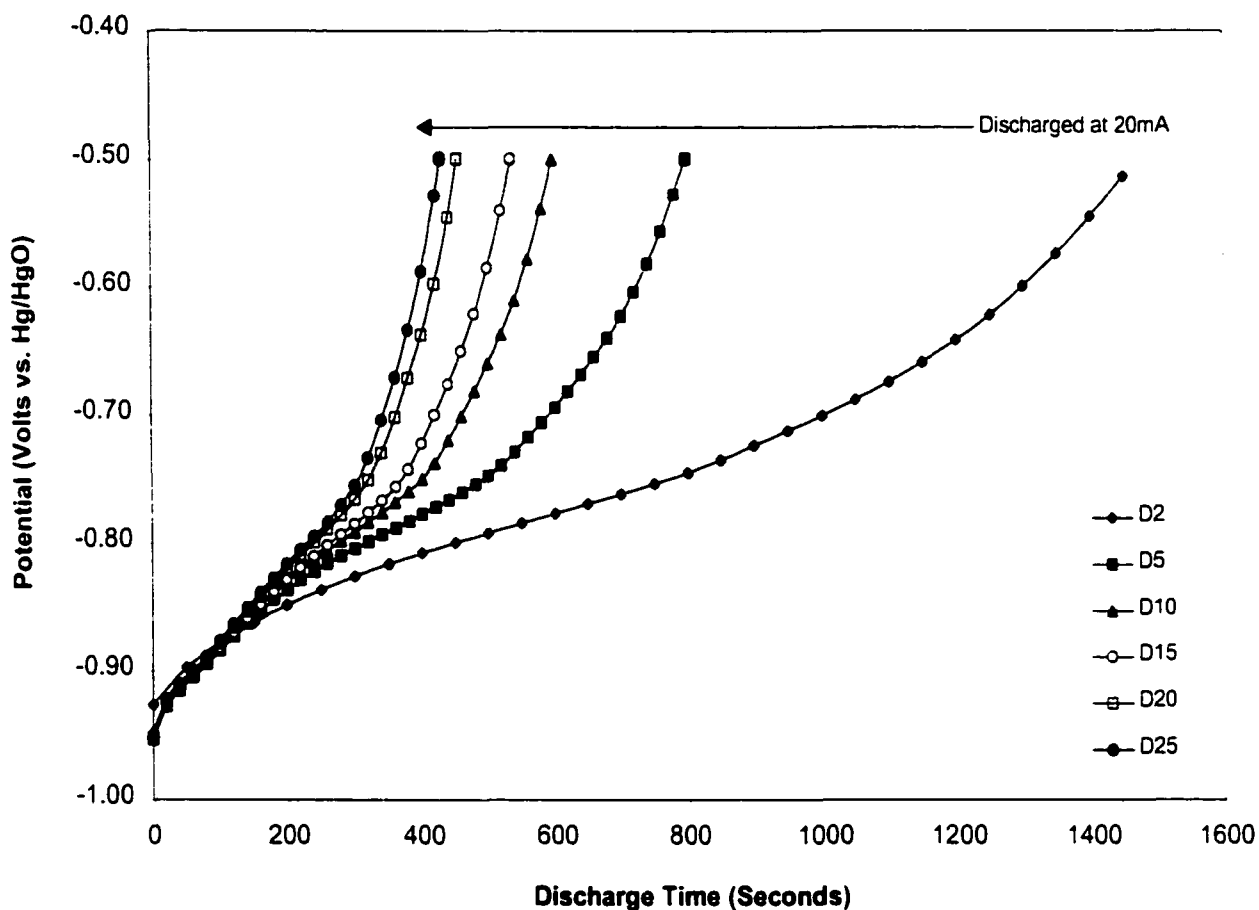


Fig.4.8 Discharge potential vs. discharge time for MG-Mg₂Ni electrode (MG 10 hours at a ball-to-powder weight ratio of 5:1)

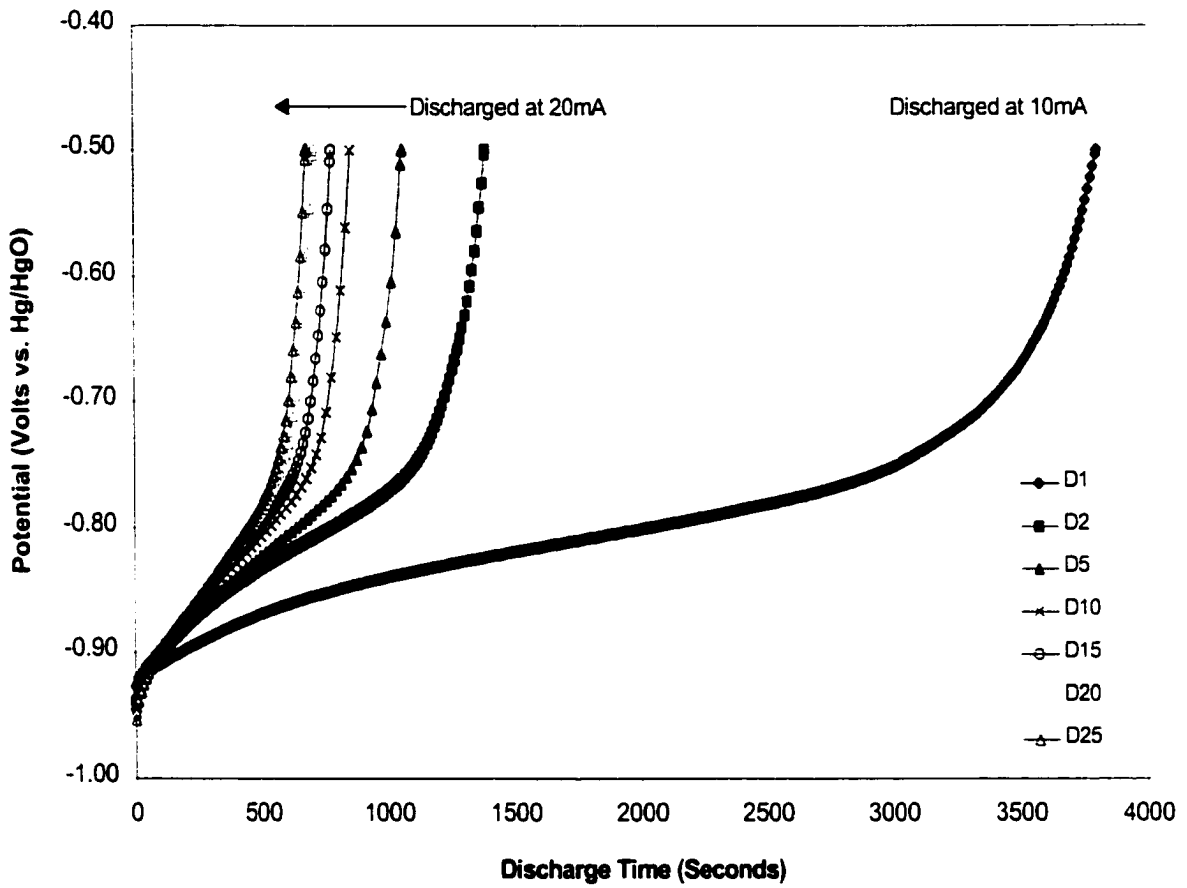


Fig.4.9 Discharge potential vs. discharge time for MG-Mg₂Ni electrode (MG 25 hours at a ball-to-powder weight ratio of 5:1)

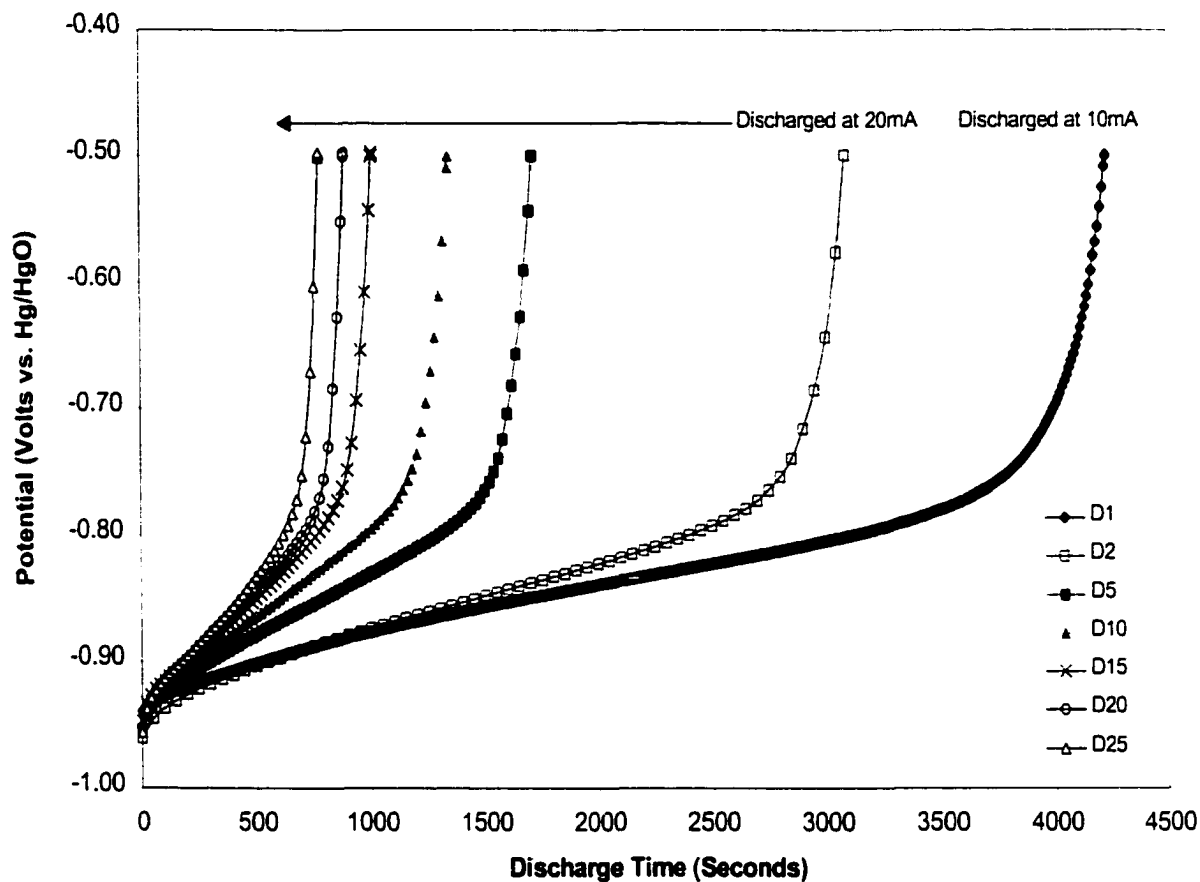


Fig.4.10 Discharge potential vs. discharge time for MG-Mg₂Ni electrode (MG 50 hours at a ball-to-powder weight ratio of 5:1)

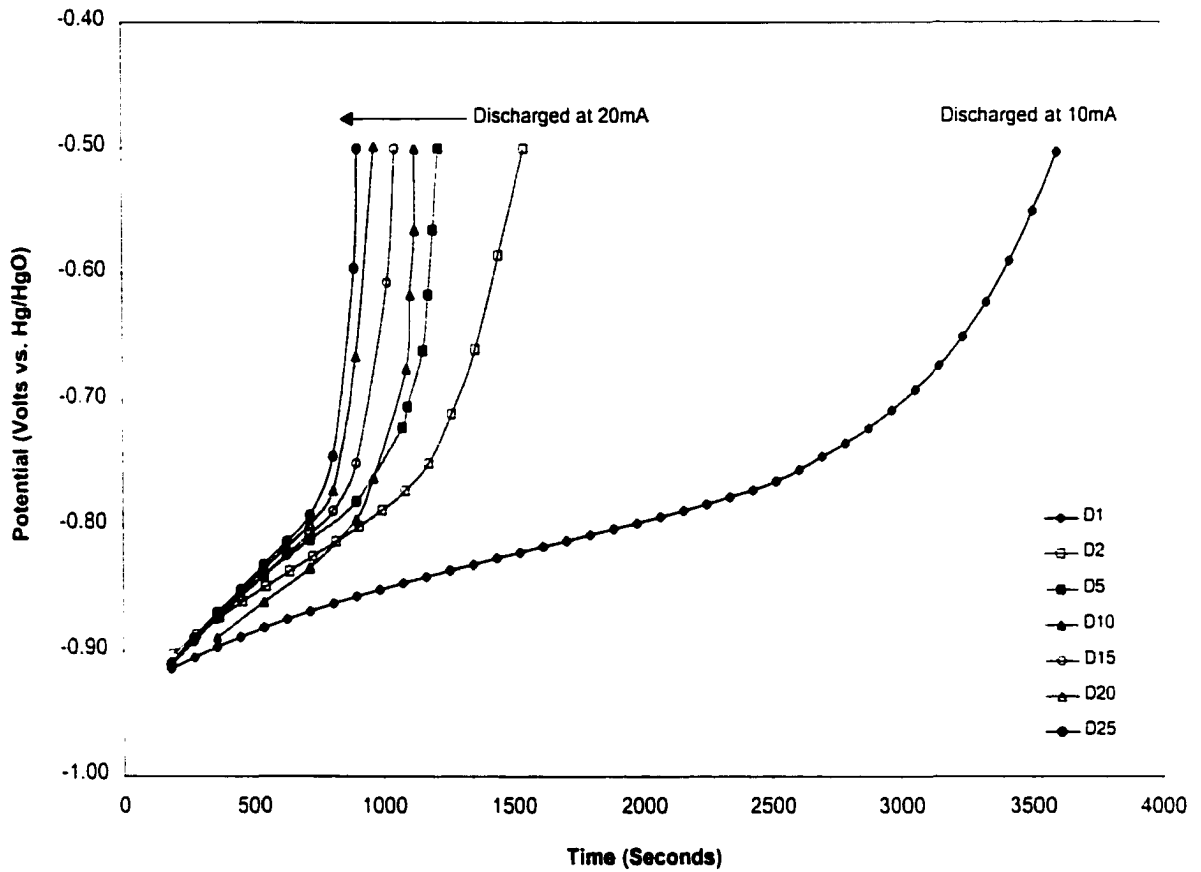


Fig.4.11 Discharge potentials vs. discharge time for MG-Mg₂Ni electrode (MG 25 hours at ball-to-powder weight ratio of 10:1)

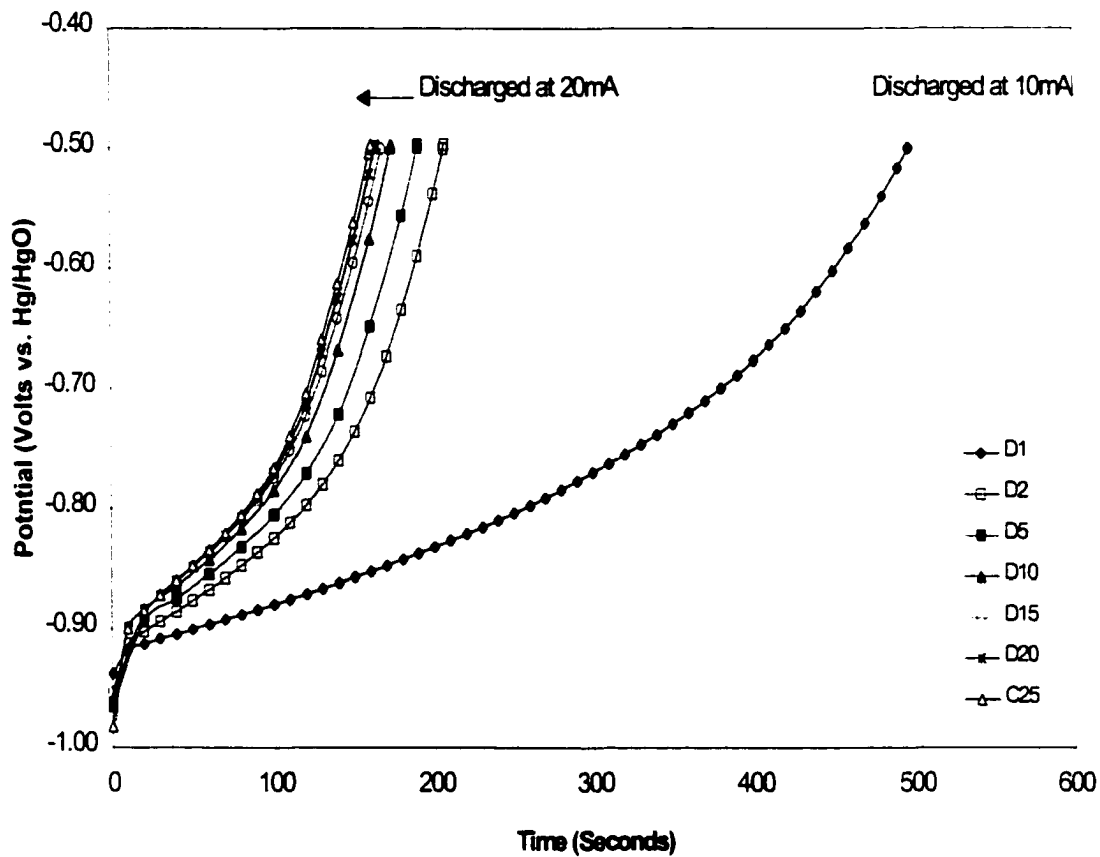


Fig.4.12 Discharge potential vs. discharge time for MG- Mg_2Ni electrode (MG 25 hours at a ball-to-powder weight ratio of 1:1)

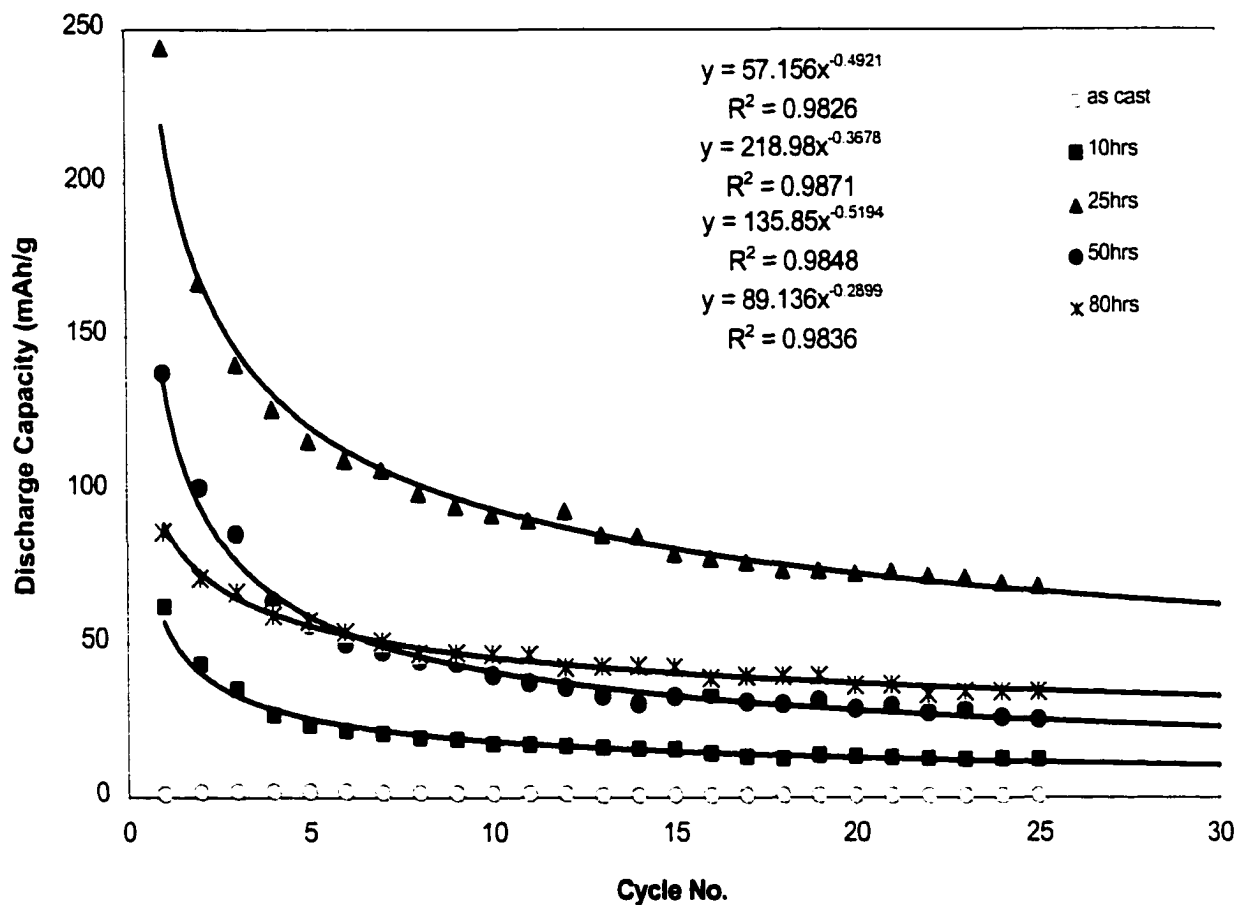


Fig.4.13 Discharge capacity of MG-Mg₂Ni electrodes vs. number of discharge cycles for different milling times

Chapter 4 Electrochemical Properties of Ball-Milled Mg₂Ni Alloys

powder ball milled for 25 hours had the maximum specific discharge capacity of 244mAh/g on the first cycle, in contrast to the very low discharge capacity (2.04mAh/g) without mechanical treatment. Also, its capacity decay (71.8%) was the smallest of the electrodes made from the ball-milled powders. Thus, mechanical treatment appears to be an effective way to improve the charge/discharge capability of the negative Mg₂Ni electrode.

Assuming that 4 hydrogen atoms are absorbed by one formula Mg₂Ni of the alloy, the theoretical capacity is calculated to be 1000mAh/g. Since the experimental capacity of the MG-Mg₂Ni was at best 244mAh/g, this is only about 25% of the theoretical capacity. The lower measured capacity is a result of a number of factors. First, the surface of the Mg₂Ni alloy is usually contaminated by oxide and/or hydroxide when it is exposed to the KOH solution. This surface layer may prohibit the reduction of H⁺ ions on the electrode surface. Thus, the oxide and/or hydroxide layer on the surface of the electrode may inhibited the nucleation and the growth of the hydride phase during charging, and thus block the migration of hydrogen to the solution/electrode interface for discharging. Secondly, the hydride formed at the surface acts as a diffusion barrier for hydrogen and the transport of hydrogen through the hydride layer is therefore slowed down. Since the diffusion of hydrogen in Mg₂NiH_x (the low temperature phase) is extremely slow, the Mg₂Ni electrode was only partially hydrided, and thus a very low discharge capacity was obtained.

Table 4.1 lists the discharge capacity for ball-milled Mg₂Ni electrodes at each charge/discharge cycle and for the different ball milling times.

After 25 discharge cycles, the calculated decay of specific discharge capacity is:

$$10 \text{ hours of ball milling: } 1 - C_{25}/C_0 = 1 - 12.67/61.9 = 1 - 20.47\% = 79.5\%$$

$$25 \text{ hours of ball milling: } 1 - C_{25}/C_0 = 1 - 68.77/244.06 = 1 - 28.18\% = 71.8\%$$

50 hours of ball milling: $1 - C_{25}/C_0 = 1 - 25.51/138.06 = 1 - 18.48\% = 81.5\%$

**Table 4.1 Discharge Capacities of Ball Milled Mg₂Ni Electrodes
at a Ball-to-powder weight Ratio of 5:1**

CYCLE NO.	AS CAST (mAh/g)	10HRS (mAh/g)	25HRS (mAh/g)	50HRS (mAh/g)	80HRS (mAh/g)
1	0.99	61.90	244.06	138.06	86.37
2	1.84	43.42	167.45	100.90	71.20
3	2.06	35.60	140.97	85.84	66.80
4	1.95	26.92	126.42	63.90	59.06
5	2.04	23.57	116.19	56.01	57.31
6	1.89	21.88	109.86	50.25	53.80
7	1.62	21.03	106.72	47.57	50.78
8	1.52	19.55	99.12	44.58	47.11
9	1.48	18.93	94.66	43.88	47.25
10	1.45	17.63	91.95	40.00	46.95
11	1.32	17.25	90.00	37.50	46.53
12	1.31	16.82	93.13	36.00	42.49
13	0.64	16.26	85.33	33.20	42.80
14	0.80	16.04	85.02	30.76	42.94
15	0.80	15.82	79.17	33.02	42.57
16	0.76	14.40	77.56	33.74	38.85
17	0.74	13.40	76.32	31.26	39.54
18	0.72	12.56	73.76	30.59	39.67
19	0.75	13.90	73.63	31.78	39.74
20	0.79	13.43	72.75	29.08	36.62
21	0.76	13.11	73.46	30.00	37.00
22	0.76	12.80	72.09	27.91	33.71
23	0.73	12.68	71.59	28.70	34.54
24	0.72	12.72	69.86	26.24	34.70
25	0.73	12.67	68.77	25.51	34.58

The decay of specific discharge capacity obeyed a power law. The corresponding equations and error (R^2) values are listed in Table 4.2.

The equations describing the specific discharge capacity at different ball milling times are of a power law form, i.e. $Q_N = kN^{-\lambda}$, where $k=Q_1$ (the specific discharge capacity of first cycle) and

λ is a constant which represents the decay exponent. The decay equations for specific discharge capacity can thus be rewritten as $Q_N = Q_1 N^\lambda$.

**Table 4.2 Relationship of Discharge Capacity to Number of Discharge Cycles
(Different Ball Milling Times at a ball-to-Powder Weight Ratio of 5:1)**

TIME	10 HOURS	25 HOURS	50 HOURS	80 HOURS
Equation	$Q_N = 57.156N^{-0.4921}$	$Q_N = 218.98N^{-0.3678}$	$Q_N = 135.85N^{-0.5194}$	$Q_N = 89.136N^{-0.2899}$
R ² (error)	0.9826	0.9871	0.9848	0.9836
Q ₁ (measured)	61.9	244.06	138.06	86.37
Q ₁ (calculated)	57.156	218.98	135.85	89.136

The specific discharge capacities of the ball-milled Mg₂Ni electrodes increased significantly compared to as-cast state and also increased with increasing ball-to-powder weight ratio from 1:1, 5:1 to 10:1(Fig.4.14). The specific discharge capacity for each charge/discharge cycle is given in Table 4.3.

The specific discharge capacity for the first cycle at a ball-to-powder weight ratio of 5:1 was larger than that for a ball-to-powder weight ratio of 10:1, but for all subsequent cycles it was smaller. The power law equations were also used to predict the specific discharge capacities for different ball-to-powder weight ratios. Table 4.4 listed the corresponding equations and error, R², values.

The formula for the specific discharge capacity at different ball-to-powder weight ratios can be generalized as $Q_N = Q_1 N^\lambda$, where Q_1 and λ have the same meaning as previously.

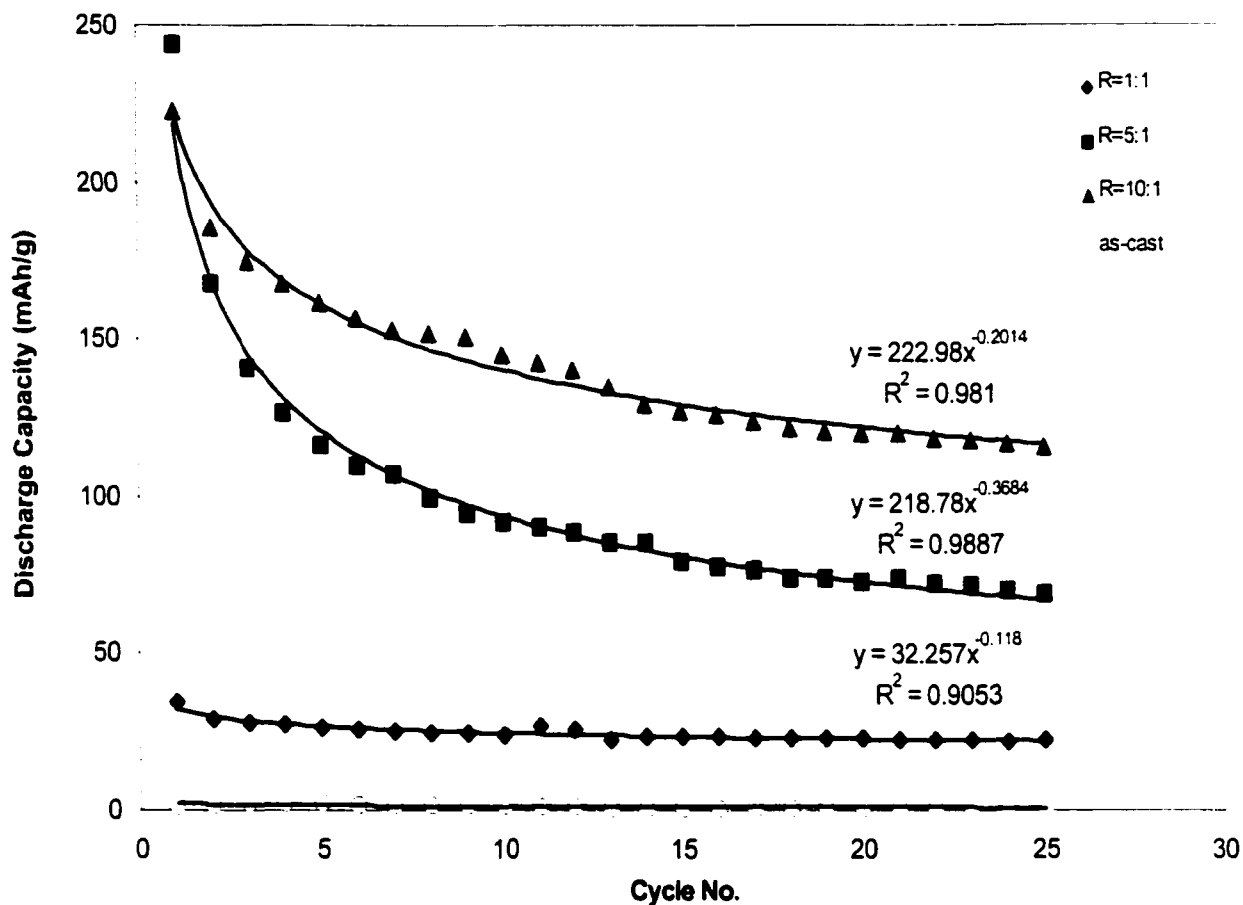


Fig.4.14 Discharge capacity of MG-Mg₂Ni electrodes vs. number of discharge cycles at different ball-to-powder weight ratios

**Table 4.3 Specific Discharge Capacity of 25 Hour Ball Milled Mg₂Ni Electrodes
at Different Ball-to-Powder Weight Ratios**

CYCLE NO.	AS CAST (mAh/g)	R=1:1 (mAh/g)	R=5:1 (mAh/g)	R=10:1 (mAh/g)
1	0.99	34.40	244.06	222.68
2	1.84	28.74	167.45	185.78
3	2.06	27.73	140.97	174.48
4	1.95	27.09	126.42	167.65
5	2.04	26.44	116.19	161.75
6	1.89	25.44	109.86	156.62
7	1.62	25.24	106.72	152.79
8	1.52	24.78	99.12	151.89
9	1.48	24.33	94.66	150.80
10	1.45	24.11	91.95	145.00
11	1.32	26.64	90.00	142.50
12	1.31	25.55	88.30	140.44
13	0.64	22.50	85.33	135.00
14	0.80	23.30	85.02	129.20
15	0.80	23.27	79.17	127.28
16	0.76	23.30	77.56	126.20
17	0.74	23.13	76.32	123.88
18	0.72	23.13	73.76	121.63
19	0.75	23.03	73.63	120.39
20	0.79	22.73	72.75	120.21
21	0.76	22.59	73.46	120.02
22	0.76	22.36	72.09	118.21
23	0.73	22.18	71.59	117.69
24	0.72	22.10	69.86	117.07
25	0.73	22.53	68.77	115.54

**Table 4.4 Relationship of Discharge Capacity to Number of Discharge Cycles
(Different Ball-to-Powder Weight Ratios and T=25 Hours)**

BALL-TO-POWDER WEIGHT RATIO	1:1	5:1	10:1
Equation	$Q_N=32.257N^{0.118}$	$Q_N=218.78N^{0.3684}$	$Q_N=222.98N^{0.2014}$
R²	0.9053	0.9887	0.9810
Q₁(measured)	34.40	244.06	222.68
Q₁(calculated)	32.257	218.98	222.98

4.2 Electrochemical Kinetics: Polarization Behavior

The charge and discharge curves showed that the hydrogen content in the ball-milled Mg₂Ni was related to the potential. Thus, the overpotentials, η (difference between measured potential and equilibrium potential) at charge and discharge are important parameters in evaluating the driving force for absorption/desorption of hydrogen.

4.2.1 Open Circuit Potentials of Charged/Discharged Mg₂Ni Electrodes

The open circuit potential measurements were carried out after the completion of each charge/discharge cycle. The charge/discharge processes made the ball-milled Mg₂Ni electrodes more active, and the open circuit potentials decreased rapidly in the first 100 seconds and then slowly became stable. They also decreased with increasing number of charge/discharge cycles: see Fig.4.15, 4.16 and 4.17 for electrodes made from material ball-milled for 10 hours, 25 hours and 50 hours, respectively.

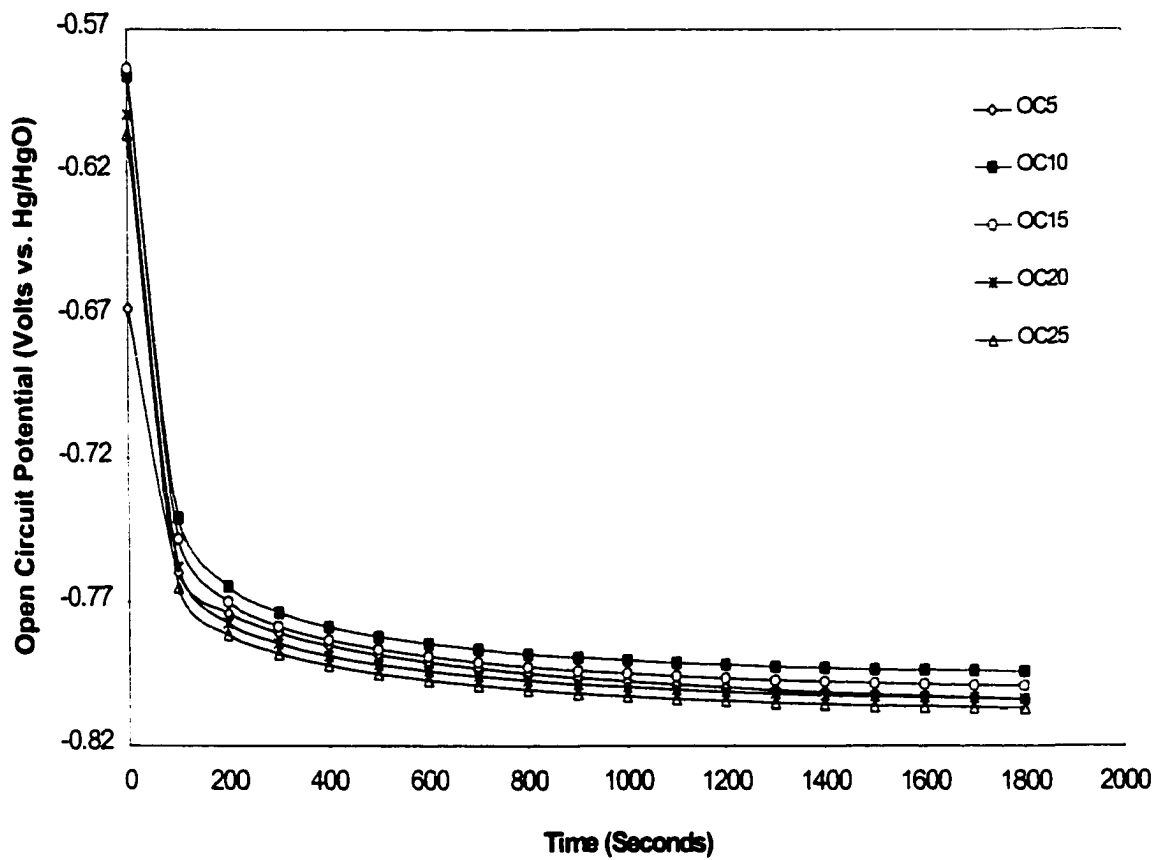


Fig.4.15 Open circuit potential vs. time for MG-Mg₂Ni electrode (MG 10 hours at a ball-to-powder weight ratio of 5:1)

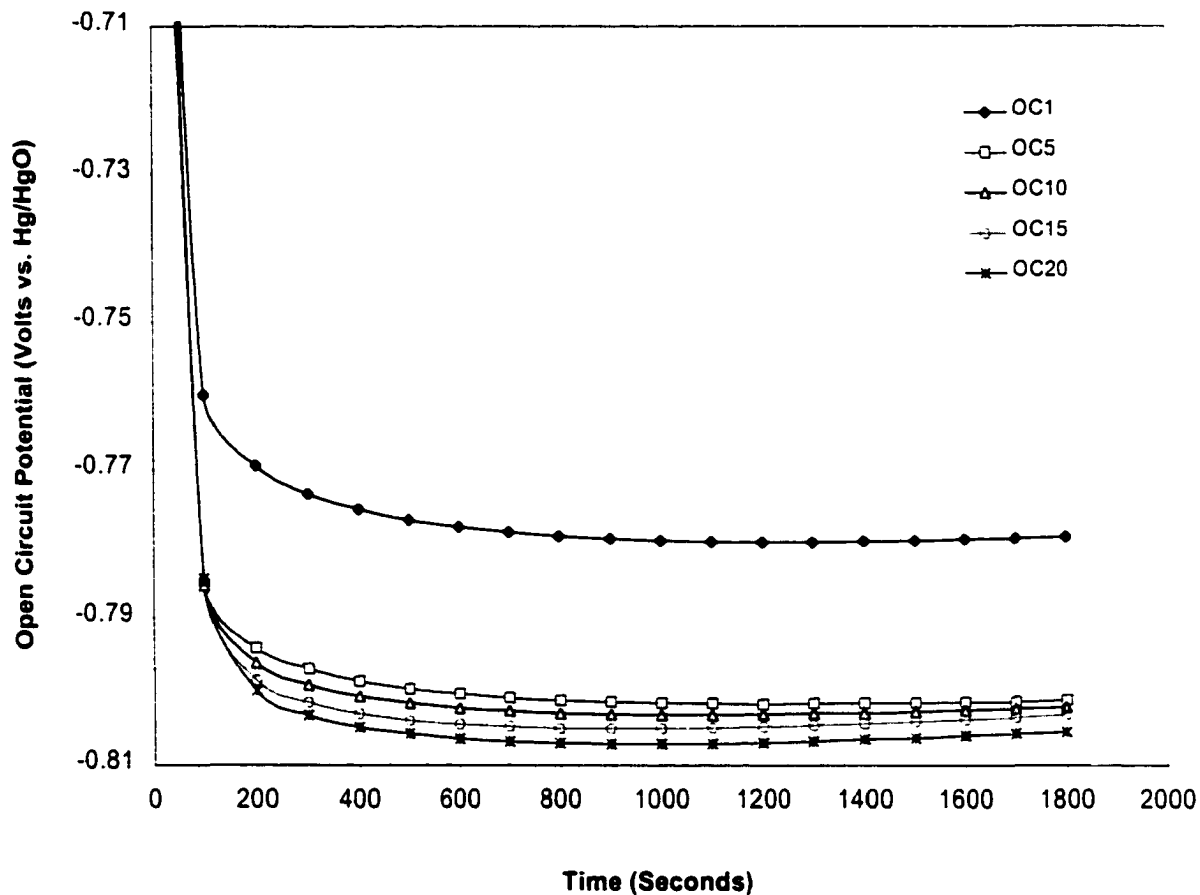


Fig.4.16 Open circuit potential vs. time for MG-Mg₂Ni electrode (MG 25 hours at a ball-to-powder weight ratio of 5:1)

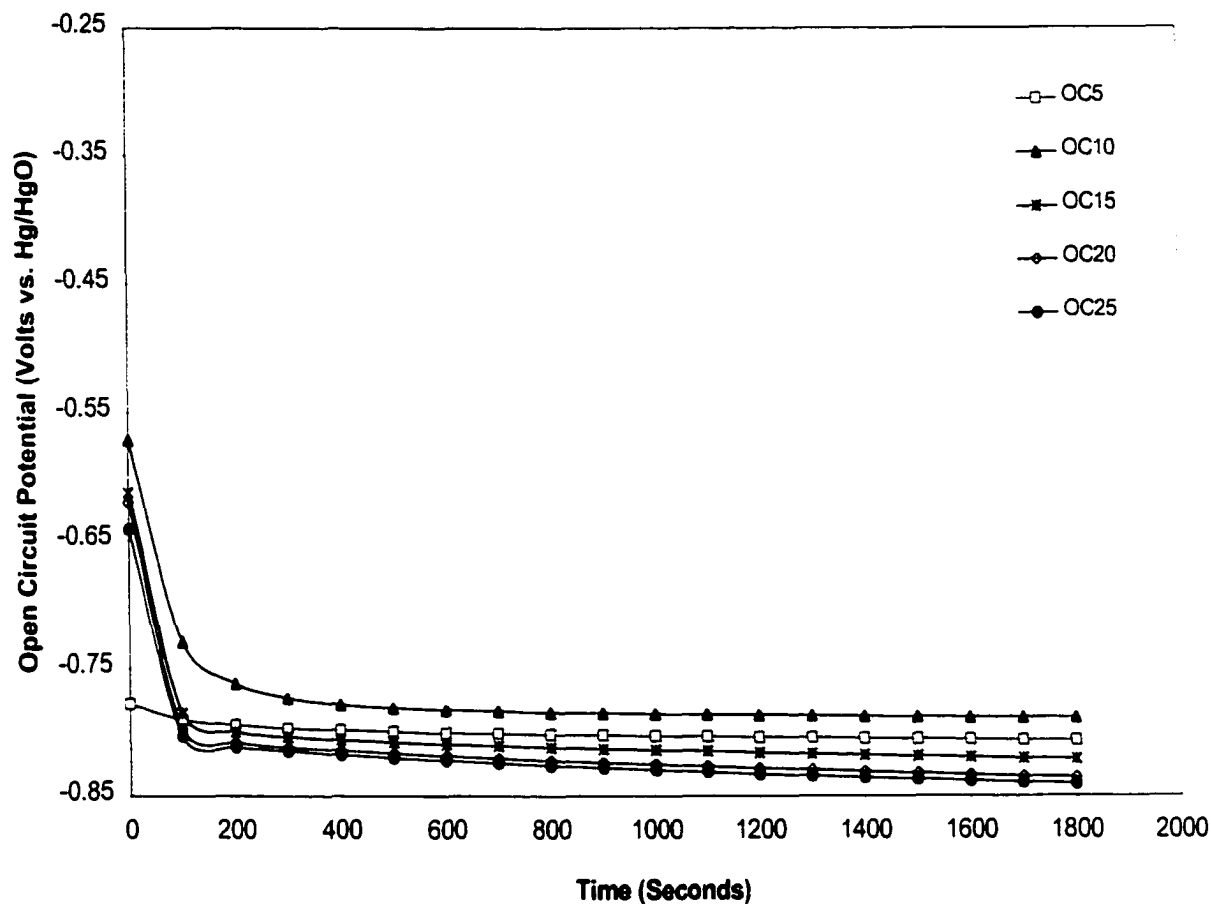


Fig.4.17 Open circuit potential vs. time for MG-Mg₂Ni electrode (MG 50 hours at a ball-to-powder weight ratio of 5:1)

4.2.2 Polarization Properties

To determine the kinetics of the absorption and desorption processes, Tafel polarization measurements were made on the MG-Mg₂Ni electrodes. The Tafel polarization measurements were carried out at a scanning rate of 10mV/min after the open circuit potential became stable. Fig.4.18 shows the Tafel polarization curves for a 10 hours ball-milled Mg₂Ni electrode after different number of charge/discharge cycles. The anodic current densities increased to a limiting value, then decreased in all cases, and the limiting current densities, i_d , decreased with increasing number of charge/discharge cycles. The existence of a limiting current density, i_d , showed that an oxidation reaction took place on the surface of the negative electrode and a passive film was generated which resisted further penetration of hydrogen atoms. The decrease of the anodic current density on cycling implies that charging was becoming difficult. Thus, the limiting current density, i_d , can be seen as the critical passivation current density and the passive film readily forms on the surface of the electrode with increasing charge/discharge cycles. In general, E_0 (equilibrium potential) also decreased with increasing number of charge/discharge cycles. From a thermodynamics point of view, a decreasing E_0 facilitates the passivation reaction.

It is thus concluded that the critical passivation current density, i_d , decreased upon charging/discharging, and that the peak passivating potential E_{pp} shifted negatively with increasing number of charge/discharge cycles, indicating an earlier commencement of the active-to-passive transition and passivation, respectively. This suggests that the electrode was more easily rendered passive with increasing number of charge/discharge cycles. The polarization curves of ball milled Mg₂Ni alloy did not conform to a linear Tafel equation, $\eta=a+b\log i$. The deviation was due to the fact that the charge process has two possible controlling steps:

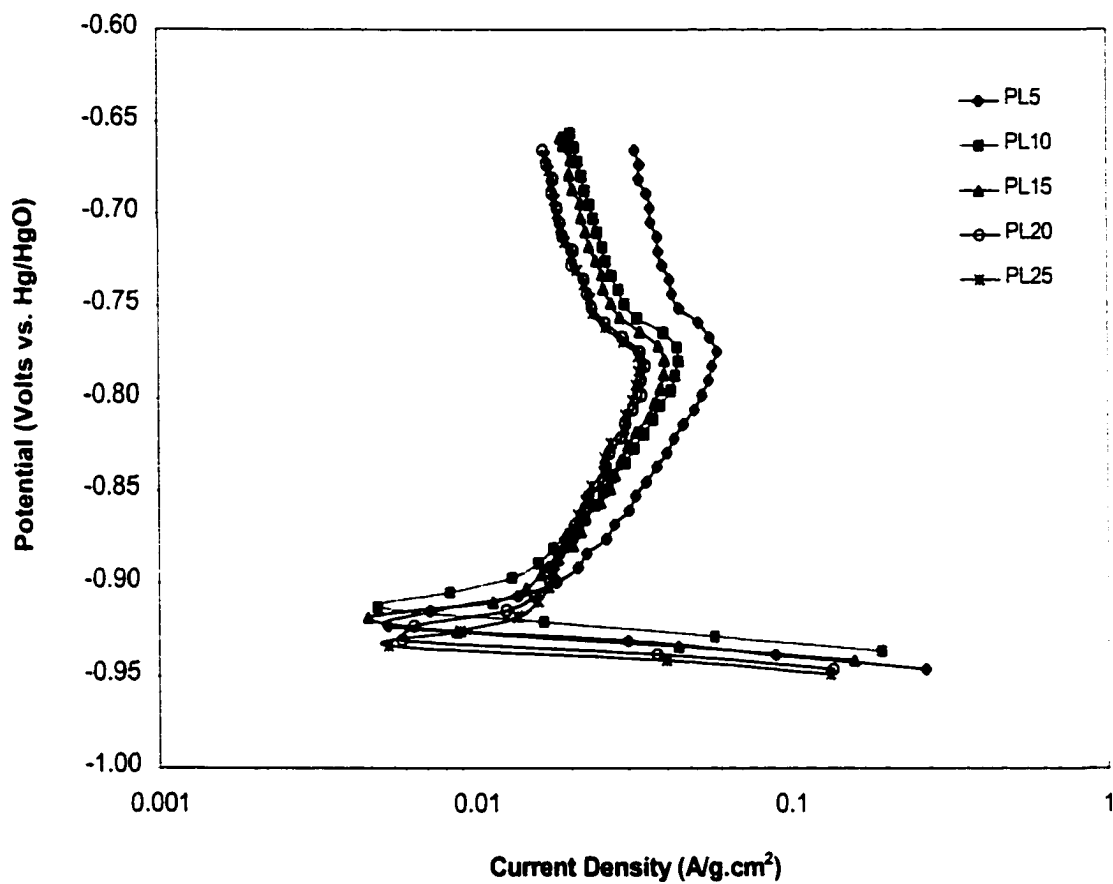


Fig.4.18 Polarization characteristics for MG-Mg₂Ni electrode (MG 10 hours at a ball-to-powder weight ratio of 5:1 and discharged at 200mA/g)

activation polarization and concentration polarization. The concentration polarization adds to the total overpotential. In the case of combined activation and concentration polarization, the anodic polarization curve obeys the mixed law:

$$\eta = \frac{RT}{\alpha F} \ln\left(\frac{i}{i_0}\right) + \frac{RT}{\alpha F} \ln\left(\frac{i_d}{i_d - i}\right) \quad (4.1)$$

The first term of the right-hand side of the equation is the overpotential due to the activation polarization, and the second term is the overpotential due to the concentration polarization. In the charging process of a ball-milled Mg₂Ni electrode, activation polarization is the controlling step at lower overpotentials. With increasing potential, the controlling step changes from activation to concentration polarization. Above the limiting current density, i_d , concentration polarization is the predominant controlling step.

The similar behavior was also observed for the Mg₂Ni electrodes ball-milled for 25 hours (Fig.4.19) and 50 hours (Fig.4.20). The corresponding electrochemical parameters are given in Table 4.5. Tafel polarization curves exhibited features similar to those for a mass-transfer-controlled process. The current tends to attain a limiting value at higher polarization due to the diffusion-limited kinetics of hydrogen absorption and desorption. The limiting process is likely to be solid state diffusion of hydrogen in the MH alloy, which is relatively slower process than the charge-transfer process.

Fig.4.21 is a comparison between the theoretical Tafel linear polarization curve and the measured polarization curve (based on sample milled for 25 hours at 5:1 ball-to-powder weight ratio). At a large anodic polarization, the Tafel relation did not hold and a limiting current, i_d , was observed. These results suggest that the current density depend not only on the charge transfer process but also on the diffusion process.

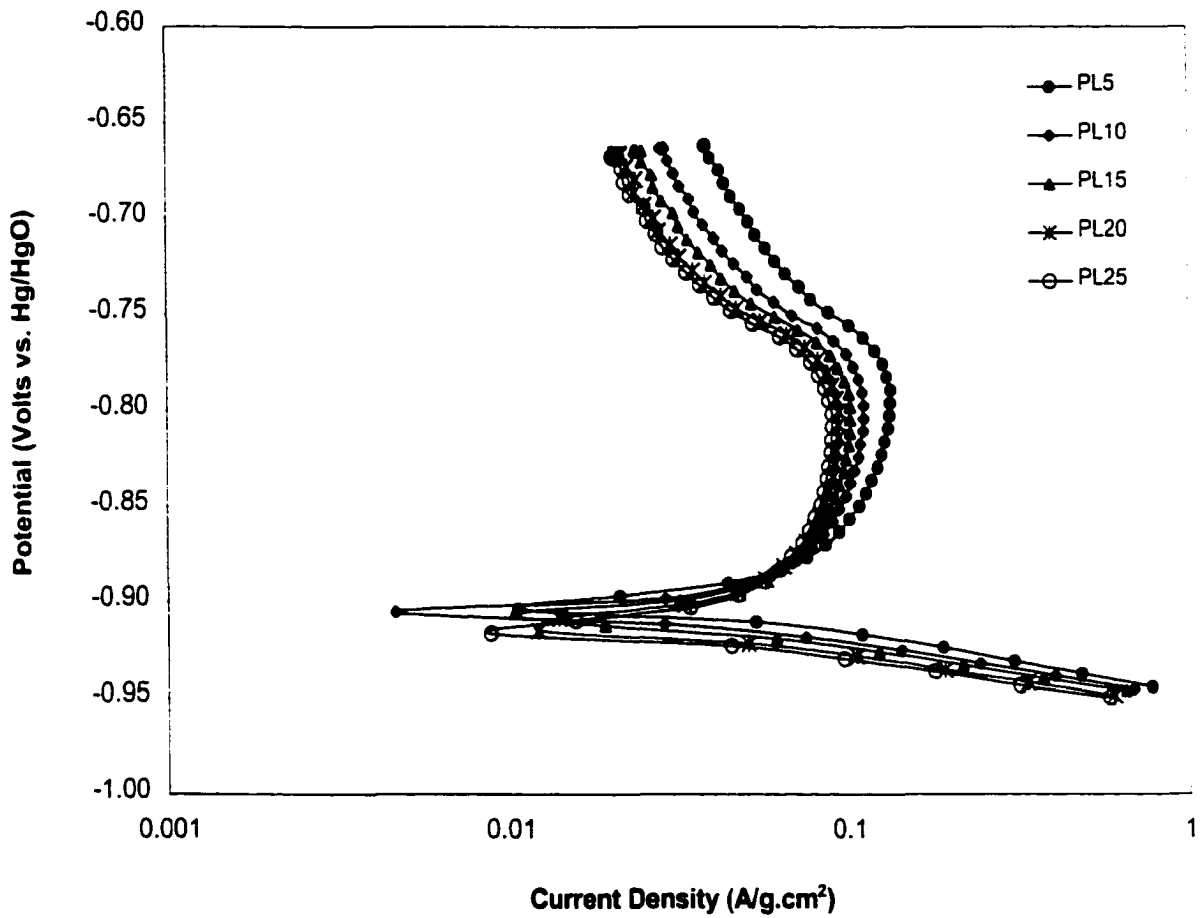


Fig.4.19 Polarization characteristics for MG-Mg₂Ni electrode (MG 25 hours at a ball-to-powder weight ratio of 5:1 and discharged at 200mA/g)

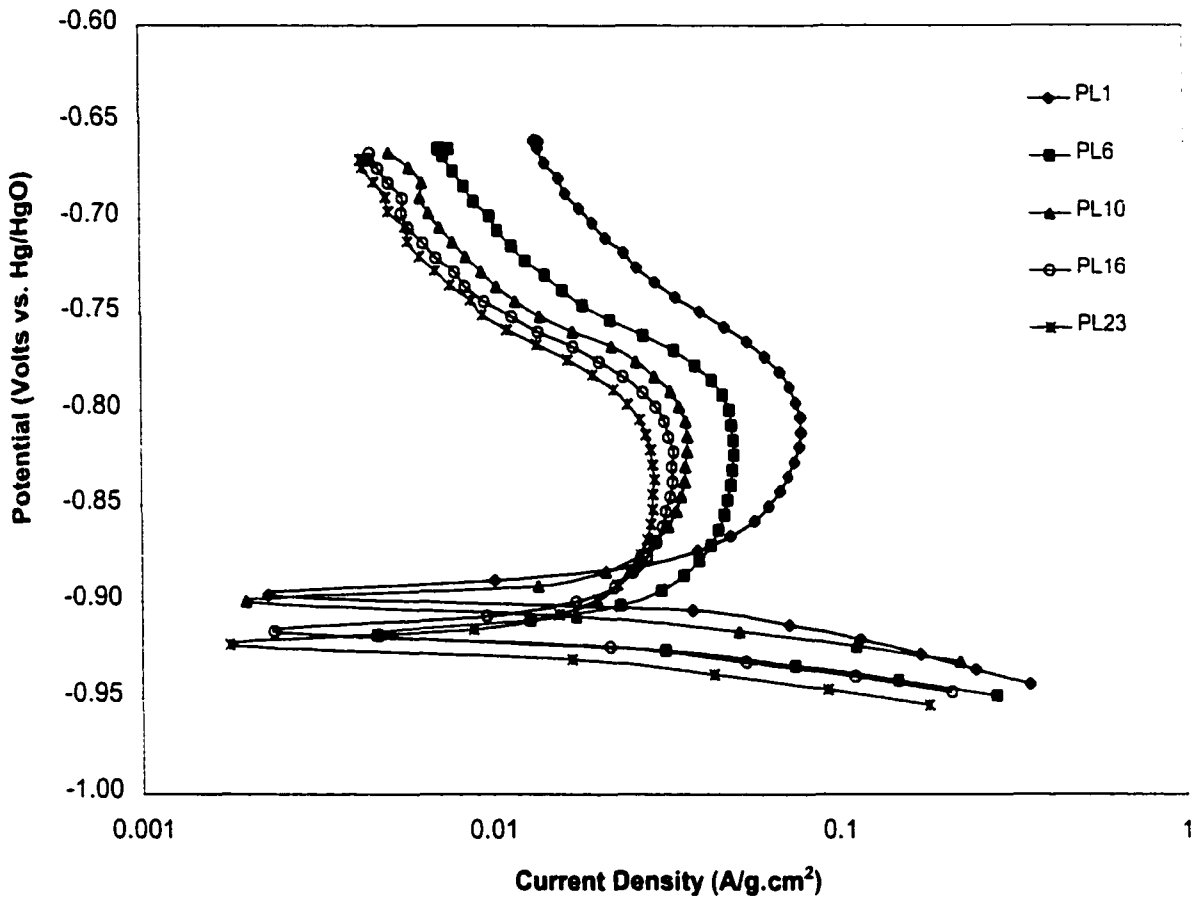


Fig.4.20 Polarization characteristics for MG-Mg₂Ni electrode (MG 50 hours at a ball-to-powder weight ratio of 5:1 and discharged at 200mA/g)

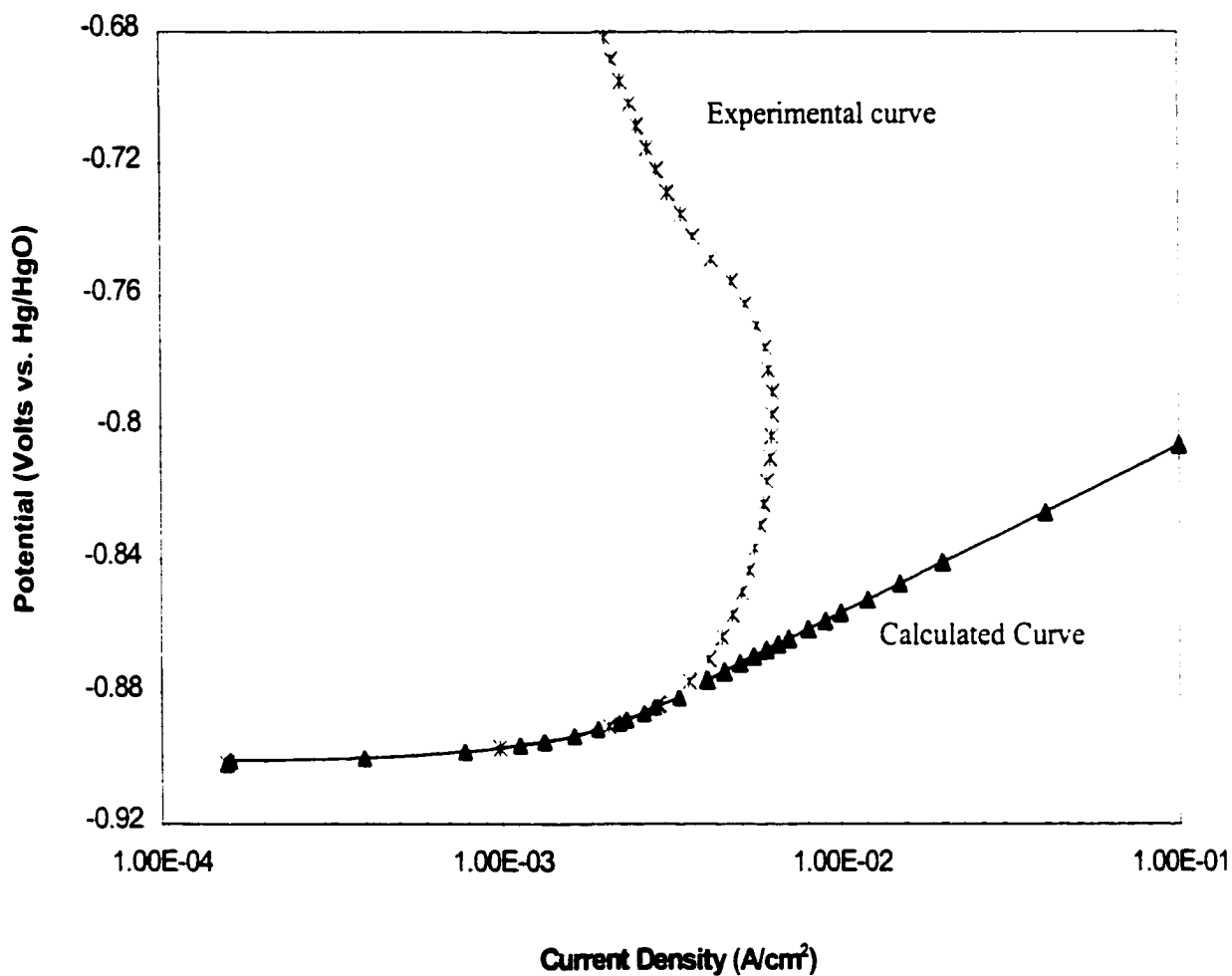


Fig.4.21 Experimental and calculated polarization curves for 25 hours ball milled Mg₂Ni electrode at a ball-to-powder weight ratio of 5:1

**Table 4.5 Electrochemical Parameters of Ball-milled Mg₂Ni Electrodes
(Different Ball Milling Times at a Ball-to-Powder Weight Ratio of 5:1)**

BALL MILLING TIME 10 HOURS					
Cycle No.	5	10	15	20	25
E_{eq} (V)	-0.91985	-0.91284	-0.92114	-0.92845	-0.93140
I_d (mA/g)	58.35	44.05	41.03	35.03	33.22
η₅ (mV)	3.93	3.99	1.9	1.9	2.88
η₃₀ (mV)	62.19	81.92	91.76	107.18	117.01
BALL MILLING TIME 25 HOURS					
Cycle No.	5	10	15	20	25
E_{eq} (V)	-0.90172	-0.90590	-0.90879	-0.91211	-0.91444
I_d (mA/g)	134.15	111.83	102.81	94.70	90.70
η₅ (mV)	1.84	0.80	1.97	0.92	1.90
η₃₀ (mV)	7.62	8.54	9.53	9.59	10.57
BALL MILLING TIME 50 HOURS					
Cycle No.	5	10	15	20	25
E_{eq} (V)	-0.91536	-0.90080	-0.91450	-0.91844	-0.92126
I_d (mA/g)	86.31	63.01	57.61	54.83	50.56
η₅ (mV)	0.98	1.97	1.84	1.91	2.09
η₃₀ (mV)	9.71	12.85	15.48	16.54	18.62

Fig.4.22 shows the polarization curves for electrodes made from a material ball-milled for 25 hours at a 10:1 ball-to-powder weight ratio. The polarization curves have the same

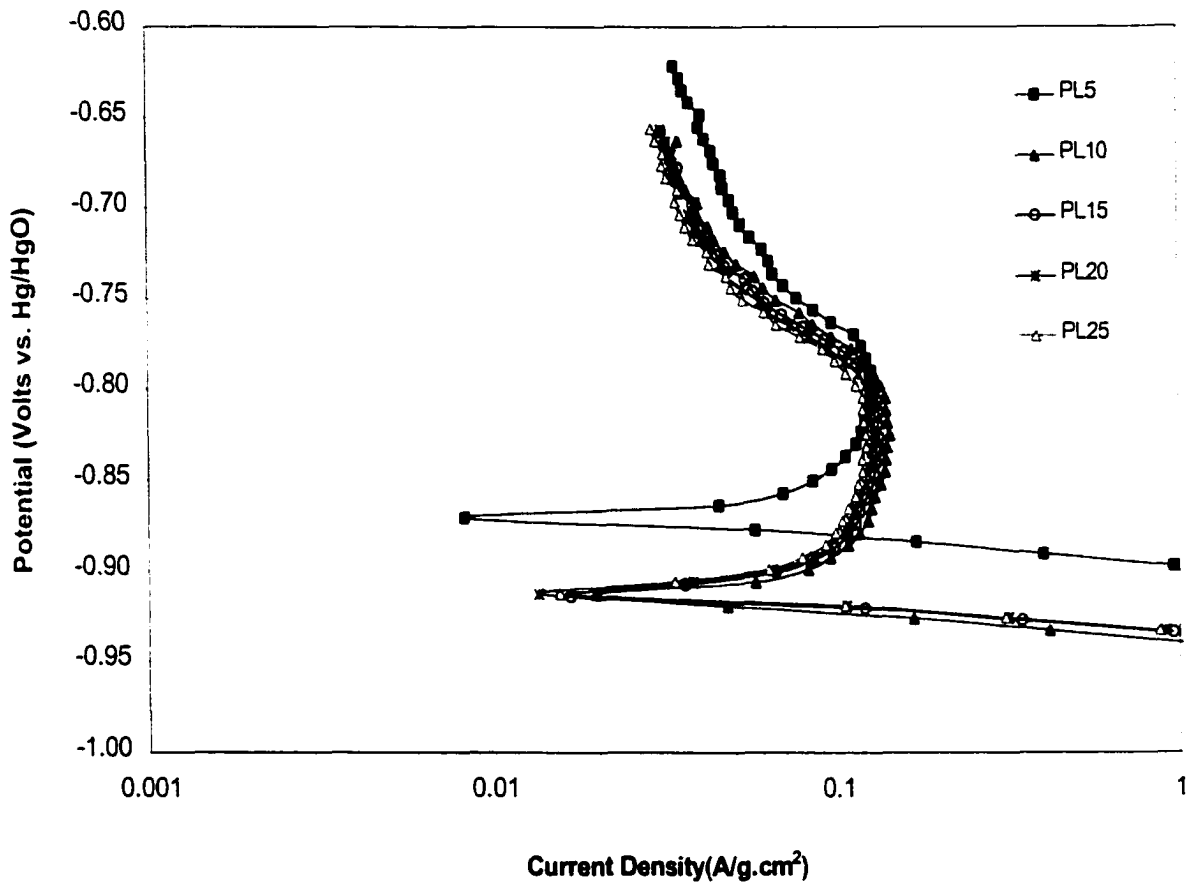


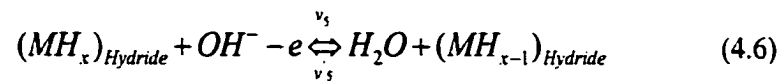
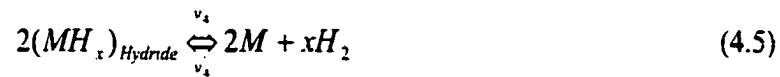
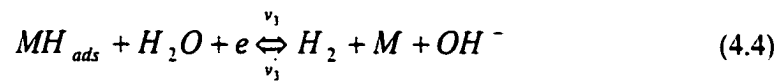
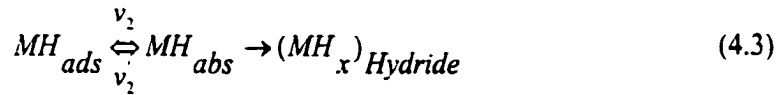
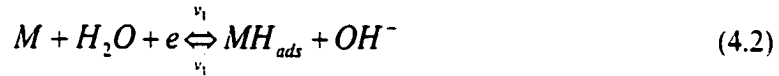
Fig.4.22 Polarization characteristics for MG-Mg₂Ni electrode (MG 25 hours at a ball-to-powder weight ratio of 10:1)

characteristics as already discussed for materials with other ball-milling parameters. The corresponding electrochemical parameters are listed in Table 4.6.

**Table 4.6 Electrochemical Parameters of Ball-milled Mg₂Ni Electrodes
(Ball Milling Time 25 Hours at a Ball-to-Powder Weight Ratio of 10:1)**

CYCLE NO.	5	10	15	20	25
E _{eq} (V)	-0.87161	-0.91481	-0.91205	-0.91198	-0.91063
I _d (mA/g)	129.38	143.5	136.91	129.56	124.02
η _s (mV)	0.93	0.92	0.86	1.04	0.82
η ₅₀ (mV)	9.65	7.62	7.56	8.78	8.54

The polarization curves will now be discussed in terms of the generally accepted mechanisms for HER (Hydrogen Evolution Reaction) for hydrogen absorbing alloys, which involves the following steps:



The electro-reduction of water with hydrogen absorption (reaction 4.2) is followed by two competing processes, namely, electrochemical desorption (reaction 4.4) or hydrogen diffusion into the bulk, with hydride formation (reaction 4.3). The hydride can be decomposed by either recombination (reaction 4.5) or electrochemical oxidation (reaction 4.6).

The dependence of overpotential on $\log i$ showed two distinct regions, namely: (i) At very low current densities, the dependence of η on $\log i$ is linear. This is consistent with a completed discharge-electrochemical desorption mechanism for HER with charge-transfer (reaction 4.2) being the rate determining step. In this region, there is practically no hydrogen bubbling on the cathode surface, so it is reasonable to assume that the diffusion of hydrogen atoms in the bulk of the alloy occurred faster than reaction 4.4, i.e. $v_1 < v_3 < v_2$. (ii) At a larger current density, intense H₂ bubbling occurred on the surface. The dependence of η on $\log i$ changed from linear to a curve relationship and the slope of E vs. $\log i$ increased. Such a change of slope indicates a change in mechanism for HER. The slope increase is ascribed to a change in the rate-determining step from charge-transfer to a mixed process of charge transfer (reaction 4.2) and hydrogen diffusion (reaction 4.3) in the bulk of the sample.

At very large cathodic current densities, the H_{abs} concentration reached a high value which is determined by the hydrogen solubility in the alloy, and the overpotential thus increases rapidly. Thus, the rate-determining step of HER becomes the diffusion of absorbed hydrogen from the surface into the bulk.

4.3 Oxidation of MG-Mg₂Ni Electrodes

Cyclic voltammograms were to obtain information on the rate-determining step during hydrogen oxidation.

The polarization measurements had shown there was an oxidation reaction occurring on the surface of the ball-milled Mg₂Ni electrodes. Fig.4.23 is a plot of anodic peak current for different number of charge/discharge cycles for a material ball milled 25 hours at a 5:1 ball-to-powder weight ratio. The anodic polarization current reaches a maximum value at approximately the same potential, about -0.8V (Hg/HgO), regardless of the number of charge/discharge cycles. This is the specific potential for the oxidation reaction. The cyclic voltammograms for ball milled Mg₂Ni and Mg₂Ni + Cu for 25 hours (Fig.4.24) showed the same value for the oxidation reaction potential. The specific potentials determined from the anodic polarization curves are given in Table 4.7.

**Table 4.7 The Oxidation Potentials for Mg₂Ni Alloy
(Ball Milling for 25 Hours at a Ball-to-Powder Weight Ratio of 5:1)**

Cycles	5	10	15	20	25
Potentials (V, Hg/HgO)	-0.794	-0.799	-0.796	-0.806	-0.804

The anodic peak current decayed with increasing number of charge/discharge cycles. This suggests that the catalytic reactivity for hydrogen oxidation decrease rapidly because of the formation of a new oxide layer on the powder surface during charge/discharge cycling. This is consistent with the fact that the capacity decay of the electrode had been attributed to oxidation and pulverization of the alloy powder.

This potential, i.e. about -0.80V, corresponds to the reaction potential for the following reaction:



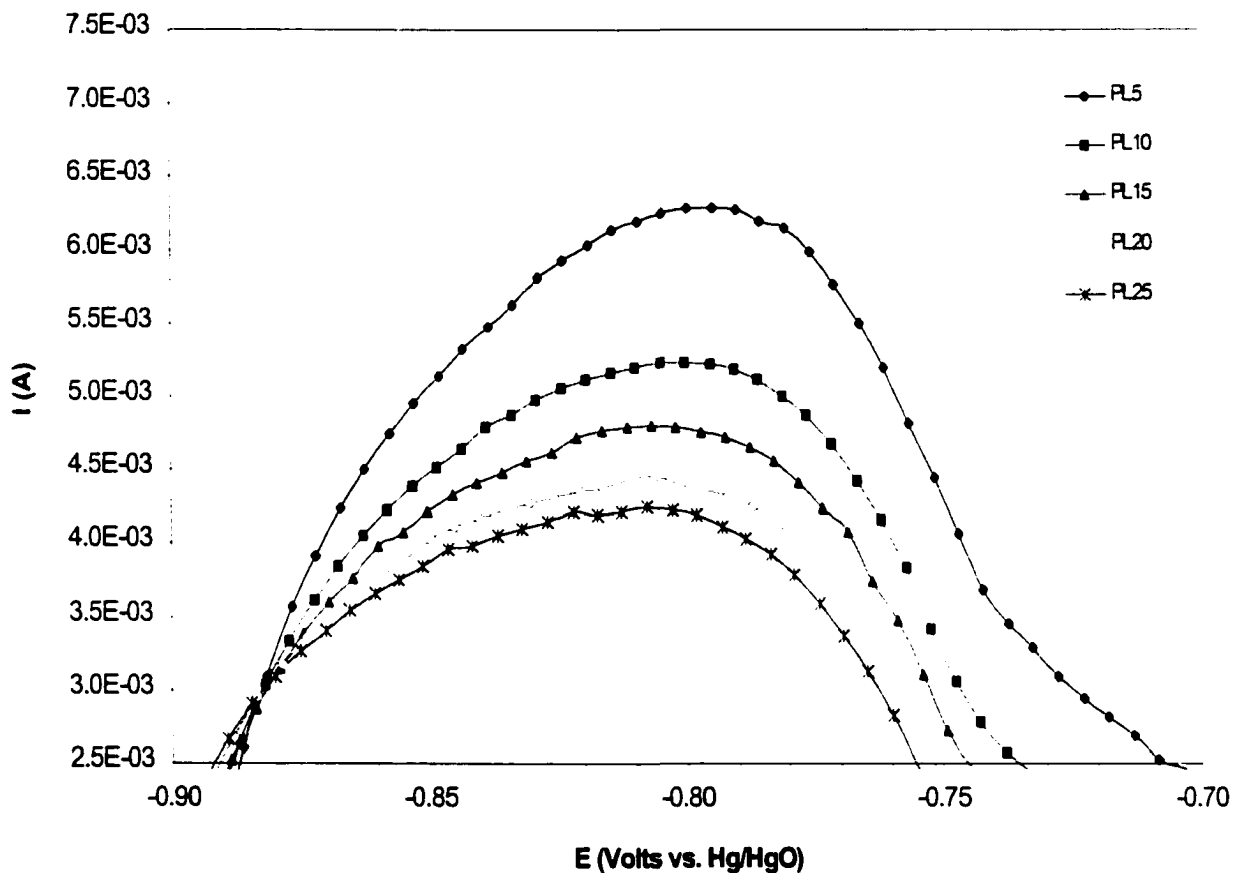


Fig.4.23 Anodic peak current change vs. number of charge/discharge cycles for MG-Mg₂Ni electrodes (MG 25 hours at a ball-to-powder weight ratio of 5:1)

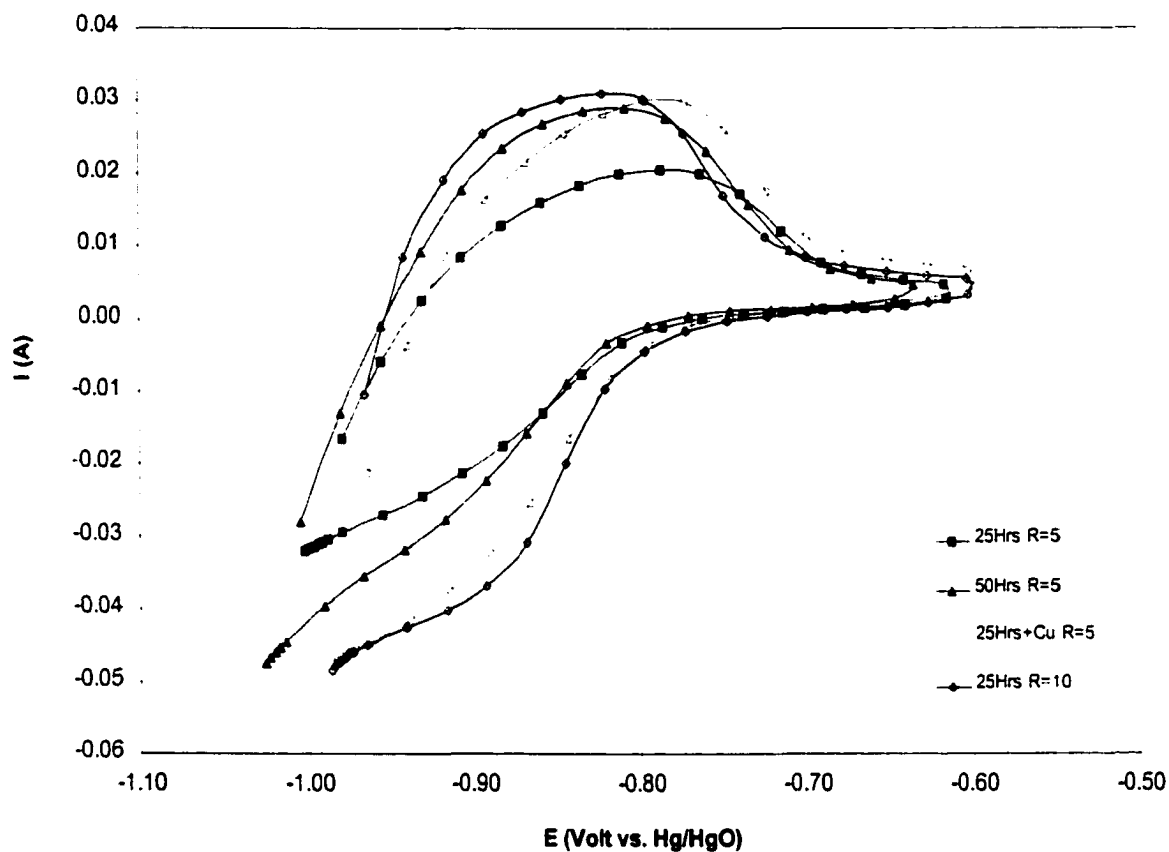


Fig.4.24 Cyclic voltammograms of MG-Mg₂Ni electrode after discharge

where $E^0 = -0.78\text{V}$. Based on the Nernst equation, the reaction potential at $C_{OH^-} = 6\text{M}$ can be calculated. The activity of 6M KOH solution was calculated as follows:

$$\text{Log}(a_{OH^-}) = -0.0225m + 0.001434m^2 + \frac{(1.38m - 0.9254m^2)}{T} \quad (4.8)$$

($T=298\text{K}$, $m=6\text{M}$), and a_{OH^-} is calculated to be 0.68018 M.

The reaction potential was then calculated as follows:

$$E = E_0 + \frac{RT}{nF} \ln\left(\frac{1}{a_{OH^-}}\right) \quad (4.9)$$

and found to be -0.793V (Hg/HgO). Comparing the calculated potential with the experimental value, we can conclude that the oxidation reaction during the discharge process was the formation of $\text{Ni}(\text{OH})_2$, and that the $\text{Ni}(\text{OH})_2$ continued to oxidize to NiOOH and precipitated on the surface of negative electrode. Thus the escape rate of hydrogen from the bulk to the surface of the electrode was gradually decreased and thus there was a corresponding decrease in discharge capacity.

4.4 Electrochemical Kinetics: Exchange Current Density i_0

The kinetics of hydrogen absorption/desorption is of primary concern in such applications as rechargeable electrodes in high energy density batteries.

Minimization of the overpotential η (to increase kinetics) with increasing current density is related to two principal factors, namely: (i) the exchange current density, i_0 , and (ii) the Tafel slope. Thus the exchange current density is an important kinetic parameter for the charge/discharge reaction. It is the rate of hydriding/dehydriding at the equilibrium state and can be used to evaluate the reversibility of the reactions.

In electrochemical reactions at lower overpotentials, the relationship between the polarization current and overpotential can be expressed by the Butler-Volmer equations:

$$i_a = i_0 \left[\exp\left(\frac{\beta n F}{RT} \eta_a\right) - \exp\left(-\frac{\alpha n F}{RT} \eta_a\right) \right] \quad (4.10)$$

$$i_c = i_0 \left[\exp\left(\frac{\alpha n F}{RT} \eta_c\right) - \exp\left(-\frac{\beta n F}{RT} \eta_c\right) \right] \quad (4.11)$$

At very small overpotentials, equations (4.10) and (4.11) can be expressed as:

$$R_p = \frac{\eta}{i} = \frac{RT}{nF} \cdot \frac{1}{i_0} \quad (4.12)$$

R_p is defined as the polarization resistance and can be calculated from the slope of the curves of overpotential vs. polarization current at the equilibrium potential. The exchange current density, i_0 , can be determined from the polarization resistance R_p using equation (4.12).

The polarization of the electrode in equations 4.10 and 4.11 is due to the charge transfer overvoltage, and increases in current density. Accordingly, the exchange current density should be as large as possible to reduce the charge transfer overvoltage and the corresponding polarization. Thus, estimation of the exchange current density can provide information on the performance of the electrode material. The conventional Tafel polarization method can not be used to estimate the exchange current density due to the large overpotential. In this study, the exchange current density of MG-Mg₂Ni alloy was calculated from linear polarization curves obtained at low overpotential (± 30 mV from the equilibrium potential).

Fig.4.25 shows the linear polarization curves of an electrode made from material ball-milled 25 hours at a ball-to-powder weight ratio of 5:1. The overpotential, which is directly proportional to the polarization current and the polarization resistance, R_p (slope of the plots), increased with increasing number of charge/discharge cycles (Fig.4.26), indicating that the

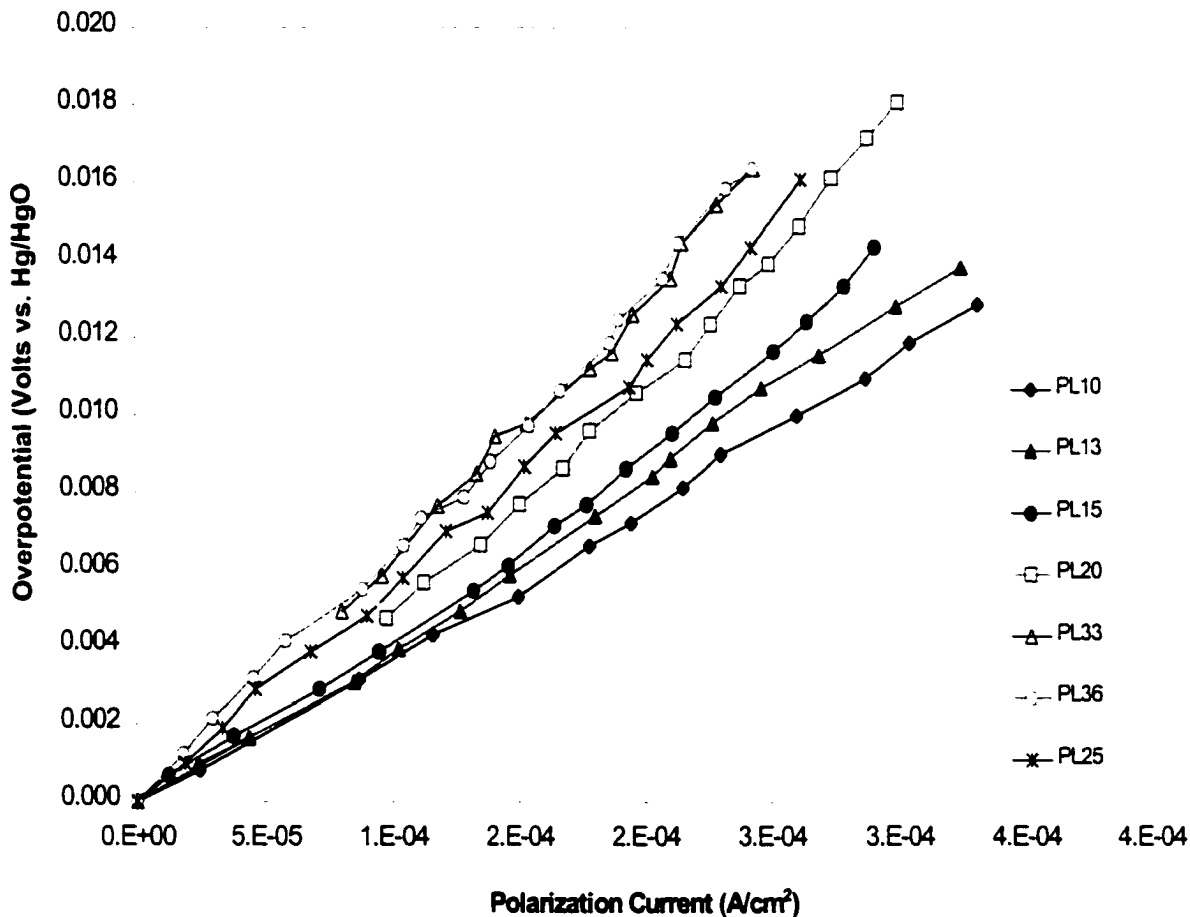


Fig.4.25 Linear polarization curves for MG-Mg₂Ni electrodes at different number of charge/discharge cycles (MG 25 hours at a ball-to-powder weight ratio of 5:1 and discharged at 50mA/g)

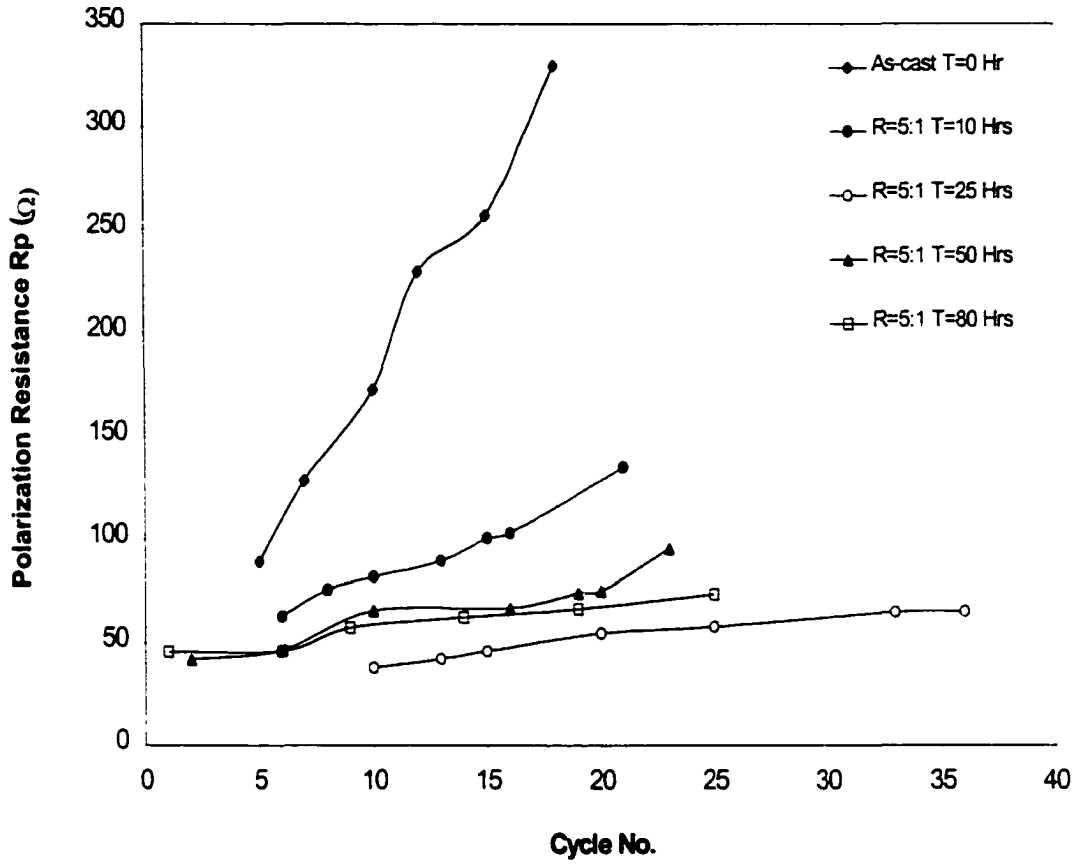


Fig.4.26 Polarization resistance, R_p , for MG- Mg_2Ni electrodes (Ball-to-powder weight ratio of 5:1 at different milling times)

polarization resistance increased with increasing amount of the hydrogen remaining in the electrode. As a result, the hydrogen diffusion became more difficult with increasing number of charge/discharge cycles. The polarization resistance of electrodes of ball-milled material decreased with increasing ball milling time from the as-cast state to 25 hours milling and then increased again with increasing ball milling time up to 80 hours. Thus the discharge of hydrogen became gradually easier from the as-cast state to 25 hours milling, but, unfortunately, discharge became more difficult from 25 hours to 80 hours milling. However, a long-time ball milling treatment still provided higher absorbing/desorbing ability than for the as-cast state.

The exchange current density, i_0 , is a measure of the hydrogen absorption/desorption rate (Fig.4.27). It decreased with the increasing number of charge/discharge cycles and, therefore, the hydrogen absorption/desorption rate became relatively slower. The exchange current density increases with decreasing hydrogen content in the alloy. As a result, the ball-milling treatments increased the hydrogen absorption/desorption rate and the hydrogen absorption/desorption rate reached a maximum after 25 hours ball milling. The exchange current densities, i_0 , and polarization resistances, R_p , after various milling times are summarized in Table 4.8.

**Table 4.8 Exchange Current Density, i_0 , and Polarization Resistance, R_p , at 10th cycle
(Different Ball Milling Times at a Ball-to-Powder Weight Ratio of 5:1)**

TIME	AS-CAST	10 HOURS	25 HOURS	50 HOURS	80 HOURS
i_0 (mA/g)	2.97	6.26	13.5	7.84	8.95
R_p (Ω)	172.67	82.06	38.01	65.47	57.36

A similar behavior with respect to exchange current density was observed for all ball-milled Mg₂Ni electrodes at the different ball-to-powder weight ratios (Fig.4.28). The exchange

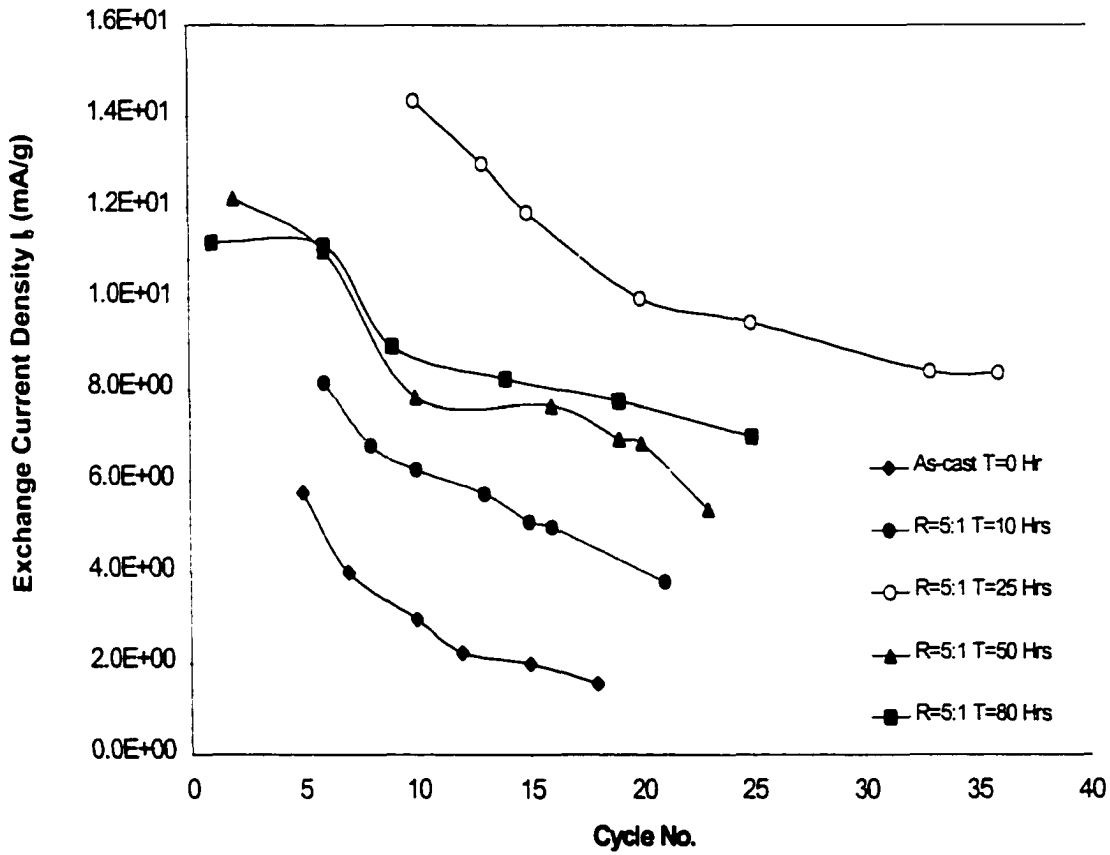


Fig.4.27 Exchange current density, i_0 , for MG-Mg₂Ni electrodes (Ball-to-powder weight ratio of 5:1 at different ball milling times)

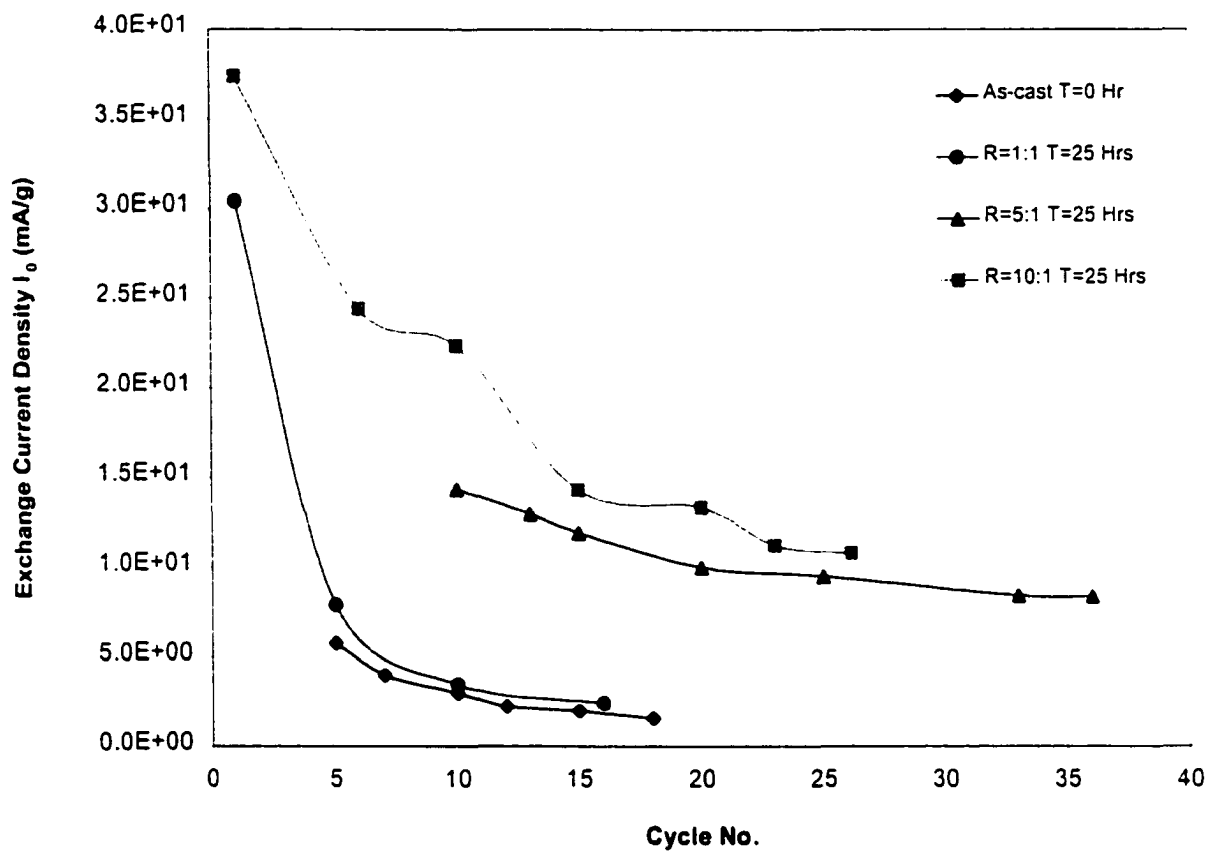


Fig.4.28 Exchange current density i_0 for MG-Mg₂Ni electrodes (MG 25 hours at different ball-to-powder weight ratios)

current densities, i_0 , and polarization resistances R_p , for the different ball-to-powder weight ratio are summarized in Table 4.9.

It is thus concluded that a ball milling treatment increased the exchange current density significantly. The activity of the Mg₂Ni electrodes was increased due to ball milling and this increase was higher at higher ball-to-powder weight ratios. However, the activity decreased with increasing number of charge/discharge cycles.

**Table 4.9 Exchange Current Density, i_0 , and Polarization Resistance, R_p , at 10th cycle
(Ball Milling Time of 25 Hours at Different Ball-to-Powder Weight Ratios)**

BALL-TO-POWDER WEIGHT RATIO	AS-CAST	1:1	5:1	10:1
i_0 (mA/g)	2.97	3.45	13.5	22.3
R_p (Ω)	172.67	148.63	38.01	23.01

The significant increase in the exchange current density, i_0 , results from a change in mechanism for the charging process for alkaline media. It is known that the hydrogen evolution reaction for hydrogen absorbing metals first comprises a discharge-absorption step in which chemisorbed H atoms are formed. This is followed by two steps: (a) transfer of H_{abs} through the interface into the interstitial sites of the material just below the surface and subsequent diffusion into the bulk; (b) the chemical or electrochemical recombination of H_{ads} with H₂ desorption.

During oxidation of the hydride, the above processes occurred in the reverse order: diffusion of bulk H atoms to surface, transfer to adsorbed state (4.5); and electrochemical oxidation of the ad-atoms (4.2).

The kinetics of the hydrogen evolution at the surface and the efficiency of H sorption in the bulk are determined by the relative rates of (a) and (b). High efficiencies of H sorption may occur if the rates of the recombination processes for H_{ads} (processes (4.4) and (4.5)) are slow compared with step (4.3). With process (4.2) occurring at a higher rate than (4.4), the coverage of hydrogen in the low overpotential range will be small as long as the transfer from absorbed to adsorbed state (4.3) has a rate comparable with (4.2) (this would require a high value for the rate constant v_p). Most H atoms absorbed on the surface will then be absorbed in the bulk. With increasing current, there was a gradual saturation with absorbed H, which decreased the rate of H transfer across the interface. This, then, increased the coverage and the rate of H recombination (4.4). As the rates of (4.3) and (4.4) become equal, H₂ starts bubbling out of the electrode. We assume that the desorption-controlled mechanism of HER describes best what happened on the surface since it accounts both for the zero coverage at near equilibrium and the fact that H₂ bubbling appeared only at relatively high currents.

The absorption/desorption ability (H/M) varied with reaction rate (Fig.4.29). H/M and exchange current density showed the same changing trend with ball milling time. An increased absorption/desorption rate increased the discharge capacity of ball-milled Mg₂Ni electrodes. For Mg₂Ni electrodes made of material ball-milled at different ball-to-powder weight ratios (Fig.4.30), the capacity (H/M) and exchange current density i_0 show the same dependence on ball-to-powder weight ratio. The increased exchange current density due to the increased ball-to-powder weight ratio lead to an increased discharge capacity.

A relatively large value of exchange current density, i_0 , is important in the practical use of the alloy as a hydrogen storage medium, since it lowers the charge transfer overvoltage (equation 4.1), which is known to cause power loss in both the charge and discharge steps. Due

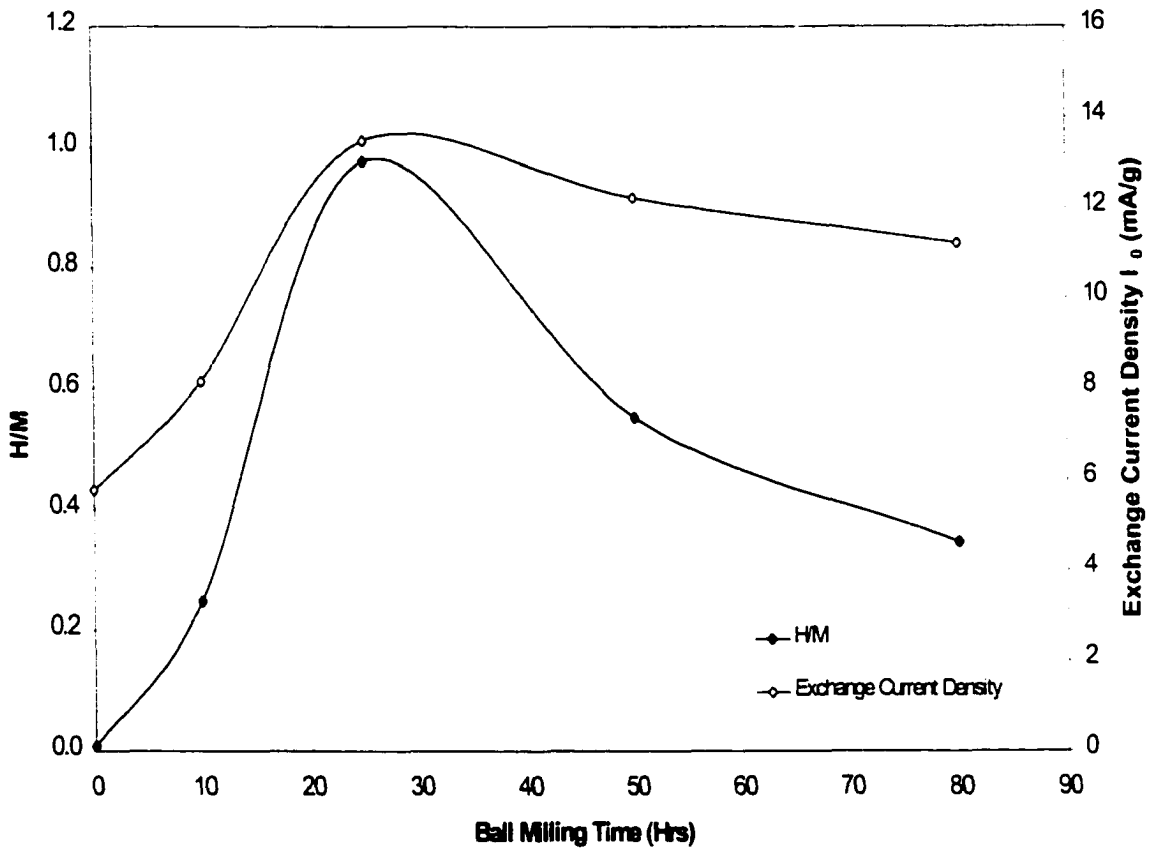


Fig.4.29 Hydrogen concentration, H/M, and exchange current density, i_0 , vs. ball milling times

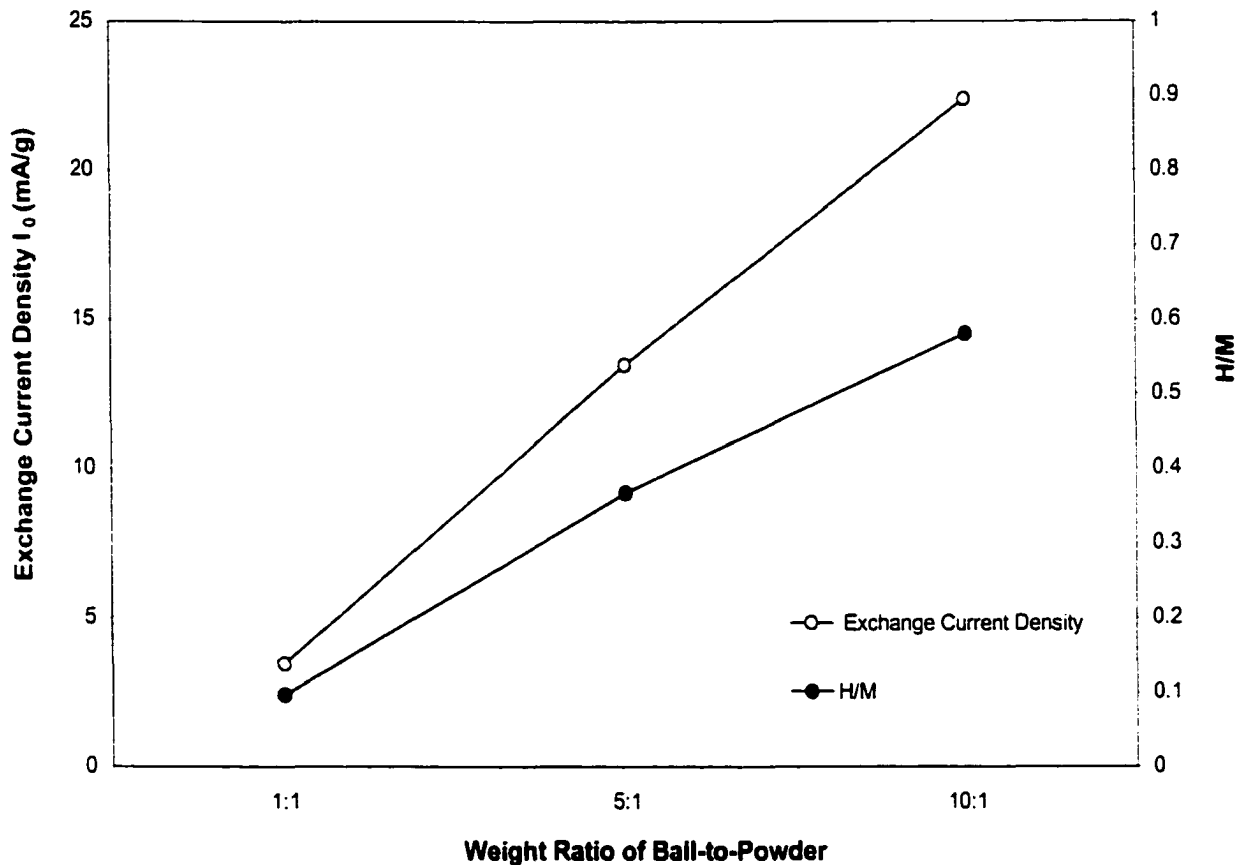


Fig.4.30 Hydrogen concentration, H/M, and exchange current density i_0 vs. ball-to-powder weight ratio at 10th cycle

to volume restrictions of the grinding jar, higher ball-to-powder weight ratios will lead to less usable powder and the static surface electricity will make the powder stick to both the walls of the jar and the ball surfaces. For optimum ball milling effects and sufficient powder to make the electrodes, a ball-to-powder weight ratio of 5:1 and a 25 hours ball-milling treatment are recommended.

4.5 Hydrogen Diffusion Rate (D_0)

The performance of a metal hydride electrode is determined both by the kinetics of the reaction occurring at the metal/solution interface and the rate of hydrogen diffusion within the bulk of the metal. The determination of the hydrogen diffusion rate in the bulk requires a solution of Fick's second law.

Assuming that the hydride alloy was in a spherical form, the diffusion equation is:

$$\frac{\partial(R'c)}{\partial t} = D_0 \frac{\partial^2(R'c)}{\partial r^2} \quad (4.13)$$

where c is hydrogen concentration in alloy, t is time, D_0 is an average diffusion coefficient of hydrogen over a concentration range, and R' is the radius of the spherical particle. The diffusion equation may be solved under two different boundary conditions, namely: (i) constant hydrogen surface concentration and a uniform initial hydrogen concentration in the bulk alloy, or (ii) constant flux at the surface and a uniform initial concentration in the bulk of the alloy.

The resulting diffusion current $I(t)$ and the discharge capacity $C(t)$ varies with time according to equations (4.14) and (4.15) respectively:

$$I(t) = \frac{6FD_0}{\delta R^2} (C_0 - C_S) \sum_{n=1}^{\infty} \exp\left(-\frac{n^2\pi^2 D_0 t}{R^2}\right) \quad (4.14)$$

$$C(t) = \frac{F(C_0 - C_S)}{\delta} \left\{ 1 - 6 \sum_{n=1}^{\infty} \left(\frac{1}{n\pi} \right)^2 \exp\left[\frac{(-n\pi)^2 D_0 t^2}{R^2} \right] \right\} \quad (4.15)$$

where C_0 and C_S are the uniform initial hydrogen concentration in the bulk of the alloy and the constant surface concentration, respectively. For large values of t , when the actual discharge capacity was more than that of the total capacity, equation (4.12) reduces to:

$$C(t) = F \frac{D\Delta C}{\delta R^2} - \frac{\pi^2 D}{R^2} I(t) \quad (4.16)$$

where $C(t) = \int_0^t I(t) dt$

From the slope of the plot of $I(t)$ vs. $C(t)$, the quantity $-D_0/R^2$ may be evaluated from equation (4.16) and if the sphere radius is known, D_0 can then be calculated.

Fig.4.31 shows the specific discharge capacity remaining in the electrode as a function of the discharge current density for different ball milling times at a ball-to-powder weight ratio of 5:1. The remaining discharge capacity is directly proportional to the current density. The corresponding hydrogen diffusion coefficients, D_0 , calculated from these plots, are given in Table 4.10. Ball milling increased the diffusion coefficient by up to nearly one order of magnitude compared to the as-cast state.

**Table 4.10 Hydrogen Diffusion Coefficient, D_0 , for MG-Mg₂Ni Electrodes
(Different Ball Milling Times at a Ball-to-Powder Weight Ratio of 5:1)**

TIME	AS-CAST	10 HOURS	25 HOURS	50 HOURS
Particle Size (μm)	25	1	0.75	0.5
D_0 (m ² /s)	3.17E-15	1.81E-14	2.83E-14	8.64E-15

(Note: Particle size after ball milling treatment was calculated from SEM metallographic observations)

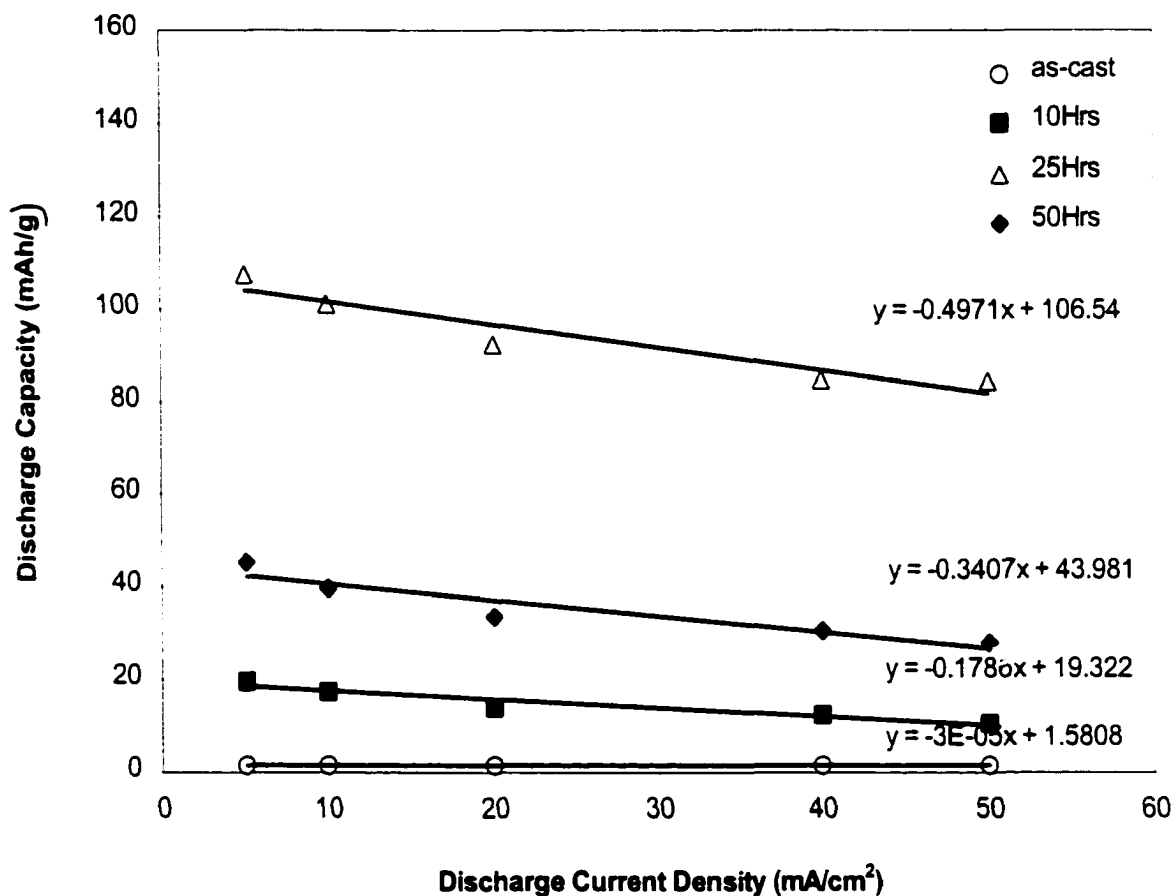


Fig.4.31 Correlation between discharge capacity and discharge current density (Ball-to-powder weight ratio of 5:1 at different milling times)

The discharge capacity is also proportional to the current density: see Fig.4.32 for data for material ball-milled 25 hours at different ball-to-powder weight ratios. The hydrogen diffusion coefficients, D_0 , calculated from this data are summarized in Table 4.11.

Ball milling greatly increased the hydrogen diffusion coefficient, D_0 , which was a maximum after 25 hours ball-milling at a 5:1 ball-to-powder weight ratio. A small particle size facilitates the inter-diffusion because the diffusion coefficient for the very small particles is much larger than that for the bulk materials and also because the total distance required for diffusion is reduced. This has been confirmed from the measurements of the exchange current density, i_0 , and the specific discharge capacity. The hydrogen diffusion coefficient, D_0 , also increases with increasing ball-to-powder weight ratio.

**Table 4.11 Hydrogen Diffusion Coefficient, D_0 , for MG-Mg₂Ni Electrodes
(Different Ball-to-powder Weight Ratios at 25 Hours Ball Milling)**

BALL-TO-POWDER WEIGHT RATIO	1:1	5:1	10:1
Particle Size (μm)	1.5	0.75	0.65
D_0 (m^2/s)	1.13E-14	2.83E-14	3.16E-14

(Note: Particle size after ball milling treatment was calculated from SEM metallographic observations)

4.6 High Rate Dischargeability of Ball-Milled Mg₂Ni Electrodes

The purpose of ball milling is to improve the discharge capacity. This is beneficial for the practical application of the ball-milled hydrogen storage alloy in an electrode of a rechargeable battery. However, from a consumer's standpoint, it would be better if it took less time to charge

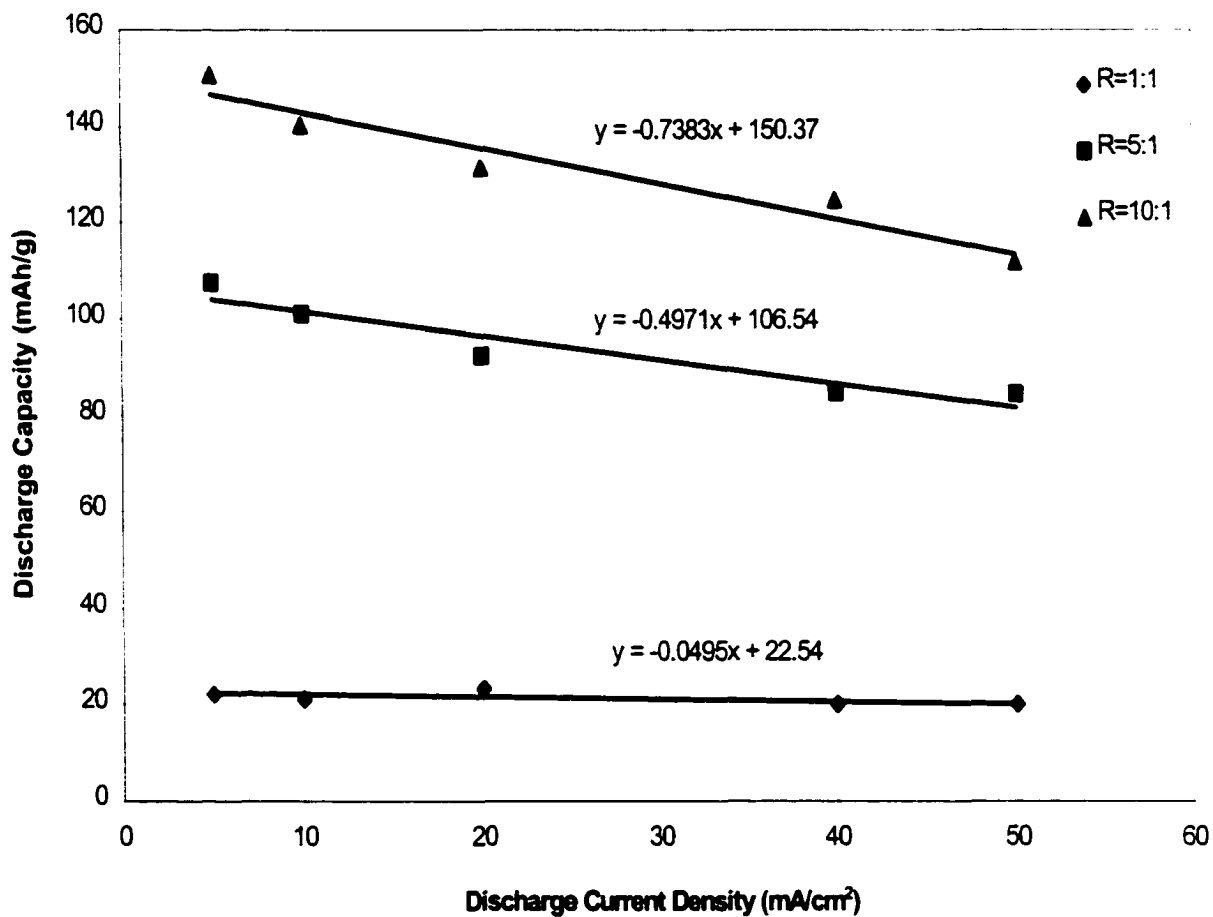


Fig.4.32 Correlation between discharge capacity and discharge current density (MG 25 hours at different ball-to-powder weight ratios)

their batteries. Charging at a large current density requires less time to reach the required potential. However, the disadvantage of a large current charge is that it results in a decreased discharge capacity because of increased overpotentials. The lower the discharge current that is used, the higher is the discharge capacity and the longer is the battery life. While very little experimental work had been done to determine the behavior of H in the absorption/desorption reaction, especially the important potential dependence of coverage by H that determines the Tafel slope of the polarization relation, and hence the practical performance of an electrode at high current densities.

The charge/discharge characteristics were studied at two different current densities, 50mA/g and 200mA/g. The discharge capacity was much higher at the lower current density than at the higher current density (Fig.4.33). The discharge capacity also exhibited less decay, 51% at 50mA/g and 72% at 200mA/g.

In order to compare the discharge current density dependence of the discharge capacity of the ball-milled Mg₂Ni electrodes, a high rate dischargeability was defined as the ratio of discharge capacity at 200mA/g to that at 50mA/g at the same number of cycles. The high rate dischargeability decreased from an initial 90% to about 50% with increasing number of charge/discharge cycles (Fig.4.33). This emphasises the advantage of discharging at a small current density. In order to improve the high rate dischargeability, the electrochemical activity of the hydrogen evolution reaction must be increased. Fig.4.34 shows that the high rate dischargeability is related to the exchange current density, i_0 , showing an approximately linear dependence. This shows that improvement in high rate dischargeability can be attributed to an increase in electrochemical activity for the hydrogen evolution reaction. With increasing ball milling time and/or ball-to-powder weight ratio, ball milling introduced more defects

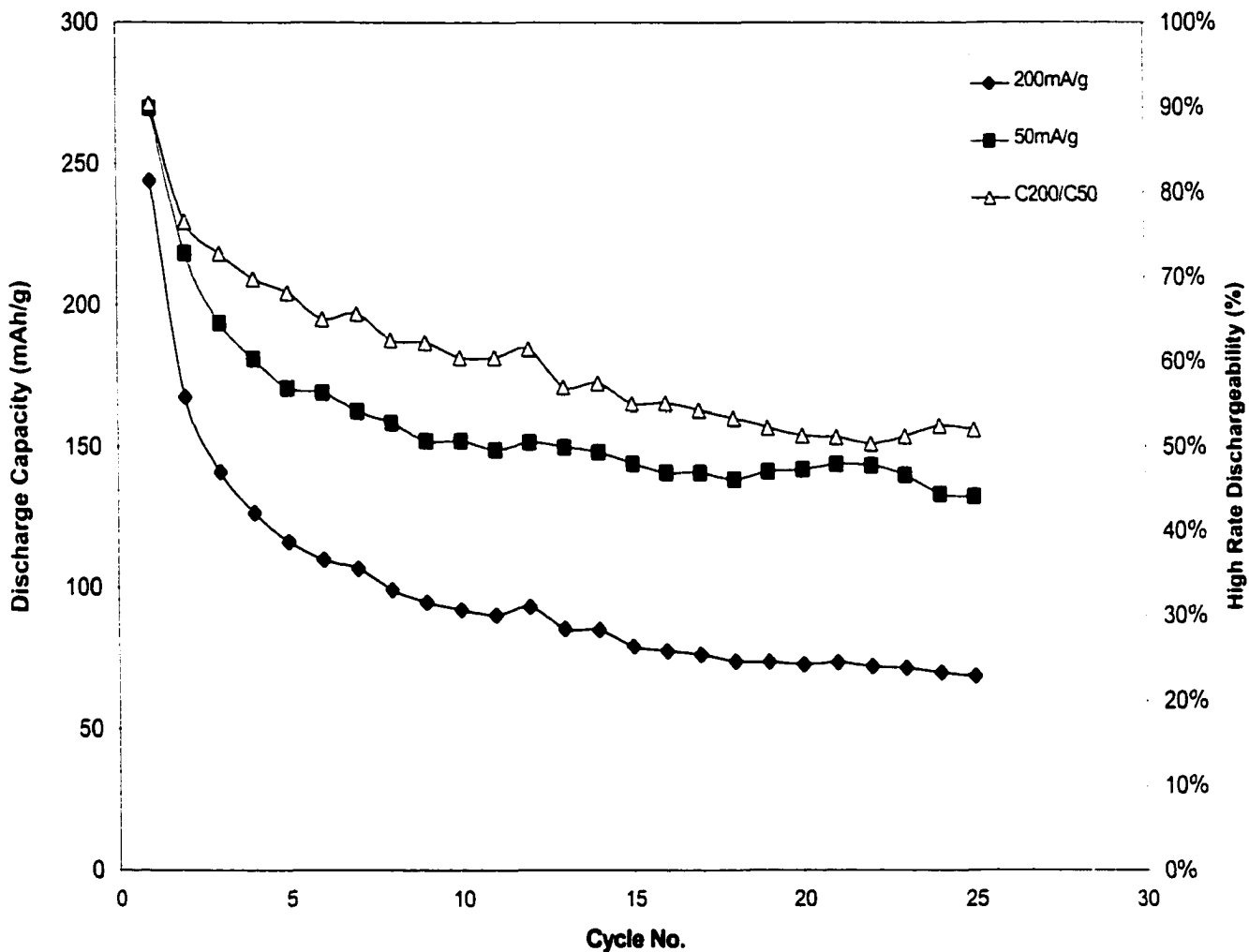


Fig.4.33 Discharge capacity vs. number of cycles for different discharge current density and high rate dischargeability

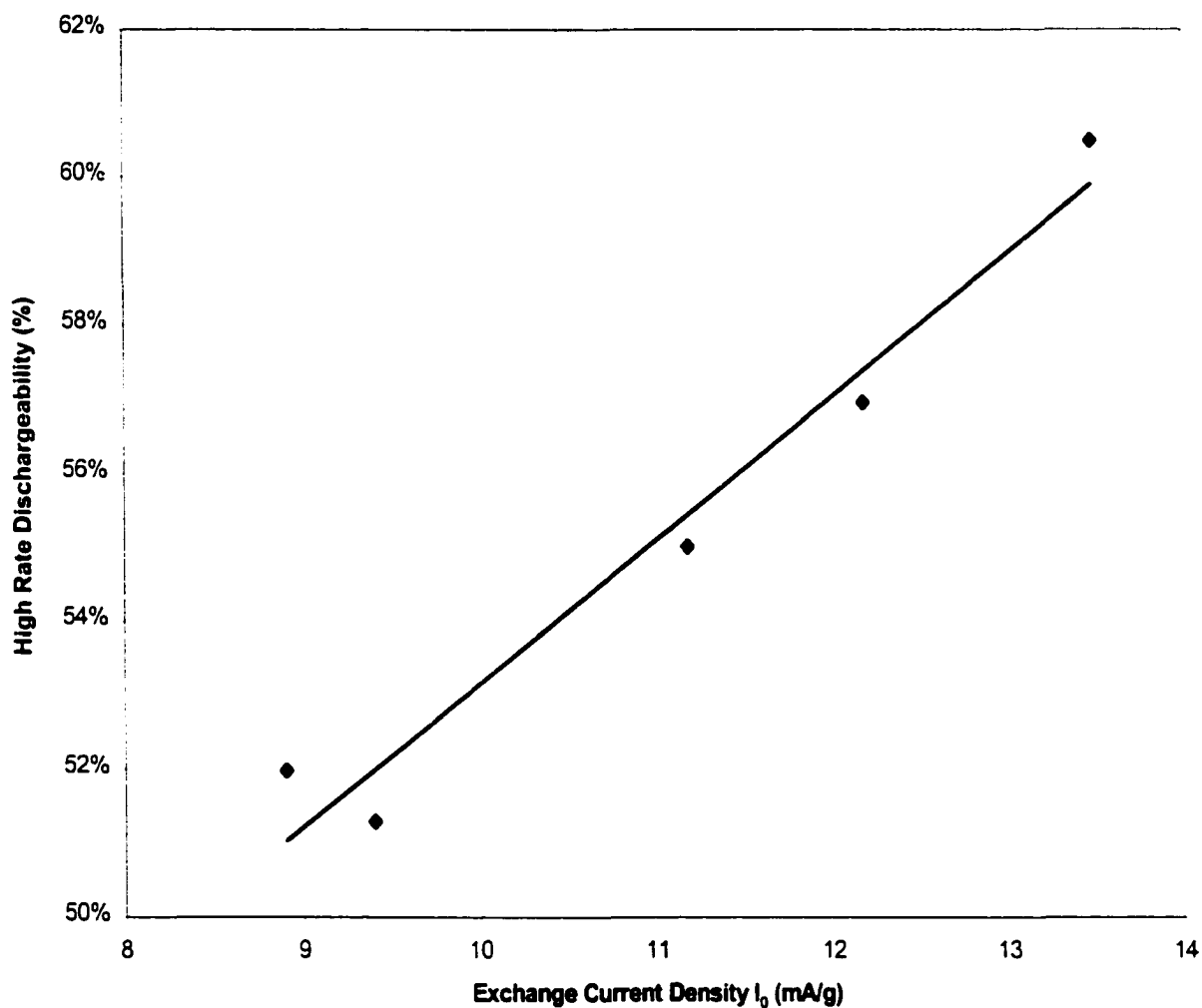


Fig.4.34 High rate dischargeability vs. exchange current density i_0

(dislocations) and increased the specific surface area (SSA) of the Mg₂Ni powder, thereby increasing the electrochemical activity of the electrode.

4.7 Effect of Additives on The Charge/Discharge Properties of Ball-Milled Mg₂Ni Electrodes

Batteries using metal hydrides as the negative electrode have several advantages over Ni-Cd battery, e.g. high energy density and long cycle life stability. Reversible alkaline batteries which use metal hydride negative electrodes require a compacting procedure for fabricating the metal hydride electrode because the intermetallic compounds which are used as the active material are brittle and disintegrate into powder upon hydride formation. The characteristics of the metal hydride electrode can be manipulated by changing the composition of the hydrogen storage alloy. Direct modification of the alloy may improve the electrode characteristics, e.g. cycle stability and high rate dischargeability.

Cu and Ni were selected as additives in making the electrodes. The effects of these additive materials on the kinetics of the electrode, such as the hydrogen diffusion coefficient, D_0 and exchange current density, i_0 , were studied. The addition of Cu or Ni is expected to play at least two important roles. First, it serves as a barrier for protecting the alloy surface from oxidation; and secondly, it provides a microcurrent collector for facilitating the charge transfer reaction on the alloy surface.

Copper is attractive as an additive from three perspectives: (i) it provides increased thermal conductivity, (ii) it provides sufficient cycling strength during hydrogen absorption-desorption, and (iii) it provides excellent resistance against impure gas. It is also well known that the copper film has excellent hydrogen permeation.

The high electronic conductivity of Ni powder provides good contact between the current collector and alloy, and contact between alloy particles. It indicates that the additive material should be considered in the manufacturing of the alloy electrode.

4.7.1 Effect of Electrode Additives on Discharge Capacity

Cu or Ni were added into the ball-milled (25 hours and R=5:1) Mg₂Ni powder at a 1:1 mole ratio, and electrochemical measurements were carried out on the electrodes fabricated from the mixed powder in the same manner as previously described. Table 4.12 gives the discharge capacities at each discharge cycle for the Mg₂Ni + Cu/Ni electrodes.

Figs.4.35a and 4.35b are the charging curves for Mg₂Ni electrodes with Ni or Cu, respectively. The potentials decreased rapidly in the first 500 seconds and gradually became stable during charging. The potential decreased with increasing number of charge/discharge cycles. This is similar behavior as electrodes without Cu/Ni addition. This behavior is related to the saturation of hydrogen on the electrode surface in the initial stages. After the electrode surface is completely covered by hydrogen atoms, the potential is almost stable. The high concentrated hydrogen accelerated the penetration of hydrogen into the electrode. Absorption of hydrogen occurs by two main processes: (i) absorption of hydrogen on the surface of the electrode, and (ii) the penetration of hydrogen into the electrode.

After charging, the ball-milled Mg₂Ni+Cu/Ni electrodes were discharged at a constant current density of 200mA/g. The discharge curves are shown in Figs.4.36a and 4.36b, respectively. The discharge potentials increased with time and increased rapidly after passing a critical potential of about -0.80V(Hg/HgO). This potential indicates that an oxidation reaction was occurring on the electrode surface thus producing a passive film which was a barrier to

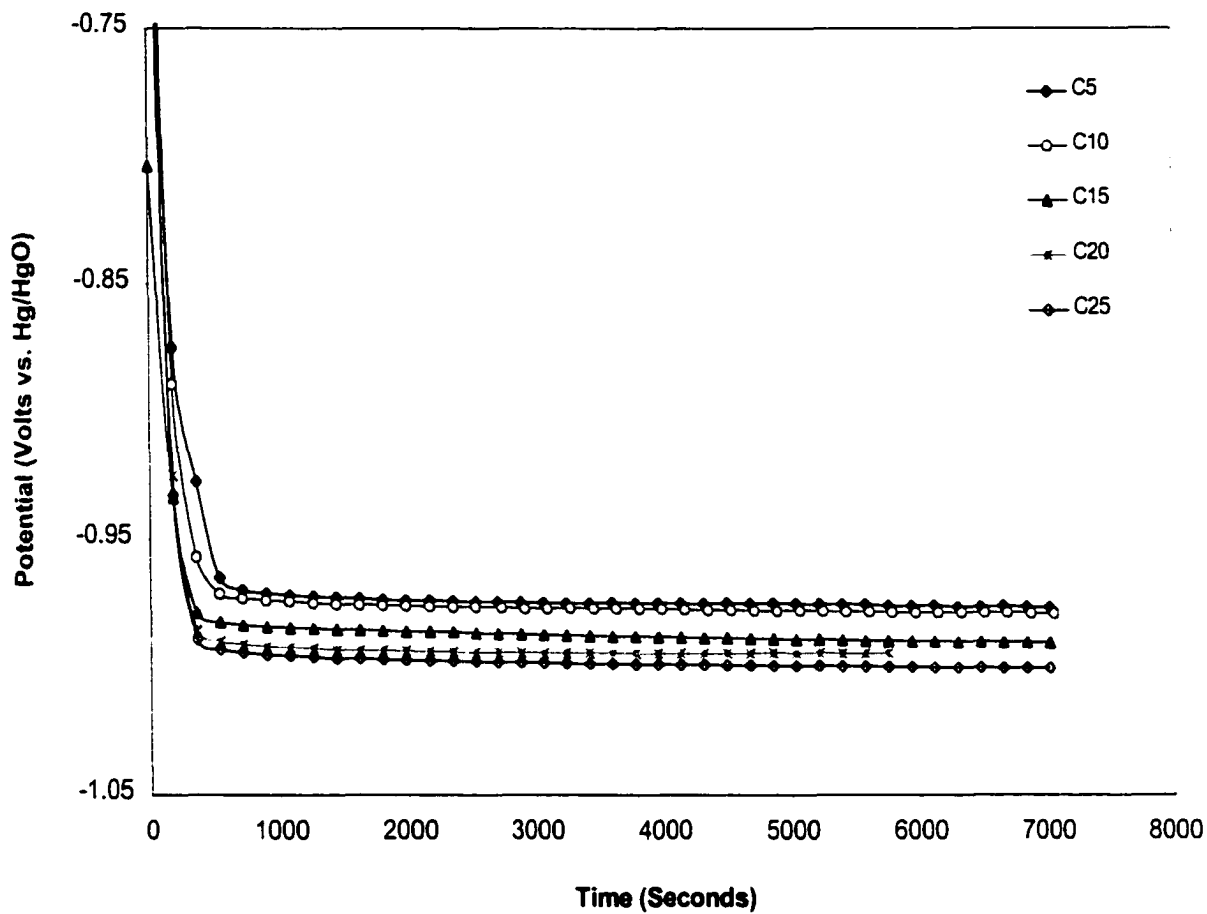


Fig.4.35a Charge potential vs. charge time for MG-Mg₂Ni+Ni electrode (MG 25 hours at a ball-to-powder weight ratio of 5:1)

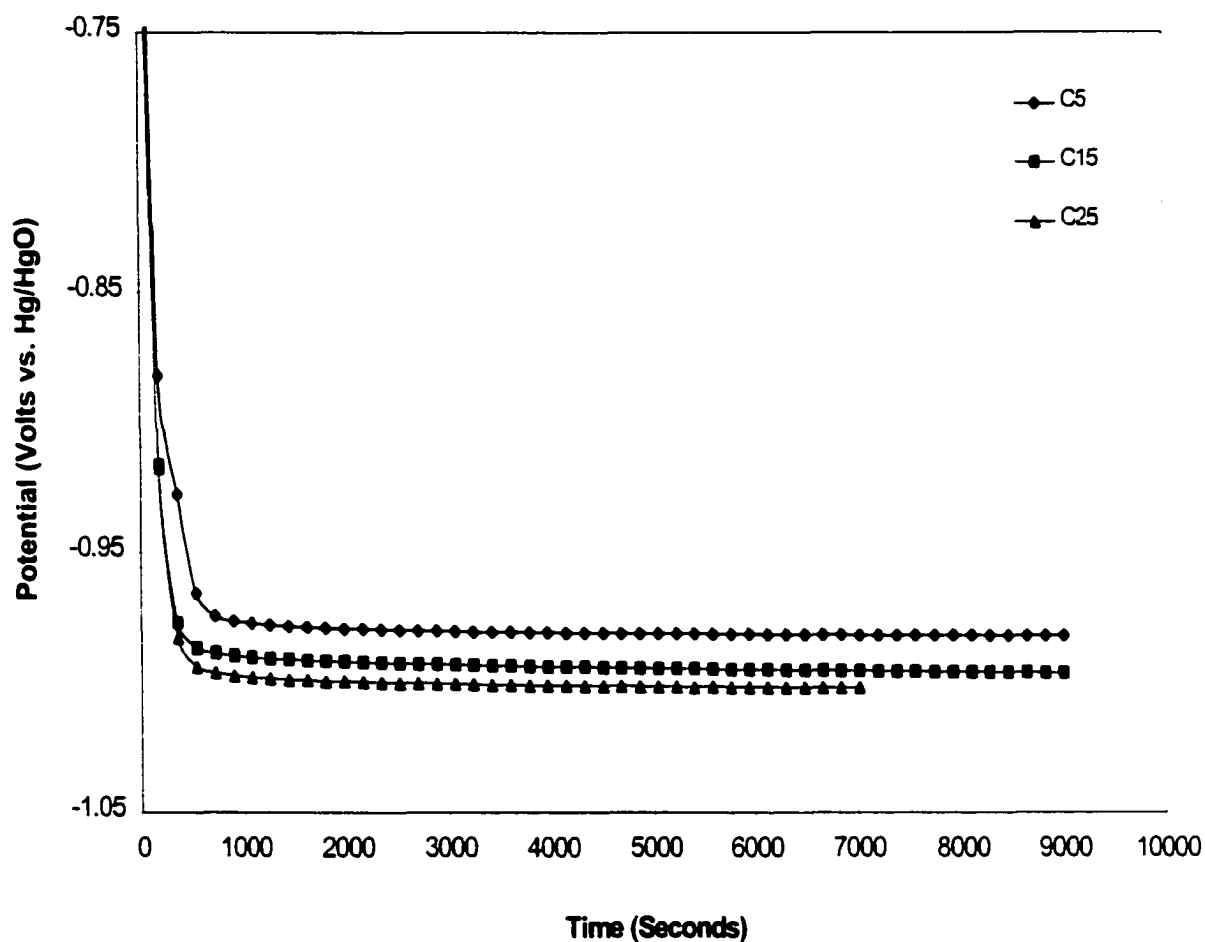


Fig.4.35b Charge potential vs. charge time for MG-Mg₂Ni+Cu electrode (MG 25 hours at a ball-to-powder weight ratio of 5:1)

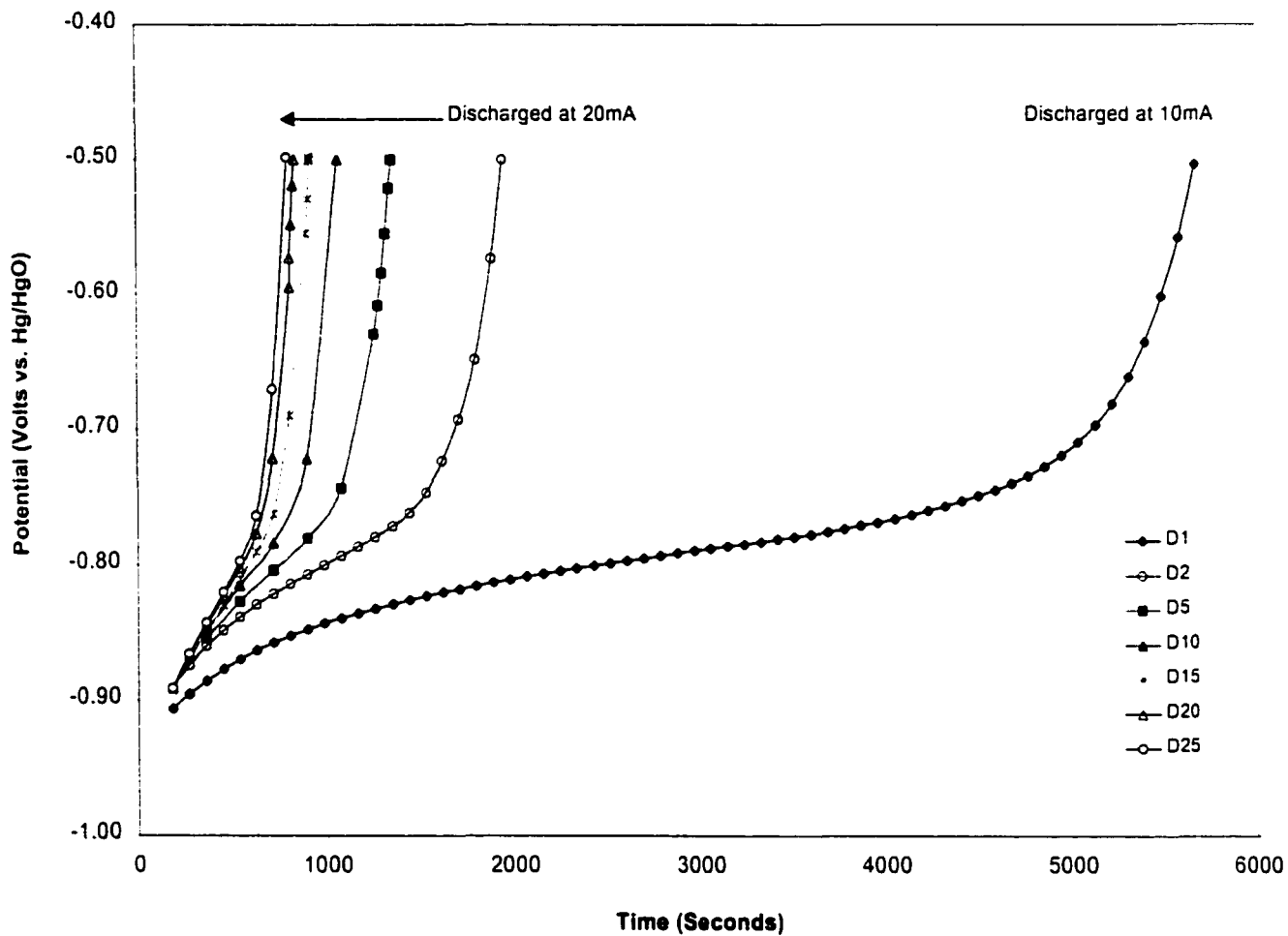


Fig.4.36a Discharge potential vs. charge time for MG-Mg₂Ni+Ni electrode (MG 25 hours at a ball-to-powder weight ratio of 5:1)

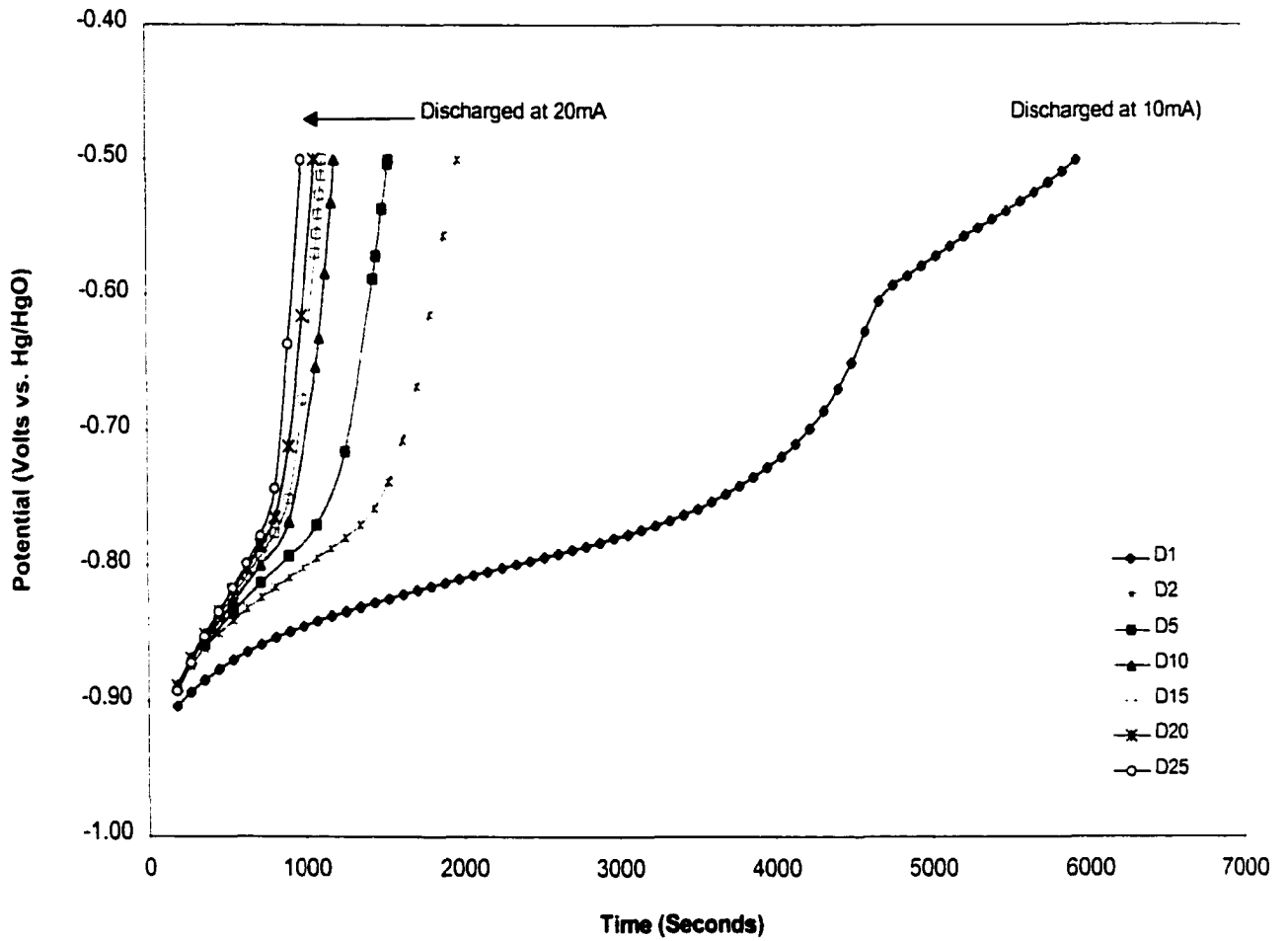


Fig.4.36b Discharge potential vs. charge time for MG-Mg₂Ni+Cu electrode (MG 25 hours at a ball-to-powder weight ratio of 5:1)

hydrogen penetration into the electrode. Therefore, the discharge potential decreased significantly after the critical potential, because a very short time was needed for the electrode to be polarized from the critical potential to terminal potential and this caused a large polarization overvoltage.

Table 4.12 Discharge Capacities at Each Discharge Cycle of Mg₂Ni + Cu/Ni Electrodes

CYCLE NO.	AS CAST (mAh/g)	Mg ₂ Ni (mAh/g)	Mg ₂ Ni+Ni (mAh/g)	Mg ₂ Ni+Cu (mAh/g)
1	0.99	244.06	224.80	330.39
2	1.84	167.45	164.48	223.74
3	2.06	140.97	145.15	195.36
4	1.95	126.42	134.67	182.11
5	2.04	116.19	125.77	171.54
6	1.89	109.86	122.66	161.70
7	1.62	106.72	116.96	152.00
8	1.52	99.12	109.64	143.92
9	1.48	94.66	105.10	138.49
10	1.45	91.95	101.42	133.73
11	1.32	90.00	95.80	127.00
12	1.31	93.13	94.10	126.00
13	0.64	85.33	93.20	125.00
14	0.80	85.02	90.70	121.00
15	0.80	79.17	92.44	125.53
16	0.76	77.56	90.70	122.71
17	0.74	76.32	88.75	120.22
18	0.72	73.76	86.01	119.72
19	0.75	73.63	84.87	119.81
20	0.79	72.75	84.07	119.71
21	0.76	73.46	84.37	118.20
22	0.76	72.09	83.39	115.41
23	0.73	71.59	82.41	113.09
24	0.72	69.86	81.70	112.12
25	0.73	68.77	80.59	110.98

It should be noted that the addition of Ni or Cu powder further improved the discharge capacity of ball-milled electrodes with Cu being more beneficial than Ni (Fig.4.37).

The equilibrium potential during discharge corresponds to the amount of hydrogen remaining in the electrode. The decreasing open circuit potentials (Fig.4.38) with increasing number of charge/discharge cycles indicates the increasing amount of hydrogen remained in electrode. As a result, the discharge capacity decreased with increasing number of charge/discharge cycles for the Mg₂Ni + Cu/Ni electrodes.

4.7.2 Effect of Additives on Electrochemical Activity of Hydrogen Evolution Reaction

The exchange current density, i_0 , is a measure of electrochemical activity with an increasing exchange current density causing an increase in capacity. Linear polarization measurements were carried out to determine the polarization resistance and exchange current density for the Mg₂Ni+Cu/Ni electrodes. Fig.4.39 shows the effect of adding Cu or Ni on the polarization resistance. The as-cast Mg₂Ni electrode had the largest polarization resistance and the polarization resistance increased rapidly with number of charge/discharge cycles. Adding Cu or Ni powder reduced the resistance of the hydrogen evolution reaction. The electrode with a Cu addition had the smallest polarization resistance and the polarization resistance increased with number of charge/discharge cycles. Correspondingly, this treatment increased the exchange current density (Fig.4.40). In particular, the electrode containing Cu had an exchange current density two times higher than the Mg₂Ni electrode without Cu in the initial cycle. Ni also had beneficial effects on the electrochemical properties of electrode.

The increased electrochemical activity of the electrode with Ni is the result of the fact that hydrogen atoms make a stronger bond with the Ni atoms than Mg the atoms. The Ni additive

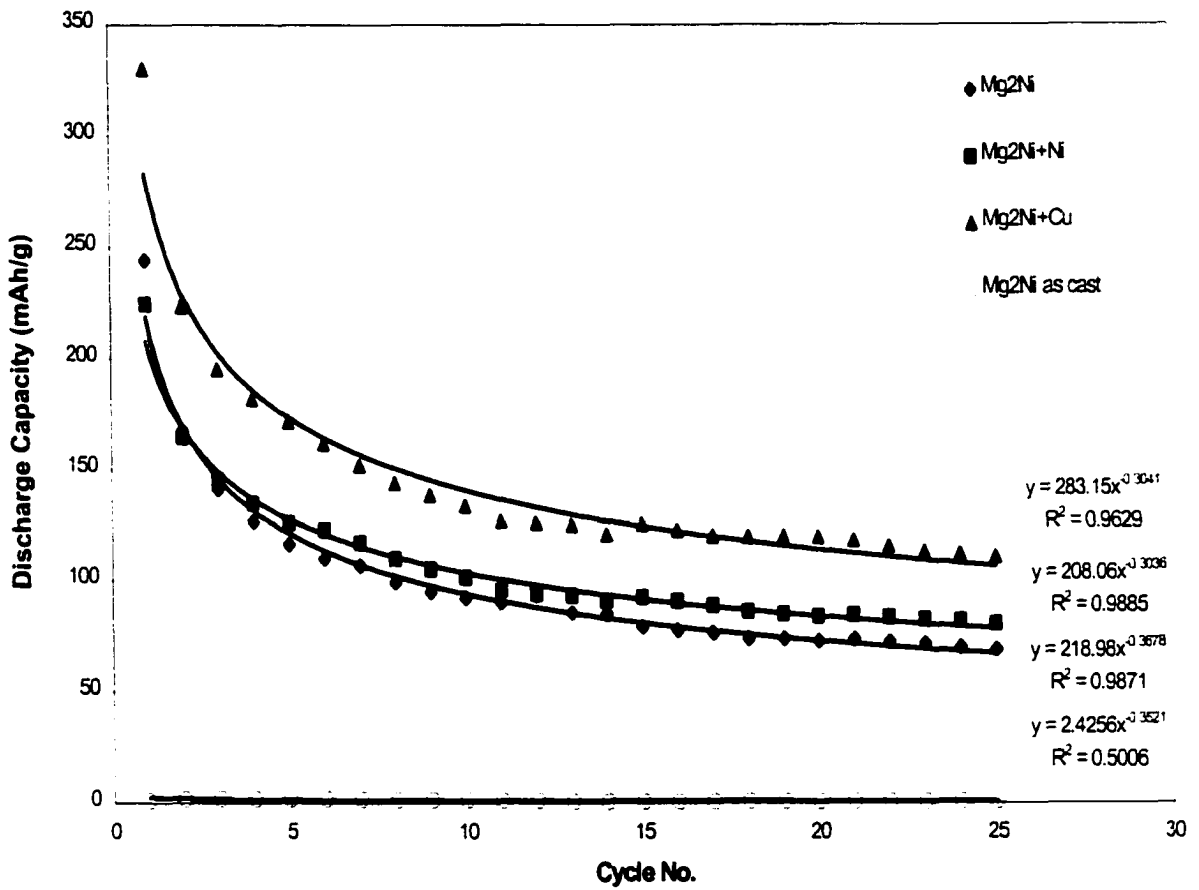


Fig.4.37 Effects of adding Cu or Ni on the discharge capacity of MG-Mg₂Ni electrodes (MG 25 hours at a ball-to-powder weight ratio of 5:1)

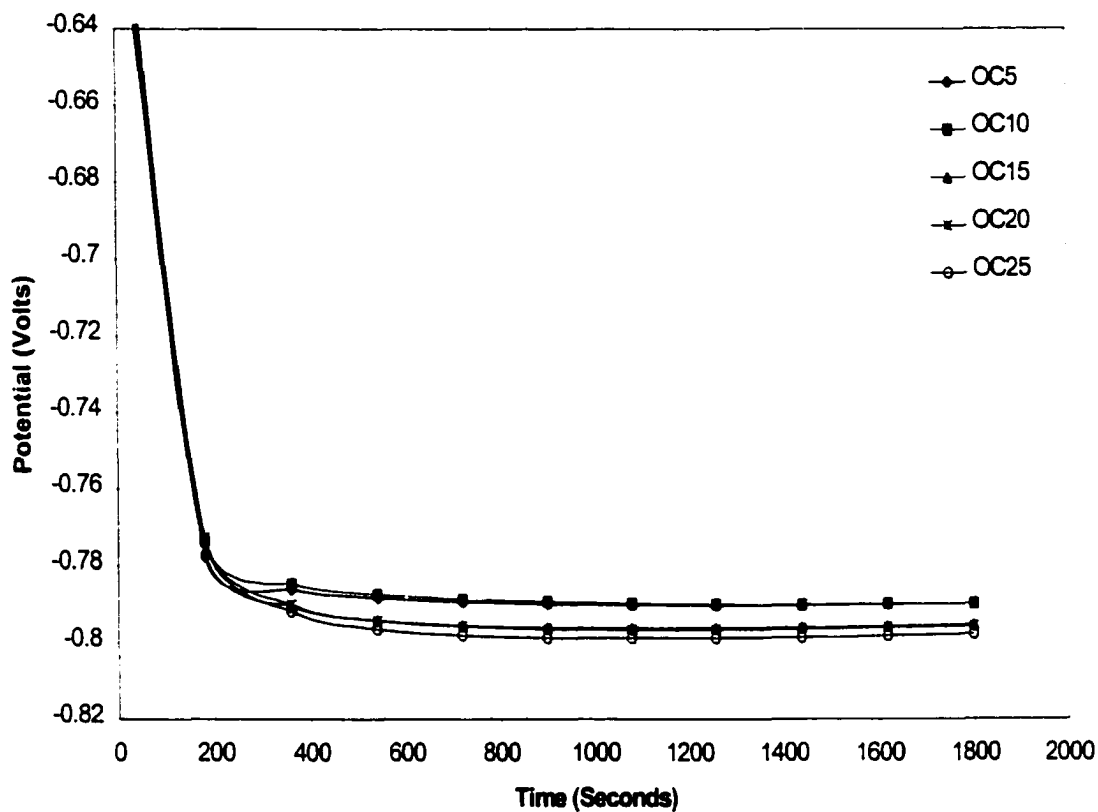


Fig.4.38 Open circuit potential vs. time for MG-Mg₂Ni+Ni electrode (MG 25 hours at a ball-to-powder weight ratio of 5:1)

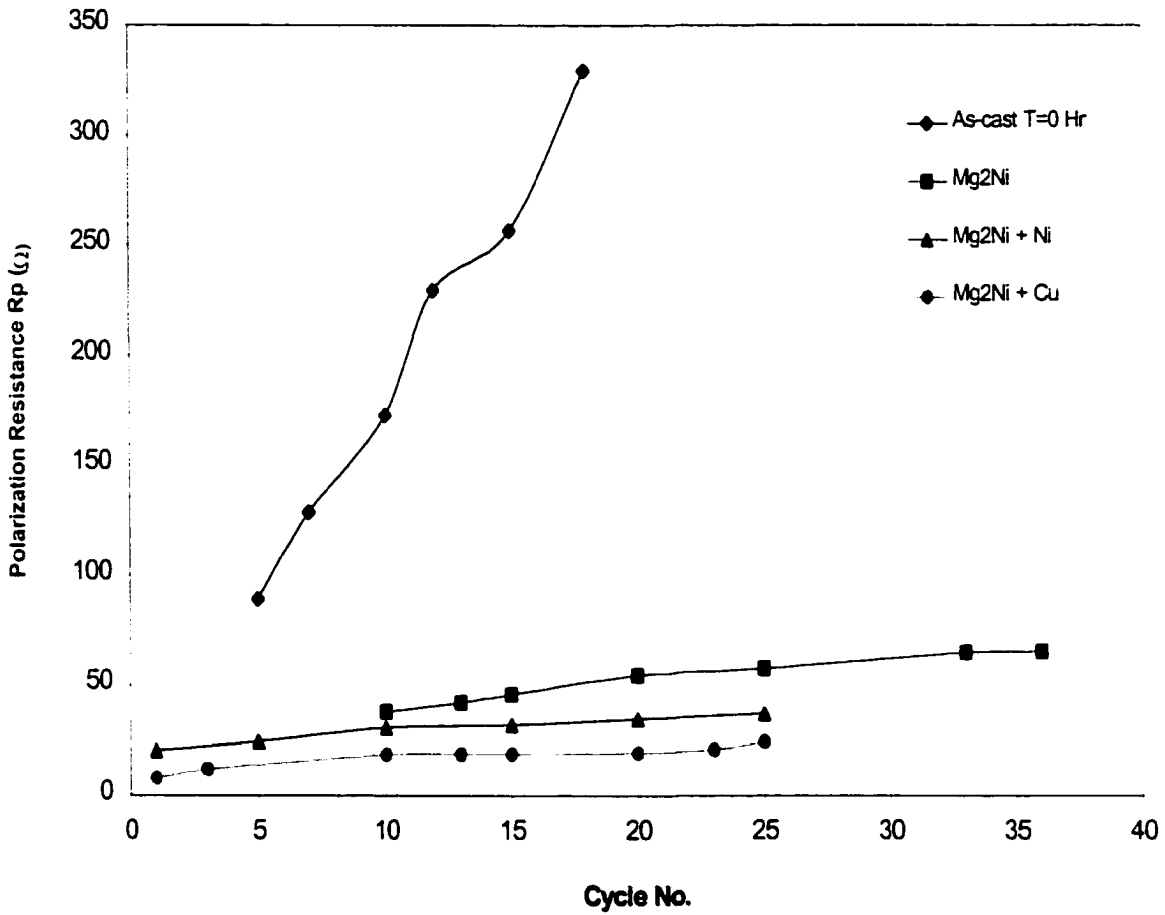


Fig.4.39 Polarization resistance, R_p , for MG-Mg₂Ni electrodes with different additives (MG 25 hours at a ball-to-powder weight ratio of 5:1)

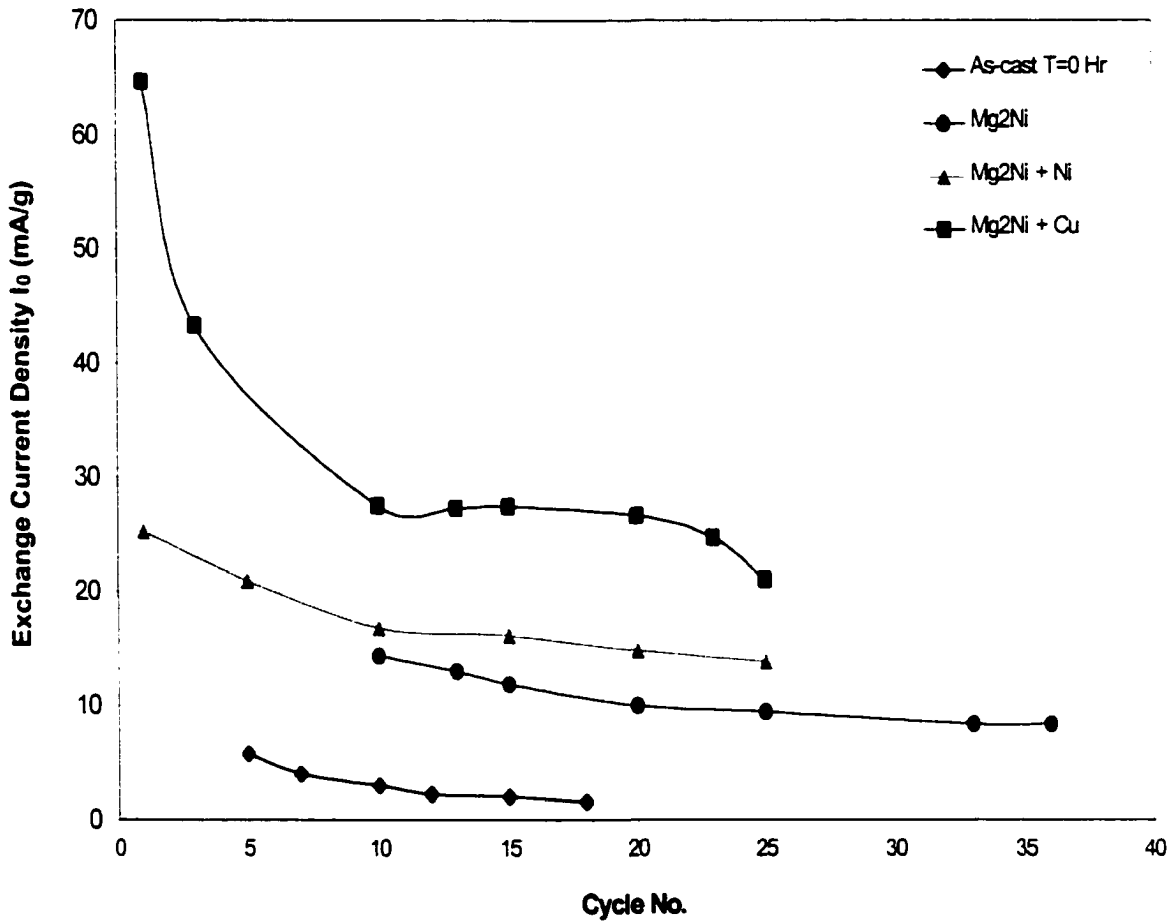


Fig.4.40 Exchange current density i_0 of MG-Mg₂Ni electrodes with different additives (MG 25 hours at a ball-to-powder weight ratio of 5:1)

became the preferential sites for hydrogen to form strong bonds and the hydride was very stable. The increased capacity introduced by Cu was due to the fact that Cu is a good conductor of electricity. Another reason for the increased electrochemical activity is that the hydrogen diffusion rate, D_0 , increases with the addition of Cu or Ni (Fig.4.41) and it is a maximum for the Cu addition.

It is concluded that addition of Cu or Ni greatly improved the electrocatalytic reaction of the negative electrode, reduced the overpotential during charging/discharging, resulting in a significant increase of the electrode capacity.

4.7.3 The Polarization Characteristics of MG-Mg₂Ni + Cu or Ni Alloy

The polarization curves for Mg₂Ni + Cu/Ni electrodes are presented in Fig.4.42 and 4.43 for the Cu or Ni additions, respectively. Generally, the critical passivation current density, i_d , decreased on charging/discharging, indicating that the Mg₂Ni electrodes were easily subjected to oxidation and an oxide layer was formed on the surface. The passivating potential, E_{pp} , shifted negatively with charging/discharging indicating an earlier commencement of the active-to-passive transition and easier formation of an oxide layer.

Compared with the pure Mg₂Ni electrodes (Fig.4.19), the polarization current density increased significantly with Cu- or Ni- additions, Cu having a much larger effect in improving the oxidation resistance.

The overpotentials of Mg₂Ni electrodes with Cu or Ni at polarization current densities of and 50mA/g are given in Table 4.13.

Table 4.13 Overpotentials of Mg₂Ni Electrodes with Cu or Ni at the 5th Cycle

MATERIALS	Mg₂Ni + Cu	Mg₂Ni + Ni	Mg₂Ni
Overpotential at 50mA/g	9.5mV	11.5mV	13.4mV

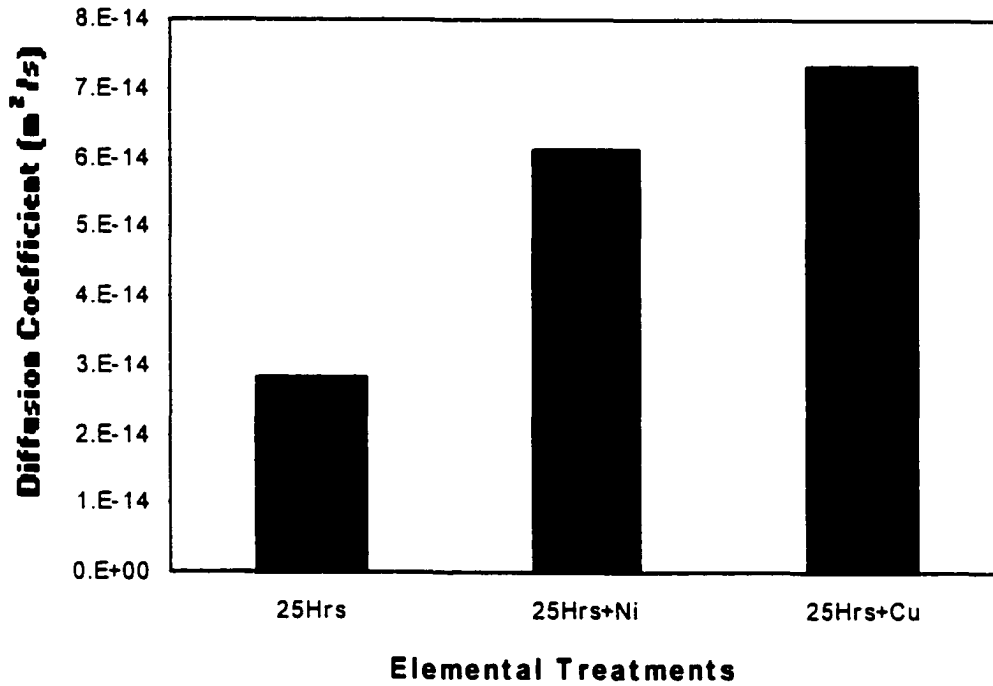


Fig.4.41 Diffusion coefficient, D_0 , of hydrogen through MG-Mg₂Ni electrodes

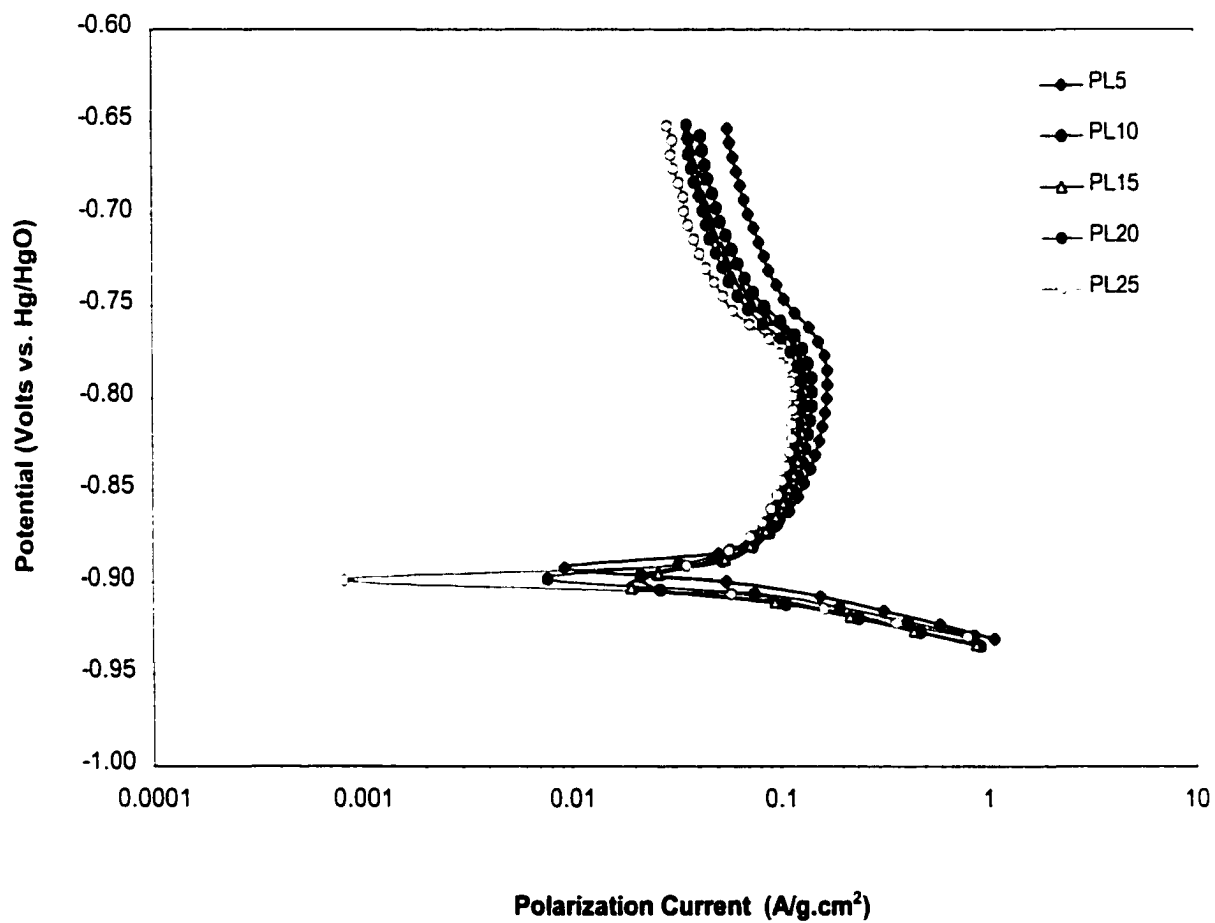


Fig.4.42 Polarization characteristics for MG-Mg₂Ni+Cu electrode (MG 25 hours at a ball-to-powder weight ratio of 5:1)

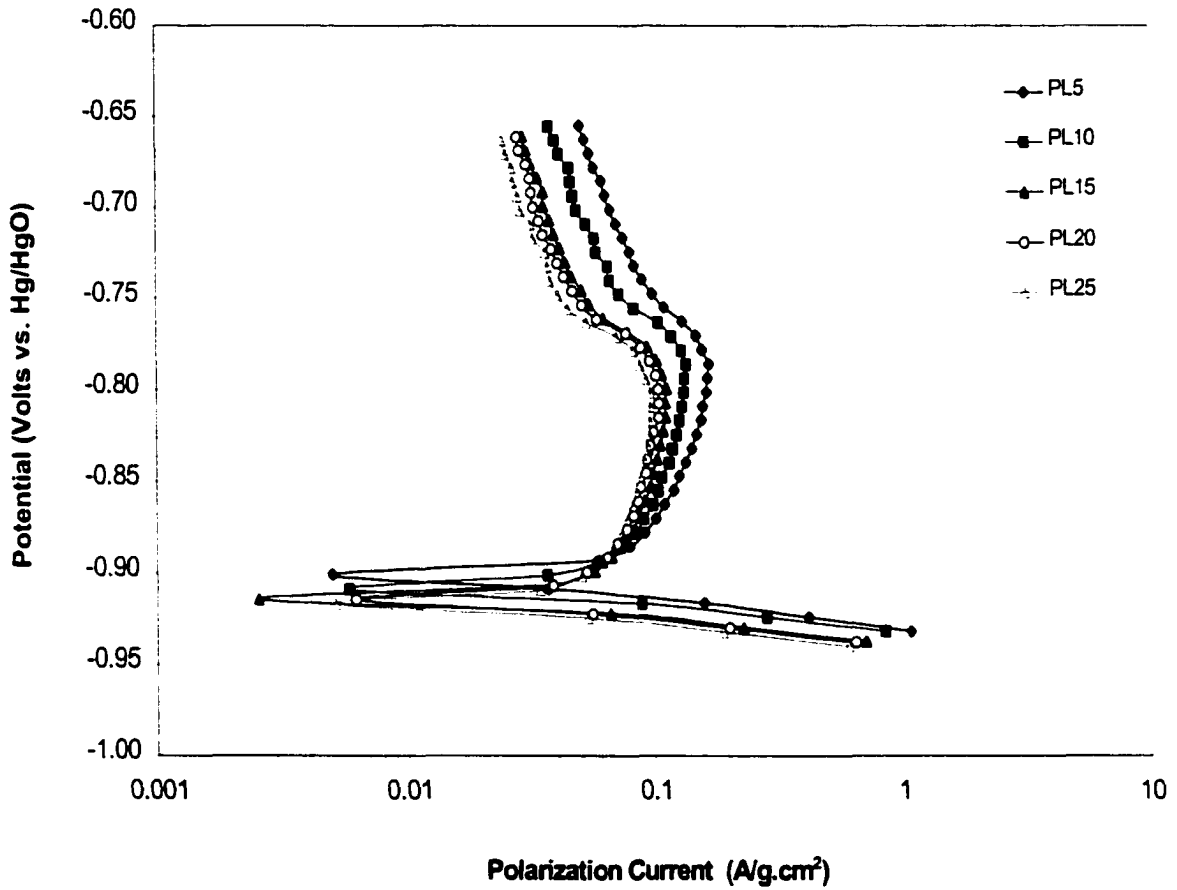


Fig. 4.43 Polarization characteristics for MG-Mg₂Ni+Ni electrode (MG 25 hours at a ball-to-powder weight ratio of 5:1)

CHAPTER 5 TRANSFORMATION FROM ELECTROCHEMICAL MEASUREMENTS TO A P-C-T CURVE

Although the theoretical discharge capacity (1000mAh/g) of the Mg₂Ni alloy is approximately 2.7 times higher than that of LaNi₅ (372mAh/g), the hydrogen absorption and desorption reactions in this alloy require high temperatures (200°C to 300°C) and pressures (up to 10atm).

The important thermodynamic properties of hydrogen absorption/desorption are the change in enthalpy, ΔH , and the change of entropy, ΔS . Both of these parameters can be determined from the pressure-composition- isothermal (P-C-T) diagrams. However, since the plateau pressures of typical hydride electrode materials at room temperature are generally lower than 1 atm, P-C-T determination requires a specially designed high vacuum equipment and the experiment is difficult, and sometimes even impossible, when the plateau pressure is much lower than 1atm. Presently, in the pressure range from 10^{-10} atm to 1 atm, the ΔH value is calculated from the van't Hoff plot which was constructed from the P-C-T curves and the P-C-T curves are obtained from the electrochemical measurements using the Nernst equation.

5.1 The Transition from Electrochemical Measurements to a P-C-T Curve for the LaNi_{4.7}Al_{0.3} Electrode

The pressures (in atm) at different temperatures were calculated from potentials according to the Nernst equation:

$$E_{eq} = E_H^0 - E_{Hg^0/Hg}^0 + \frac{RT}{2F} \ln\left(\frac{\alpha_{H_2O}}{\gamma_{H_2} P_{H_2}}\right) \quad (5.1)$$

where α_{H_2O} is the activity of water and P_{H_2} is the hydrogen pressure.

$$E_H^0 - E_{Hg^0/Hg}^0 = -1.18041 + (4.4666 \times 10^{-3} - 6.93606 \times 10^{-4} \ln T)T + 1.0788 \times 10^{-6} T^2 - 4.512 \times 10^{-10} T^3 + \frac{5.232}{T} \quad (5.2)$$

Using equation:

$$\log \alpha_{H_2O} = -0.0225m + 0.001434m^2 + \frac{1.38m - 0.9254m^2}{T} \quad (5.3)$$

where m is the concentration of KOH (mol/l), in this case $m = 6M$.

$$\text{Thus: } \ln \gamma_{H_2} = \frac{20.5T - 1857}{83.1447T^2} + \frac{-351T^2 + 12760T^{1.5} - (20.5T - 1857)^2}{1.4009 \times 10^{-4} T^4} \quad (5.4)$$

At $T=298K$ and $m=6M$, the calculated $(E_H^0 - E_{Hg^0/Hg}^0)$, α_{H_2O} and γ_{H_2} are $-0.9255V$, $0.6817M$ and 1.0006 , respectively. Substituting the above values into the Nernst equation, the relationship between equilibrium potential of the electrode and pressure at a temperature of $298K$ is^[123]:

$$E(V) = -0.9324 - 0.0291 \log P_{H_2} (atm) \quad (5.5)$$

The measured P-C-T curve and the calculated P-C-T curve are given in Fig.5.1. We can see that in the plateau region and the high H/M region, the P-C-T curve obtained from the electrochemical measurements is in good agreement with the experimental curve obtained from manometric measurements. Only in the low H/M region, the E-C-T curve is about 0.1 H/M lower than the P-C-T curve, but they have the same trend.

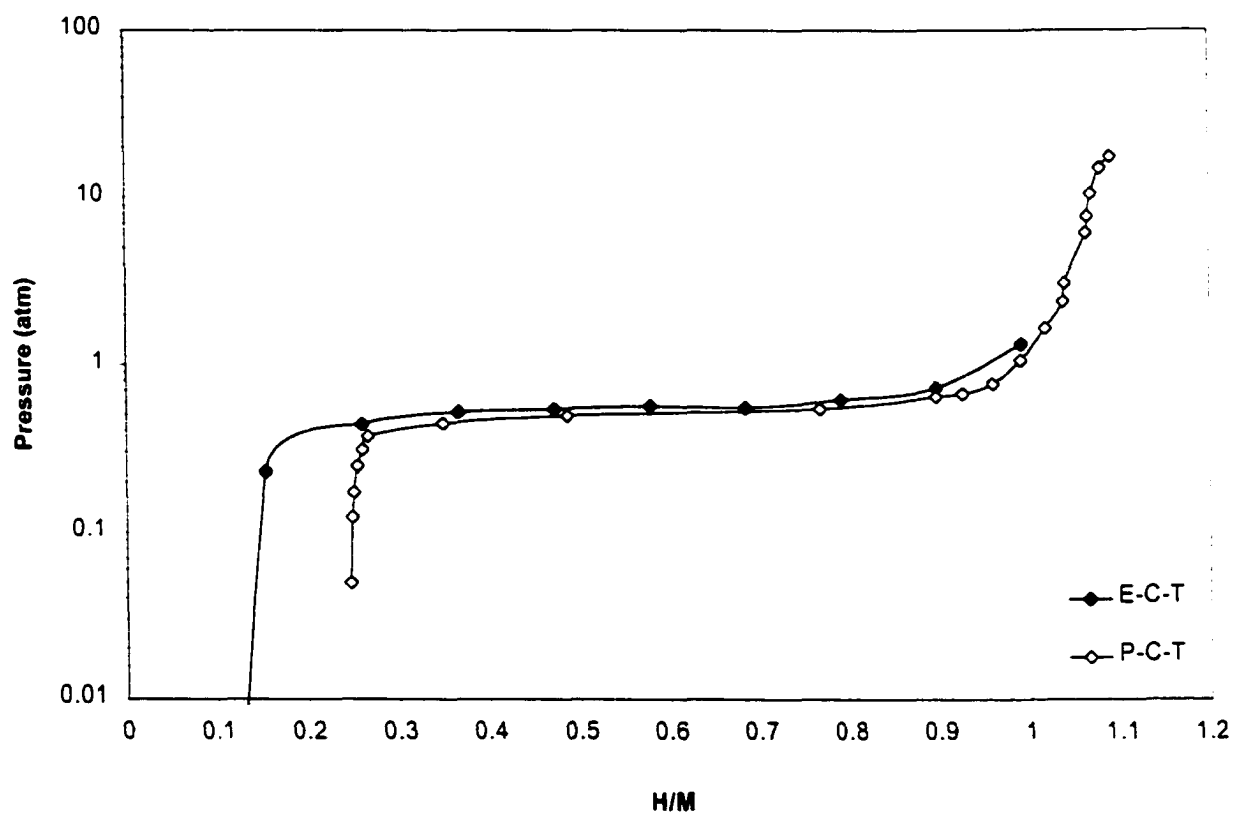


Fig. 5.1 Transition from electrochemical measurements to P-C-T curve for LaNi_{4.7}Al_{0.3} at room temperature

5.2 Determination of ΔH and ΔS from Electrochemical Reactions for $\text{LaNi}_{4.7}\text{Al}_{0.3}$ Electrode

The relationship between potential and temperature for a $\text{LaNi}_{4.7}\text{Al}_{0.3}$ electrode can be expressed as follows^[52]:

$$E_{eq} = -0.8788 - 3.0 \times 10^{-4}(T - 273) \quad (5.6)$$

According to electrochemical principles^[123]:

$$\Delta H_c^0 = 2F[E_{eq} - T(\frac{\partial E_{eq}}{\partial T})_p] \quad (5.7)$$

and

$$\Delta S_c^0 = 2F(\frac{\partial E_{eq}}{\partial T})_p \quad (5.8)$$

Substituting equation (5.6) into equations (5.7) and (5.8), and taking $R=8.314\text{J/mol.K}$, $F=96500\text{J/mol.K}$, we obtain $\Delta H_c^0 = -153.63\text{kJ/mol}$ and $\Delta S_c^0 = -57.83\text{J/mol.K}$ at 298K.

Combining equations (5.2) and (5.4), we can obtain the relationship between potential and hydrogen pressure:

$$E_{eq} = 1.1804 + (4.4666 \times 10^{-3} - 6.93606 \times 10^{-4} \ln T)T + 1.0788 \times 10^{-6} T^2 - 4.512 \times 10^{-10} T^3 + \frac{5.232}{T} - \frac{RT}{2F} (0.19198 - \frac{57.64383}{T}) - \frac{RT}{2F} \ln(\gamma_{H_2} P_{eq}) \quad (5.9)$$

$$\begin{aligned} \Delta H_c^0 &= 2F[E_{eq} - T(\frac{\partial E_{eq}}{\partial T})_p] \\ &= 2F(-1.18041 + 6.936 \times 10^{-4} T - 1.0788 \times 10^{-6} T^2 + 9.024 \times 10^{-10} T^3 \\ &\quad + \frac{10.464}{T} - 57.64383R) + RT^2 \left\{ \frac{\partial}{\partial T} [\ln(\gamma_{H_2} P_{eq})] \right\} \end{aligned} \quad (5.7a)$$

We assume that $\gamma_{H_2} \approx 1$. From the van't Hoff equation, we obtain^[123]:

$$\Delta H_p^0 = R \times \frac{\partial(\ln P_{eq})}{\partial(\frac{1}{T})} = -RT^2 \frac{\partial(\ln P_{eq})}{\partial T} \quad (5.10)$$

and

$$\Delta S_p^0 = - \frac{\partial(RT \ln P_{eq})}{\partial T} \quad (5.11)$$

Then

$$\begin{aligned} \Delta H_c^0 = 2F(-1.18041 + 6.93606 \times 10^{-4} T - 1.0788 \times 10^{-6} T^2 \\ + 9.024 \times 10^{-10} T^3 + \frac{4640}{T}) - 57.64383 R - \Delta H_p^0 \end{aligned} \quad (5.7b)$$

$$\begin{aligned} \Delta S_c^0 = 2F(4.4666 \times 10^{-3} - 6.93606 \times 10^{-4} \ln T - 6.93606 \times 10^{-4} \\ + 2.157 \times 10^{-6} - 1.3536 \times 10^{-9} T^2 - \frac{5.232}{T^2}) + \Delta S_p^0 \end{aligned} \quad (5.8a)$$

For T=298K.

$$\Delta H_p^0 = -195.29 - \Delta H_c^0 \quad (\text{kJ/mol})$$

$$\Delta S_p^0 = -53.45 + \Delta S_c^0 \quad (\text{J/mol.K})$$

Substituting the ΔH_c^0 and ΔS_c^0 into the above two equations.

$$\Delta H_p^0 = -195.29 + 153.63 = -41.66 \text{ kJ/mol}$$

$$\Delta S_p^0 = -53.45 - 57.83 = -111.28 \text{ J/mol.K}$$

Comparing the above data with the values of ΔH_p^0 (-38.038 kJ/mol) and ΔS_p^0 (-117.458 J/mol.K) obtained from manometric experiments^[124,125], we find reasonable agreement with relative errors being less than 10%, namely,

$$\eta(\Delta H_p^0) = \frac{-38.038 - (-41.66)}{-38.038} = -9.5\%$$

$$\eta(\Delta S_p^0) = \frac{-117.458 - (-111.28)}{-117.458} = -5.3\%$$

5.3 The Construction of a P-C-T Curve from Electrochemical Measurements of the Mg₂Ni Alloy

From the viewpoint of thermodynamic parameter calculations, the transformation from electrochemical measurements to a P-C-T curve has been shown to be valid for hydrogen storage materials in sections 5.1 and 5.2.

The measured equilibrium potentials for Mg₂Ni electrode and the calculated P_{eq} are given in Table 5.1, and the calculated P-C-T curve is shown in Fig.5.2. Therefore the P-C-T curve can be constructed in a relatively easy fashion, namely by electrochemical testing.

Table 5.1 Measured Potential, E_{eq}, and Calculated P_{eq} for MG-Mg₂Ni Electrodes

E _{eq} (V vs. Hg/HgO)	P _{eq} (atm)	Q (mAh/g)	H/M
-0.8771	1.35E-2	33.125	0.924
-0.8485	1.46E-3	66.250	0.792
-0.8280	2.97E-4	99.375	0.659
-0.8123	8.76E-5	132.500	0.526
-0.7977	2.81E-5	165.625	0.394
-0.7827	8.76E-6	198.750	0.228
-0.7569	1.18E-6	231.875	0.090
-0.6743	1.00E-9	264.073	0

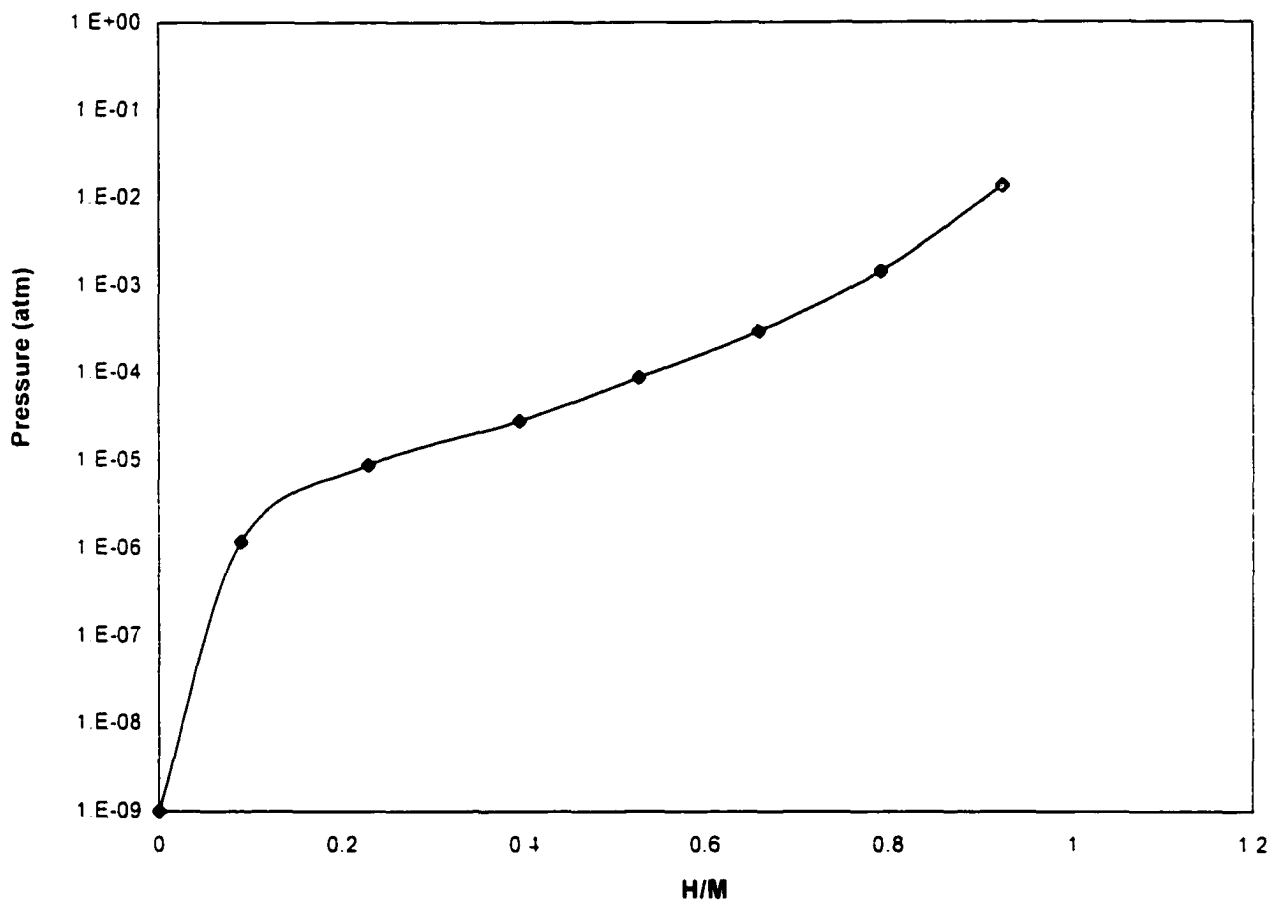


Fig. 5.2 P-C-T diagram for MG-Mg₂Ni electrode at room temperature (MG 25 hours and ball-to-weight ratio of 5:1)

CHAPTER 6 ACCELERATION MECHANISMS FOR HYDRIDING OF MG-Mg₂Ni ELECTRODES

There has been considerable interest in recent years in the synthesis of amorphous structures by high-energy ball milling of either elemental powder mixtures or powders of intermetallics. In the case of amorphization of intermetallics, defects introduced by the deformation during milling are responsible for raising the free energy of the crystalline compound to that of the amorphous phase. Milling the cast intermetallic leads to a number of effects which often act together simultaneously:

- (i) Production of dislocations and other defects;
- (ii) The material is crushed to powder. This increases the surface area. A subsequent stress will bond two particles together.
- (iii) The continuous sequences of shocking and welding enhance the mixing process. Diffusion processes are accelerated either by increasing the diffusion velocity (e.g. pipe and boundary diffusion) or by decreasing the diffusion path length (due to a smaller particle size).

6.1 Amorphization of Mg₂Ni by Ball Milling

XRD patterns for MG-Mg₂Ni alloy after different ball milling times are shown in Fig.6.1. The intensity of the Bragg peaks for Mg and Ni decreased rapidly after 0.5 hour of ball milling. Broad, diffuse peaks appeared after 25 hours of ball milling and the background level also increases to a significant degree, suggesting the formation of an

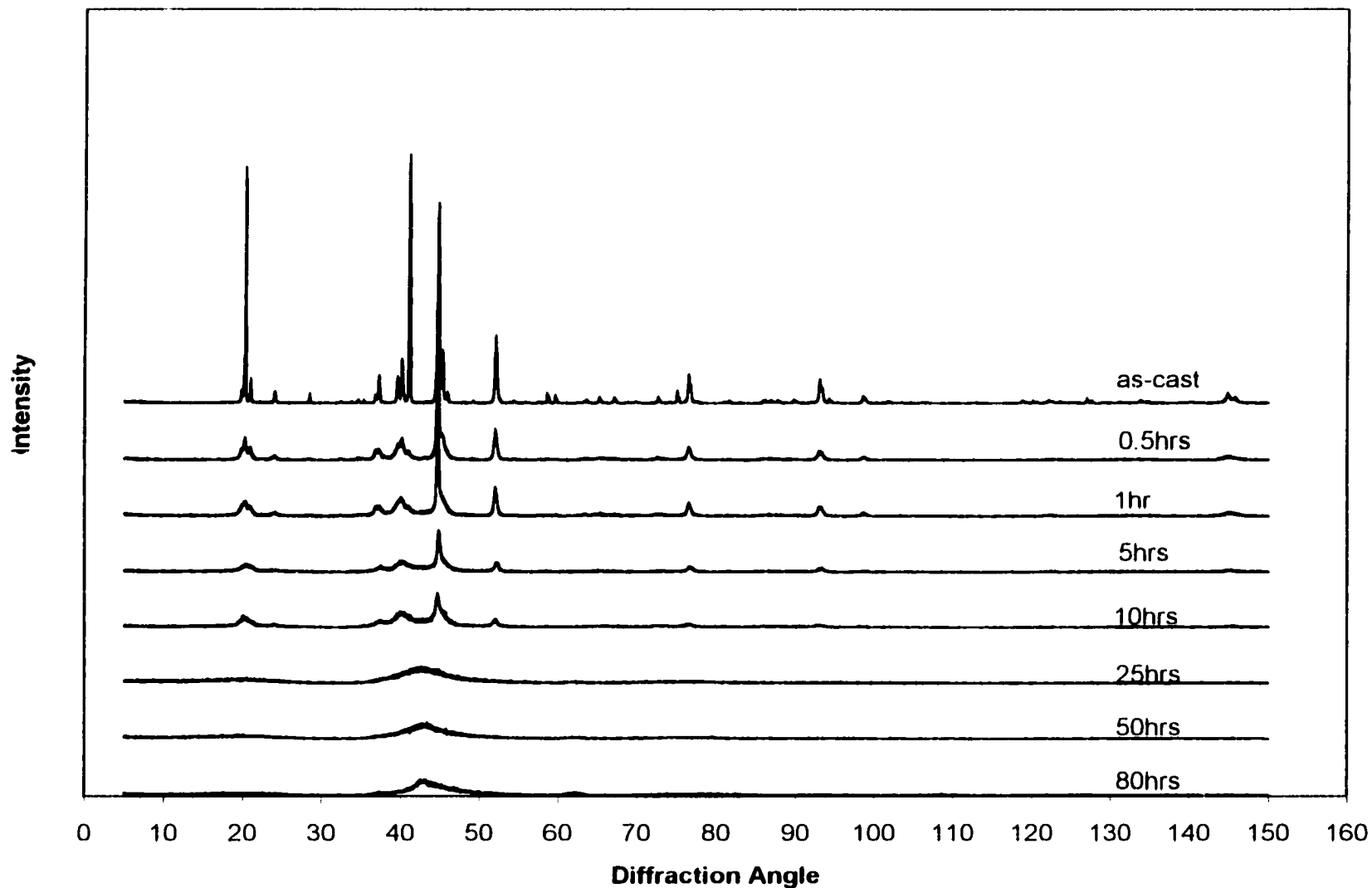


Fig. 6.1 X-ray diffraction patterns of Mg₂Ni alloy for different ball milling times at a ball-to powder weight ratio of 5:1

amorphous phase. The peaks corresponding to Mg₂Ni almost disappear, and those of nickel decrease in intensity and get broader, reflecting a well-known decrease in the crystallite size and an increase of internal strain as the result of the mechanical deformation and fracture. Experiment results (see section 4.1.2) showed that the discharge capacity increased to the maximum from the as-cast state to 25 hours of ball milling. Thus mechanical treatment is effective to improve the charge/discharge capacity of a negative electrode containing Mg₂Ni alloy.

Amorphization by MG consisted of energizing the crystalline solid by the severe plastic deformation that the ball milling provided. The plastic deformation and the shear impact introduced defects in the MG-Mg₂Ni, which will increase the free energy of the amorphous phase. The difference in free energy is the driving force for the hydriding acceleration. The question is, what defects can provide the required increase in free energy? The free energy differences between the crystalline compound and the amorphous phase are typically 5 to 20 kJ/mol. The stored energy of deformation from conventional deformation processes is rarely more than about 1 to 2 kJ/mol. The maximum value of the stored energy associated with a very high dislocation density of about $10^{14}/\text{cm}^2$ in cold rolled phase is estimated to be 2.2 kJ/mol. Amorphization in intermetallics by the plastic deformation supplied by ball milling is analogous to amorphization in intermetallics irradiated with energetic particles, such as electrons, ions or neutrons. While the energy increase due to chemical anti-site disordering was the major driving force behind the electron-irradiation introducing amorphization in intermetallic compounds, it is likely that anti-site disordering can provide sufficient energy for amorphization of intermetallics by milling in some cases. Contributions from

dislocations and grain boundaries were estimated to be 1 kJ/mol and 1.6-2.9 kJ/mol respectively. The remainder of the stored energy required for amorphization was believed to come from the disordering at anti-phase boundaries. The anti-site chemical disorder is the main source of energy storage in ball-milled intermetallics. The amorphous phase resulted if the free energy of the disordered compound exceeded the free energy of the amorphous state. Amorphization was not initiated until 25 hours ball milling. It was suggested that the additional stored energy required for the crystalline-to-amorphous transformation came from the grain boundary energy of the fine grain structure that evolved during milling of the disordered compound. Thus the significant contributions to stored energy come from two major sources: (1) anti-site disorder $\Delta G^{\text{disorder}}$, and (2) grain boundary energy of grains $\Delta G^{\text{grain-boundary}}$. The occurrence, or not, of amorphization by ball milling was consistent with estimated values of free energy, such that $\Delta G^{\text{disorder}} + \Delta G^{\text{grain-boundary}} \geq \Delta G^{\text{a-c}}$, where $\Delta G^{\text{a-c}}$ was the difference in free energy between the ordered crystalline and amorphous phase.

The internal energy of the compound is raised by ball milling as a result of atomic disordering in the compound. It is then suggested that if disordered compound attains a state of higher energy than amorphous state, a transformation to amorphous state will take place.

6.2 Surface Area and Particle Size

Various hydriding characteristics, such as kinetics of hydrogen absorption/desorption and rate of degradation during cyclic charge/discharge depend on the particle morphology.

In metal hydride systems, surface area and the particle size are important parameters for enhancement of hydrogen uptake through reduction in the activation time, temperature and pressure and improvement in the reaction kinetics of absorption/desorption reaction. Fig.6.2 shows the dependence of crystal size on ball milling time. During the initial few hours of ball milling, the crystal size decreases rapidly and then becomes stable with increasing ball-milling time. Fig.6.3 is scanning electron micrographs (SEM) of the Mg₂Ni alloy milled for different periods in a nitrogen atmosphere. The as-cast sample shows block-like, cleavage fracture morphology and an inhomogeneous particle size distribution. After milling for 0.5hours, the large particles are broken down, the particle shape becomes rounded, and the particle size is reduced. Only flaky particles of ~100µm in size were observed after 2 hours of ball milling. The flaky particles then gradually disappeared, and equiaxed particles of an irregular shape appeared together with very fine particles which may have been fragmented from the coarse particles. Many small particles adhere to the large ones. It is suggested that the coarse particles are formed from the cold welding of the flaky powders, and/or the fine powders are formed from the fragmentation of the coarse powders. After 15 hours ball milling, the coarse powders were completely broken up and only fine powders about 1µm in size are present. In general, the fragmentation of large, cold welded particles into the fine powders indicated the start of amorphization. The calculated particle size (from SEM micrographs) and the specific surface area (SSA) are given in Table 6.1.

A critical factor for hydrogen absorption by metals is the metal surface, which should be able to dissociate the hydrogen molecules and also allow easy penetration of

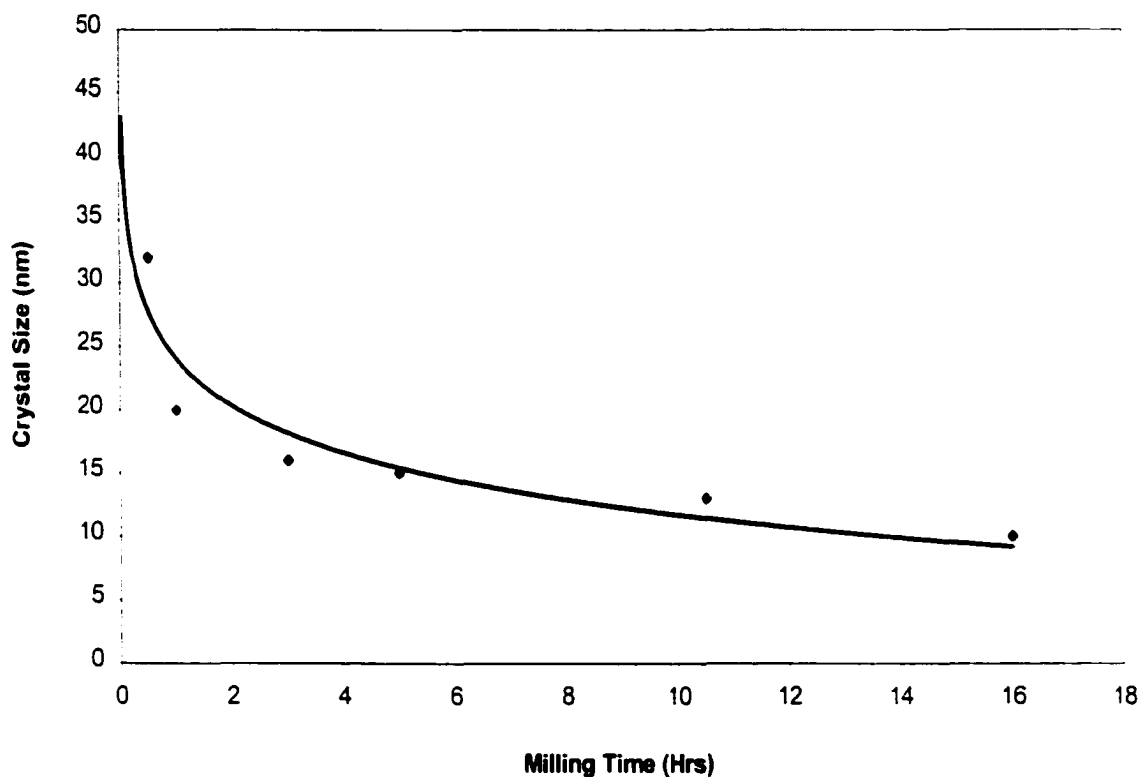
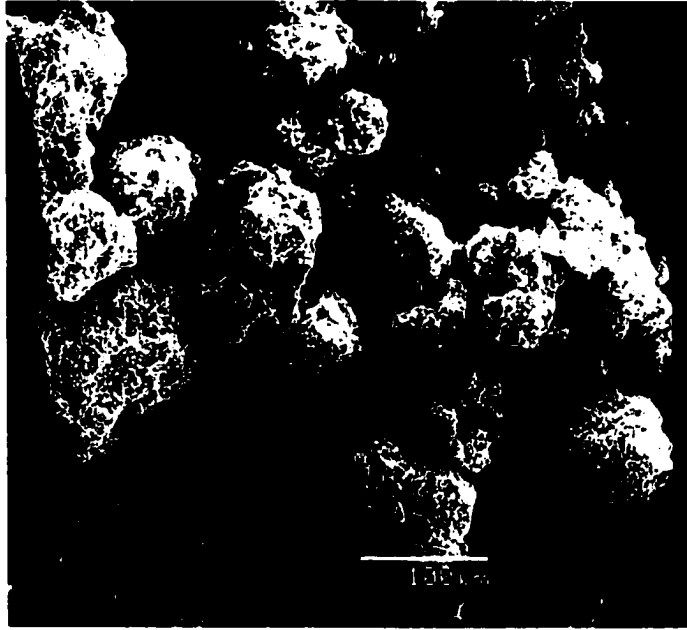
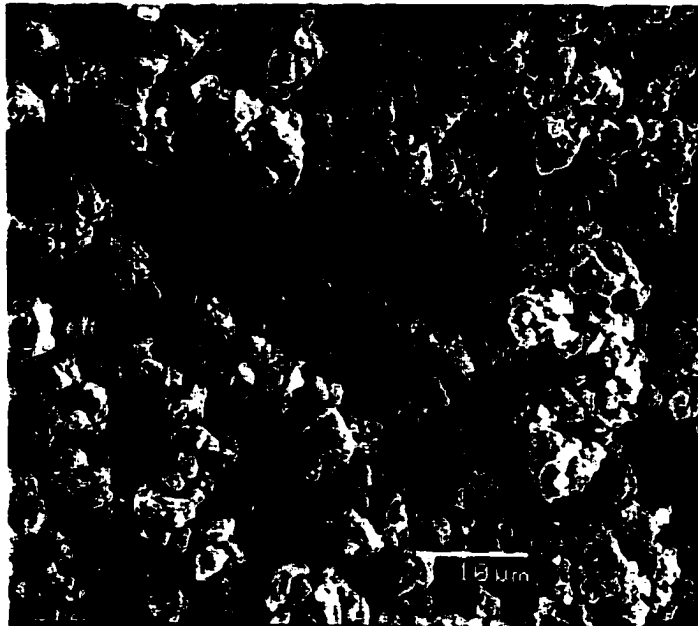


Fig. 6.2 Crystal size vs. ball milling time for Mg₂Ni alloy



(a) Ball milling time 0.5 hours

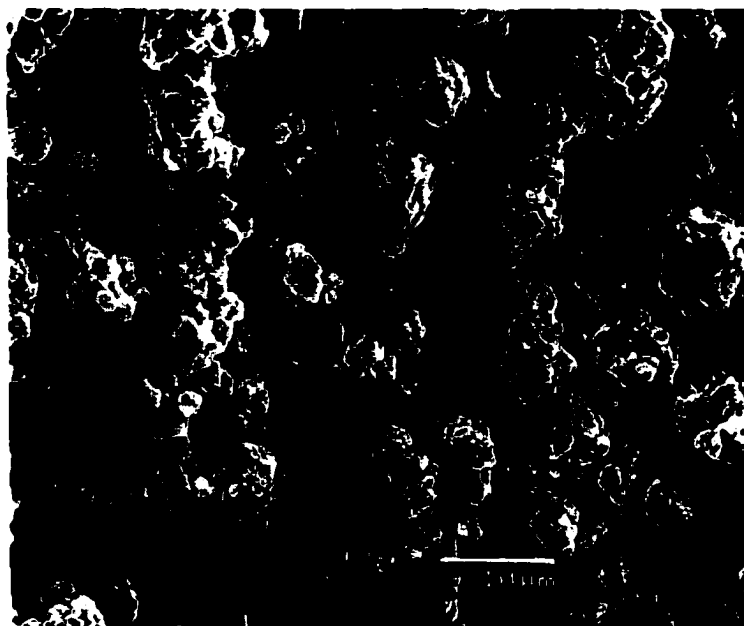


(b) Ball milling time 5 hours

Fig. 6.3 Particle morphologies of Mg₂Ni alloy at different ball milling times for Mg₂Ni alloy

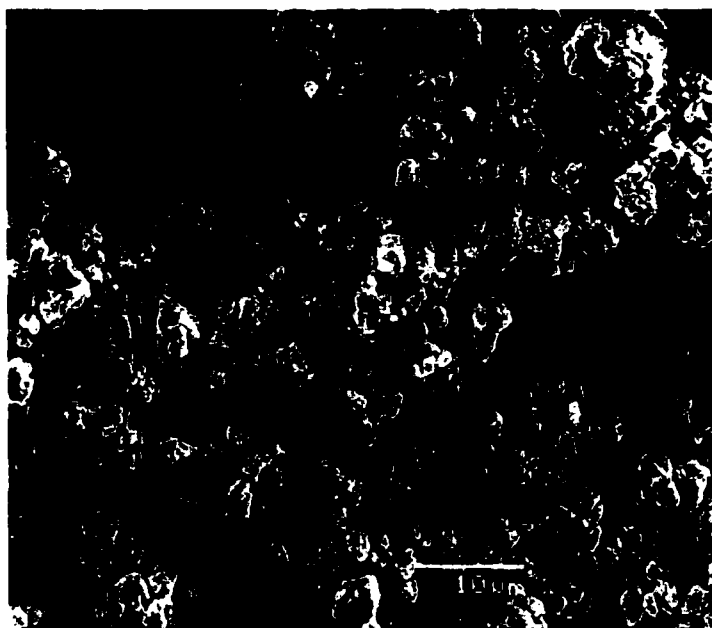


(c) Ball milling time 10 hours

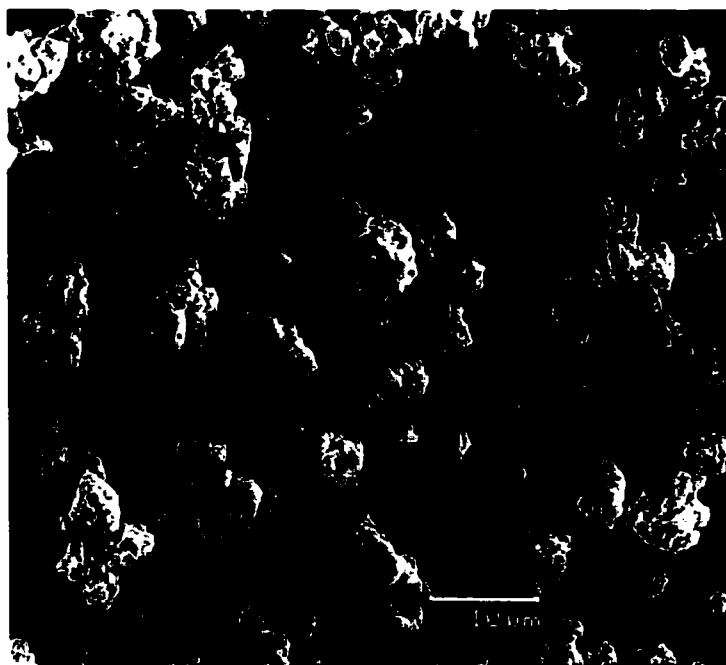


(d) Ball milling time 25 hours

Fig. 6.3 Particle morphologies of Mg₂Ni alloy at different ball milling times for Mg₂Ni alloy



(e) Ball milling time 50 hours



(f) Ball milling time 80 hours

Fig. 6.3 Particle morphologies of Mg₂Ni alloy at different ball milling times for Mg₂Ni alloy

hydrogen into the bulk. Ball milling constantly creates fresh surfaces during the process as a result of repeated cold welding and fracturing. This, and the high surface-to-volume ratios can explain why the activation procedure is much easier in the case of the ball-milled powder than for the non-ball milled material.

**Table 6.1 Particle Size and Specific Surface Area of Mg₂Ni
at Different Ball Milling Times**

TIME	AS-CAST	10 HOURS	25 HOURS	50 HOURS
Particle Size (μm)	25	1	0.75	0.5
SSA (m²/g)	0.0375	0.09375	0.1250	0.1870

The particle size decreased with ball milling time and, correspondingly, the SSA increased. For example, the SSA of MG-25 hours was three times larger than that of as-cast Mg₂Ni and this increased SSA lead to a 120 times larger discharge capacity of the Mg₂Ni electrode. The difference in reaction rate can be explained, in part at least by the fact that the smaller particle size resulted to a larger surface area per volume ratio and hence, more surfaces sites were available for the catalytic dissociation of hydrogen.

The final particle size was presumably due to repeated fragmentation: the particles are repeatedly flattened, fractured and re-welded. Finer particles facilitated the inter-diffusion between particles because the diffusion coefficient for the very fine particles was much larger than that for the usual bulk material, and also because the total distance required for diffusion is reduced. It is suggested that enhanced diffusion rate and a reduced diffusion distance both lead to a increased hydriding rate.

6.3 Internal Strain

When crystalline materials, including ordered alloys, are milled, they became at least partially disordered. And at same time, defects such as dislocations, stacking faults and grain boundaries are introduced. It was understandable that a large amount of internal energy would be stored and led to non-stabilization of the lattice, yielding the fine grain sizes and eventually an amorphous phase. Generally, the broadening of X-ray diffraction peaks can be ascribed to the change of crystal grain size and a heterogeneous strain. From the broadening of the Bragg peaks and using the Williamson and Hall method, it is possible to determine the crystallite size and internal strain components. This technique was used to analyze the X-ray powder patterns of ball-milled sample. Independent of the ball milling parameters, the crystal size decreased and the internal strain (Fig.6.4) increased with increasing ball-milling time.

As noted, the internal strain increased with increasing milling time. The longer the milling time, the more defects are introduced into the Mg₂Ni alloy. During the plastic deformation of intermetallics, different types of dislocation will occur, depending on the crystal structure. The defects introduce distortion of crystal lattice, as a result, internal strain will be produced. Storing sufficient energy as chemical disorder and the defects (including both crystal faults as well as grain boundary) can ultimately destabilize the crystal structure and lead to its conversion to a new structure, including the amorphous state.

The introduction of defects, disordering and internal strain gives rise to an increasing hydriding/dehydriding rates and capacity. Enhancements were found in kinetics of hydrogen absorption and in activation pretreatment (expressed by diffusion

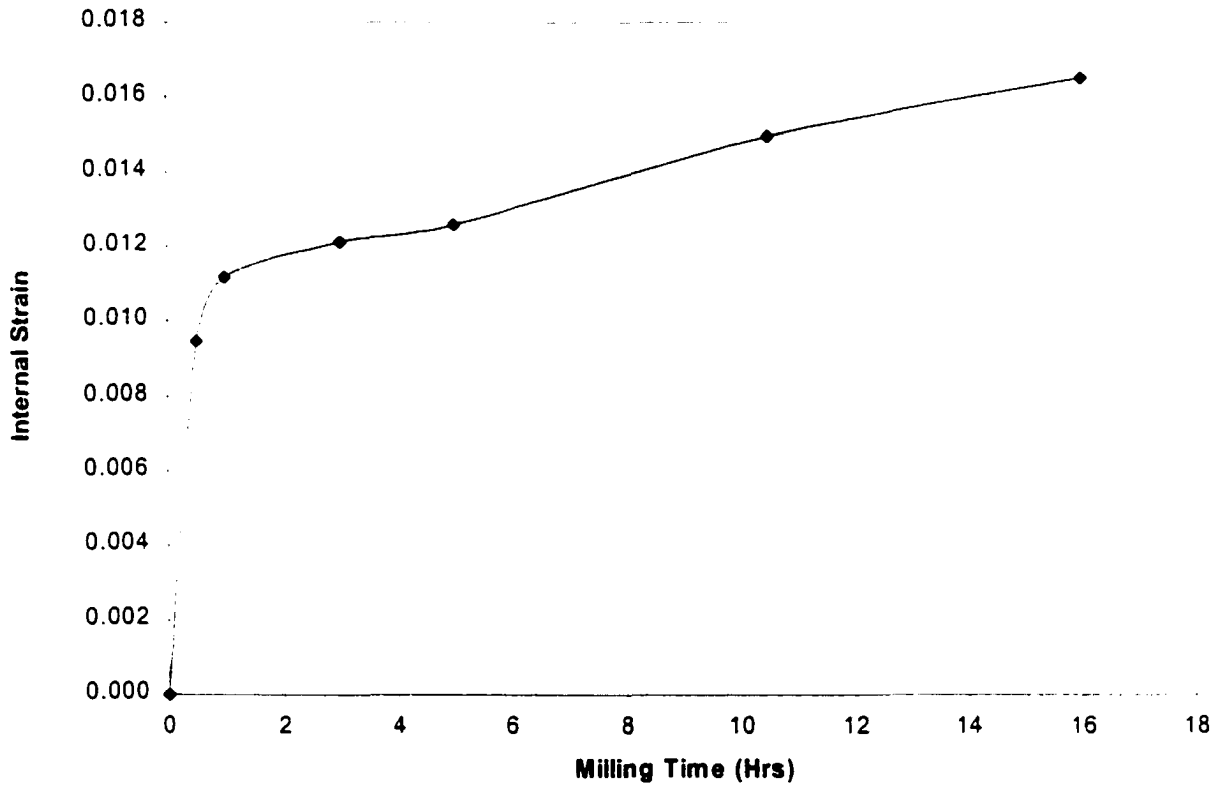


Fig. 6.4 Internal strain vs. ball milling time for Mg₂Ni alloy

coefficient, D_0). First of all, the internal strain increases with the decreasing crystal size (Fig.6.5). The internal strain introduced by the defects increased the activity of hydrogen absorbing/desorbing process. Since the exchange current density (Fig.6.6) and the diffusion coefficient (Fig.6.7) were directly proportional to the internal strain, the amount of absorbed hydrogen in ball-milled Mg₂Ni increased with the increasing internal strain (Fig.6.8). Because the surface area of the MG powders was larger than in the as-cast state, it was anticipated that the hydriding/dehydriding processes would be faster.

Collisions are the main mechanism by which energy was transferred to the powder during the ball milling process. Powder particles were trapped between colliding balls during milling and undergo deformation and/or fracture which define the ultimate structure of the powder. The nature of these processes depends upon the mechanical behavior of the powder compounds, their phase equilibrium and the stress during milling.

The equation for the energy transferred per unit of mass is as follows ^[126]:

$$\Delta E = \frac{[7.66 \times 10^{-2} R_p^{1.2} \rho^{0.6} E^{0.4}] d_b \omega_p^{1.2}}{\theta} \quad (6.1)$$

where R_p is the radius of the plate of the mill, E is the Young's modulus of the Mg₂Ni alloy, d_b is the diameter of the milling balls, ρ is the density of milling balls, ω_p is the angular velocity of the mill and θ is the surface density of materials.

In this study, d_b , ω_p , R_p , ρ and E are constants. When the ball-to-powder weight ratio increased, the surface density, θ , decreased. Thus the transferred energy per unit of mass increased. As a result, the ball-milled Mg₂Ni alloy has a high chemical potential, high hydriding/dehydriding rate (can be expressed by exchange current density, hydrogen diffusion coefficient) and corresponding by a high hydrogen capacity.

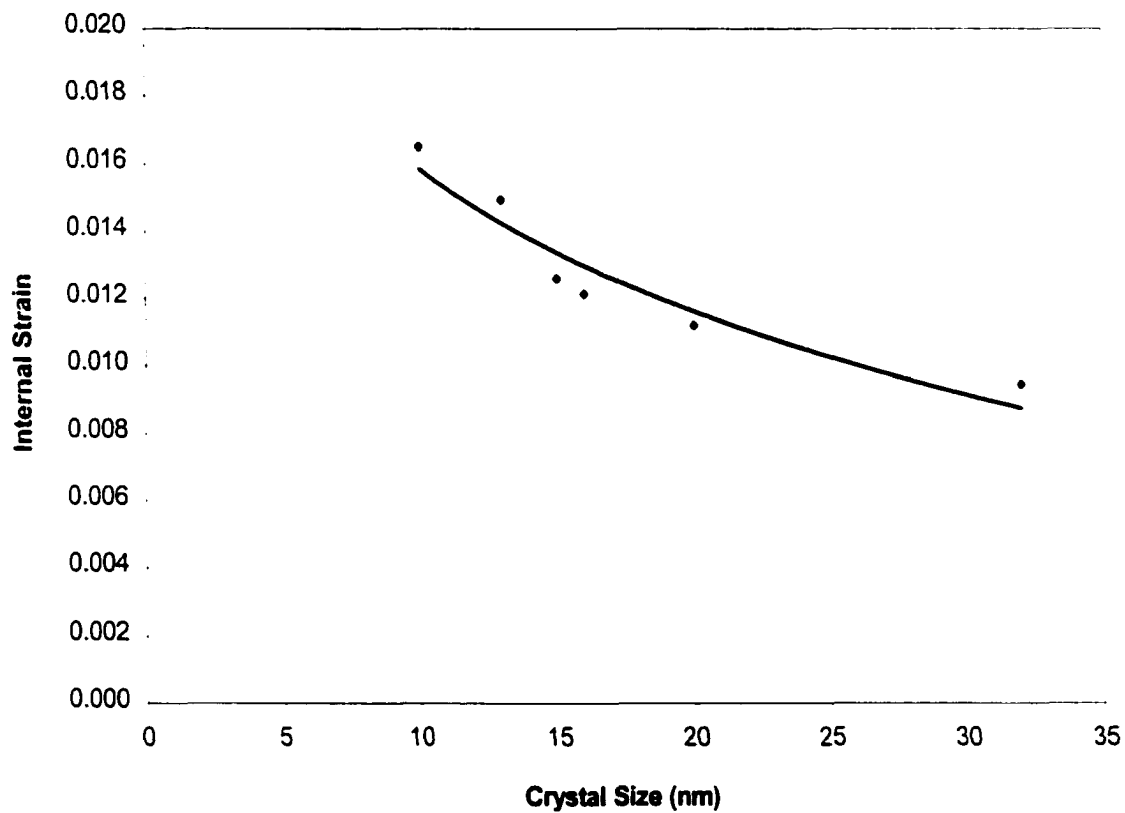


Fig. 6.5 Internal strain vs. crystal size for ball-milled Mg₂Ni alloy

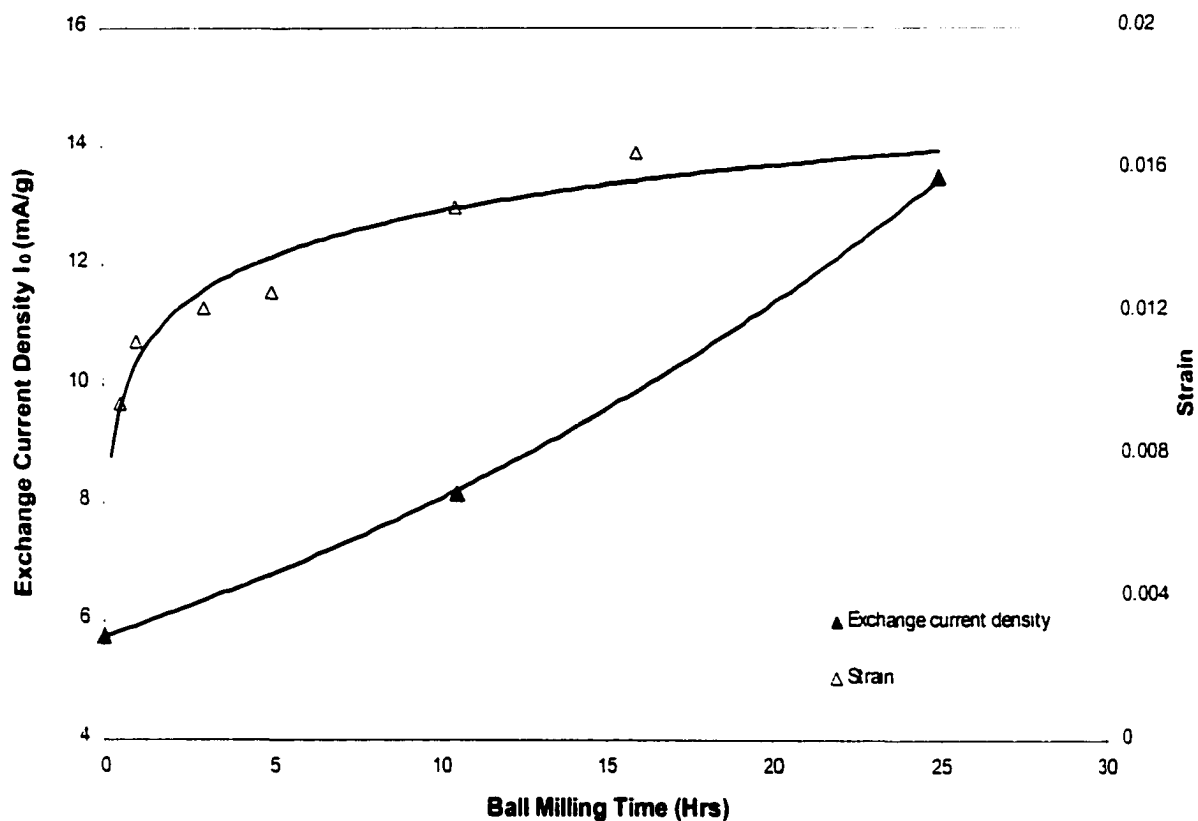


Fig. 6.6 Internal strain and exchange current density vs. ball milling time for Mg₂Ni alloy

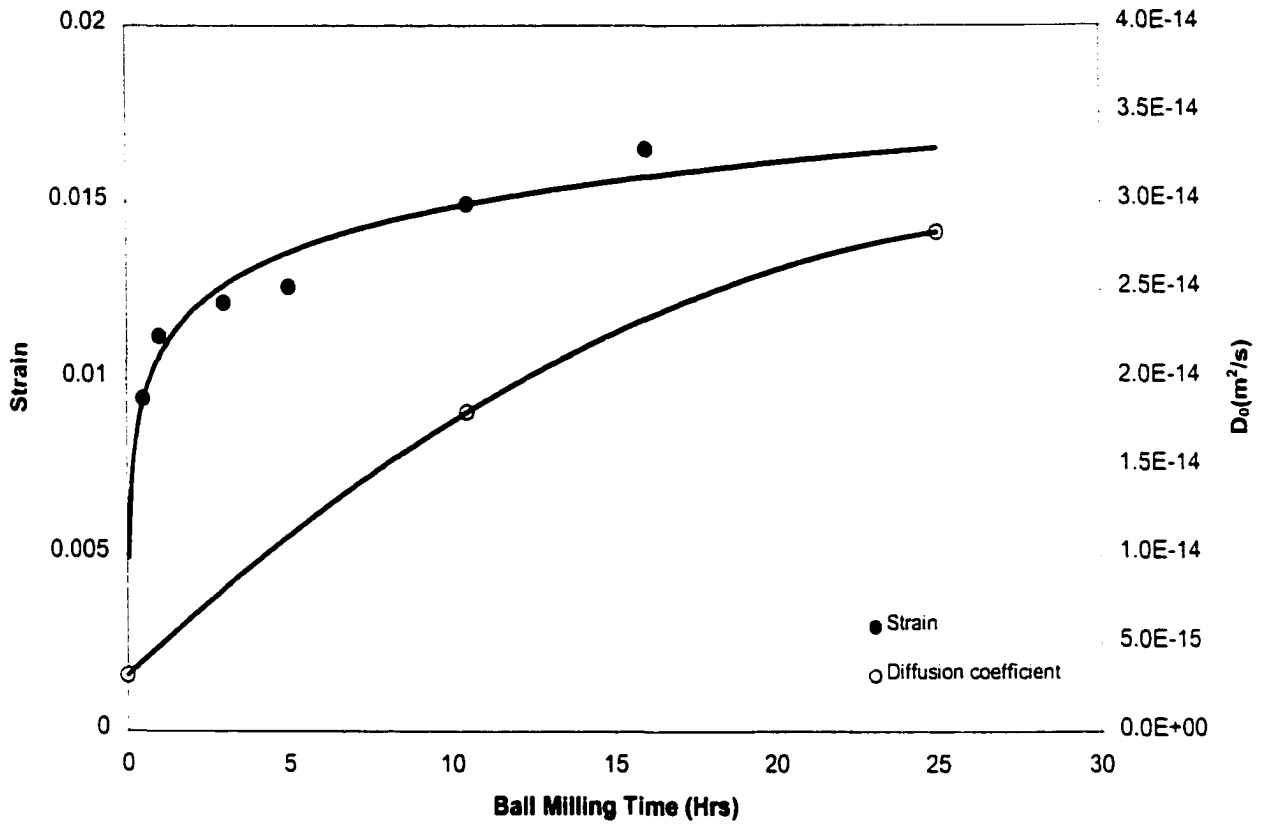


Fig. 6.7 Internal strain and hydrogen diffusion coefficient D_0 vs. ball milling time for Mg₂Ni alloy

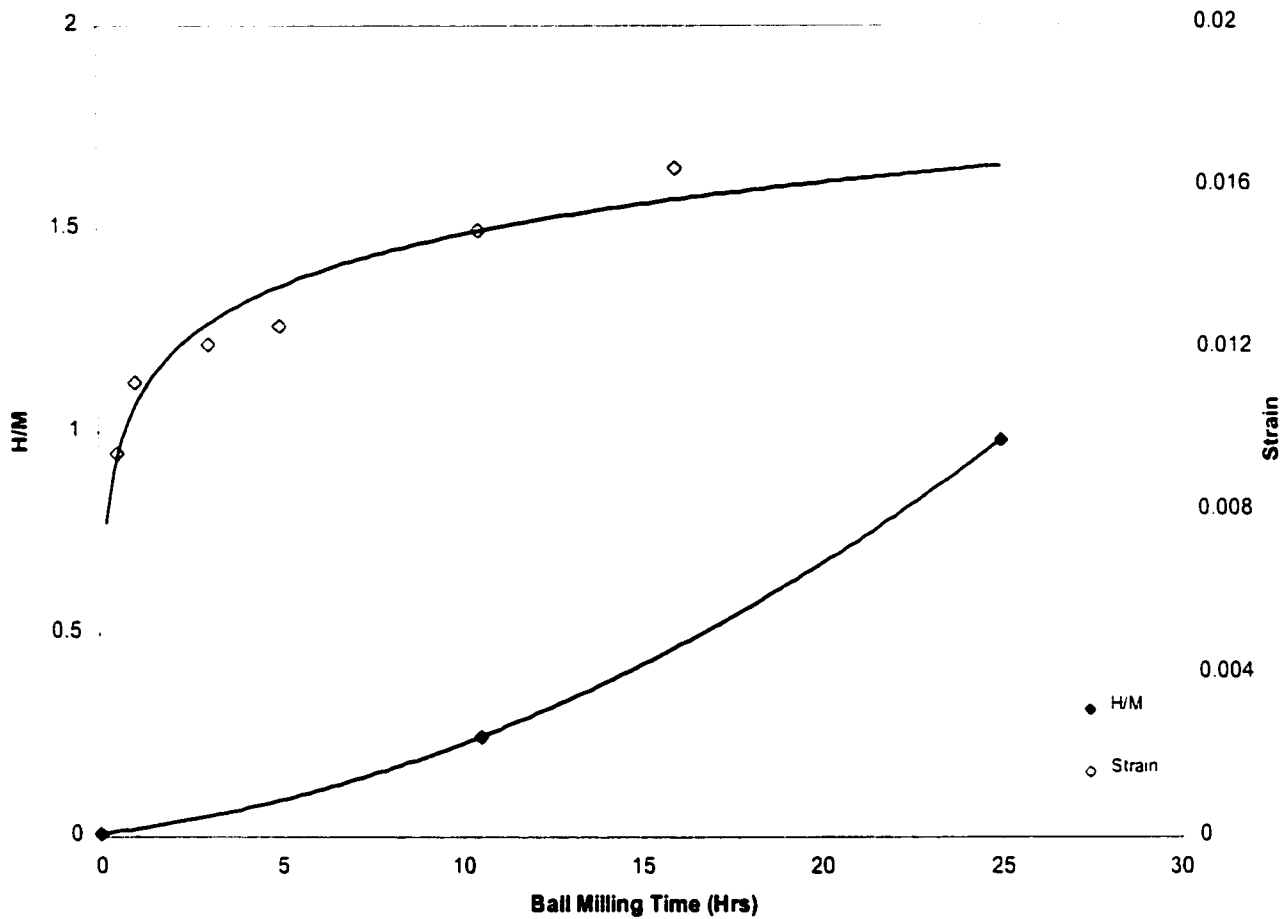


Fig. 6.8 Internal strain and hydrogen concentration, H/M, vs. ball milling time for Mg₂Ni alloy

CHAPTER 7 CONCLUSIONS AND RECOMMENDATIONS FOR FUTURE WORK

7.1 Conclusions

This thesis reports the effects of ball milling on the structure of Mg_2Ni powders and the electrochemical properties when they are incorporated into the negative electrode of a Ni-MH battery. The main conclusions to come from this study are as follows:

1. A high-energy ball milling treatment is effective in accelerating the hydriding/dehydriding processes for the Mg_2Ni alloy.
2. The hydriding/dehydriding characteristics of Mg_2Ni alloy can be evaluated by electrochemical measurements at room temperature rather than using the conventional P-C-T method in gaseous environment which requires high temperatures and pressures, and is time consuming.
3. A ball milling treatment increases significantly the discharge capacity. From a kinetics viewpoint, ball milling increases the exchange current density, i_0 , and hydrogen diffusion coefficient, D_0 . From a thermodynamic viewpoint, ball milling increases the internal strain energy, decreases the overpotential for the hydrogen absorption/desorption processes. Ball milling creates an amorphous structure, greatly reduces the particle size and correspondingly increases the specific surface area.
4. The discharge capacity increases from only about 2mAh/g in the as-cast state to a maximum value of 244mAh/g after 25 hours ball milling. It then decreases gradually for longer milling times. As ball milling proceeds, the Mg_2Ni powders are fragmented and the amount of

amorphous material continuously increases. However, re-welding, static electricity and contamination balance off some of the beneficial changes introduced by ball milling. There is an optimum milling time, 25 hours, which leads to the maximum discharge capacity. Kinetic parameters, including exchange current density, i_0 , hydrogen diffusion coefficient, D_0 , also reach a maximum for 25 hours ball milling.

5. The discharge capacity, Q , exchange current density, i_0 , and hydrogen diffusion coefficient, D_0 , increase with increasing ball-to-powder weight ratios from 1:1, 5:1 to 10:1. From the standpoint of discharge capacity, milling time and the amount of Mg_2Ni powder required to fabricate an electrode, ball milling for 25 hours at a ball-to-weight ratio 5:1 is considered to be the optimum treatment.
6. Ball milling treatments introduce defects into MG- Mg_2Ni , indicating a much higher free energy in the bulk of MG- Mg_2Ni . X-ray diffraction analysis shows that internal strain formed during the ball milling process increases linearly with ball milling time.
7. X-ray diffraction analysis showed that the Mg_2Ni changed from a crystalline to an amorphous structure with increasing milling time. The particle size and crystallite size reduce rapidly with milling time.
8. The addition of Cu or Ni into electrodes made from the MG- Mg_2Ni powders significantly increases the discharge capacity (from 224mAh/g to 330mAh/g and 244mAh/g for Cu and Ni respectively). The increased electrochemical activity of the electrodes with Ni is considered to result from the fact that hydrogen atoms bond more strongly with Ni atoms than Mg atoms. The increased capacity introduced from Cu is due to the increased electrical conductivity.
9. Thermodynamic parameters and P-C-T curves have been calculated and constructed from

measured E-C-T curves for a $\text{LaNi}_{4.7}\text{Al}_{0.3}$ alloy. For the first time, the P-C-T curves for a Mg_2Ni alloy have been constructed from the E-C-T curves at room temperature.

7.2 Recommendations for future work

1. Use TEM to observe the defects in the ball-milled Mg_2Ni alloy, and to determine the types, properties and the distribution of the defects, which will help in understanding the distribution of absorbed hydrogen and the discharge capacity acceleration by the ball milling treatment. The defects contribute to the energy for hydrogen absorption.
2. Determine the relationship between the strain that is introduced by the ball milling and the hydrogen absorption/desorption kinetics. The ball milling treatment introduces deformation in the Mg_2Ni alloy, causing distortion, cracking and defect generation.
3. Calculate the strain energy in the ball-milled Mg_2Ni alloy, and determine the critical required energy for the transformation from a crystalline to an amorphous state. The strain energy can be calculated using a theoretical elastic strain energy model developed by Sinha and Wallace^[127]. The free energy of the crystalline phase, G_C , the free energy increasing due to the defects, G_D , (introduced by ball milling) and the free energy of the amorphous phase, G_A , should be calculated using thermodynamic methods. Amorphization can occur when $G_C + G_D > G_A$.
4. To determine the mechanisms of hydrogen absorbing/desorbing, and the hydrogen penetration, distribution of hydrogen in the ball-milled Mg_2Ni alloy using SEM, TEM and X-ray diffraction methods. X-ray diffraction illustrates the phases formed by the hydriding reaction, and the TEM shows the change in the crystal structure.

Chapter 7 Conclusions and Recommendations for Future Work

5. To determine the mathematical relationship between the discharge capacity, Q , and the electrochemical parameters, such as, hydrogen diffusion coefficient, D_0 , exchange current density, i_0 , or overpotentials, η . The discharge capacity, Q , is thus calculated in terms of thermodynamic and kinetic parameters of the hydriding reactions.

REFERENCES

- [1] H. F. Bittner, C. C. Badcock, *J. Electrochem. Soc.*, **V30** (1983), 193C.
- [2] J. J. G. Willems, *Philips J. Res.*, **V39**, Suppl. (1984).
- [3] N. Cui, B. Luan, H. K. Liu, *Journal of Power Sources*, **V55** (1995), 263.
- [4] G. Sandrock, *Proceedings of the Symposium on Hydrogen and Metal Hydride Batteries*, **V94-27**, (1994), 1.
- [5] D. G. Ivey, *Hydrogen Storage with Zirconium Pseudobinarys*, M.A.Sc Thesis, University of Windsor (1982).
- [6] J. H. N. van Vucht, *Phillips Research Reports*, **V25** (1970), 133.
- [7] H. H van Mal, K. H. J Buschow, A. R. Miedema, *J. Less-Common Met.*, **V35** (1974), 65.
- [8] J. F. Lakner, F. S. Uribe, S. A. Steward, *J. Less-Common Met.*, **V72** (1980), 87.
- [9] A. C. Switendick, *Theoretical Studies of Hydrogen In Metals: Current Status and Further Prospects*, Sandia Laboratories Report, SAND 78-0250 (1978).
- [10] M. H. Mendelsohn, D. M. Gruen, *Nature*, **V269** (1977), 45.
- [11] M. H. Mendelsohn, D. M. Gruen, A. E. Dwight, *Materials Research Bulletin*, **V13** (1978), 1221.
- [12] K. H. J. Buschow, *J. Less-Common Met.*, **V42** (1975), 163.
- [13] J. J. Reilly, R. H. Wiswall, Jr., *Inorg. Chem.*, **V13** (1974), 218.
- [14] G. D. Sandrock, P. D. Goodell, *J. Less-Common Met.*, **V73** (1980), 161.
- [15] P. Fischer, *Materials Research Bulletin*, **V13** (1978), 931.
- [16] J. J. Reilly, *1st World Hydrogen Energy Conference*, **V4** (1979), 29
- [17] P. S. Rudam, *J. Less-Common Met.*, **V58** (1978), 231.
- [18] Q. D. Wang, *Proceedings of the 2nd Pacific Rim International Conference on Advanced Materials and Processing*, The Korean Institute of Metal and Materials. Korea (1995), 1529.
- [19] D. Shaltiel, *J. Less-Common Met.*, **V53** (1977), 117.
- [20] A. Pebler, E.A.Gulbransen, *Transactions of the AIME*, **V239** (1967), 1593.
- [21] J. J. Didisheim, *J. Less-Common Met.*, **V73** (1980), 355.

References

- [22] D. Fruchart, *J. Less-Common Met.*, **V73** (1980), 363.
- [23] J. B. Friauf, *Physical Review*, **V29** (1927), 34.
- [24] J. B. Friauf, *Journal of American Chemical Society*, **V49** (1927), 3107.
- [25] R. Wiswall, *Hydrogen In Metals II*, **V29** (1978), 201.
- [26] I. Jacob, *Solid State Communications*, **V23** (1977), 369.
- [27] M. H. Mendelsohn, D. M. Gruen, *J. Less-Common Met.*, **V78** (1981), 275.
- [28] I. Jacob, *J. Less-Common Met.*, **V73** (1980), 369.
- [29] H. Oesterreicher, *Materials Research Bulletin*, **V13** (1978), 83.
- [30] J. J. Reilly, R. H. Wiswall, *J. Inorg. Chem.* **V7** (1968), 2254.
- [31] J. J. Reilly, R. H. Wiswall, *J. Inorg. Chem.* **V6** (1967), 2220.
- [32] D. A. Ruhy, J. F. Nachman, A. N. Hammer, T. E. Duffy, *Reports SAN-1167-1(1979)*;
Energy Res. Abst. **V5** (1980), 27052.
- [33] H. Oesterricher, K. Ensslen, A. Kerlin, E. Bucher, *Mat. Res. Bull.* **V15** (1980), 275.
- [34] J. J. Reilly, *Z. Phys. Chem. N. F.* **V117** (1979), 155.
- [35] J. F. Stampfer, J.C.E.Holly, J. F. Shuttle, *J. Am. Chem. Soc.* **V82** (1960), 3504.
- [36] J. P. Darnaudery, B. Darriet, M. Pezat, *Int. J. Hydrogen Energy*, **V8** (1983), 705.
- [37] D. Lupu, A. Biris, E. Indrea, N. Alden, R.V. Bucur, M.Morariu, *Int. J. Hydrogen Energy*, **V8** (1983), 797.
- [38] D. Lupu, A. Biris, E. Indrea, N.Alden, *Int. J. Hydrogen Energy*, **V7** (1982), 783.
- [39] T. Hirata, T. Matsumoto, M. Amano, Y. Sasaki, *J. Less-Common Met.*, **V89** (1983), 85.
- [40] O. Bernauer, *Int. J. Hydrogen Energy*, **V13**, No.3 (1988), 181
- [41] J. J. Reilly, *Hydrogen: Its Technology and Implications*, **V2** (1977), 13.
- [42] D. G. Ivey, D. O. Northwood, *J. Mater. Sci.*, **V18** (1983), 321.
- [43] J. Koh, A. J. Goudy, *J. Less-Common Met.*, **V153** (1989), 89.
- [44] K. R. Clay, A. J. Goudy, *J. Less-Common Met.*, **V166** (1990), 153.
- [45] P. Selvan, B. Viswanathan, C. S. Swamy, *Int. J. Hydrogen Energy*, **V16** (1991), 23.
- [46] P. G. Goodell, *J. Less-common Met.*, **V89** (1983), 45.
- [47] H. C. Siegmann, L. Schlapbach, C.R. Brundle, *Phys. Rev. Lett.*, **V40** (1978), 972.
- [48] V. Walskirch, P. Zurcher, *Appl. Phys. Lett.*, **V33** (1978), 689.
- [49] L. Schlapbach, *Solid State Commun.*, **V38** (1981), 117.

References

- [50] F. J. Liu, G. Sandrock, *J. Alloys and Compounds*, **V190** (1992), 57.
- [51] E. H. Kisi, C. E. Buckley, *J. Alloys and Compounds*, **V185** (1992), 369.
- [52] W. Zhang, J. Cimato, A. J. Goudy, *J. Alloys and Compounds*, **V201** (1993), 175.
- [53] P. Y. Lee, C. N. Park, *J. Less-Common Met.*, **V89** (1983), 169.
- [54] S. Qian, D. O. Northwood, *Int. J. Hydrogen Energy*, **V15** (1990), 649.
- [55] N. A. Scholtus, W. K. Hall, *J. Chem. Phys.*, **V39** (1963), 868.
- [56] T. B. Flanagan, J. D. Clewley, *J. Less-Common Met.*, **V83** (1982), 127.
- [57] C. E. Ludin, F. E. Lynch, *Hydrides for Energy Storage*, Pergaman, Oxiford (1978), 385.
- [58] P. D. Goodell, G. D. Sandrock, *J. Less-Common*, **V73** (1980), 135.
- [59] E. W. Justi, H. H. Ewe, A. W. Kalberlah, *Energy Conver.*, **V10** (1970), 183.
- [60] M. A. Gutjahr, H. Buchner, K.P. Beccu, *Power Sources*, IV, S. H. Collins ed.
- [61] H. H. Ewe, E. W. Justi, K. Stephan, *Energy Conver.*, **V13** (1973), 109.
- [62] T. L. Markin, N. Bridger, R. Bennett, *Proceedings of 28th Power Source Symp.*, (1978), 136.
- [63] H. Ishikawa, *J. Electrochem. Soc.*, **V134** (1987), 558.
- [64] K. Saprun, K. C. Hong, M. A. Fetcenko, *U. S. Patent 4*, 551, 402 (1985).
- [65] A.J. Aldykiewicz, Jr., H.S. Isaacs, A.J. Davenport, *Extended Abstracts*, Abstract No.43. Spring Meeting, California, **V94-1** (1994), 71.
- [66] M. Ikoma, S. Hamada, N. Morishita, *Proceedings of the Symposium in Hydrogen and Metal Hydride Batteries*, **V94-27** (1994), 371.
- [67] N. Kuriyama, T. Sakai, H. Miyamura, *Vaccum*, **V47**, **No.6-8** (1996), 889.
- [68] L. Zhang, T. J. O'Hara, M. G. Michal, *Proceedings of the Symposium in Hydrogen and Metal Hydride Batteries*, **V94-27** (1994), 45.
- [69] X.G. Yang, Y. Q. Lei, J. Wu, *Transactions of NFSOC*, **V5**, **No.3** (1995), 61.
- [70] T. Sakai, H. Miyamura, N. Kuriyama, *J. Electrochem. Soc.*, **V137** (1990), 795.
- [71] Y. Chikano, M Kimoto, R. Maeda, *Proceedings of the Symposium in Hydrogen and Metal Hydride Batteries*, **V94-27** (1994), 403.
- [72] Z. Ye, T. Sakai, *Proceedings of the Symposium in Hydrogen and Metal Hydride Batteries*, **V94-27** (1994), 184.
- [73] A. Percheron-Guegan, M. Latroche, *Proceedings of the Symposium in Hydrogen and Metal Hydride Batteries*, **V94-27** (1994), 196.

References

- [74] J. Chen, Y. S. Zhang, *J. Mater. Res.*, **V9**, No.7 (1994), 1802-1804.
- [75] J. J. G. Willems, K. H. Bushow, *J. Less-Common Met.*, **V129** (1987), 13.
- [76] Y. Q. Lei, Z. P. Li, C. P. Chen, *J. Less-Common Met.*, **V172-174** (1991), 1265.
- [77] F. Meli, L. Schlapbach, *J. Less-Common Met.*, **V172-174** (1991), 1252.
- [78] L. Zaluski, A. Zaluska, *J. Alloys and Compounds*, **V217** (1995), 245.
- [79] H. Aoyagi, K. Aoki, T. Masumoto, *J. Alloys and Compounds*, **V231** (1995), 804.
- [80] G. M. Friedlmeier, J. C. Bolcich, *Int. J. Hydrogen Energy*, **V13**, No.8 (1988), 467.
- [81] L. Zaluski, A. Zaluska, P. Tessier, *J. Alloys and Compounds*, **V217** (1995), 295.
- [82] C. Iwakura, S. Nohara, H. Inoue, *Chem. Commun.*, (1996), 1831.
- [83] N. Cui, B. Luan, H. K. Liu, *12th Annual Battery Conf.on Applications & Advances*, Long Beach, CA 1997, 317.
- [84] T. Kohno, M. Kanda, *J. Electrochem. Society*, **V144**, No.7 (1997), L198.
- [85] L. Zaluski, A. Zaluska, J. O. Strom-Olsen, *J. Alloys and Compounds*, **V217** (1995), 245.
- [86] N. Cui, B. Luan, H. J. Zhao, *J. Alloys and Compounds*, **V233** (1996), 236.
- [87] T. Sakai, T. Hazama, H. Miyamura, *J. Less-Common Met.*, **V172-174** (1991), 1175.
- [88] T. Akiyama, T. Fukutani, H. Ohta, *AIChE Journal*, **V41**, No.5 (1995), 1349.
- [89] T. Sakai, *J. Electrochem. Society*, **V134**, No.7 (1987), 558.
- [90] Y. Q. Lei, J. J. Jiang, D. L. Sun, Q. D. Wang, *Symposium on Metal Hydrogen Systems*, Japan (1994).
- [91] T. Ikeya, K. Kumai, T. Iwahori, *J. Electrochem. Soc.*, **V140**, No.11 (1993), 3082.
- [92] M. P. Sridhar Kumar, W. L. Zhang, K. Petrov, *Proceedings of the Symposium in Hydrogen and Metal Hydride Batteries*, **V94-27** (1994), 111.
- [93] S. Yang, R. Ye, T. Huang, *Int. J. Hydrogen Energy*, **V13** (1986), 335.
- [94] A. W. Weeber, H. Bakker, *Physica B.*, **V153** (1988), 93.
- [95] T. Fukunaga, M. Mori, K. Inouard, *Mater. Sci. Eng. A*, **V134** (1991), 863.
- [96] J. Eckert, L. Schultz, K. Urban, *Appl. Phys. Lett.*, **V55** (1989), 117.
- [97] H. J. Fecht, E. Hellstern, Z. Fu, W. L. Johnson, *Metall. Trans. A*, **V21** (1990), 2333.
- [98] A. Kumar Singh, A. Kumar Singh, *J. Alloys and Compounds*, **V227** (1995), 63.
- [99] R. B. Schwarz, *Scripta Materialia*, **V34**, No.1 (1996), 1-4.
- [100] J. S. Benjamin, *Mater. Sci. Forum* (1992), 88-90.

References

- [101] J. S. Benjamin, *Metall. Trans. A*, **V1**(1970), 294.
- [102] M. J. Fleetwood, *Mater. Sci. & Technology*, **V2** (1986), 1176.
- [103] G. H. Li, Q. P. Kong, *Scripta Metallurgica et Materialia*, **V32**, No.9 (1995), 1435.
- [104] C. C. Koch, J. D. Whittenberger, *Intermetallics*, **V4** (1996), 339.
- [105] J. S. Benjamin, J. E. Volin, *Metall. Trans.*, **V5** (1974), 1929.
- [106] D. R. Maurice, T. H. Courtney, *Metall. Trans. A*, **V21** (1990), 289.
- [107] K. M. Lee, P. H. Shingu, *J. Alloys and Compounds*, **V241** (1996), 153.
- [108] Y. D. Dong, W. H. Wang, *Materials Science & Engineering*, **V134** (1991), 867.
- [109] M. Y. Song, *Int. J. Hydrogen Energy*, **V20**, No.3 (1995), 221.
- [110] P. Y. Lee, J. Jang, *J. Less-Common Met.*, **V140** (1988), 73.
- [111] R. B. Schwarz, C. C. Koch, *Appl. Phys. Lett.*, **V49** (1986), 146.
- [112] C. C. Koch, M. S. Kim, *J. Phys. (Paris), Colloq.*, **V46** (1985), C8.
- [113] J. H. Ahn, H. Chung, *Materials and Manufacturing Processes*, **V9**, No.4 (1994), 637.
- [114] M. S. El-Eskandarany, K. Aoki, *J. Less-Common Met.*, **V169** (1991), 235.
- [115] F. D. Manchester, D. Khatamian, *Materials Science Forum* **V31** (1988), 261.
- [116] W. L. Wasz, R. B. Schwarz, *Materials Science Forum*, **V225-227** (1996), 859.
- [117] P. Tessier, L. Zaluski, *Mat. Res. Soc. Symp. Proc.*, **V286** (1993), 209.
- [118] J. Chen, S. X. Dou, *J. Alloys and Compounds*, **V244** (1996), 184.
- [119] T. Kohno, S. Tsuruta, *J. Electrochem. Society*, **V143**, No.9 (1996), L198.
- [120] T. Kohno, M. Kanda, *J. Electrochem. Society*, **V144**, No.7 (1996), 2385.
- [121] G. Willamson, W. Hall, *Acta Metall.* **V22** (1953), 1.
- [122] ASTM Standard Test Method for Conducting Cyclic Potentiodynamic Polarization Measurements for Localized Corrosion Susceptibility of Iron-, Nickel-, or Cobalt- Based Alloys, *ASTM Standard G61-86*, re-approved 1993.
- [123] C. S. Wang, X. H. Wang, Y. Q. Lei, C. P. Chen, Q. D. Wang, *Int. J. Hydrogen Energy*, **V22**, No.12 (1997), 1117.
- [124] M. H. Mendelsohn, D. M. Gruen, *Nature*, **V269**, No.1 (1977), 45.
- [125] E. L. Huston, , *Journal of Less-Common Metals*, **V74** (1980), 435.
- [126] M. Magini, A. Iasonna and F. Padella, *Scripta Materialia*, **V34**, No.1 (1996), 13.
- [127] V. K. Sinha and W. E. Wallace, *J. Less-Common Metals*, **V91** (1983), 249.

VITA AUCTORIS

NAME: Hao (Shirley) Niu

PLACE OF BIRTH: Beijing, China

YEAR OF BIRTH: 1968

EDUCATION: Beijing NO.2 Middle School, Beijing, China
1984-1987 Diploma

University of Science & Technology Beijing, China
1987-1991 B. Sc in Material Science and Engineering

University of Windsor, Windsor, Ontario
1996-1999 M. Sc in Engineering Materials